

Analysis and modelling of respiratory metabolism in *Neisseria meningitidis*

Andrew Schofield

Submitted for the degree of Doctor of Philosophy

The University of York

Department of Biology

September 2012

Abstract

The bacterium *Neisseria meningitidis* is capable of respiration in both aerobic and microaerobic environments by reduction of oxygen and nitrite respectively. The respiratory chain and genetic regulation of this system are already well understood, but there are complex interactions between components which make predicting which respiratory path will be used difficult. To predict the respiratory behaviour of *N. meningitidis* a mathematical model has been constructed which describes the behaviour of the respiratory system using a set of differential equations. A novel combination of experimental data gathering and successive Bayesian fitting was then used to populate and parameterise the model. The resulting model and parameter probability distributions represent a working system for predicting respiratory behaviour in *N. meningitidis*. These parameter distributions represent new knowledge in the field as almost none of the values had been previously determined. The model also gives access to otherwise inaccessible information regarding the flux of electrons through the respiratory chain in addition to the reduction states of the respiratory enzymes during aerobic and microaerobic respiration.

Contents

1	Introduction	11
1.1	Biology of <i>Neisseria meningitidis</i>	11
1.2	Pathogenicity of <i>N. meningitidis</i>	12
1.3	Growth of <i>N. meningitidis</i>	14
1.4	Organisation of the Respiratory Chain of <i>N. meningitidis</i>	15
1.4.1	Nitric Oxide	19
1.5	Respiratory Enzymes in <i>N. meningitidis</i>	21
1.5.1	Cytochrome <i>cbb</i> ₃ oxidase	21
1.5.2	NorB Nitric Oxide Reductase	23
1.5.3	AniA Nitrite Reductase	24
1.6	Respiratory Electron Transporters in <i>N. meningitidis</i>	25
1.6.1	NADH Dehydrogenase	25
1.6.2	Cytochrome <i>bc</i> ₁ Complex	26
1.6.3	Cytochromes <i>c</i> ₄ , <i>c</i> _x and <i>c</i> ₅	26
1.6.4	Quinone Pool	28
1.7	Respiration Regulatory Proteins in <i>N. meningitidis</i>	29
1.7.1	NsrR - Nitrite Sensing Repressor Protein	29
1.7.2	FNR - Fumarate and Nitrate Reductase Regulator	30
1.7.3	NarQ/NarP - Nitrite Response Sensor/Regulator	30
1.8	Organisation of Respiratory Chains in Other Bacteria	31
1.8.1	The Respiratory Chain of <i>Paracoccus denitrificans</i>	32
1.8.2	The Respiratory Chain of <i>Escherichia coli</i>	33
1.8.3	The Respiratory Chain of <i>Rhodobacter sphaeroides</i>	34
1.9	Computational Biology and Systems Biology	35
1.10	Modelling	39
1.10.1	Modelling Respiratory Systems	39
1.10.1.1	Current Attempts to Model Respiratory Systems	39
1.10.1.2	Other Relevant Modelling	40
1.10.1.3	Important Considerations	40
1.10.2	Modelling Tools	41
1.11	Aims	42
2	Materials and Methods	44
2.1	<i>Neisseria meningitidis</i> Strains Used in This Work	44
2.2	Culturing <i>Neisseria meningitidis</i>	45
2.2.1	Growth of <i>Neisseria meningitidis</i>	45
2.2.2	Preparation of Antibiotic Selective Media	45
2.2.3	Preparation of Frozen Bacterial Stocks	45

2.2.4	Streaking Plates for OD to CFU Ratio Calculation	46
2.3	Measuring Oxygen Concentration	46
2.3.1	Calibration of Oxygen Electrode	48
2.4	Measuring Nitric Oxide Concentration	48
2.4.1	Calibration of Nitric Oxide Electrode	48
2.5	Measuring Nitrite Concentration (Giess Assay)	49
2.6	Nitric Oxide Production	50
3	Model - Construction and Parameters	53
3.1	Construction	53
3.1.1	Normalising the Data	54
3.1.2	Converting Biological Reactions into Differential Equations	54
3.1.2.1	Respiratory Substrates	55
3.1.2.2	Electron Transporters	58
3.1.2.3	Terminal Reductases	60
3.1.3	Assumptions and their Justifications	62
3.2	Parameters and their Prior Distributions	63
3.3	Solving Ordinary Differential Equations	70
3.4	Implementation of the Model in Software	70
3.5	Parameter Estimation	71
4	Parameter Estimation Methodologies	72
4.1	The Challenge of Parameter Estimation	72
4.2	Methods and Algorithms Used	73
4.2.1	Difference Functions	73
4.2.2	Monte Carlo Methods	75
4.2.2.1	Markov Chain Monte Carlo	75
4.2.3	Simulated Annealing	76
4.2.4	Approximate Bayesian Computation by Sequential Monte Carlo	79
4.2.5	Metropolis Hastings Monte Carlo	83
4.3	Validating the Parameter Estimation Algorithm	85
4.4	An Integrated Parameter Estimation Scheme Combining MHMC With Bayesian Inference	88
4.5	Implementing the Integrated Scheme	89
5	Oxygen Reduction in <i>N. meningitidis</i>	92
5.1	Reduction of Oxygen	92
5.1.1	Introduction	92
5.1.2	Experimental Results	93
5.1.2.1	Generation of Prior Probability Distributions	97
5.1.2.2	Initial Parameter Estimation Results	98
5.1.2.3	Secondary Prior Probability Distributions	106
5.1.2.4	Secondary Parameter Estimation Results	109
5.1.2.5	Analysis of Convergence	114
5.1.2.6	Analysis of Correlation	114
5.1.3	Discussion	118

6 Nitric Oxide Reduction in <i>N. meningitidis</i>	120
6.1 Aerobic Nitric Oxide Reduction	120
6.1.1 Introduction	120
6.1.2 Experimental Results	122
6.1.2.1 Prior Probability Distributions	125
6.1.2.2 Parameter Estimation Results	129
6.1.2.3 Adapted Parameter Estimation Protocol	130
6.1.2.4 Secondary Parameter Estimation Results	131
6.1.2.5 Tertiary Parameter Estimation Results	133
6.1.2.6 Analysis of Convergence	137
6.1.2.7 Analysis of Correlation	142
6.1.3 Discussion	142
6.2 Aerobic Nitric Oxide Reduction in <i>nsrR</i> ⁻ mutant	146
7 Nitrite Reduction in <i>N. meningitidis</i>	149
7.1 Microerobic Nitrite Reduction	149
7.1.1 Introduction	149
7.1.2 Experimental Results	151
7.1.3 Prior Probability Distributions	153
7.1.4 Parameter Estimation Results	156
7.1.5 Second Parameter Estimation Results	158
7.1.6 Analysis of Convergence	165
7.1.7 Analysis of Correlation	166
7.1.8 Discussion	166
7.1.8.1 Using Nitrite Posterior Parameters	168
8 Discussion and Completed Model	172
8.1 Amalgamation of Cytochromes	174
8.2 Parameter Changes Throughout this Work	177
8.3 Testing the Model	179
8.3.1 Addition of Nitric Oxide to an <i>nsrR</i> ⁻ mutant	179
8.3.2 <i>In silico</i> cyt Knockouts	180
8.4 Single Parameter Scaling Fits	183
8.5 Concluding Remarks	184
9 AniA and NorB Expression in <i>N. meningitidis</i>	187
A Appendix	191
A.1 Monte Carlo Estimation of π	191
A.2 Adaptive step sizes and numerical instability	192
A.3 Affinity of <i>cbb₃</i> for Oxygen	192
A.4 Software Used During this Work	193
References	195

List of Figures

1.1	Complete denitrification.	15
1.2	Layout of the components of the respiratory system in <i>Neisseria meningitidis</i>	17
1.3	Regulation of respiratory components in <i>Neisseria meningitidis</i>	20
1.4	The <i>cbb₃</i> oxidase.	22
1.5	3D Structure of <i>cbb₃</i> oxidase.	23
1.6	The modified Q-cycle used by the bacterial <i>bc₁</i> complex.	27
1.7	Structure of the ubiquinone molecule.	29
1.8	Branched electron transport chains of <i>N. meningitidis</i>	31
1.9	Branched electron transport chains of <i>Paracoccus</i> species.	32
1.10	Branched electron transport chains of <i>E. coli</i>	33
1.11	Branched electron transport chains of <i>Rhodobacter sphaeroides</i>	35
1.12	Systems biology cycle.	37
1.13	System complexity.	38
2.1	Exploded view of the oxygen electrode	47
2.2	Oxygen electrode chamber with nitric oxide probe inserted	49
2.3	NO making apparatus.	51
3.1	Electron flow through the respiratory chain	62
3.2	Oxygen Diffusion Rates	68
4.1	Pseudo-code showing how rejection sampler works.	77
4.2	Example simulated annealing temperature schedule	78
4.3	Schematic diagram showing the technique used to generate a spread of parameters using a synthetic chromosome.	79
4.4	Simulation results of the Lotka-Volterra validation run.	87
4.5	MHMC results of the Lotka-Volterra validation run.	88
4.6	The Integrated Bayesian Parameter Estimation Scheme	90
5.1	Oxygen reducing electron transport chain of <i>N. meningitidis</i>	93
5.2	Highly repeatable oxygen reduction	94
5.3	Aerating oxygen reducing cultures with significant delay	95
5.4	Oxygen Reduction in <i>Neisseria meningitidis</i>	96
5.5	Prior probability distributions for oxygen reduction	99
5.6	Oxygen Reduction in <i>Neisseria meningitidis</i>	101
5.7	Simulation <i>F</i> value improves as parameter estimation progresses	102
5.8	Individual parameter trajectories for multiple runs on the same experimental dataset	103

5.9	Posterior probability distributions for oxygen reduction	105
5.10	Prior probability distributions for oxygen reduction	107
5.11	Oversampled Posterior Distributions	110
5.12	Posterior probability distributions for oxygen reduction	111
5.13	Oxygen Reduction in <i>Neisseria meningitidis</i>	113
6.1	Nitric oxide reducing electron transport chain of <i>N. meningitidis</i> . .	121
6.2	Nitric Oxide Reduction in <i>Neisseria meningitidis</i>	123
6.3	Nitric Oxide Reduction in <i>Neisseria meningitidis</i>	124
6.4	Nitric Oxide Reduction in <i>Neisseria meningitidis</i>	125
6.5	Nitric Oxide Reduction in <i>Neisseria meningitidis</i>	126
6.6	Prior probability distributions for aerobic nitric oxide reduction . .	128
6.7	Nitric Oxide Reduction in <i>Neisseria meningitidis</i>	131
6.8	Nitric Oxide Reduction in <i>Neisseria meningitidis</i>	132
6.9	Nitric Oxide Reduction in <i>Neisseria meningitidis</i>	133
6.10	Local Fitness Minima During Parameter Estimation.	135
6.11	Nitric Oxide Reduction in <i>Neisseria meningitidis</i>	136
6.12	Posterior Distributions for Datasets 1 and 4	138
6.13	Addition of Nitric Oxide to Aerobic Cultures.	145
6.14	Addition of Nitric Oxide to <i>in silico</i> norB mutant.	145
6.15	Reduction States During Nitric Oxide Reduction.	147
6.16	Nitric Oxide Reduction in an nsrR Mutant.	148
7.1	Nitrite reducing electron transport chain of <i>N. meningitidis</i>	150
7.2	Nitrite Reduction in <i>Neisseria meningitidis</i>	152
7.3	Nitrite Reduction in <i>Neisseria meningitidis</i>	153
7.4	Prior probability distributions for microaerobic oxygen and nitrite reduction	154
7.5	Solved Nitrite Reduction in <i>Neisseria meningitidis</i>	156
7.6	Reduction States During Nitrite Reduction	157
7.7	Effect of Nitrite Addition on Aerobically Respiring Cultures . . .	158
7.8	Reduction States During Nitrite Reduction	159
7.9	Prior probability distributions for microaerobic oxygen and nitrite reduction	160
7.10	Effect of Nitrite Addition on Aerobically Respiring Cultures . . .	161
7.11	Reduction States During Nitrite Reduction	162
7.12	Posterior probability distributions for microaerobic oxygen and nitrite reduction	163
7.13	Aerobic Oxygen Respiration with Nitrite Posteriors	169
7.14	Aerobic Oxygen Respiration with Nitric Oxide Addition with Nitrite Posteriors	170
7.15	Nitrite Reduction using Modified Nitrite Posteriors	171
8.1	Final Posterior probability distributions	176
8.2	Nitric Oxide Reduction in an nsrR Mutant.	179
8.3	Nitric Oxide Addition to In silico nsrR Mutant	180
8.4	In Silico Cytochrome Mutant	181
8.5	In Silico Cytochrome Mutant Redox States	182
8.6	Improved Fit with Scaling Factor	183

8.7	Dataset Scaling Factors	185
9.1	Effect of Nitric Oxide on NsrR and FNR Dependent Gene Expression	189
9.2	Effect of Expression of AniA and NorB	190
A.1	Circle circumscribed by a square	191
A.2	Lineweaver-Burk Plot for Oxygen Reduction in <i>Neisseria meningitidis</i> .	193

List of Tables

1.1	The reductions catalysed by the respiratory enzymes in <i>N. meningitidis</i>	16
2.1	Bacterial strains and sources	44
2.2	Final antibiotic concentrations	45
2.3	Sodium Nitrite concentrations used to calibrate ISO-NOP Nitric Oxide sensor.	49
2.4	Chemicals needed for preparation of Nitric Oxide solution.	51
3.1	Model parameters	64
5.1	First Prior Probability Table	98
5.2	Second Prior Probability Table	108
5.3	Posterior Probability Statistics	112
5.4	Gelman-Rubin Convergence Statistic	115
5.5	Regression Analysis of Oxygen Reduction Parameters	116
5.6	Regression Analysis of Oxygen Reduction Parameters	117
6.1	Prior Probability Table	127
6.2	Posterior Probability Statistics	139
6.3	Gelman-Rubin Convergence Statistic	140
6.4	Regression Analysis of Nitric Oxide Reduction Parameters	141
6.5	Regression Analysis of Nitric Oxide Reduction Parameters	143
7.1	Prior Probability Table	155
7.2	Posterior Probability Statistics	164
7.3	Gelman-Rubin Convergence Statistic	165
7.4	Regression Analysis of Nitrite Reduction Parameters	167
8.1	Model parameters	175
8.2	Change in Parameter Values	177
8.3	Dataset Scale Factors	184

Acknowledgements

I would like to thank Dr James Moir and Dr Jamie Wood for their guidance and supervision. Their knowledge and encouragement has been appreciated throughout this project and they were always on hand to help work through any problems.

I would also like to thank Dr Leo Caves and Dr Gavin Thomas for being members of my training committee. They helped keep my project on track and encouraged me to continually improve the project as it progressed.

I thank all the members of the Moir Lab and others - Mrs Diana Quinn, Mrs Judith Hawkhead, Dr James Edwards, Dr Stacey Edmonson, Chiara Catenazzi and Xi Li for their advice and friendship throughout the project.

My thanks to all at York Community Church, but especially those in "The Other Monday Home Group" for their prayer and support over the past 4 years.

Finally I would like to thank all my friends and family for their support throughout the project. I would especially like to thank my wife Jenni for putting up with me for the last 3 years without complaint and for keeping me sane. Without her I would be nothing.

Chapter 1

Introduction

1.1 Biology of *Neisseria meningitidis*

Neisseria meningitidis is a Gram-negative, bean-shaped diplococcal bacterium¹, surrounded by a lipid membrane containing outer membrane proteins and lipopolysaccharides¹. When pathogenic, the bacteria also has a polysaccharide capsule attached to the membrane¹. It is non-spore forming, non-motile but pilated, and lives as an obligate human pathogen (humans being its only host)². *N. meningitidis* inhabits the mucosal membranes primarily in the respiratory tract, and it is estimated that up to 20-25% of the population have this bacteria in their nasopharynx while being asymptomatic²⁻⁴.

The *Neisseria* genus contains a number of non-pathogenic species which are part of the normal human flora including *N. subflava*, *N. flavescens*, *N. lactamica* and *N. sicca*⁵. Two species of *Neisseria* are the causative agents of human diseases, *N. meningitidis*, which causes bacterial meningitis and *N. gonorrhoea* which causes gonorrhoea. Being β -proteobacteria², the *Neisseria* genus is also related to a number of other pathogenic bacteria including *Bordetella*, *Burkholderia* and *Spirillum*. This taxa also includes ammonia-oxidising bacteria such as *Nitrosomonas*⁶.

N. meningitidis is classified into 13 different serogroups based on the differences in lipopolysaccharides, capsules, outer membrane proteins and adhesion molecules^{1,2,7}. 3 of these 13 serogroups are the main cause of meningococcal

meningitis, with serogroups B and C being the most prevalent¹. Vaccines for serogroup C are available, but serogroup B currently has no effective vaccine, as it mimics human antigens² and it is a poor immunogen⁸. The polysaccharide capsule of serogroup B is composed of sialic acid which has structural homology to the polysialylated form of the neural cell adhesion molecule^{9,10}. In addition to being the causative agent for meningococcal meningitis, *N. meningitidis* also causes septicaemia and the combination has a mortality rate of $\approx 10\%$ even with therapy^{1,2}.

N. meningitidis is dependent on a source of iron, and must source this from its environment¹¹. It does this by directly capturing iron from the host via human transferrins¹¹⁻¹³ and lactoferrin¹¹. This capture is brought about by membrane surface receptors that can bind the transferrins which then go on to internalise the iron into the bacterium for growth¹⁴.

1.2 Pathogenicity of *N. meningitidis*

Meningitis is caused by *N. meningitidis* entering the bloodstream and travelling to the meninges, a set of membranes that envelope the central nervous system, where the bacteria goes on to cause inflammation. Once it has entered the bloodstream, *N. meningitidis* is capable of switching its capsule by phase-variation to avoid host-immune detection^{15,16}. After colonisation by the bacterium, in order to enter the bloodstream, it must first adhere to the mucosal tissue. This is facilitated by adhesion molecules on the outer membrane and by pili, with the latter being the primary source of adhesion^{1,7}. Once the bacteria are adhered to the mucosal cells, additional contacts are made with the outer membrane proteins. Interestingly, the presence of the polysaccharide capsule, which is required for survival in the bloodstream, interferes with these additional contacts². *N. meningitidis* invades the bloodstream by being endocytosed by the mucosal epithelial cells, a process which is triggered by the pili and outer membrane proteins on the bacteria.

N. meningitidis is able to survive in the bloodstream (typically an antimicrobial environment) mainly by virtue of its polysaccharide capsule as this is able to protect the bacteria against various immune responses by the host including complement-mediated bacteriolysis and phagocytosis by neutrophils¹. Despite these protective features, specific antibodies *do* provide full protection against the bacteria, but the time taken for these antibodies to be produced means that the host has a period of at least 1 week in which it must rely on innate immune response¹. Evidence suggests that systemic infection by *N. meningitidis* can only occur in hosts which are immunocompromised in some way, specifically if they do not have the serum bactericidal antibodies against capsular or non-capsular antigens, or they are missing certain complement components⁴. A number of factors can increase the likelihood of contracting bacterial meningitis including smoking and travelling to epidemic regions². In developed countries, the highest rates of invasive meningococcal meningitis are seen in infants and children less than 4 years-old, adolescents, military recruits and groups where crowding and new exposures occur such as college students living in dormitories, however the disease is capable of affecting all age groups².

There is evidence to suggest that much of the damage done to the host during a meningococcal infection is actually caused by the host in an attempt to rid itself of the bacteria¹⁷. A systemic infection causes a massive inflammatory response and the resulting quantities of cytokines produced eventually lead to organ dysfunction and the proteases produced by neutrophil activation also lead to endothelial injury¹⁷.

Once *N. meningitidis* has entered the bloodstream, it goes on to invade the cerebro-spinal fluid (CSF), which serves as an excellent culture medium for the bacteria⁴. The host response to this infection is inflammation of the meninges, the membranes surrounding the central nervous system. This leads to a build-up of serous fluid in the brain causing cerebral swelling. Once the bacteria have entered the CSF, antimicrobial treatment is required otherwise the effects are almost

invariably fatal⁴.

Initially a meningococcal infection presents as a slight fever and chills, which may improve after 4-6 hours. Haemorrhagic skin lesions may appear between 8 and 18 hours, however roughly 20% of sufferers never present with lesions. These skin lesions are possibly the most well known symptom of bacterial meningitis as they are characterised by a non-blanching (does not turn white under mild pressure) rash. The clearest evidence for meningococcal infection is a fever, stiff neck, aversion to bright light, vomiting, skin lesions and headaches. Unfortunately not all these symptoms may be present in all cases⁴.

When meningococcal septicaemia occurs, renal function may be impaired as a direct consequence of cardiac impairment. Septicaemia causes “capillary leak” which reduces cardiac output and increases the effort required to breathe normally. Reduced cardiac output can also affect the gastrointestinal tract leading to reduced function. Once treated these symptoms will usually subside as cardiac output improves¹⁷.

In most cases the treatment for meningococcal meningitis is with antibiotics, where the primary aim is to achieve a rapid bactericidal effect in the CSF¹. This treatment is suggested prior to positive identification of cultures of the bacteria obtained from the CSF as any delay is potentially life-threatening if the bacteria have indeed invaded the CSF⁴.

1.3 Growth of *N. meningitidis*

Bacteria require carbon and energy sources in order to grow, and these are often sourced from sugars present in the environment. *N. meningitidis* can only use the sugars glucose and maltose as carbon sources^{18,19}, however they can use peptides as carbon sources. The bacteria are usually grown on Müller-Hinton broth and Columbia agar which are peptide-based formulations.

1.4 Organisation of the Respiratory Chain of *N. meningitidis*

N. meningitidis is classified as an aerobe and as such has an oxidase pathway for reducing oxygen (O_2), but given that the environment in the nasopharynx is poor in oxygen, the bacteria must also be capable of respiring in a microaerobic environment. This is evidenced by the fact that bacterial isolates from the nasopharynx routinely contain both strict aerobes and strict anaerobes²⁰. Genomic analysis of 2 strains of *N. meningitidis* shows that there are 3 terminal oxidases; 1 of each for reducing oxygen, nitrite (NO_2^-) and nitric oxide (NO)²¹. This analysis may be expanded as there are now many more genomes published. Experiments showed that under oxygen limiting conditions, *N. meningitidis* was capable of growth when nitrite was present in the media (Müller-Hinton Broth), and that nitrate (NO_3^-), the probable source for nitrite, had no effect on growth²¹. Additionally the bacteria require carbon dioxide, as shown by Tuttle and Scherp²² and have 2 enzymes which catalyse the reduction of CO_2^4 .

In vivo, nitrite is obtained as a product of digesting nitrate in food. There are a number of facultative nitrate-reducing bacteria present in the mouth and pharynx responsible for this²⁰ which additionally have a proposed benefit of protecting the host against periodontal and cariogenic bacteria²³. Nitrite is also created by oxidation of nitric oxide, which is produced as a host signalling molecule and as a toxin as part of the host immune response^{20,23}.

The respiratory pathway for reducing nitrite in *N. meningitidis* involves two steps; nitrite is reduced to nitric oxide, which is then further reduced to nitrous oxide. This represents incomplete reduction, as a further reduction step is possible (shown in Figure 1.1), reducing nitrous oxide to dinitrogen gas^{20,24}.

Reduction of oxygen is favourable over nitrite reduction due to the redox po-

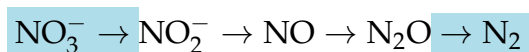


Figure 1.1: **Complete denitrification.** The process of reducing nitrite to nitrogen gas. In *N. meningitidis* the first and final steps highlighted in blue do not occur.

Reduction	Enzyme
$\text{NO}_2^- \rightarrow \text{NO}$	AniA
$\text{NO} \rightarrow \text{N}_2\text{O}$	NorB
$\text{O}_2 \rightarrow \text{H}_2\text{O}$	<i>cbb</i> ₃

Table 1.1: The reductions catalysed by the respiratory enzymes in *N. meningitidis*

tential differences. The redox potential of $\text{O}_2/\text{H}_2\text{O}$ is +820 mV, NO_2^-/NO is +348 mV, thus O_2 has a higher tendency to acquire electrons resulting in a electro-chemically favourable reaction²⁵. The electron flow towards the oxidase is also preferred physiologically as it liberates more energy by virtue of the translocation of more protons than the reduction of nitrite. The translocated protons are ultimately used in the synthesis of ATP molecules for energy. This results in reduction of oxygen in preference to nitrite when both are present (in most cases).

Reduction of oxygen in *N. meningitidis* is carried out by the oxygen reductase cytochrome *cbb*₃ oxidase, a membrane-bound heme-copper oxidase²⁶. *cbb*₃ is capable of binding oxygen and nitric oxide, which means that during nitrite reduction (denitrification), the oxidase can be competitively inhibited (chemically) by the intermediate product of denitrification. *cbb*₃ can be permanently damaged at high concentrations of NO and O_2 , as they can both bind at the *cbb*₃ active site and react together to form peroxynitrite²⁷⁻²⁹.

Nitrite is reduced by the nitrite reductase AniA, which is a copper containing reductase. This reduction does not involve translocation of protons, and thus does not produce any usable energy. Nitrite is reduced to nitric oxide which can then be further reduced by a nitric oxide reductase NorB. Since *N. meningitidis* is capable of reducing nitric oxide, a host toxin, directly, this may help it defend itself against part of the host immune response^{20,30} as has been shown in tissue culture by Anjum et al.²⁹.

The reduction processes carried out by these enzymes are shown in Table 1.1.

The major source for electrons in both respiratory pathways is NADH, although electrons can also be obtained from pyruvate and lactate amongst others.

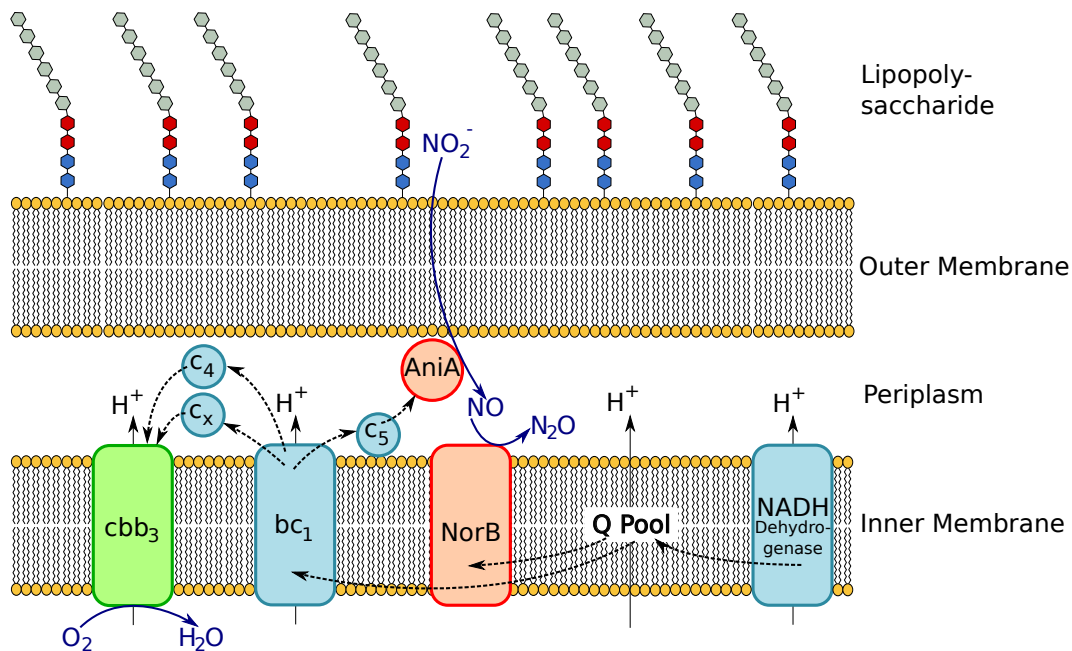


Figure 1.2: Layout of the components of the respiratory system in *Neisseria meningitidis*. Oxygen reducing components are shown in green, nitrogen reducing components in red. Components transporting electrons are coloured light blue, and their transport is indicated by dashed arrows. Respiratory substrates are shown in dark blue, with corresponding arrows linking them to their reducing enzymes. Components which produce membrane potential are also indicated.

These reduced substrates lead to reduction of ubiquinone to ubiquinol in the ubiquinone pool that exists within the bacteria. Ubiquinol is oxidised either by the cytochrome *bc*₁ complex or directly by the NorB enzyme whilst reducing NO to N₂O. Cytochrome *bc*₁ is oxidised by a number of intermediate cytochromes which act to transport electrons to the terminal oxidases; AniA and *cbb*₃. The *c*₅ cytochrome transports electrons from the *bc*₁ complex to AniA, and two cytochromes, *c*_{2/x} and *c*₄, transport electrons to *cbb*₃. It is not understood why *cbb*₃ has 2 alternate cytochromes, and there is evidence to suggest that it can also be supplied, in a limited capacity, by the *c*₅ cytochrome as well³¹. The electron transport chain (ETC) is shown graphically in Figure 1.2.

In addition to the difference in favourability between the two respiratory pathways, there is also a great deal of regulation, both at the enzymatic and transcriptional level. Chemical inhibition also plays a part in regulation as briefly mentioned previously. Expression of AniA is regulated by two processes, the

reduction of oxygen and the presence of nitrite. The presence of oxygen down-regulates the expression of an activator of AniA expression. This activator is FNR (fumarate and nitrate reduction regulator), and the presence of oxygen effectively means that AniA expression is repressed by the reduced expression of FNR. In *N. meningitidis*, FNR appears to work slightly differently than in facultative anaerobes such as *E. coli*, in that FNR is still expressed at quite high concentrations of oxygen, and is itself down-regulated by a separate co-factor³².

The presence of nitrite triggers the two component NarP/NarQ system which activates expression of AniA in response to increasing levels of nitrite²⁰. The activity of AniA is also controlled by the competition for electrons by the other reductase enzymes in the respiratory chain. Both NorB and *cbb*₃ have a higher affinity for electrons than AniA, and as a result the presence of these enzymes (when active) has an inhibitory effect on AniA. The regulation of AniA is further complicated by the production of nitric oxide, and the presence of a protein, NsrR.

Nitric oxide has a direct inhibitory effect on the expression of AniA, as does the NsrR protein. Nitric oxide also inhibits the NsrR protein, leading to a de-repression of AniA³⁰. In the absence of nitric oxide, AniA is almost fully repressed by active NsrR. As NO concentrations increase, NsrR is inactivated allowing full activation of AniA. Once NO reaches a sufficiently high level it will begin to inhibit AniA^{20,32}.

NorB is less tightly regulated by respiratory components, as it is only acted upon by NsrR, however it is regulated by FNR and NrsR outside the respiratory chain³³. This regulation by NsrR works in a similar way to how NsrR acts upon AniA. When there is no nitric oxide present, the NsrR acts to inhibit NorB since there is no substrate for it to reduce. In the presence of nitric oxide, NsrR is inhibited, leading to the activation of NorB which is now able to reduce NO to N₂O. In this case nitric oxide is acting as a de-repressor of NorB.

This complicated set of regulatory relationships between the different compo-

nents of the respiratory pathways is shown in Figure 1.3.

1.4.1 Nitric Oxide

Nitric oxide is a small molecule with chemical formula NO. It exists as a free radical; the nitrogen having an unpaired electron in its outer valence shell. Nitric oxide is an important cell signalling molecule in mammals, including humans³⁴. Given its small, hydrophobic nature it easily passes through cell membranes, but can only diffuse small distances from where it has been synthesised as it reacts easily with other reactive oxygen species in addition to cysteine and tyrosine residues in proteins and heavy metals³⁵. NO regulates a number of cellular processes by post-translational modification of proteins. Sufficiently high concentrations of nitric oxide also cause cells to undergo apoptosis or necrosis (depending on the activation state of PARP-1 (Poly-ADP-Ribose Polymerase))³⁴.

Nitric oxide functions as part of the human immune system, being generated by phagocytes which contain an inducible nitric oxide synthase. The phagocytes release nitric oxide as a free radical which is toxic to bacteria as it causes DNA damage³⁶ and degradation of iron sulfur centres^{37,38}. In response many bacterial pathogens have evolved resistance mechanisms against nitric oxide^{39,40}.

The respiratory system of *Neisseria meningitidis* is such that it conveys a degree of resistance to host-generated nitric oxide. Given that *N. meningitidis* is capable of denitrification and capable of reducing nitric oxide created from reduction of nitrite, it is also capable of removing extracellular nitric oxide. This confers a natural advantage on the bacteria as the only environment in which it can survive is also one which will expose it to the human immune system and the sinus cells in the nasopharynx express NOS (nitric oxide synthase)⁴¹ constitutively. It has been shown that NorB expression in *N. meningitidis* can actually halt the production of S-nitrosothiol produced by macrophages⁴². Additionally NorB appears to be minimally controlled so that it can respond quickly to NO production⁴¹.

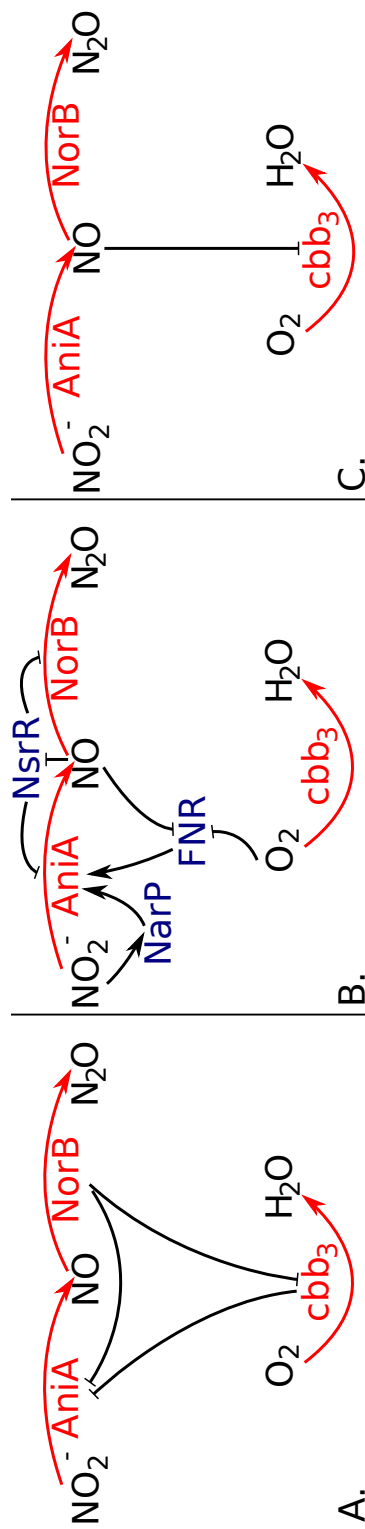


Figure 1.3: **Regulation of respiratory components in *Neisseria meningitidis*.** Enzymes and enzymatic reactions are shown in red. A. describes the regulation caused by competition for electrons between the respiratory enzymes. B. shows the genetic regulation, which also involves a number of additional components in dark blue. C. shows chemical inhibition of the respiratory components.

1.5 Respiratory Enzymes in *N. meningitidis*

1.5.1 Cytochrome *cbb*₃ oxidase

Cytochrome *cbb*₃ oxidase is a Haem Copper Oxidase (HCO) enzyme found commonly in proteobacteria. They have been characterised in at least *Pseudomonas denitrificans*, *Rhodobacter sphaeroides*, *Rhodobacter capsulatus* and *Bradyrhizobium japonicum*⁴³. HCOs catalyse the reduction of Oxygen molecules to water whilst translocating protons across the inner membrane, from the cytoplasm to the periplasm, producing an electrochemical gradient.

HCOs can be separated into two categories by their electron donor type. Cytochrome *c* oxidases accept electrons from *c*-type cytochromes, and quinol oxidases accept electrons from ubiquinol. The major difference between these two categories is a missing Cu_A site in quinol oxidases⁴⁴. HCOs can be further broken down to 3 types, the *aa*₃-type cytochrome *c* oxidase, the *bo*₃-type quinol oxidase and the *cbb*₃-type cytochrome *c* oxidase⁴⁵. Alternatively 5 different HCO subclasses may be classified, the *aa*₃, *caa*₃ and *cbb*₃-type cytochrome *c* oxidases, and the *bo*₃ and *aa*₃-type quinol oxidases⁴⁶. All of these different types of cytochrome *c* oxidases are found in bacteria, whereas those in mitochondria are limited to *aa*₃-type cytochrome *c* oxidases⁴⁷.

HCOs are themselves “defined by the primary sequence of their catalytic subunit, which is composed of twelve transmembrane helices with six invariant histidines ligating three cofactors; a high spin heme (one His ligand) and a copper (3 His ligands) in the catalytic site and an additional low-spin heme (two His ligands)”⁴⁸. Sequence alignment has also indicated that bacterial NO-reductase (NOR) might also be a divergent member of the HCO family. A schematic diagram of the *cbb*₃ oxidase is shown in Figure 1.4, and the 3D structure of *cbb*₃ from *Pseudomonas stutzeri* is shown in Figure 1.5. *cbb*₃ is composed of three main subunits with CcoN being the catalytic subunit, which is related to subunit I of *aa*₃ oxidases and NorB. This latter relation to NorB explains why *cbb*₃ has some Nitric

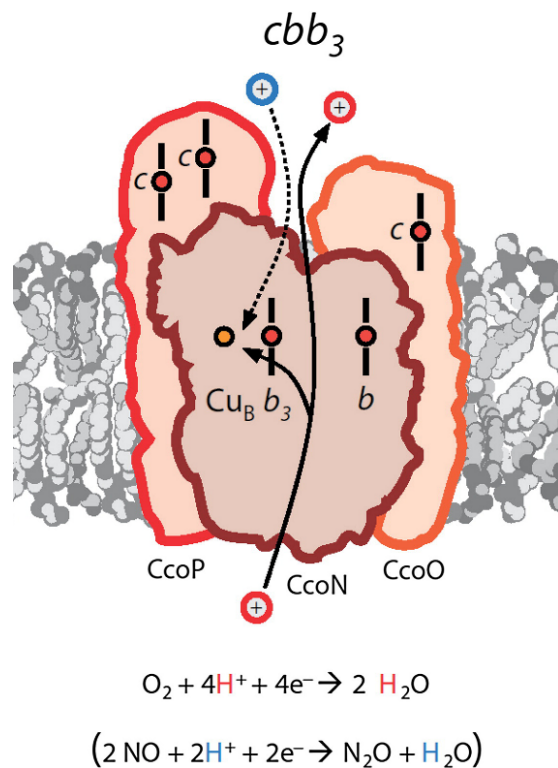


Figure 1.4: **The *cbb*₃ oxidase.** This diagram shows the proton input pathway for Oxygen reduction shown in red, and the putative pathway for Nitric Oxide reduction in blue. Also shown are the 3 subunits and their associated heme centres. Adapted from Huang et al.⁴⁸.

Oxide reduction activity (and conversely why NorB has some Oxygen reduction activity)⁴⁸. CcoN contains the catalytic site – the high-spin heme *b*₃-Cu_B – and a low spin heme *b*. CcoO is anchored in the inner membrane and contains just one *c-type* heme. CcoP contains two *c-type* hemes and is anchored to the inner membrane. CcoQ, the fourth subunit is small, and helps to stabilise the complex⁴⁸.

The mechanism of reduction of O₂ by *cbb*₃ oxidases is not fully understood, as the reduction intermediates currently remain unknown⁴⁸. The cytochrome *cbb*₃ oxidases have very low *K_M* values, allowing them to operate even under oxygen limiting conditions. *cbb*₃ from *Bradyrhizobium japonicum* has a *K_M* of 7 nM, much lower than that of the mitochondrial *aa*₃ oxidase⁵⁰. This high affinity for oxygen suggests that *N. meningitidis* may have become adapted to surviving in the human host in areas of low oxygen concentration. Since this type of oxidase is also found in other human pathogens it is likely that it is used to allow those

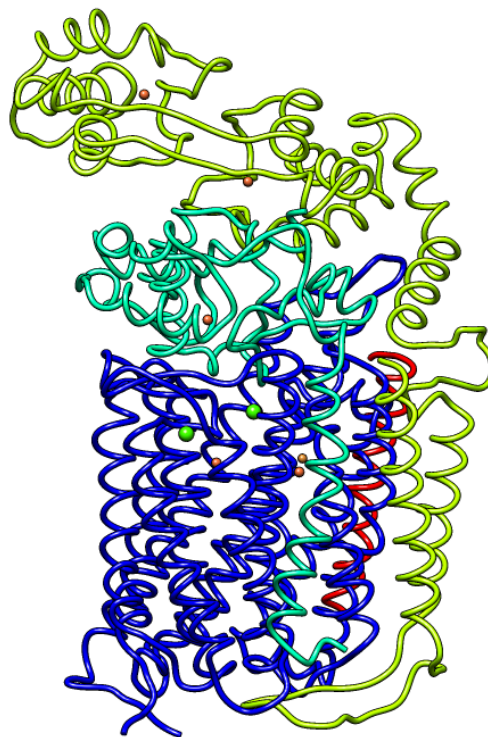
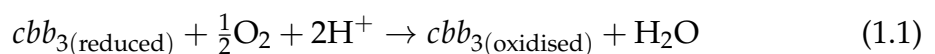


Figure 1.5: 3D Structure of cbb_3 oxidase. This figure shows the structure of cbb_3 from *Pseudomonas stutzeri*⁴⁹. CcoN is shown by the blue chain, with the heme and copper centres being brown. CcoP is shown by the green chain, and CcoO by the cyan chain. The PDB ID for this structure is 3MK7.

pathogens to survive in hypoxic environments in the human host⁵¹.

The catalytic reaction for the cbb_3 oxidase is:



1.5.2 NorB Nitric Oxide Reductase

Nitric Oxide Reductase is also a Haem Copper Oxidase enzyme which is found in bacteria as an integral membrane protein. There are three types of NOR, the cytochrome *bc* type complex (cNOR), the cytochrome *b* type complex lacking the cytochrome *c* component (qNOR) and a qNOR-type reductase that also includes Cu_A (qCu_ANOR). cNOR-type reductases receive electrons from soluble redox protein donors, whereas qNOR-type reductases receive electrons from quinol⁵².

The NOR in *N. meningitidis* is a qNOR-type reductase⁵³, and is encoded by the

norB gene (NMB1622). It catalyses the reduction of Nitric Oxide to Nitrous Oxide receiving electrons directly from the quinone pool. Under microaerobic conditions this enzyme is important as during denitrification to support growth, Nitric Oxide accumulates as a result of reduction of Nitrite. The build up of Nitric Oxide inhibits aerobic respiration as it binds competitively to the *cbb₃* oxidase. NorB protects the bacteria from the toxicity of extracellular NO which is produced by host tissues and macrophages, which produce NO in quantity during infection³⁰.

The nitric oxide reductase in *Neisseria gonorrhoeae* is predicted to be an 84.3 kDa protein sharing significant sequence identity with the nitric oxide reductases in *Ralstonia eutropha*, a Gram-negative soil bacterium, and consists only of the NorB subunit⁵². The NorB protein is highly conserved across all *Neisseria* species as evidenced by sequence analysis⁵⁴.

The catalytic reaction for NorB is:



1.5.3 AniA Nitrite Reductase

AniA nitrite reductase is an anaerobically induced, outer membrane associated protein which uses nitrite as an electron acceptor⁵⁵. It is a copper-containing protein found in many denitrifying proteobacteria.

Nitrite reductases catalyse the reduction of nitrite to nitric oxide with no associated proton translocation. There are two types of nitrite reductase, those that have haem centres, and those which have copper centres. AniA in *N. meningitidis* is a copper-containing and accepts electrons from *c*-type cytochromes (*c₅*).

In *N. meningitidis* this enzyme is important during oxygen limiting conditions as it allows microaerobic respiration which can supplement growth by denitrification²⁰.

Interestingly, according to its genome sequence *N. meningitidis* strain 053442 appears to lack the *aniA* gene in its entirety, suggesting that this strain would be

unable to perform denitrification and respire anaerobically⁵⁴. 32% of *N. meningitidis* strains sequenced by Barth et al.⁵⁴ contain non-functional copies of *aniA* with frameshift mutations. These strains do still possess the *norB* gene for reducing Nitric Oxide however allowing them to prevent its toxic effects. It has been suggested by some that this may actually be evidence that *Neisseria meningitidis* is in the process of evolving away from denitrification to being a Nitric Oxide tolerant aerobe³⁹.

The catalytic reaction for AniA is:



1.6 Respiratory Electron Transporters in *N. meningitidis*

1.6.1 NADH Dehydrogenase

NADH (Reduced Nicotinamide Adenine Dinucleotide) Dehydrogenase is an inner membrane bound enzyme that catalyses the transfer of electrons from NADH to the quinone pool in many bacteria. There are three types of NADH dehydrogenase enzymes found in bacteria, NDH-1, NDH-2 and Na⁺-NDH. NDH-1 is related to Complex I of the mitochondrial respiratory chain and translocates protons across the inner-membrane whilst reducing the quinone pool^{56–58}. NDH-2 does not have any proton pump activity, nor does it have any Fe-S clusters⁵⁹. Na⁺-NDH translocates Na⁺ ions across the membrane⁶⁰. The NADH dehydrogenase of *N. meningitidis* is of the NDH-1 type²⁵.

Mitochondrial complex I catalyses the oxidation of NADH and the reduction of ubiquinone whilst translocating 4 protons across the membrane. It does so using the following reaction scheme:

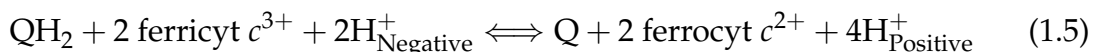


1.6.2 Cytochrome bc_1 Complex

The cytochrome bc_1 complex oxidises quinols and reduces metalloprotein electron transporters (usually c-type cytochromes). It is an important part of bacterial respiratory chains, and is also analogous to the mitochondrial complex III⁶¹. Whilst catalysing the reduction of ubiquinone and the oxidation of c-type cytochromes, the bc_1 complex also translocates protons across the inner membrane from the cytoplasm to the periplasm producing an electrochemical gradient. The bc_1 complex is found in both Gram negative and Gram positive bacteria, however *E. coli* has no bc_1 complex. A homologue, the b_6f complex is also used for electron transfer during photosynthesis in higher plants and phototrophic bacteria⁶².

In bacteria the bc_1 complex is formed of one cyt *b* subunit which contains two *b*-type hemes, one cyt *c*₁ subunit which contains a single *c*-type heme and an Rieske iron-sulfur protein. These subunits form the two catalytic sites of the bc_1 complex. The reduction of ubiquinone appears to occur in a concerted manner at one of these sites, Q_o ⁶². Electrons from the quinol are shared between two reaction chains, one which transfers electrons to the high-potential iron-sulfur protein and *c*₁, and another which transfers electrons to the low-potential cytochrome *b*. The other catalytic site Q_i uses the two electrons from the high and low potential chains to reduce quinone, or other metalloprotein electron transporters^{63,64}. This modified Q-cycle is shown in Figure 1.6.

The reaction scheme for the bc_1 complex is:



1.6.3 Cytochromes *c*₄, *c*_x and *c*₅

Cytochromes *c*₄, *c*_x and *c*₅ are soluble *c*-type cytochromes. These are small heme proteins that are found in the periplasm and are loosely associated with the inner membrane. Along with their presence in proteobacteria, the *c*-type cytochromes also form part of the mitochondrial respiratory apparatus in the form of cyto-

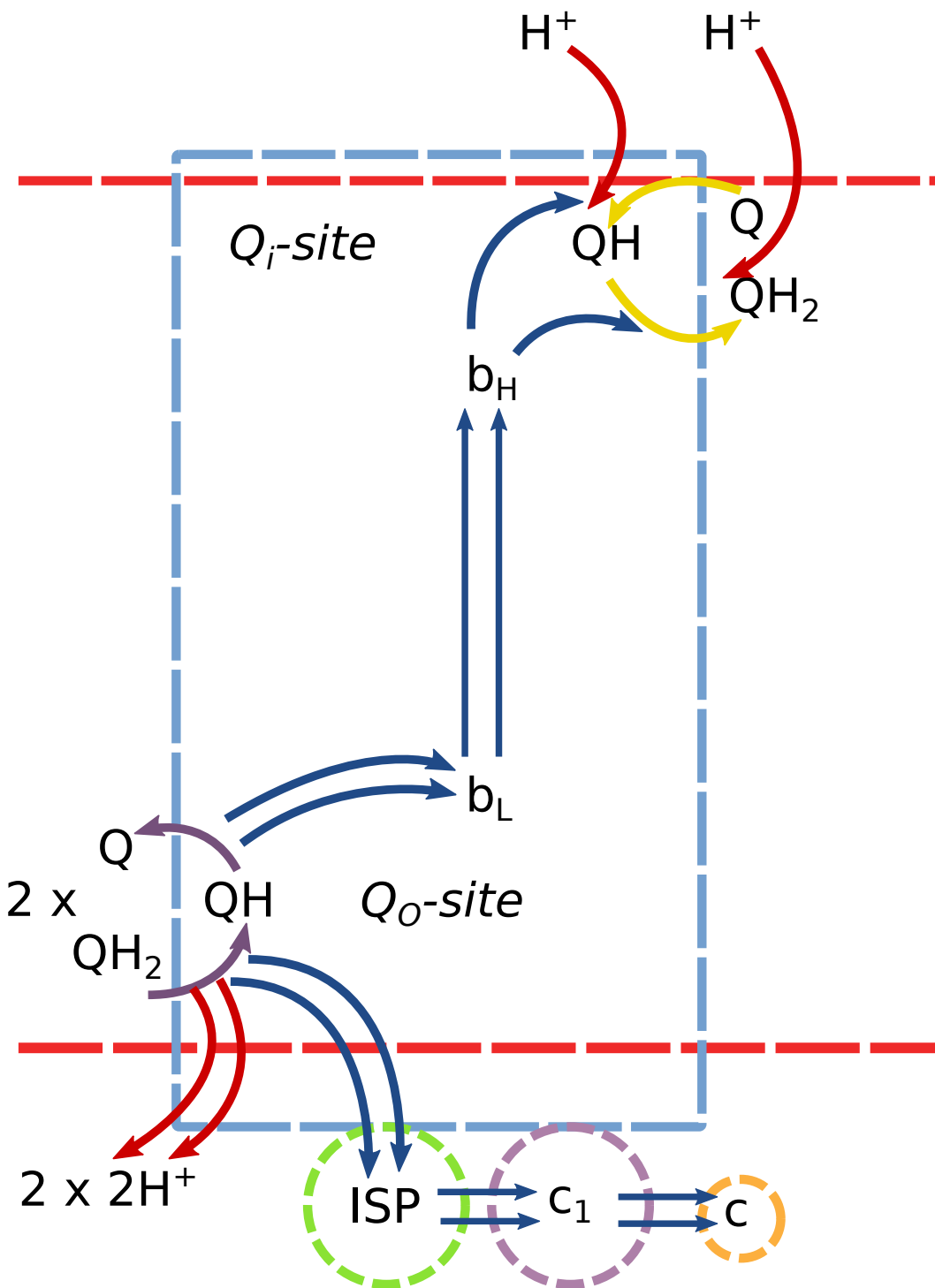


Figure 1.6: **The modified Q-cycle used by the bacterial *bc*₁ complex.** The cyt *b* subunit is represented by the *dashed blue* outline, and contains the *Q_o*- and *Q_i*-sites, connected by hemes b_L and b_H . The ISP (Rieske Iron-Sulfur Protein) and cyt *c*₁ catalytic domains and cyt *c* are represented by *dashed circles*. Electron transfer steps are shown by *blue arrows*, proton release and uptake by *red arrows*, binding and release of quinone species by *purple arrows* for *Q_o*-site and *yellow arrows* for *Q_i*-site. Adapted from Crofts et al.⁶⁵.

chrome *c*. Bacterial *c*-type cytochromes perform a very similar function to mitochondrial cytochrome *c* in that they transport electrons from the *bc*₁ complex to the terminal reductases. Cytochromes *c*-552, *c*-553 & *c*-554 from algal chloroplasts and cyanobacteria, *c*₂ from purple photosynthetic bacteria and *c*₄ and *c*₅ from *Azotobacter vinelandii* along with many others all have sequence and structural homology with mitochondrial cytochrome *c*⁶⁶. The mitochondrial and bacterial soluble cytochromes all fall within Ambler's Class I of *c*-type cytochromes⁶⁷. The heme-attachment site of Class I *c*-type cytochromes is towards the N-terminus, and a methionine residue 40 residues further down the chain towards the C-terminus provides the sixth ligand⁶⁷.

- Cytochrome *c*₄ is a diheme cytochrome and is the electron donor to *cbb*₃ transferring electrons from the *bc*₁ complex in *N. meningitidis*^{25,31,68}.
- Cytochrome *c*_x is a monoheme cytochrome which is also able to transfer electrons from the *bc*₁ complex to *cbb*₃^{25,31}.
- Cytochrome *c*₅ is a diheme cytochrome which appears to be membrane associated. It transfers electrons from the *bc*₁ complex to AniA during Nitrite reduction^{25,31}.

1.6.4 Quinone Pool

The quinone source in *N. meningitidis* is predicted to be ubiquinone²⁵. Ubiquinone, also known as Coenzyme Q₁₀ is found in most eukaryotes. It is a vitamin-like lipid soluble molecule with a long tail made of 10 isoprenyl subunits. This is shown in Figure 1.7.

In its oxidised form it is known as ubiquinone, whereas when reduced it is called ubiquinol. In the *N. meningitidis* respiratory chain, ubiquinone is reduced to ubiquinol by the acceptance of 2 electrons from NADH (amongst others). Ubiquinol then donates electrons either directly to the terminal reductase NorB, or to the *bc*₁ complex.

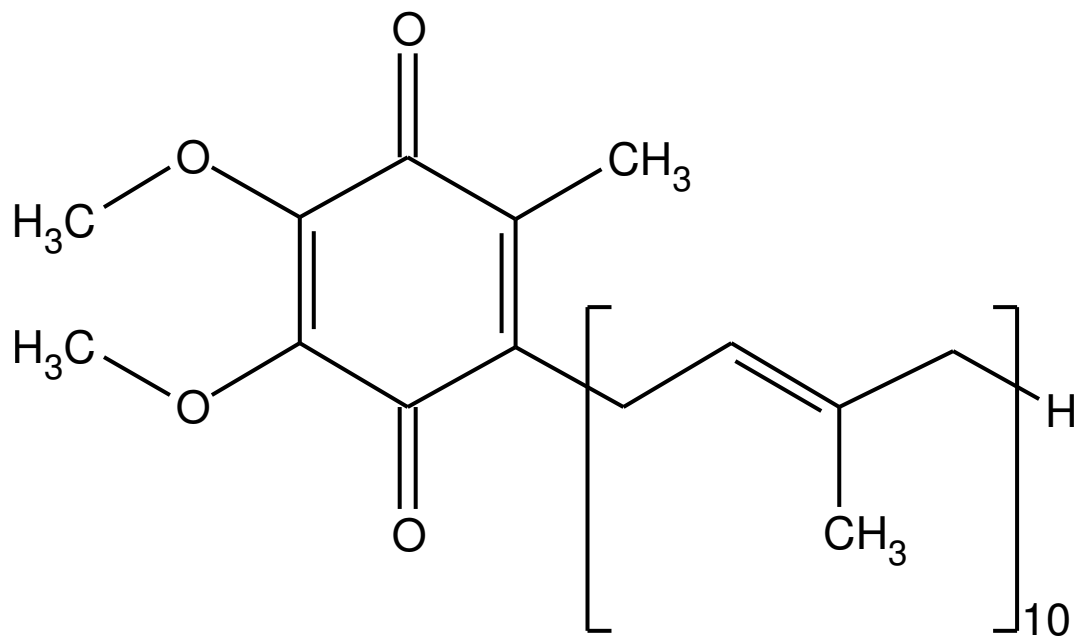


Figure 1.7: Structure of the ubiquinone molecule.

1.7 Respiration Regulatory Proteins in *N. meningitidis*

1.7.1 NsrR - Nitrite Sensing Repressor Protein

“NsrR is an NO-sensing Rrf2-type transcriptional repressor”⁵⁴. In *N. meningitidis* (and *N. gonorrhoeae*) it negatively regulates *aniA* and *norB*, and derepression is caused by NO^{30,32,33}. Rrf2 proteins have two DNA-binding helix-helix domains³², with a putative iron-sulfur cluster inbetween. In NsrR, NO is expected to bind to the iron-sulfur cluster, perturbing the structure of the repressor protein and prevent DNA binding³².

norB is expressed in the absence of both a repressor and an activator, in that with no repression and no NO present *norB* is still expressed to some extent⁶⁹. NsrR represses this expression until NO is present, at which point *norB* can be expressed and the NorB enzyme can start removing the NO that is present.

aniA is positively regulated by FNR, but this seems to be quite insensitive to oxygen in *N. meningitidis*, thus *aniA* would be expressed even at 60 to 80% air saturation with oxygen³². *aniA* therefore needs to be corepressed in order to prevent it being expressed excessively in aerobic conditions.

1.7.2 FNR - Fumarate and Nitrate Reductase Regulator

Fumarate Nitrate Reductase is a transcriptional activator which binds to a 4Fe-4S cluster under anaerobic conditions. When oxygen concentrations are low, FNR causes increased expression of proteins that are necessary for anaerobic respiration. “The presence of the 4Fe-4S cluster is correlated with protein dimerization, which enables it to bind promoter DNA”⁷⁰. Four cysteine residues are believed to be ligated to the iron-sulfur cluster and these are required for FNR function. The oxygen sensitivity of FNR is achieved by the iron-sulfur cluster breaking down into 2Fe-2S via 3Fe-4S which is unable to bind DNA. In *N. meningitidis*, *aniA* expression is directly linked to the presence of FNR²⁰. When no NsrR is present, *aniA* expression continues even up to 80% oxygen saturation suggesting that FNR is actually quite insensitive to oxygen, an unusual response compared to FNR from *E. coli*. FNR also becomes less sensitive to oxygen when it is bound to its cognate DNA⁷⁰.

1.7.3 NarQ/NarP - Nitrite Response Sensor/Regulator

NarP and NarQ are a two component signal transduction pathway that regulate expression of *aniA* in *Neisseria*. NarQ is the sensor protein located in the inner membrane, while the regulator protein, NarP is found in the cytoplasm. Being a two component system, the sensor protein phosphorylates the regulator allowing it to bind the target DNA (which may consist of multiple sequences) to activate expression of genes.

In *N. gonorrhoeae*, NarP was shown to enhance the expression of *aniA* in response to the presence of nitrite, as a mutant lacking *narP* was significantly slower at growing under denitrifying conditions⁷¹.

In *N. meningitidis* expression of *aniA* is increased greatly in conditions of high nitrite concentration²⁰. This effect is much more pronounced than simply being in oxygen limiting conditions. FNR appears to be required for *aniA* expression even when NarP/NarQ are present²⁰. This suggests that the organism is inten-

tionally preventing expression of nitrite reducing components until there is both a high concentration of nitrite *and* a very low concentration of oxygen. This is plausible as even under oxygen limiting conditions oxygen reduction is still favoured over nitrite reduction.

1.8 Organisation of Respiratory Chains in Other Bacteria

The respiratory chain of *N. meningitidis* is shown in a simplified form in Figure 1.8. The components are coloured consistently throughout this section to allow

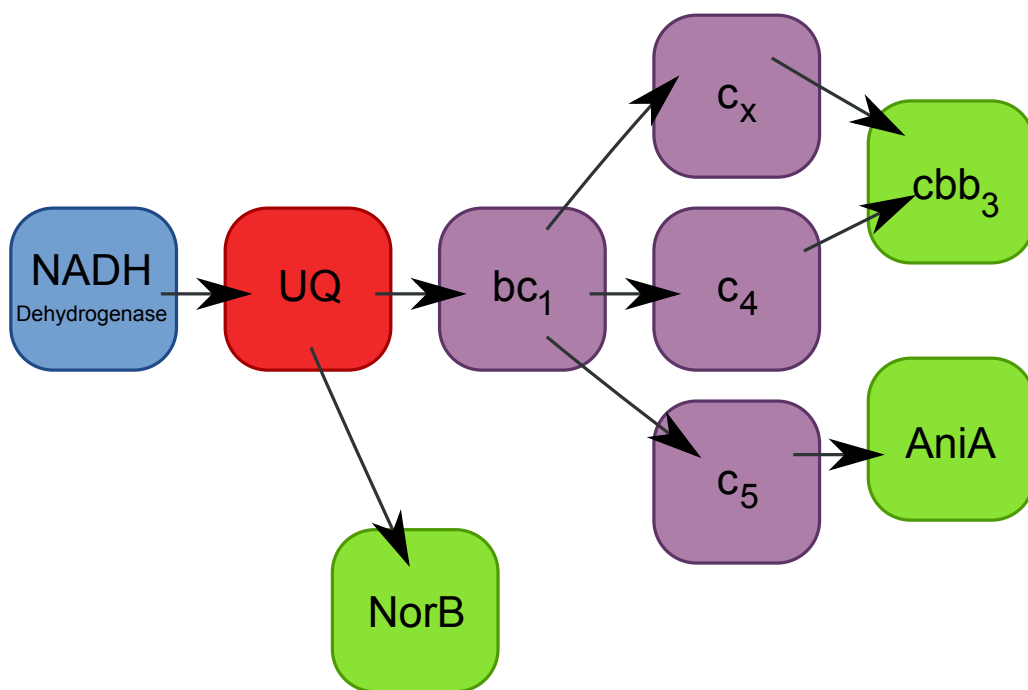


Figure 1.8: **Branched electron transport chains of *N. meningitidis*.** Blue denotes initial electron donor, red denotes quinone pool, purple denotes cytochrome electron transporters and green denotes terminal reductases. UQ = ubiquinone.

easy comparison between the respiratory chains being discussed. As discussed previously, the respiratory chain of *N. meningitidis* contains an initial electron donor, in this case NADH dehydrogenase. This actually represents all the possible electron donors. NADH is considered to be the main electron donor along with succinate⁷². There is also a quinone pool, consisting of ubiquinone/ubiquinol, intermediate *c*-type cytochromes and terminal reductases. The following section introduces the electron transport chains of a number of other bacteria as they are

well studied model organisms for comparison with *N. meningitidis*.

1.8.1 The Respiratory Chain of *Paracoccus denitrificans*

The respiratory chain of *P. denitrificans* is shown in Figure 1.9. It is quite similar to that of *N. meningitidis* with the exception of having a larger number of terminal reductases, and the ability to perform complete denitrification. The chain possesses an initial electron donor, a quinone pool, intermediate cytochrome electron transporters and terminal reductases.

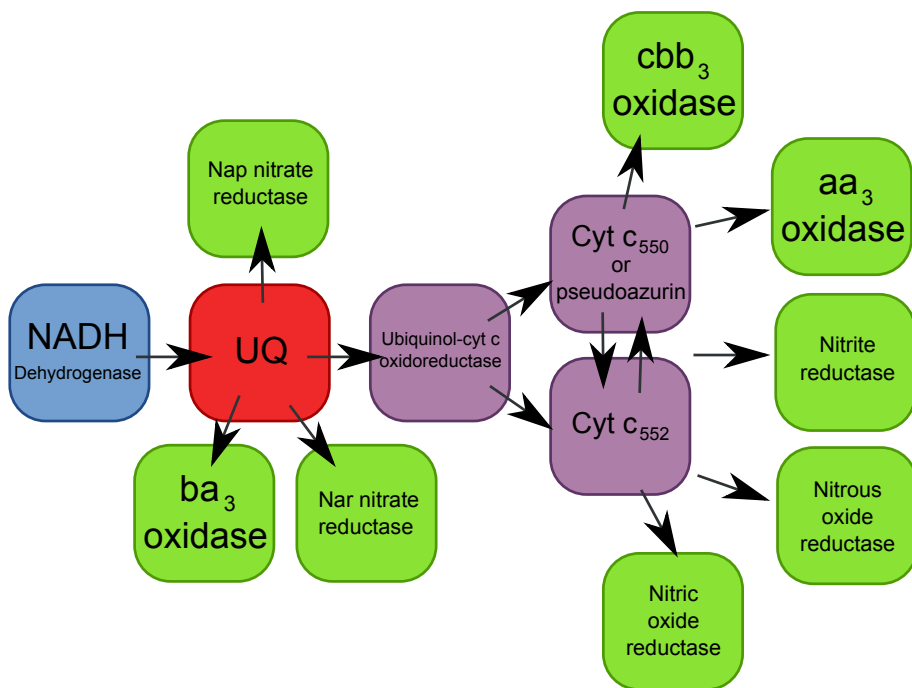


Figure 1.9: **Branched electron transport chains of *Paracoccus* species.** Blue denotes initial electron donor, red denotes quinone pool, purple denotes cytochrome electron transporters and green denotes terminal reductases. UQ = ubiquinone. Electron transfer between cytochromes c_{552} and c_{550} has not been demonstrated experimentally but is possible, given the redox potential of the proteins. Adapted from Baker et al.⁷³.

The bc_1 complex of *N. meningitidis* is present as an analogue (Ubiquinol-cyt c oxidoreductase), and the chain includes 2 further downstream c -type cytochromes. *P. denitrificans* has 3 terminal oxygen reductases, ba_3 , which oxidises the quinone pool directly, and cbb_3 and aa_3 which oxidise the c -type cytochromes. All three oxygen reductases are HCOs. The branching of the aerobic ETC is quite common among bacteria, but the reason for this is not currently fully understood.

The reductase enzymes found in *P. denitrificans* are capable of complete denitrification as described in Figure 1.1. The nitrate reductases directly oxidise the quinone pool, whereas the nitrite and nitric oxide and nitrous oxide reductases oxidise the *c*-type cytochromes instead.

As with *N. meningitidis* there are a number of potential initial electron donors, but only NADH is shown for simplicity of comparison.

1.8.2 The Respiratory Chain of *Escherichia coli*

The respiratory chain of *E. coli* is shown in Figure 1.10. It can be seen to be quite distinct from other bacteria, and indeed from the mitochondrial respiratory chain. The most obvious difference between *E. coli* and many other bacteria is the lack

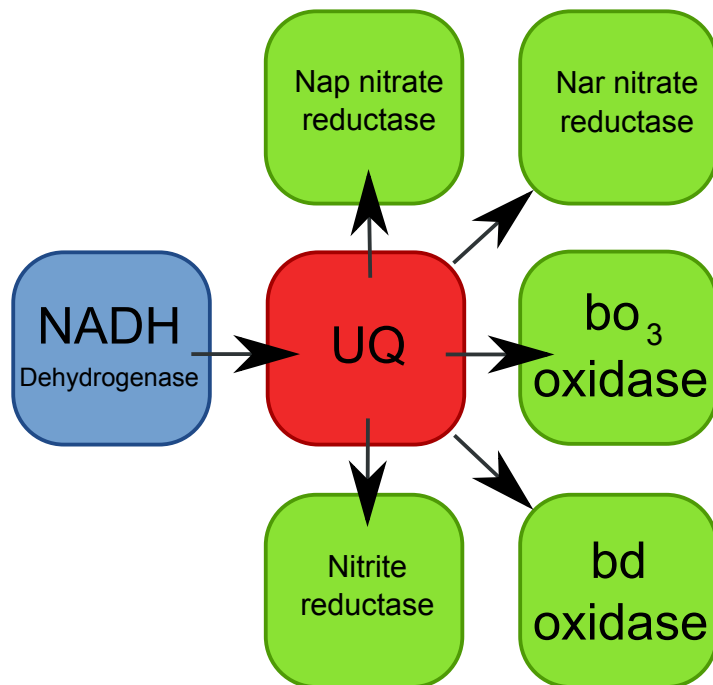


Figure 1.10: **Branched electron transport chains of *E. coli*.** Blue denotes initial electron donor, red denotes quinone pool and green denotes terminal reductases. UQ = ubiquinone. Under anaerobic conditions, ubiquinone is replaced by menaquinone. Adapted from Nicholls and Ferguson⁷⁴.

of *c*-type cytochromes in its aerobic respiration chain. The terminal reductases are able to be reduced directly by the quinone pool. Additionally, under anaerobic conditions, the quinone pool changes from being ubiquinone/ubiquinol to menaquinone/ubiquinol. *E. coli* also has no *bc*₁ complex.

E. coli also has a number of different terminal reductases in the form of cyt *bo*₃ and cyt *bd*. Cyt *bo*₃ is an HCO and is structurally very similar to cyt *aa*₃. Cyt *bd* shows no sequence similarity with the HCO superfamily and has no Cu_B site. Cyt *bd* has a much higher affinity for oxygen than cyt *bo*₃ so is synthesised at low oxygen concentration. In addition *E. coli* has a further cytochrome cyt *bd-II* which is speculated to be important in microaerobic respiration. Initially it was thought to be unlike other cytochromes as it appeared to contribute nothing to the proton motive force by not translocating protons across the membrane⁷⁵, however this was later shown to be incorrect and in fact cytochrome *bd-II* does produce a measurable proton motive force⁷⁶.

E. coli is also capable of ammonification and possesses enzymes to reduce nitrate and nitrite, which are also under the regulatory control of FNR. The reduction of nitrite differs from *N. meningitidis* and *P. denitrificans* as NO₂⁻ is not reduced to NO, but to NH₄⁺ instead.

As with *N. meningitidis* and *P. denitrificans* there are a number of potential initial electron donors, but only NADH is shown for simplicity of comparison.

1.8.3 The Respiratory Chain of *Rhodobacter sphaeroides*

The respiratory chain of *R. sphaeroides* is shown in Figure 1.11. This is more similar to *N. meningitidis* and *P. denitrificans* than to *E. coli* in that it has c-type cytochromes in the aerobic respiratory chain. *R. sphaeroides* has 3 terminal oxidases, *cbb*₃ and *aa*₃ which are reduced by cytochromes, and *Q_{ox}* which is reduced directly by the quinone pool.

The reductases involved in denitrification are all reduced directly by the quinone pool as with *E. coli*

There are two possible electron donors to the quinone pool, NADH dehydrogenase and succinate dehydrogenase, but only NADH is shown for simplicity of comparison.

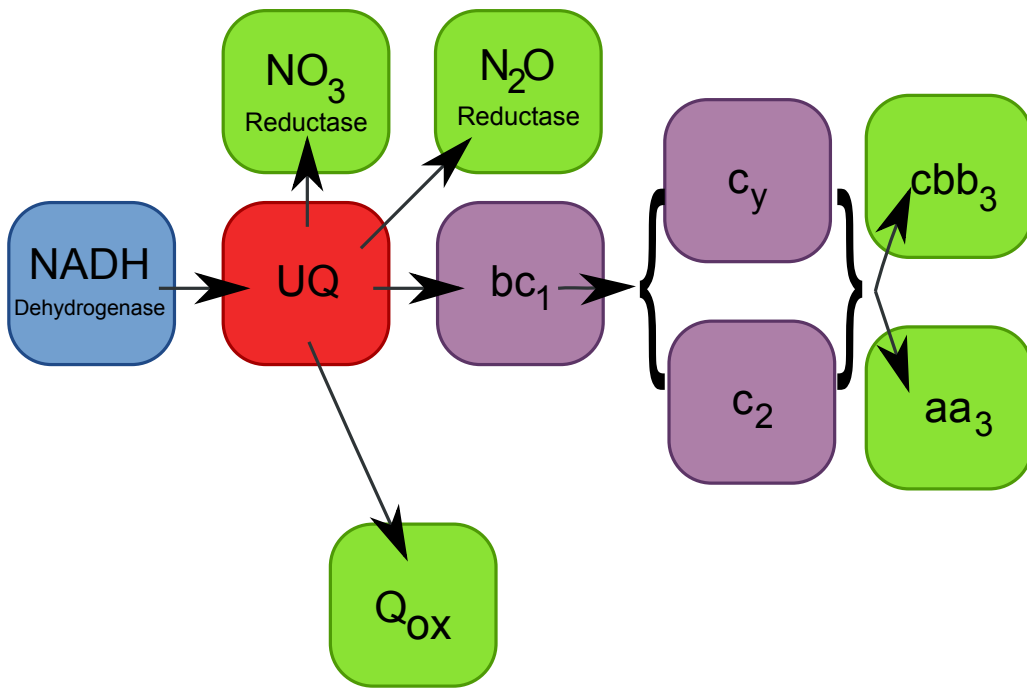


Figure 1.11: Branched electron transport chains of *Rhodobacter sphaeroides*. Blue denotes initial electron donor, red denotes quinone pool and green denotes terminal reductases. UQ = ubiquinone. This diagram does not include any of the photosynthetic pathways that *R. sphaeroides* also has. Adapted from Ferguson et al.⁷⁷, Daldal et al.⁷⁸, Pappas et al.⁷⁹

1.9 Computational Biology and Systems Biology

Computational biology is a broadly defined field primarily centred around developing and applying various mathematical and computational techniques to the study of biological systems. These may include data-analysis and mathematical modelling to improve the understanding of the biological system in question. The field could be considered a fusion of multiple different fields (computer science, biochemistry, mathematics, genetics etc.) into one multidisciplinary field.

Systems biology is the process of studying biological systems as a whole, and using sophisticated computer modelling backed up by high-throughput molecular tests⁸⁰. Systems biology “combines approaches and methods from systems engineering, computational biology, statistics, genomics, molecular biology, biophysics and other fields”⁸¹.

The aim of Systems biology is to take our detailed understanding of organisms

beyond the molecular and cellular level. These are the levels to which the disciplines of molecular biology and biochemistry (among others) are more suited. It aims to take our understanding to the level of the entire “complex system”. Which is to say we gain understanding into the way the organism behaves as a whole, rather than just having knowledge of the individual parts.

The level of complexity in biological systems is far greater than the popular notion of what defines a complex system, however. Biological systems consist of multiple different individual elements each performing specific tasks interacting with each other to create ‘coherent’ behaviour. This is very different from popular complex systems which are collections of simple, identical components interacting to produce ‘complex’ behaviour⁸².

Gaining understanding such a complex system is difficult, and Kitano suggests that it requires insight into the following properties⁸³:

1. **Structure of the system.** This includes the way the system interactions are “laid out” both at a component level and an organismal level.
2. **The dynamics of the system.** This involves understanding how the organism behaves under any given conditions over a particular time period. This may include understanding how the metabolic processes change under these conditions etc.
3. **How the system is controlled.** The control mechanisms can be tailored to suit the desired function or to minimise the chance of malfunction.
4. **How the system is designed.** “Trial and error” experimentation can be done away with, as the system can be designed based on defined properties, backed up by models and simulations.

The level of integration between systems biology approaches and experimentation can be seen in Figure 1.12. This shows the iterative cycles that are necessary to gain understanding in both areas. The experimentation provides data to refine

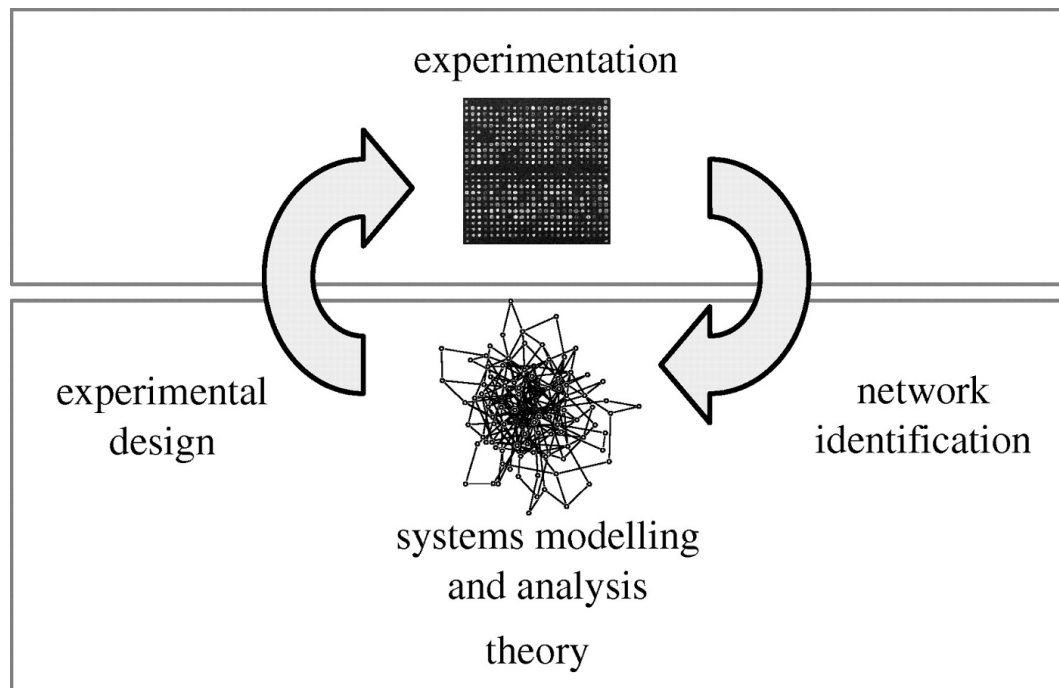


Figure 1.12: **Systems biology cycle.** Interactions between experimental analysis and theoretical approaches, and the main tasks for theory at the interfaces. Doyle and Stelling⁸¹

and develop the system model, and data from that model can go on to improve the design of the experiment.

Systems biology extends further into a computational discipline when you consider that if you can create a model of a system, you can potentially run a simulation of the system using the model. Simulations can be developed for multiple stages of the process, from molecular to organismal. Simulations of interactions based on gene regulatory network models are being studied⁸⁴, as are complete plant development models^{85–87}.

Figure 1.13 shows one of the limitations of the current technology “powering” systems biology. As organisms get more complex, the models we can produce get less complex and less quantitative⁸⁰. This concomitant lack of data in models of complex organisms decreases the likelihood of being able to produce a simulation of the model. We might be able to simulate *aspects* of a complex organism, such as the human heart⁸⁸ but we are still a long way from being able to simulate the entire human body.

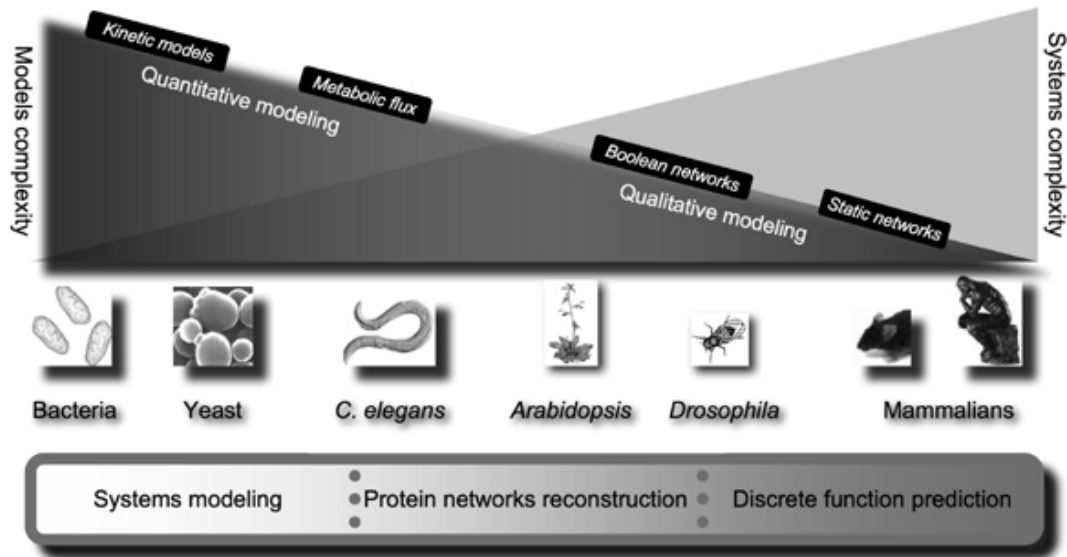


Figure 1.13: **System complexity**. Diagram showing how system complexity varies across organisms, and how the complexity of the models we can produce is currently the inverse of systems complexity. Kahlem and Birney⁸⁰

For simpler systems, like yeast, or *E. coli* an enormous amount of data already exists about individual gene regulation, protein interactions etc. and it is possible to build sophisticated models of the entire gene regulatory network and more^{89,90}.

Computational systems biology forms part of what is known as “Complex Systems Analysis” and is concerned with developing and using mathematical models and algorithms to simulate biological systems. In the case of *Neisseria meningitidis*, the layout of the complex system of interest, the respiratory system, is well understood in terms of the position of all the components in the system. What is not known is how electrons traverse the system, how the various components interact with each other, and how they react to changes in external conditions (changes in respiratory substrates). Computational systems biology can be used to create a mathematical model of the current understanding of the respiratory system in *Neisseria meningitidis* which can then be simulated and the results compared to experimental data. The experimental data can then be used to inform the parameters of the mathematical model.

A systems biology approach to understanding the mechanism of respiration

in *Neisseria meningitidis* is necessary as there are a number of components in the system which are inaccessible to the standard reductionist approach to biological systems. These components cannot be isolated from the system in order to analyse them, therefore any information must be gained from looking at the system as a whole.

1.10 Modelling

1.10.1 Modelling Respiratory Systems

1.10.1.1 Current Attempts to Model Respiratory Systems

The following list details some of the modelling carried out on bacterial respiratory chains:

- Almeida et al.⁹¹ created a kinetic model of denitrification in *Pseudomonas fluorescens* and *Paracoccus denitrificans* by assuming that the components of the respiratory chain were arranged like an electrical circuit. They produced a simple and predictive model of denitrification using this approach.
- Jin and Bethke⁹² proposed a new rate law that can be used to model the rate of respiration in *Pseudomonas*. They showed the predictive power of the rate law by looking at rates of benzoate oxidation.
- Cavaliere and Ardelean⁹³ developed an alternative approach involving modelling respiration using “P systems” which are probabilistic models of events. This assigned a probability of each reaction happening, dependant on the state of the system and then iterated through a given set of steps evaluating probabilities and altering values based on the outcome. This approach to modelling was limited in that it was only predicting the quantities of 1 component in each of 2 “compartments”; oxygen in the cell membrane and carbon dioxide in the thylakoid membrane (the model was developed using cyanobacteria).

- Peercy et al.⁹⁰ created a kinetic model of how cytochrome production is regulated by oxygen in the respiratory system of *Escherichia coli*. They created a set of differential equations to describe the relevant reactions and then populated the model using parameters gathered from the literature. They were able to obtain good fits to experimental data from the ArcAB subsystem of the *E. coli* respiratory system.
- Klamt et al.⁹⁴ created a model of the steady-state behaviour of the electron transport chain in purple non-sulfur bacteria (*Rhodospirillaceae*). This model was also created using differential equations to describe rates of change of components.
- Aguiar-González et al.⁹⁵ used an enzyme kinetic model to examine oxygen consumption rates in the marine bacteria *Pseudomonas nautica* and *Vibrio natriegens*. This simple model only describes the respiration rate however, nothing more.

1.10.1.2 Other Relevant Modelling

- Baart et al.⁷² created a flux model of primary metabolism in *Neisseria meningitidis*. This model didn't contain any useful information about the respiratory system, but showed that the flux model could predict substrate preference *in silico*, and this was confirmed *in vivo*.
- Bernard Korzeniewski has been quite prolific in using mathematical models to create computer simulations which describe biological processes, oxidative phosphorylation in particular^{96–98}.

1.10.1.3 Important Considerations

When modelling respiration in a cell, the most important factor is the change in concentration of components over time without any particular spatial constraints, ordinary differential equations (ODEs) are an appropriate technique. In these

systems the model does not change with regard to the spatial arrangement of any of the components. If the system requires changes in time *and* space, then partial differential equations (PDEs) would be necessary (and more complicated)⁹⁹.

Ordinary differential equations only depend on one variable; the time (t). In this case, the change in concentration over time for each component can be modelled as a single differential equation. For multiple components this leads to multiple differential equations with some that rely on the result of another (if the rate of one reaction is directly related to the concentration of another component). These ODEs must then be solved in parallel at a suitable time-scale.

Complications arise when using differential equations if the processes are considered to be stochastic, as a differential equation model assumes that every component can have a continuous value, which is not the case as molecules are discrete. However if the system being modelled is sufficiently large, this effect can be ignored. If the reaction component size is small (< 100s of molecules) stochastic simulation algorithms have to be used as described by Gillespie¹⁰⁰. These methods are usually slower than the simpler deterministic algorithms because of the added complexity of modelling individual components⁹⁹.

1.10.2 Modelling Tools

A number of software packages exist that are capable of this type of modelling such as the Systems Biology Workbench¹⁰¹ and COPASI¹⁰². These allow you to enter biochemical reactions in a format familiar to biologists, and have pre-defined libraries for types of reactions such as mass-action, or one with Michaelis-Menten kinetics etc. The mathematical equations are then derived automatically from the reactions and can be modified by hand if necessary. Parameters for the mathematical equations must be entered, and these will usually be derived from experimental data, or in some cases educated guesses (at least initially). Once a parameter set has been created, the modelling software can run a time-course using a relevant solver-algorithm. COPASI (as at version 4.8) includes

7 solvers, LSODA (Livermore Solver for Ordinary Differential Equations)¹⁰³ for deterministic systems (such as ODEs), Gibson-Bruck¹⁰⁴, Direct Method, τ -leap and Adaptive-SSA/ τ -leap for stochastic systems, and Runge-Kutta and LSODA for hybrid systems (where portions are not considered to be stochastic). A large number of general and specific modelling tools also exist including but not limited to: Mathematica¹⁰⁵, Matlab¹⁰⁶, Gepasi^{107,108}, E-Cell¹⁰⁹, PyBioS^{99,110}, CellDesigner^{111–113} and STOCKS 2¹¹⁴.

1.11 Aims

The over-arching aim of this study was to produce a working mathematical model of the respiratory system of *N. meningitidis* which has been refined and parameterised by experimental biological data. This mathematical model should be able to accurately simulate experimental datasets with known outcomes, and also be able to predict the outcome of experiments that have not been performed. This model, will also be able to provide insight into the states of various components throughout the respiratory process, such as enzymatic oxidation states, some of which are very difficult, if not impossible, to obtain in an *in vivo* study.

The layout of *N. meningitidis* respiratory chain, even though it is longer than that of the model organism *Escherichia coli* is more similar to most other bacteria. This, along with its profound medical importance make it an excellent target for the type of mathematical modelling described above.

The individual aims of the study are therefore:

1. Construct a mathematical model of the *N. meningitidis* respiratory chain.

This will involve the conversion of the kinetic reactions involved in respiration into mathematical equations that can be linked together, and if justified simplifying the chain.

2. Obtaining experimental data on respiratory rates and enzyme kinetics.

This will involve performing experiments on respiring *N. meningitidis* and

recording the concentrations of respiratory substrates under different conditions.

3. **Parametrise the model using experimental data.** To do this a system will need to be developed which can iteratively fit experimental data to specific parts of the mathematical model.

Chapter 2

Materials and Methods

2.1 *Neisseria meningitidis* Strains Used in This Work

Name	Description	Source
MC58	Wild-Type Strain	McGuinness et al. ¹¹⁵
$\Delta norB::spc^r$	Wild-Type with insertion of spectinomycin resistance cassette into <i>norB</i> gene	Heurlier et al. ³⁰
$\Delta nsrR::spc^r$	Wild-Type with insertion of spectinomycin resistance cassette into <i>nsrR</i> gene	Rock et al. ³²
$\Delta norB::spc^r\text{-}\Delta nsrR::tet}^r$	Wild-Type with insertion of spectinomycin resistance cassette into <i>norB</i> and insertion of tetracycline resistance cassette into <i>nsrR</i> genes	Heurlier et al. ³⁰
$\Delta aniA::spc^r\text{-}\Delta nsrR::tet}^r$	Wild-Type with insertion of spectinomycin resistance cassette into <i>aniA</i> and insertion of tetracycline resistance cassette into <i>nsrR</i> genes	Heurlier et al. ³⁰

Table 2.1: Bacterial strains and sources

2.2 Culturing *Neisseria meningitidis*

2.2.1 Growth of *Neisseria meningitidis*

N. meningitidis strains were grown on plates on Columbia Agar Base (CAB) with defibrinated horse blood, and in liquid culture in Müller-Hinton Broth (MHB).

Plates were prepared by adding horse blood to a final concentration of 5% to molten agar, and poured into plastic petri dishes. After streaking with *N. meningitidis* the plates were incubated at 37 °C in a 5% carbon dioxide/air mixture.

Aerobic liquid cultures were grown in 10 ml MHB with 10 mM NaHCO₃ in plastic Sterilin tubes, and incubated at 37 °C at 200 rpm. Microaerobic cultures were suspended in 20 ml MHB, 10 mM NaHCO₃ in plastic Sterilin tubes, incubated at 37 °C at 100 rpm.

2.2.2 Preparation of Antibiotic Selective Media

Liquid stock solutions of required antibiotics were either added directly to liquid culture, or, if growing on plates, to the molten agar when also adding horse blood. The final concentrations of antibiotics are given in Table 2.2.

Antibiotic	Final concentration ($\mu\text{g/ml}$)
Spectinomycin	50
Tetracycline	2.5

Table 2.2: Final antibiotic concentrations

2.2.3 Preparation of Frozen Bacterial Stocks

Bacteria were grown in liquid culture until late log phase prior to harvesting. Liquid cultures were then centrifuged at 4000 g for 15 minutes, and the pellet was then re-suspended in a 25% glycerol, 25% water and 50% MHB, all of which had been autoclaved beforehand. The bacterial stocks were then frozen at -80 °C.

2.2.4 Streaking Plates for OD to CFU Ratio Calculation

Bacterial cultures were grown overnight and then transferred into aerobic liquid culture and samples taken throughout the day to obtain a range of different optical densities. The optical density was recorded at 600 nm on a Jenway 6305 Spectrophotometer (Bibby Scientific Limited, Staffordshire UK), and each sample was serially diluted to the following levels: 10^{-5} , 10^{-6} and 10^{-7} . 100 μl of each of these dilutions was plated on a fresh blood agar plate and left to grow overnight. The following morning the number of colonies on each plate was counted and used to create a simple conversion factor for Optical Density to Colony Forming Units.

2.3 Measuring Oxygen Concentration

Oxygen concentration in respiring cultures was measured using a Clark electrode¹¹⁶ from Rank Brothers, Cambridge, UK. This electrode has a silver anode and a platinum cathode and uses a saturated potassium chloride solution as electrolyte. The electrode is set at the bottom of a 7 ml reaction chamber separated from its contents by a thin Teflon™ membrane. This apparatus is shown in Figure 2.1. The Teflon™ membrane is permeable to dissolved oxygen, which is reduced by the electrode producing a measurable electrical current. The reaction chamber is maintained at 37 °C by an attached water bath. When performing experiments, 5 ml of culture is added to the reaction chamber, which is stirred by use of a magnetic flea, and the chamber covered with a plastic stopper. The stopper has a number of holes through which the NO probe, or Hamilton syringe can be inserted. Data is collected by attaching the electrode to an external data logger (Pico ADC20, Pico Technology).

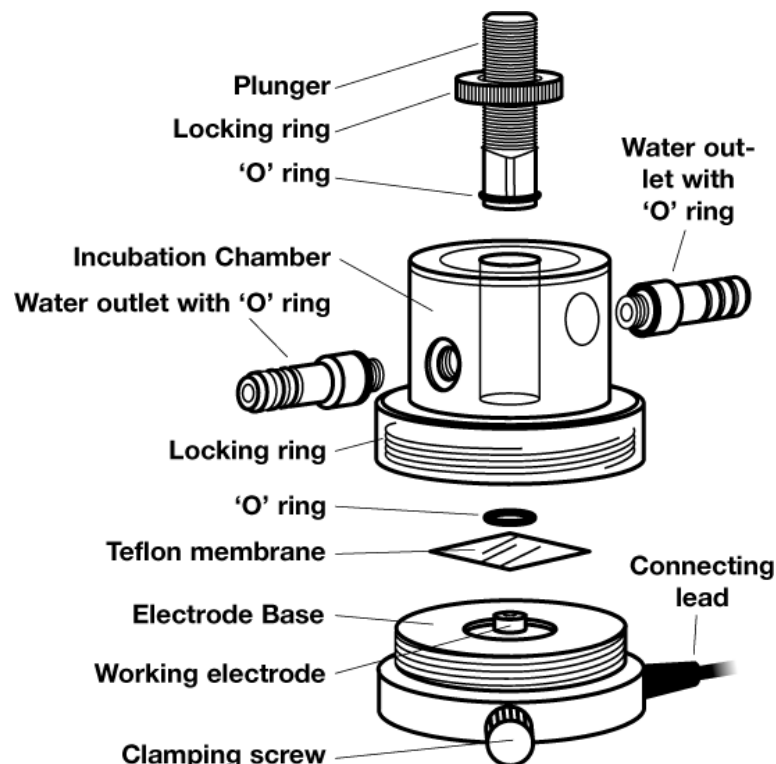


Figure 2.1: **Exploded view of the oxygen electrode.** This assembly sits atop a Rank Brothers Digital Model 10 Controller which acts as a magnetic stirrer and provides the polarising voltage to the electrode (Rank Brothers Ltd¹¹⁷).

2.3.1 Calibration of Oxygen Electrode

Calibration of the oxygen electrode assumes that anaerobic water will not produce any measurable current at the electrode. Oxygen saturated water contains $210 \mu\text{M}$ Oxygen at 37°C ¹¹⁸. 5 ml of ultra pure ($18 \text{ M}\Omega$) water was added to the electrode chamber, and then aerated to saturation by use of a Pasteur pipette. The maximum value recorded by the data logger then corresponds to a concentration of $210 \mu\text{M}$ Oxygen, with the relationship between mV as recorded against concentration being linear.

2.4 Measuring Nitric Oxide Concentration

Nitric Oxide concentration was measured using a Nitric Oxide probe (ISO-NOP, World Precision Instruments) connected to a Nitric Oxide Meter (ISO-NO mkII, World Precision Instruments). This is also a Clark type electrode, contained within a steel sleeve with a semi-permeable membrane separating the working electrode from the system being measured^{119–121}. The NO probe is inserted through one of the holes in the plastic lid of the reaction chamber of the oxygen electrode assembly. The tip of the electrode should be immersed in the culture, with care being taken not to trap any air bubbles on the surface of the probe. The sensor is also attached to the same data logger as above. In this way both Oxygen and Nitric Oxide concentrations can be measured in parallel. A diagram of the apparatus when set up is shown in Figure 2.2.

2.4.1 Calibration of Nitric Oxide Electrode

Calibration of the nitric oxide electrode relies on adding known quantities of Nitric Oxide to the electrode chamber. Sodium Nitrite will liberate Nitric Oxide with a 1:1 ratio when added to a solution of excess Potassium Iodide and Sulfuric acid based on the following reaction:



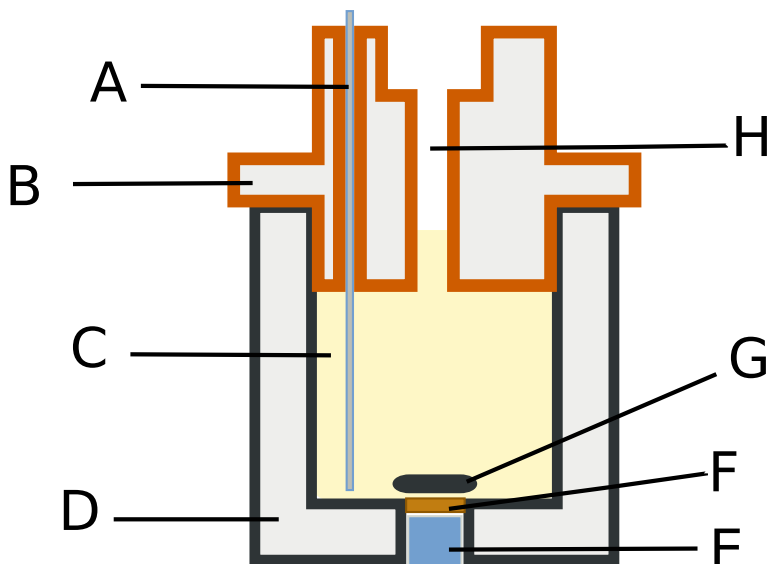


Figure 2.2: **Oxygen electrode chamber with nitric oxide probe inserted.** This shows the set up used to obtain all oxygen and nitric oxide measurements. A - ISO-NOP Nitric Oxide probe. B - Electrode chamber cap. C - Culture medium. D - Oxygen electrode chamber. E - Oxygen working electrode. F - Teflon™ membrane. G - Magnetic flea. H - Air gap.

NaNO_2 Concentration (μM)	Volume (μl)	NO Concentration (nM)
10	50	99
100	25	591
100	50	1561

Table 2.3: Sodium Nitrite concentrations used to calibrate ISO-NOP Nitric Oxide sensor.

5 ml of 0.1 M Potassium Iodide/Sulfuric Acid was added to the electrode chamber and allowed to stabilise. Then, increasing concentrations of Sodium Nitrite solution were successively added to produce a standard curve of Nitric Oxide concentration to recorded electrode mV. The volume and concentrations of Sodium Nitrite added to the electrode chamber are detailed in Table 2.3.

2.5 Measuring Nitrite Concentration (Griess Assay)

Nitrite concentration in liquid culture was determined using the colorimetric assay described by Nicholas and Nason¹²². This reaction is based on chemical diazotization which uses sulfanilamide and *N*-1-naphthylethylenediamine dihy-

drochloride (NED) under acidic (hydrochloric acid) conditions. Nitrite is converted to nitrous acid under acidic conditions and this then forms a diazonium salt with the sulfanilamide. The diazonium salt combines with NED and forms a pink azo dye which can be detected using absorbance spectrophotometry at a wavelength of 540 nm. Depending on the expected concentration of nitrite, different sample volumes are used in the assay. The most common sample volume used was 25 μ l which allows detection up to around 1 mM nitrite with the following reagent volumes: 875 μ l of 1% sulfanilamide in 1 M HCl and 100 μ l of 0.02% NED in 1 M HCl. When using different sample volumes, the volume of sulfanilamide was altered such that the volume of sample + sulfanilamide always equalled 900 μ l. After adding the sample to the reagents, it was left for 20 minutes for the colour to develop, then the absorbance at 540 nm was measured and compared to a standard curve.

2.6 Nitric Oxide Production

Solutions of Nitric Oxide were prepared using a method derived from one described by Aga and Hughes¹²³. The apparatus setup is shown in Figure 2.3. A concentrated solution of Sulfuric acid was added from a pressure-equalizing dropping funnel to a concentrated solution of Sodium Nitrite solution in a stirred, round-bottomed flask. This released NO gas which passed through a solution of Sodium Hydroxide to neutralise any Sulfuric acid present, then through distilled water to remove any Sodium Hydroxide and Nitrogen Dioxide before finally being bubbled into a collection vessel with a sealed rubber septum containing distilled water. The concentrations of the chemicals used in this preparation are shown in Table 2.4.

The system should be set up in a fume cupboard as shown in Figure 2.3 and sparged with N₂ gas for 15 minutes (the dropping funnel will allow gas to pass into the round bottomed flask even when the bottom valve is closed). The H₂SO₄ should be sparged separately. Valve 2 should be left open at all times. After

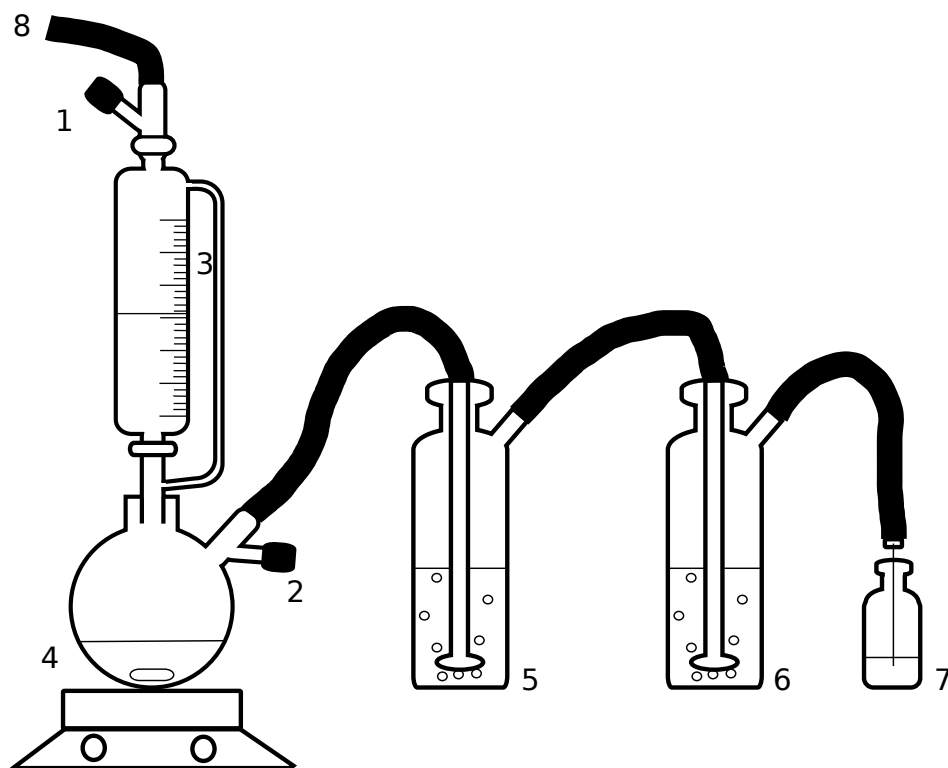


Figure 2.3: **NO making apparatus.** 1 & 2 - N₂ release valves. 3 - Pressure equalizing dropping funnel, containing 50 ml 4 M H₂SO₄. 4 - Stirred, round-bottomed flask, containing 200 ml 2 M NaNO₂. 5 - Dreschel bottle with sintered bulb, containing \approx 200 ml 1 M NaOH ($\frac{2}{3}$ full). 6 - Dreschel bottle with sintered bulb, containing \approx 200 ml dH₂O ($\frac{2}{3}$ full). 7 - Small glass bottle with rubber septum and needle entry valve, containing dH₂O $\frac{2}{3}$ full. This bottle either needs to also have a gas exit needle, or at least not be sealed during the process.. 8 - To N₂ gas bottle. Viton rubber tubing is used for all the flexible hoses in this apparatus.

Chemical	Volume (ml)	Concentration (M)
NaNO ₂	200	2
H ₂ SO ₄	50	4
NaOH	200	1

Table 2.4: Chemicals needed for preparation of Nitric Oxide solution.

sparging close valve 1 and then add the Sulfuric acid drop-wise from the dropping funnel. Brown gas will start to bubble through to the collection vessel. This apparatus should produce enough NO gas to saturate several small (10 ml) collection vessels which should have the needle removed and be sealed once saturated. Once all the Sulfuric acid has been added the reaction was left to finish for up to 2 hours. Before disassembly the apparatus was sparged with N₂ gas to remove any residual NO gas.

The eventual concentration of NO in the solution will vary depending on the temperature, but at 25 °C in ultra pure ($18\text{ M}\Omega$) water the concentration will be between 1.88 and 1.96 mM^{123,124}.

Chapter 3

Model - Construction and Parameters

3.1 Construction

The model was constructed based on existing knowledge of the respiratory chain in *Neisseria meningitidis* from the ETC shown in Figure 1.2 (Chapter 1). No *a priori* assumptions are made about separation of time-scales that would permit the use of Michaelis-Menten kinetics, as the rates of intermediate reaction steps are not known. This approach also permits tracking of the oxidation state of all the intermediates which allows understanding and offers the potential for predictions that may be explored in future *in vivo* studies.

The model was generated as a set of ordinary differential equations which describe the bulk-average concentration of substrates, products, enzymes and their activity within a well-mixed vessel. It is assumed that the bacterial population structure is homogeneous and that there are no variations in concentrations of substrates between the bulk media and within the bacterial cells. Stochastic effects are ignored at the protein level, but they are unlikely to be of importance. Initially protein production is largely ignored as the switching mechanism is thought to happen on a time-scale that is much shorter than the transcription and translation of new proteins, they are therefore assumed to be expressed constitutively except where stated otherwise. However some datasets were available in the published literature²⁰ that suggested otherwise, and were tested using an

extension to the model described below which includes transcription and translation of certain components.

3.1.1 Normalising the Data

The model contains no implied information about cell density. This means the values for various component concentrations will differ between experiments. Initially the optical density of cultures was used to determine the cell density however experiments proved that this was not a completely reliable proxy as the optical density is also affected by dead cells. Using optical density as a cell density proxy should give linear relationships between cell densities and overall reduction rates, however this proved not to be the case, with rates of oxygen reduction differing between cultures with the same optical density (data not shown). Therefore where possible, any normalisation that was carried out used the initial oxygen reduction rate as a relative indicator of living cells. Plating out serial dilutions of high density cultures showed that a culture with $OD_{600} = 1$ contains approximately 1×10^9 cells/ml.

3.1.2 Converting Biological Reactions into Differential Equations

The rationale for obtaining the form for each of the 9 component equations is described below. Throughout the model the reduced components, i.e. those with available electrons, are denoted as active and have a subscript a . Components lacking a subscript denote the total, constant, amount of a component. \emptyset denotes nothing (this is used as the source or sink when substrates are entering or exiting the system). It is assumed that all the chemical reactions occur with mass action kinetics. That is to say that the rate of the reaction is proportional to the product of the concentrations of the reactants, this assumption is made in the absence of any knowledge of reaction kinetics. This kinetic scheme allows simple conversion of a chemical reaction to final differential equations. The equation $A + B \rightarrow C$ the

rate of reaction is proportional to $[A][B]$. Therefore reaction can be modelled as:

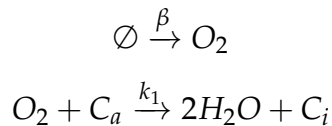
$$\begin{aligned}\frac{d[A]}{dt} &= -k[A][B] \\ \frac{d[B]}{dt} &= -k[A][B] \\ \frac{d[C]}{dt} &= k[A][B]\end{aligned}$$

The reactions below are stoichiometrically balanced with respect to the respiratory substrates. In cases where the product is not tracked (such as where the product is water, or nitrous oxide), the equations is left with a non-integer right-hand-side.

3.1.2.1 Respiratory Substrates

Oxygen

The change in concentration of oxygen is affected by the following kinetic processes.



where β is the rate constant of passive diffusion (as a function of O_2 concentration) of O_2 into the electrode chamber. The rate constant k_1 describes the reduction of oxygen by the oxygen reductase cbb_3 ; this value depends on the concentration of reduced (i.e. active) cbb_3 , C_a and the concentration of O_2 . The differential equation that gives the change in oxygen concentration is

$$\frac{d[O_2]}{dt} = \beta(1 - [O_2]/K_O) - k_1[C_a][O_2] \quad (3.1)$$

In isolation the first term gives rise to a simple exponential input of oxygen until the saturation level (K_O) is reached to account for diffusion into the system. The rationale for the form of the equation is given below.

During the course of the experimental stages of this work, on occasions where the respiring cultures had died, either through being left in essentially anaero-

bic conditions for too long, or were treated with Chloramphenicol (which stops all protein production in the cell), the oxygen levels in the culture media would begin to rise slowly. This did not occur in every case, and after some further experimentation it was concluded that it probably occurs when an air bubble gets trapped underneath the lid of the oxygen electrode chamber. To try and abate the rate of diffusion in all subsequent experiments particular care was taken to avoid an air bubble being trapped in the electrode chamber.

Unfortunately even with no air bubble a small amount of oxygen was diffusing in, so an experiment was set up to try and quantify the rate of diffusion. Wild-type *N. meningitidis* cultures were grown to various different cell densities and left to respire aerobically. Once the cultures had used all the available oxygen they were killed either by adding a small volume of Potassium Cyanide (50 μl of a 50 μM solution), or by heating the culture to 95 °C for 10 minutes. Oxygen concentrations were then recorded as the gas diffused back into the electrode chamber.

The experimental data showed that the increasing oxygen concentration takes the form of an inverse exponential decay and therefore can be fit very easily to an exponential function. The exact parameters of the diffusion seem to differ between cultures but it appeared to have a dependence on the cell density whereby lower cell densities generally had higher rates of diffusion than higher cell densities, but there was no obvious direct relationship. The equation used to fit raw data for oxygen diffusion is a 3 parameter exponential:

$$f(x) = c - ae^{-bx}$$

In the differential equation this collapses to two parameters, the oxygen saturation level, and the rate of oxygen recovery thus:

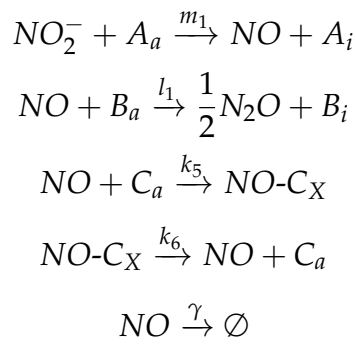
$$\frac{d[O_2]}{dt} = \beta(1 - O_2/K_O)$$

Integrating and separating this equation gives:

$$\begin{aligned} -\beta \frac{t}{K_O} + C &= \ln([O_2] - K_O) \\ \Rightarrow [O_2] - K_O &= Ae^{\left(-\beta \frac{t}{K_O}\right)} \\ \Rightarrow [O_2] &= K_O + Ae^{\left(-\beta \frac{t}{K_O}\right)} \end{aligned}$$

Nitric Oxide

The change in nitric oxide concentration is affected by the following kinetic processes.



The equations above have a number of additional interactions in comparison to O₂. NO is created by the reduction of NO₂⁻ by AniA, is reduced by its dedicated reductase, NorB, and converted to N₂O which is lost from the cell, interacts with *cbb*₃, and is also spontaneously lost from the electrode chamber. It is assumed that the interaction with *cbb*₃ occurs only in a reversible manner, leading to an NO bound and temporarily inactive form C_X. There is evidence that this interaction can also lead to permanent degradation of *cbb*₃ via the formation of peroxy nitrite at the terminal oxidase^{28,125}. This is not currently considered in this version of the model. These effects are described mathematically in the equation below.

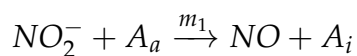
$$\frac{d[NO]}{dt} = m_1[NO_2^-][A_a] - l_1[NO][B_a] - k_5[C_a][NO] + k_6[C_X] - \gamma[NO] \quad (3.2)$$

The rate of synthesis of NO is captured by the first term, with rate constant *m*₁ and depends on the both the concentration of NO₂⁻ and reduced AniA (*A*_a). The

reduction of NO is described by the next term with the rate constant l_1 and also depends on the concentration of NO and reduced NorB (B_a). Inhibition of cbb_3 by NO is modelled by the 3rd component of the equation. k_5 is the rate constant describing the reversible binding of NO to cbb_3 to form the inactive form of cbb_3 , C_X . k_6 is the rate of recovery of this inhibited cbb_3 . γ is the spontaneous rate of loss of NO from the electrode chamber.

Nitrite

The change in nitrite concentration is affected by the following kinetic process.



Which can be modelled mathematically by this equation

$$\frac{d[NO_2^-]}{dt} = -m_1[NO_2^-][A_a] \quad (3.3)$$

where m_1 is the rate constant for reduction of NO_2^- by reduced (active) AniA (A_a).

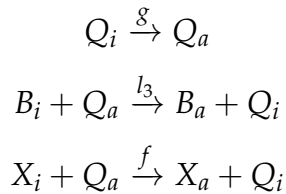
3.1.2.2 Electron Transporters

In addition to the rate of change of concentration of the respiratory substrates, the model also contains information about the upstream state of components of the transfer chain, starting from the quinone pool. The ultimate upstream source of electrons into the respiratory chain is from NADH, but for the sake of simplicity all processes prior to the quinone pool are subsumed into a simple single rate constant. This simplification is made to avoid further complications associated with varying metabolism and to avoid distraction from the stated primary aim of understanding the switching behaviour of the downstream chain. The quinone pool was chosen as the starting point because it is known that NorB draws electrons directly from this point and therefore this represents the first branch in the chain. The desire was to understand how competition for electrons at branches

affects function and therefore the quinone pool is included in the model.

Quinones

The change in concentration of reduced quinones is affected by the following kinetic processes.



The differential equation that models these reactions is

$$\frac{d[Q_a]}{dt} = g([Q] - [Q_a]) - l_3[Q_a](B - B_a) - f[Q_a](X - X_a) \quad (3.4)$$

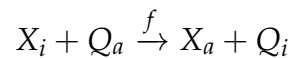
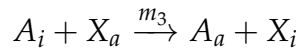
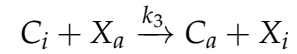
Q_a is the reduced quinone, and Q the total concentration of quinones in the system (Q_i is calculated from these two values). g represents the constant rate of availability of electrons into the quinone pool from NADH. The reduction of NorB by active quinones is parameterised by the rate constant l_3 . NorB and reduced NorB are given by B and B_a respectively. As the quinones also reduce the cytochromes, this also needs to be modelled. f is the rate constant parameterising the reduction of cytochromes by the active quinones. Total cytochromes and total reduced cytochromes are given by X and X_a respectively which are used to calculate X_i in the kinetic process.

Cytochromes

A simplified version of cytochromes was used and therefore X actually represents a pool of different cytochromes, c_x, c_4, c_5 and the bc_1 complex. These are amalgamated into one here to simplify the equations and focus on the simple branching of the chain and competition for electrons. This is a modelling choice and it is further discussed in Chapter 8.

The concentration of active cytochrome pool changes due to both reduction by the upstream quinone pool and oxidation by both of the remaining downstream

terminal enzymes can be seen in the following kinetic processes.



These are modelled with the following differential equation

$$\frac{d[X_a]}{dt} = -k_3([C] - [C_a] - [C_X])[X_a] - m_3([A] - [A_a])[X_a] + f[Q_a]([X] - [X_a]) \quad (3.5)$$

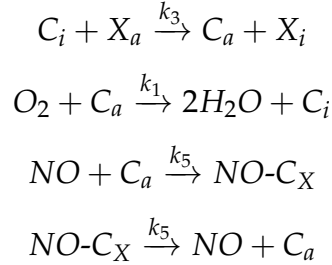
where k_3 is the rate constant describing the reduction of the available oxidised cytochrome c oxygen reductase (cbb_3) by the quinone pool (via c_x & c_4). C , C_a and C_X represent the overall concentration of cbb_3 , reduced (active) cbb_3 and NO inhibited cbb_3 respectively. m_3 is the rate constant describing the reduction of AniA by the cytochrome pool (via c_5). The concentration of active cytochromes is thus increased by their reduction by the quinone pool, but this in turn can reduce the flux from the pool because less oxidised cytochrome is available to accept electrons. As stated previously, the relative time scales are unknown so all processes appear explicitly.

3.1.2.3 Terminal Reductases

Finally, the changes in concentration of reduced terminal oxidases, cbb_3 , AniA and NorB are described by the following equations. All the terms present in this section have been introduced previously. These equations could equally have been written for the oxidised form but these can easily be recovered because it is assumed that the total concentration of the oxidases remains constant.

Reduced cbb_3

The kinetic processes which affect the concentration of reduced (active) cbb_3 are



which is described by

$$\frac{d[C_a]}{dt} = k_3([C] - [C_a] - [C_X])[X_a] - k_1[C_a][O_2] - k_5[C_a][NO] + k_6[C_X] \quad (3.6)$$

Inhibited cbb_3

The following kinetic process alters the concentrations of reversibly inhibited cbb_3 .

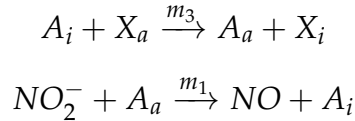


which is described by

$$\frac{d[C_X]}{dt} = k_5[C_a][NO] - k_6[C_X] \quad (3.7)$$

Reduced AniA

The concentration of reduced AniA is affected by the following kinetic processes.

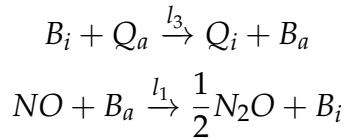


which can be modelled by

$$\frac{d[A_a]}{dt} = m_3([A] - [A_a])[X_a] - m_1[NO_2^-][A_a] \quad (3.8)$$

Reduced NorB

Changes in NorB concentration occur via the following kinetic processes.



and are modelled by this equation

$$\frac{d[B_a]}{dt} = l_3[Q_a]([B] - [B_a]) - l_1[NO][B_a] \quad (3.9)$$

The flow of electrons and how this relates to the parameters described above is shown in Figure 3.1.

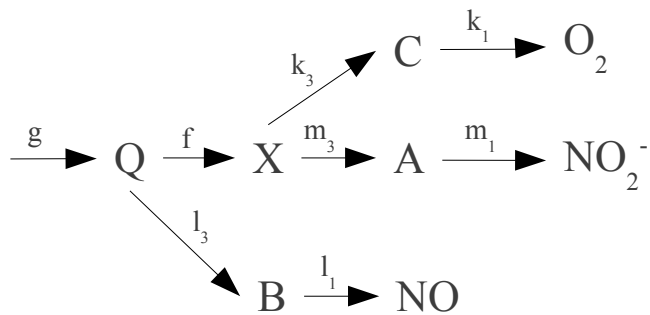


Figure 3.1: Electron flow through the respiratory chain.

3.1.3 Assumptions and their Justifications

A number of assumptions were made regarding the kinetics and reactions taking place in the model.

1. **It is assumed that NO inhibits the reduced cbb_3 and not the oxidised form, since it is not expected that Nitric oxide to bind to an inactive enzyme.**

This is corroborated by Giuffre et al.¹²⁶, who show significant levels of inhibition of reduced cytochrome. They do also however observe low levels of inhibition of the oxidised enzyme also. Their experiments used cytochrome c oxidase (aa_3) rather than cbb_3 , but this assumption should still stand as the enzymes are of the same family. This also implies that the model deals

exclusively with reversible inhibition.

2. Bacterial population structure and concentration variation not considered.

The primary substrates of interest are gases and substrates which are thought to freely diffuse in and out of the cells. Additionally the culture is kept well-mixed at all times, thus it can be assumed that the culture is homogeneous.

3. No backwards reactions. For simplicity, backwards reactions are not included. However they may be important, and could easily be included in a future study with the concomitant increase in parameter count.

4. No Michaelis-Menten kinetics. Separation of time-scales cannot be assumed as the rates of intermediate reaction steps are not known. Future information regarding time-scale separation could easily be incorporated.

5. All cytochromes can be modelled as one. The main effort of modelling was to concentrate on the position of branches in the respiratory chain. In the same way the effects of Laz and c_5 on AniA and cbb_3 respectively are ignored. They are not the prime electron donors to their terminal reductases and contribute very little overall to the reduction²⁵. All the electron donors are treated as a single modelled entity.

3.2 Parameters and their Prior Distributions

None of the rate constants or concentrations which were required for this model have previously been determined for *Neisseria meningitidis*, so values from other similar organisms had to be used instead. In some cases there appears to be no data in the literature regarding values of particular components. Table 3.1 lists the values that have been obtained from the literature.

Symbol	Description	Value	Source
k_1	Rate constant for O_2 reduction by reduced cbb_3	$415 \mu M^{-1}s^{-1}$	Forte et al. ¹²⁷ and Hunter ¹²⁸
k_3	Rate constant for cbb_3 reduction by cytochrome pool	$3 \mu M^{-1}s^{-1}$	Chang et al. ⁶⁸
l_1	Rate constant for NO reduction by reduced NorB	$0.27 - 500 \mu M^{-1}s^{-1}$	Rock et al. ³² and Wasser et al. ⁵³
l_3	Rate constant for NorB reduction by quinone pool	Unknown	N/A
m_1	Rate constant for NO_2^- reduction by reduced AniA	Unknown	N/A
m_3	Rate constant for AniA reduction by cytochrome pool	$4.8 \pm 0.2 \mu M^{-1}s^{-1}$	Nojiri et al. ¹²⁹
k_5	Rate constant for cbb_3 inhibition by NO	$100 \mu M^{-1}s^{-1}$	Giuffre et al. ¹²⁶ and Blackmore et al. ¹³⁰
k_6	Rate constant for recovery of NO inhibited cbb_3	$38 s^{-1}$	Rock et al. ²⁰
β	Rate constant for passive diffusion in of O_2	Unknown	N/A
K_O	Saturation O_2 level	$48 \mu M$	This work
g	Rate of electrons in from NADH	$0.8 s^{-1}$	This work
f	Rate constant for reduction of cytochromes by quinones	$8 \mu M^{-1}s^{-1}$	This work
γ	Spontaneous loss of NO	Unknown	N/A
Q	Concentration of quinones	$0.3 \mu M$	Hedrick and White ¹³¹
X	Concentration of cytochromes	$\approx 3.97 \mu M$	Deeudom ²⁵
A	Concentration of AniA	$0.003 - 0.03 \mu M$	This work
B	Concentration of NorB	$0.003 - 0.03 \mu M$	This work
C	Concentration of cbb_3	$0.003 - 0.03 \mu M$	This work

Table 3.1: **Model parameters.** This table shows all the parameter values that have been obtained from the extant literature, or interpolated from preliminary experiments done during the course of this work. These values represent the initial data that is used to populate the model, from which all subsequent parameter sets are generated. For values that show concentrations of components, they represent the value for a culture with $OD_{600} = 1.00$.

Variables

O₂ - Oxygen concentration

This variable is always obtained directly from the experimental dataset as it indicates the starting point for oxygen in the model. It is calculated from a linear regression analysis of the first linear section of oxygen reduction to eliminate noise in the data.

NO - Nitric oxide concentration, and NO₂⁻ - Nitrite concentration

As for Oxygen concentration, these variables are simply obtained from the dataset and the same conditions apply.

X_a, A_a, B_a, C_a, Q_a - Reduced enzyme concentrations, and C_X - Reversibly NO inhibited cbb₃

These values are unknown at start of simulations. They have to be lower than the total concentrations for each enzyme, and the model enforces this. Given the rates of reduction of these enzymes they are all set to very low values, determined from exploratory runs of the parameter estimation algorithm. The rates of reduction for these enzymes actually make the initial value (so long as it is low) largely irrelevant as they reach their steady-state after only a few integration cycles.

Parameters

k₁ - Rate constant for O₂ reduction by reduced cbb₃

A value for k_1 , the constant for O₂ reduction by reduced cbb₃ was calculated by using the k_{cat} value from *Pseudomonas stutzeri*, and the K_M value from *Neisseria lactamica*, which Forte et al.¹²⁷ and Hunter¹²⁸ determine are 166 s⁻¹ and 0.4 μM respectively. k_1 can be calculated as $\frac{166 \text{ s}^{-1}}{0.4 \mu\text{M}} = 415 \mu\text{M}^{-1}\text{s}^{-1}$.

k₃ - Rate constant for cbb₃ reduction by cytochrome pool

k_3 , the rate constant for reduction of cbb_3 by the cytochromes was calculated from values obtained from the maximum reduction rate of cbb_3 by cytochrome c_4 in *Vibrio cholerae* by Chang et al.⁶⁸. A rate of 300 electrons transported per second was observed with a cytochrome c_4 concentration of 100 μM . This concentration was not saturating, but there appears to be a linear relationship between rate and concentration. It is assumed that 1 electron equals 1 reduction of cbb_3 , thus the rate constant for reduction of cbb_3 by cytochromes is $\frac{300 \text{ s}^{-1}}{100 \mu\text{M}} = 3 \mu\text{M}^{-1}\text{s}^{-1}$.

l₁ - Rate constant for NO reduction by reduced NorB

An estimate for the rate constant for NO reduction by reduced NorB can be obtained from Rock et al.³².

They observed rates of NO reduction of $54 \pm 6 \text{ nmol min}^{-1}\text{mg}^{-1}$ in total protein content from dry weight. Thus the rate of NO reduction is $0.9 \pm 0.1 \mu\text{mol s}^{-1}\text{g}^{-1}$ bacterial protein. The protein content of the cells was assumed to be similar to that of *E. coli* at 50% of dry weight, where each cell weighed 0.6 pg. A culture of *Neisseria meningitidis* with $OD_{600} = 1$ has 1×10^9 cells/ml, and the reaction volume is 5 ml. $5 \times 10^9 \text{ cells} \times 0.6 \times 10^{-12} \text{ g} \times 50\% \times 0.9 \mu\text{mol s}^{-1}\text{g}^{-1}$ results in 1.35 nmol s^{-1} of quinones in 5 ml, which when converted to molarity is $0.27 \mu\text{M}^{-1}\text{s}^{-1}$.

Wasser et al.⁵³ suggest that the rate constant may be as high as $500 \mu\text{M}^{-1}\text{s}^{-1}$, although this was estimated for a cNOR type nitric oxide reductase.

l₃ - Rate constant for NorB reduction by quinone pool

No information available in the literature, so the rate constant is set to $1 \mu\text{M}^{-1}\text{s}^{-1}$.

m₁ - Rate constant for NO₂⁻ reduction by reduced AniA

No information available in the literature, so the rate constant is set to $1 \mu\text{M}^{-1}\text{s}^{-1}$.

m₃ - Rate constant for AniA reduction by cytochrome pool

The value for m_3 , the rate constant for reduction of AniA by cytochromes, is the observed electron transfer rate between the equivalent cytochrome and nitrite reductase from *Achromobacter xylosoxidans*. A value of $4.8 \pm 0.2 \mu\text{M}^{-1}\text{s}^{-1}$ was observed during stopped-flow experiments by Nojiri et al.¹²⁹.

k₅ - Rate constant for cbb₃ inhibition by NO

Giuffre et al.¹²⁶ and Blackmore et al.¹³⁰ showed with cytochrome *c* oxidase that NO could bind reversibly and inhibit the activity of the enzyme. The rate constant they calculated was $10^8 \text{ M}^{-1}\text{s}^{-1}$. An assumption was made that even though the enzyme is different, its NO binding characteristics would be similar to that of *cbb₃* as it is of the same family.

k₆ - Rate constant for recovery of NO inhibited cbb₃

Giuffre et al.¹²⁶ calculated a half-life of $t_{1/2} \approx 80 \text{ min}$, however without any concrete values for concentration of $C_X\text{-NO}$ this cannot be used to calculate a rate constant. Rock et al.²⁰ observed the apparent K_i and calculated it to be 380 nM at 50 $\mu\text{M O}_2$. Since $K_i = \frac{k_6}{k_5}$, a value for k_6 can be estimated as $k_6 = K_i \times k_5 = 0.38 \mu\text{M} \times 100 \mu\text{M}^{-1}\text{s}^{-1} = 38 \text{ s}^{-1}$.

 β - Rate constant for passive diffusion in of O₂, and K_O - Saturation O₂ level

The parameters obtained from fitting oxygen diffusion data showed a small difference in K_O between cell densities, thus $K_O = 48 \mu\text{M}$ was selected as the standard value for this parameter. β differed more between the experiments thus in the parameter estimation system it is not fixed and allowed to be modified freely. An example of the experimentally observed diffusion rates are shown in Figure 3.2. K_O is the apparent saturation concentration of Oxygen in the respiring culture and forms part of the exponential diffusion equation mentioned earlier in this chapter.

Oxygen Diffusion Rates

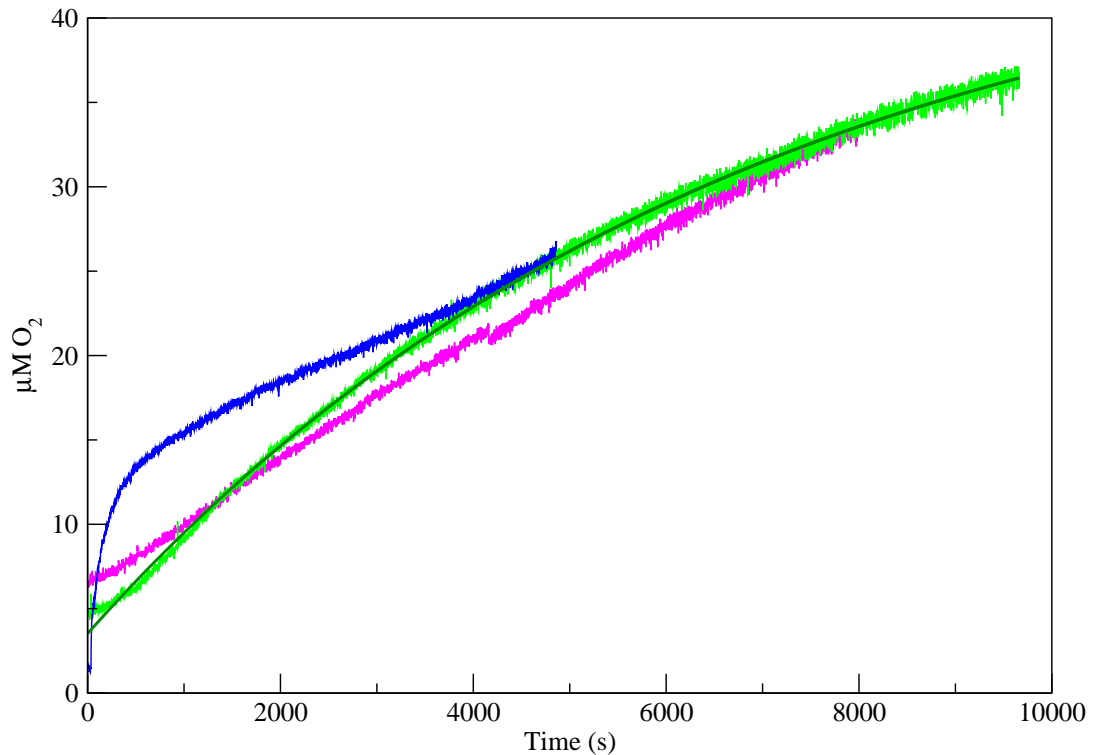


Figure 3.2: Oxygen Diffusion Rates. This figure shows experimentally observed rates of oxygen diffusion back into the electrode chamber. An exponential decay function has been fitted to the green dataset and produces the K_O value (the effective saturation concentration) of $\approx 48 \mu\text{M}$.

g - Rate of electrons in from NADH (or rate of reduction of quinones)

This value is unknown, but initial runs of the algorithm suggest the value to be about 0.8 s^{-1} .

f - Rate constant for reduction of cytochromes by quinones

Snyder et al.⁶³ showed by reducing yeast cytochrome bc_1 by using $25 \mu\text{M}$ menaquinol the rate constants were 7.9 s^{-1} for cytochrome b , and $1.55 - 6.9 \times 10^5 \text{ M}^{-1}\text{s}^{-1}$ for cytochrome c_1 (second order). However preliminary tests showed that a value of $8 \mu\text{M}^{-1}\text{s}^{-1}$ was more appropriate.

γ - Spontaneous loss of NO

This value is assumed to be the same as the β , the rate constant for oxygen diffusion in across the liquid-gas barrier, as this is simply the reverse, given the physical similarity of Nitric Oxide and Oxygen.

Q - Concentration of quinones

Q , the concentration of quinones was calculated based on data from Hedrick and White¹³¹. The protein content of the cells was assumed to be similar to that of *E. coli* at 15% of wet weight, where each cell weighed 2 pg, and that there were $1\text{ }\mu\text{mol}$ of respiratory quinones per g of bacterial protein¹³². A culture of *Neisseria meningitidis* with $OD_{600} = 1$ has 1×10^9 cells/ml, therefore there are 1.5 nmol of quinones in 5 ml culture ($5 \times 10^9 \text{ cells} \times 2 \times 10^{-12} \text{ g} \times 15\% \times 1 \text{ }\mu\text{mol/g}$), converted to molarity is $0.3 \text{ }\mu\text{M}$.

X - Concentration of cytochromes

Deeudom²⁵ suggests that the total cytochrome concentration (inc. cbb_3) is about $4 \text{ }\mu\text{M}$ in *Neisseria meningitidis*. Thus subtracting the value for C leaves a concentration of $\approx 3.97 \text{ }\mu\text{M}$.

A, B, C - Concentration of Respiratory enzymes

Given the lack of concrete values for these parameters, the assumption is that all the respiratory enzymes are present in roughly equal quantities. Based on the values given for Q above, there are 1.5 mg of cell protein in 5 ml of $OD_{600} = 1$ culture. cbb_3 is thought to be about 0.1%-1% of the total cell protein and is approximately 100 kDa in molecular weight. Therefore converting these values to molarity gives a concentration of approximately 3-30 nM.

3.3 Solving Ordinary Differential Equations

The model equations (given previously) are solved in parallel using the common 6th order Runge-Kutta-Fehlberg algorithm for integrating ordinary differential equations¹³³. Adaptive step-sizes were implemented using the Cash-Karp method¹³⁴. The adaptive step size system was required as it prevented the introduction of systemic numerical instabilities (see appendix for further details of why this was necessary).

3.4 Implementation of the Model in Software

The parameter estimation system and ODE solver were a bespoke implementation written in Java. The Runge-Kutta algorithm was modified from that found in Numerical Recipes in C¹³⁵. A custom implementation was written rather than using off the shelf systems for solving ODEs and parameter estimation as maximum flexibility was required for integrating the two techniques (parameter estimation and ODE solving), and it allowed adaptation of the code to the requirements more quickly and more easily. Alternative systems are available such as COPASI¹⁰², but with more limited scope for customisation and integration of techniques.

The implementation of the model has no constraints on respiratory substrate concentration, thus allows the altering of these concentrations whilst solving the equations. This ability means that the switch between aerobic and anaerobic respiration can be examined synthetically, and the model is also capable of simulating how the respiratory system responds to the sudden addition of substrates such as Nitric Oxide. More complicated methods are possible, but given the high diffusion of the substrates concerned as well as the deliberate injection of the relevant substrate this method was a simpler and reasonable mimic for my empirical method. This ability was an absolute requirement, as in order to fully parameterise the model it was necessary to isolate sections of the model, which required

adding aliquots of respiratory substrate during respiration.

3.5 Parameter Estimation

Estimating the parameter values for the components in the mathematical model involved comparing the biological results with those produced by solving the ODEs and adjusting the parameter values to minimise the difference between the two results. The different methods for parameter estimation that were investigated are detailed in Chapter 4.

Chapter 4

Parameter Estimation Methodologies

4.1 The Challenge of Parameter Estimation

Parameter estimation is a technique that attempts to estimate the values of a set of parameters based on measured data. This involves creating an estimator - an algorithm that generates new parameter estimates - and some form of calculation to assess how good the estimate is. The model being discussed in this thesis has a large number of unknown values which need to be estimated and it was not clear what values many of these parameters should take, or even if the initial values used are close to the “true” values. Given the inherent variability of experimental data in biology, point estimates for parameters are not going to be representative of the true state of that parameter unless a near infinite number of datasets are analysed. Thus the output of the parameter estimation needed to be a probability distribution, with probability densities that reflected the probability of the parameter taking on a particular range of values. Another requirement of the estimator is that it needs to be able to select new estimates based on prior probability distributions, since some information about certain parameters is known beforehand, and this knowledge will improve as more datasets are analysed.

These requirements lend themselves well to Monte-Carlo type methods, which produce output which can be represented as a probability distribution and can be selected from a prior probability distribution.

4.2 Methods and Algorithms Used

Below are the various different methods for parameter estimation that were investigated during the course of this work. All of these methods involve a sampling system that attempts to select parameter values which minimise the difference between the simulation result and the experimental data by using a difference function. The main difference between the parameter estimation methodologies laid out below are the ways in which they generate new parameter values, either from a probability distribution or based on the previous value, and the way this is applied and tested against the experimental data. The aim of the parameter estimation methodology was to achieve an output from the difference function that was as close to zero (perfect fit/no difference) as possible. The value produced by the difference function is hereby referred to as the *Goodness of Fit* or *F* value, with larger values representing worse fits to the experimental data.

4.2.1 Difference Functions

Two different difference functions were used to calculate the *F* value. One was the sum of the Least Squares Differences between the measured components in the experimental data and the simulation result. This was used in early parameter estimation runs.

$$F = \sum_{j=1}^n \left(\sqrt{\sum_{i=1}^m (\Delta x_{ij})^2} \right) \quad (4.1)$$

Where j is the current component, n the number of components, i the current data point, m the total number of data points and $(\Delta x_{ij})^2$ the square of the residuals between the experimental and simulated data for component j at data point i . Therefore the *F* value becomes “the sum of the squares of the residuals for each data point for each parameter.”

The second method for calculating the *F* was a log-likelihood calculation. This method calculates the likelihood of the simulated data falling under a normal

distribution which has the experimental data as its μ , and a preset error value as its σ . The method was used as it allowed tuning of the σ value, which provided more control over how new parameter sets were accepted. The lower the value of σ , the closer the simulated data needs to be to the experimental data to achieve a low F value.

$$F = \sum_{j=1}^n \left(\sum_{i=1}^m \ln(\text{norm}(x_1, \mu_1, \sigma)) - \ln(\text{norm}(x_2, \mu_2, \sigma)) \right) \quad (4.2)$$

Where j is the current parameter, n is the number of parameters, i is the current data point, m is the total number of data points, norm is a function that accepts 3 arguments (x, μ, σ) and returns the probability density associated with x in a normal distribution with parameters μ and σ (the probability of a continuous parameter taking on a particular value is zero), x_1 and μ_1 are zero, x_2 is the solved value at data point i for parameter j , μ_2 is the experimental value at data point i for parameter j and σ is the preset standard deviation.

x_1 and μ_1 are set to zero because this likelihood calculation can also be used on the time axis in addition to the value axis. Since there is no time uncertainty in the data, this can be ignored by setting these values to zero and the equation becomes:

$$F = \sum_{j=1}^n \left(\sum_{i=1}^m \ln(\text{norm}(0, 0, \sigma)) - \ln(\text{norm}(x_2, \mu_2, \sigma)) \right) \quad (4.3)$$

The value for σ is determined such that the first few iterations of parameter estimation generate very high F values (with the knowledge that this will always decrease) subject to the computational limits imposed by floating point precision (values of σ which are too low generate nonsensical F values).

In most cases the components used for calculating the likelihood are Oxygen and Nitric Oxide, as these were the primary measured chemicals.

4.2.2 Monte Carlo Methods

A brief section is included here to describe Monte Carlo Methods, as the techniques used for parameter estimation all use this method as their estimator in some form. “Monte Carlo Methods” is a generalised term to describe a stochastic technique that makes use of random numbers to examine a problem in conjunction with probability statistics. Monte Carlo Methods allow modelling of complex systems without having to exhaustively search every possible outcome. Large systems are sampled in random configurations and that data applied in such a way that it can be used to describe the system as a whole. “Monte Carlo techniques are often the only practical way to evaluate difficult integrals or to sample random variables governed by complicated probability density functions”¹³⁶. The generalized form of Monte Carlo Methods involves generating a set of random numbers which conform to a particular probability distribution (depending on the problem) and observing the fraction of those numbers which fulfil a particular set of properties (when transformed by some algorithm). The larger the number of random numbers generated, the more useful the output.

As a simple example, the value of π can be estimated using a Monte Carlo method. With the prior knowledge that $\frac{\pi}{4}$ is equal to the area of a circle with diameter d , divided by the area of a square with sides d (see appendix), the value of π can be estimated simply by generating uniformly distributed random points on the square and the counting the number that also lie inside the circle. The value of π is $4 \times \frac{\text{number of points in circle}}{\text{total number of points}}$. The estimate for the value of π improves with the number of points (and in this case converges slowly on the true value).

4.2.2.1 Markov Chain Monte Carlo

Markov Chain Monte Carlo algorithms use Monte Carlo Methods to create a Markov chain whose stationary distribution is the desired (posterior) distribution. Markov Chains are sequences of states where state x_{t+1} depends only on state x_t . Given suitably large numbers of iterations, the chain will forget the ini-

tial state (x_0) and the resulting chain will represent the posterior (stationary) distribution. This distribution won't depend on either t or x_0 ¹³⁷. The states in the chain prior to arriving at the stationary distribution are known as "burn in" and are discarded, and the stationary distribution is the usable output which can then be converted into a more convenient format to use as a posterior probability distribution.

4.2.3 Simulated Annealing

This technique was described independently by Kirkpatrick et al.¹³⁸ and Černý¹³⁹. The name comes from the metallurgical annealing process whereby large crystals are formed while a material is slowly cooled. The slow cooling increases the probability of individual crystals obtaining lower energy states than the initial. As the material cools the "distance" each crystal can move along the energy landscape decreases. In a simulated annealing algorithm, "distance" is controlled by a perturbation kernel which takes the "temperature" as input to change how much each parameter can be perturbed. Simulated annealing "consists of a discrete-time inhomogeneous Markov chain"¹⁴⁰ whereby the previous state is modified with a perturbation kernel (the neighbouring states) and then accepted or rejected using a transition probability which depends on the current temperature and the energies of the previous and current states. The advantage of this scheme is that areas of local minima have a lesser effect on the outcome of the Markov chain as the high initial temperature allows for the chain to "jump" out of these minima.

Simulated annealing is an extension of a simple rejection sampler¹⁴¹. Figure 4.1 contains some simple pseudo-code which shows how the rejection sampler algorithm works. This will provide a "best" parameter set, but there is no information about the possible spread of values in the parameter set. A spread, or distribution of values that can describe the system is required because, although there may be a particular parameter vector value that can accurately describe the system, it is very unlikely that there will be enough data to determine it. To

```
c1 = c0;
c2 = mutate(c1);
i = 0;
while i < i_max
    if fitness(c1) > fitness(c2)
        c2 = mutate(c1)
    else
        c1 = mutate(c2)
    i = i + 1
if fitness(c1) > fitness(c2)
    return c1
else
    return c2
```

Figure 4.1: **Pseudo-code showing how a rejection sampler works.** Simulated annealing extends this algorithm by having an annealing temperature which defines how much the parameter sets are mutated.

At this end a modified version of simulated annealing was used integrated with aspects of a simple genetic algorithm. In the genetic algorithm paradigm a synthetic “chromosome” is created which contains “genes” representing the parameters in the simulation. These include the rate constants, concentrations of various components and initial concentrations of substrates and products. This chromosome is then copied and perturbed several times (depending on the eventual population size required), with the size of the perturbation being dependent on the current annealing temperature. For instance the highest temperature could indicate that the individual parameters can be perturbed by up to $\pm 10\%$, and as the temperature decreases the perturbation percentage has a concomitant decrease. An example annealing temperature schedule is shown in Figure 4.2. The annealing temperature is programmed to decrease after a defined number of iterations such that the magnitude of individual mutations becomes smaller as the simulation progresses. This should have the effect of honing in on a set of parameters with a better fitness value. Once the chromosome population has been created, 2 are selected at random and their fitness values evaluated, in this case by the Least Squares Difference method. The chromosome with the lowest fitness value is discarded and the other is cloned and perturbed. The two chromosomes are then added back to the chromosome population. The genetic algorithm is used to

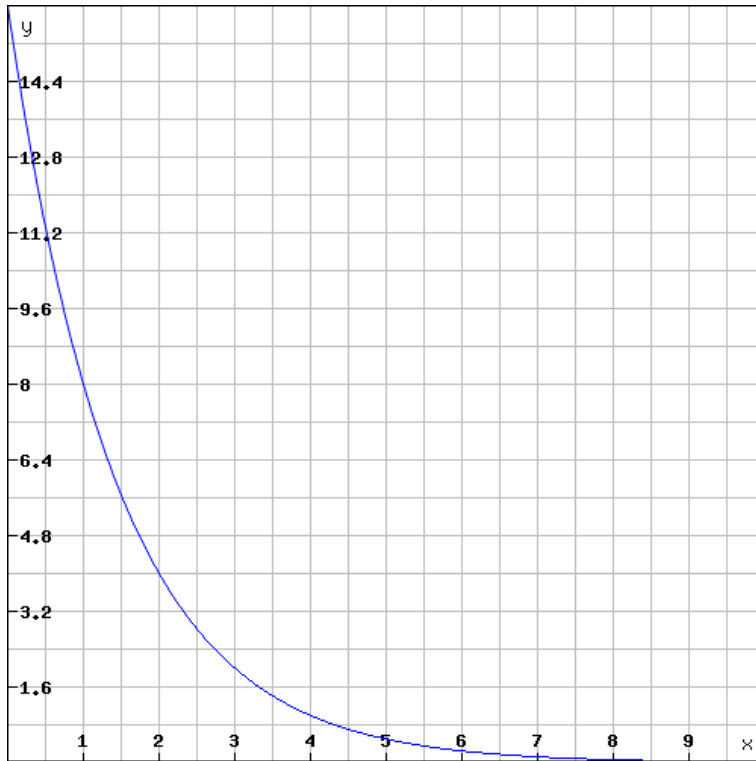


Figure 4.2: **Example simulated annealing temperature schedule.** This represents how the annealing temperature changes as the annealing process progresses. Temperature is denoted by the y-axis value, and simulation progress by the x-axis value. This is a heavily compressed time-frame, as in reality the system would normally process 10,000 sets of parameters at each annealing temperature.

improve the parameters sets by perturbing genes (individual parameters) from fit chromosomes (complete parameter sets), re-running the simulation and discarding unfit parameter sets. An unfit parameter set is defined as one with a fitness value lower than the highest so far. This technique involves having two chromosomes selected at any one time. The parameters from each chromosome are simulated and the least fit one is discarded. At this point the contents from the fitter chromosome are cloned and perturbed, and the cycle is repeated. Figure 4.3 shows this diagrammatically. After many cycles (upwards of 1000) the chromosome pool should only contain the best fitting parameter sets to the experimental data. The spread of the parameters can be used to infer the sensitivity of the simulation to changes in parameter values in a similar way to that described by Toni et al.¹⁴².

This algorithm was rejected as unsuitable as it seemed to be incapable of set-

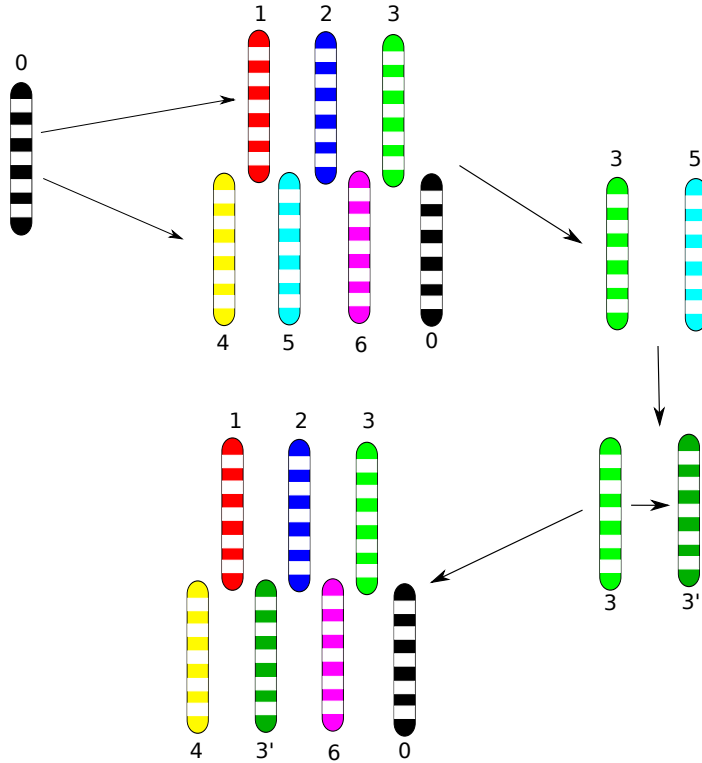


Figure 4.3: **Schematic diagram showing the technique used to generate a spread of parameters using a synthetic chromosome.** The parameters are loaded as genes on the chromosome which are then perturbed, 2 chosen and the fittest kept and perturbed. Each time a chromosome is perturbed it is reintroduced into the chromosome pool, and the next 2 chromosomes are chosen at random.

tling on solutions to the Nitric Oxide reduction datasets during testing. Additionally this technique does not produce probability distributions which were eventually required to incorporate data from previous datasets.

4.2.4 Approximate Bayesian Computation by Sequential Monte Carlo

“Approximate Bayesian Computation methods have been conceived with the aim of inferring posterior distributions where likelihood functions are computationally intractable or too costly to evaluate. They exploit the computational efficiency of modern simulation techniques by replacing calculation of the likelihood with a comparison between the observed data and simulated data”¹⁴².

To incrementally improve the parameter sets, a version of Bayesian inference is used in conjunction with a standard Monte Carlo method in a system called Approximate Bayesian Computation by Sequential Monte Carlo (ABC-SMC) as

described by Toni et al.¹⁴². An implementation of algorithm (S) was used from that paper.

Bayesian Inference - This is a statistical method for inferring the probability of a hypothesis based on available evidence. As more evidence is accumulated, the inference is updated and the probability of the hypothesis being true is changed. Given enough evidence, the probability of the hypothesis being true should either be very high or very low causing you to either accept or reject the hypothesis. Bayesian inference relies on having a prior probability (or probability distribution) for the hypothesis, and this can inevitably introduce a level of bias into the inference. Bayesian inference can be described thus:

$$P(H | E) = \frac{P(E | H)}{P(E)} \cdot P(H) \quad (4.4)$$

- $P(H | E)$ is the posterior distribution of H given E .
- $P(H)$ is the prior distribution
- $\frac{P(E | H)}{P(E)}$ is the impact of E on the degree of belief in H .

A simplistic example of using Bayesian inference to alter a hypothesis could happen in the case of having two jars of sweets. Jar 1 has 15 strawberry sweets and 25 raspberry sweets. Jar 2 has 20 of each. Supposing a third party selects 1 sweet at random from 1 of the jars. They select a strawberry sweet, what is the probability that it came from Jar 1? From the point of view of our third party both jars are identical, therefore $P(H_1) = P(H_2)$ and the total probability must equal 1, so the prior probability of each jar is 0.5. The observation, E is of a strawberry sweet, which we can then use to calculate the likelihood of it being from each jar individually by $P(E | H_1) = 15/40 = 0.375$ and $P(E | H_2) = 20/40 = 0.5$. The Generalised Bayes formula can then be used to work out the probability of the strawberry sweet being from jar 1, that is $P(H_1 | E)$.

$$\begin{aligned}
 P(H_1 | E) &= \frac{P(E | H_1)P(H_1)}{P(E | H_1)P(H_1) + P(E | H_2)P(H_2)} \\
 &= \frac{0.375 \times 0.5}{0.375 \times 0.5 + 0.5 \times 0.5} \\
 &= 0.429
 \end{aligned} \tag{4.5}$$

Before the observation of the sweet, the probability of the third party taking from jar 1 was the prior probability of 0.5. After the observation this probability must be revised to 0.429.

Bayesian inference is widely used in computational analysis for artificial intelligence and email spam identification. It is also used in the field of population genetics and phylogenetics¹⁴³.

Approximate Bayesian Computation - This is an extension of Bayesian inference which allows approximately the same inferences to be made, with considerably less computation. It also enables approximation of posterior values within the Bayesian scheme. It operates on summary statistics of the datasets rather than the datasets themselves. Common examples are population mean and variance. The summary statistic needs to be a sufficient statistic, that is, the sample from which the statistic is calculated provides no additional information than does the statistic. This is useful for large complex datasets where the probability of a simulation of the dataset matching the original is very small (unacceptably so), in this case a summary statistic of the datasets can be used, and the difference calculated. If the difference is less than a pre-defined acceptance threshold, then the simulated dataset is accepted. ABC originally came from the fields of population and evolutionary genetics¹⁴⁴, but is now being applied to complex and stochastic dynamical systems^{142,145,146}.

ABC differs from standard Bayesian inference shown in Equation 4.4 in that

the likelihood term does not need to be calculated. Instead the difference between the summary statistics of the observed data and the simulated data is used. The simulated data is considered an acceptable sample from the posterior distribution if the difference in summary statistics is less than a predefined acceptance threshold. The most basic ABC methods takes the following form:

θ is a parameter vector to be estimated, $\pi(\theta)$ is the prior probability distribution, and x is the observed data. The posterior distribution is $\pi(\theta | x) \propto f(x | \theta) \cdot \pi(\theta)$.

1. Create a candidate parameter vector θ^* from the prior distribution $\pi(\theta)$.
2. Simulate dataset x^* using the model and parameter vector θ^* .
3. Compare x^* with x using a distance function d and an acceptance criteria ϵ .
If $d(x, x^*) \leq \epsilon$, accept θ .

Given a low enough value for ϵ , the output distribution should approximate the true posterior distribution if sampled a large enough number of times.

Sequential Monte Carlo - This is a method of particle filtering whereby a large set of samples (N) are drawn from the prior distribution, and for each sample, the probability is calculated. Weights for each particle are assigned based on the probabilities, and these affect how likely a particle is to be selected in subsequent rounds of selection. At the end of each round, the posterior distribution of the N particles becomes the prior distribution for the next round.

Approximate Bayesian Computation by Sequential Monte Carlo - This combines the previous two methods by drawing a large number of particles from the prior distribution using Bayesian inference. The prior distribution is a discrete approximation to a continuous distribution in the scheme used here (algorithm S1 from Toni et al.¹⁴²), so a perturbation kernel based on a Laplacian or Gaussian distribution is used on each sample to provide small deviations to better approximate a continuous prior distribution. Each sample is simulated and only accepted if it exceeds the acceptance threshold. This is calculated based on the least-squares difference (LSD) between the simulated data and the original

dataset. If a sample is rejected, a new one is drawn from the prior distribution and SMC then continues as described above. The weights of the accepted samples are calculated based on the probabilities of being selected from the prior and the samples go on to form the posterior distribution. For each subsequent round, the mean LSD of the posterior distribution from the previous round is used as the acceptance threshold. This ensures that each round results in better fitting parameter sets. The cycle is then repeated until a pre-defined cycle limit is reached¹⁴². The above description shows only one particular method of performing ABC-SMC, but it should be made clear that this is not the only method.

A significant advantage of this technique is that it is readily parallelisable, as each particle in the SMC process is independent, thus can be simulated in parallel. This advantage is not unique, as many other sampling approaches are parallelisable also. A parallel version of this algorithm was implemented in the JAVA programming language which resulted in significant speed-ups when multiple processing threads can be used. The threading manager means that the algorithm is theoretically most efficient (in terms of computational time) when the number of particles is an exact multiple of the number of processing threads. In practice however this is negated by the fact that some particles require multiple samples due to them not meeting the acceptance criteria.

This algorithm was rejected on the grounds that it seemed incapable of settling on sensible posterior distributions with some datasets. It is suspected that the distance function used was causing a conflict which meant the algorithm was accepting bad parameter sets and rejecting good ones. The requirement of a suitable distance function or summary statistic is a major disadvantage of this algorithm.

4.2.5 Metropolis Hastings Monte Carlo

The Metropolis-Hastings algorithm is a Markov Chain Monte Carlo method to retrieve sequences of random samples from a probability distribution which can-

not be sampled directly (or would be very difficult) such as when the probability distribution function carries no prior information. Such a case exists when the proposal distribution is a discrete rather than a continuous distribution. The algorithm was originally developed by Metropolis et al.¹⁴⁷ for generating samples from the Boltzmann distribution. It was later extended to a more general form for any distribution by Hastings¹⁴⁸.

This algorithm is much simpler than the previously described ABCSMC and takes the following form¹³⁷:

```

Initialise  $X_0$ ; set  $t = 0$ ;
Repeat {
    Sample a point  $Y$  from  $q(\cdot | X_t)$ 
    Sample a Uniform(0,1) random variable  $U$ 
    If  $U \leq \alpha(X_t, Y)$  set  $X_{t+1} = Y$ 
        otherwise set  $X_{t+1} = X_t$ 
    Increment  $t$ 
}

```

For the parameter estimation problem being solved, in the algorithm above, X_0 is the initial set of parameters, t is the iteration number, $q(\cdot | X_t)$ is the *proposal distribution* which is the prior probability distribution and $\alpha(X_t, Y)$ is the acceptance probability. The prior probability distribution is used as the proposoal distribution as in this case samples need to be taked from a constrained space due to the high dimensionality of the space available (there are a large number of possibly correlated parameters). Typically a uniform proposal distribution is used, but this could result in biologically incorrect values being selected. The acceptance probability is calculated from the likelihood of Y being from the prior probability distribution and the likelihood of the simulated data being from a normal distribution surrounding the experimental data. Mathematically it is described thus:

$$\alpha(X_t, Y) = \frac{q(Y_t | X)}{q(Y_{t-1} | X)} \cdot e^{F(Y_{t-1}) - F(Y_t)}$$

This process can be described as below:

1. Create a set of starting parameter values, calculate the probability of them

from the prior distribution, and their likelihood of fitting the experimental data.

2. Sample new parameter values from the prior probability distribution, calculate probabilities and likelihoods.
3. Calculate acceptance based on the above values.
4. If acceptance is greater than a random number generated in the range 0-1 then save the new parameters. (Acceptance will be greater than 1 if the parameters are more likely *and* the results fit better). This allows slightly less probable, and less likely results to be accepted
5. Otherwise save the old parameters.
6. Go Back to step 2
7. After enough repeats the saved results will resemble the posterior probability distribution.

This was the algorithm selected to perform the parameter estimation as it was simple to implement, generated the required probability distributions and didn't require complex functions to determine acceptance. Its only major disadvantage was that it was an unparallel algorithm, thus it was quite slow as each iteration depended on the results of the previous.

4.3 Validating the Parameter Estimation Algorithm

The Metropolis Hastings Monte Carlo algorithm was validated by using a much simpler ODE system than is required by the respiratory model, to make sure it was capable of parameter estimation and producing the necessary output for creating probability distributions. The simpler ODE system selected was the Lotka-Volterra model as this can be tested much more quickly by virtue of having far fewer parameters to estimate (4 as opposed to >20) and has only 2 differential

equations to solve. The Lotka-Volterra model describes a simple predator-prey relationship^{149,150} and only requires two first-order, non-linear differential equations, which are shown in equation 4.6.

$$\begin{aligned}\frac{dx}{dt} &= x(\alpha - \beta y) \\ \frac{dy}{dt} &= -y(\gamma - \delta x)\end{aligned}\tag{4.6}$$

The algorithm was validated by generating a dataset using the Lotka-Volterra equations with a known set of parameters. The dataset was generated using the same ODE solving equations described in Chapter 3 for 1000 generations. The Metropolis Hastings algorithm was given uniform distributions to sample from for each of the priors (this means that there is more-or-less no sampling distribution), and the acceptance criteria for each iteration were based upon the log-likelihood (described previously) values between the input dataset and the solved output from the new parameters. The algorithm was allowed to continue for 10000 iterations, generating 4 Markov-Chains of length 10000. During this time the algorithm will be altering the 4 input parameters trying to improve them based on the log-likelihood values produced. The resulting Markov Chains were likely to represent the stationary or posterior distributions of the 4 parameters and were very close to the true values from the input data.

Given the simplicity of this system, a particularly bad set of initial parameter estimates (i.e. x_0 as described previously) were given to exaggerate the burn in period, and to show that given a long enough time the algorithm will eventually settle on “correct” values. This validation step also informs the likely values for two tuning variables in the algorithm; the *acceptance* - how stringent the algorithm is on accepting new parameter sets, which is the σ value of the log-likelihood calculation, and the *internal sigma* value - this describes the magnitude of parameter perturbation at each iteration. The graphical results of the Lotka-Volterra validation are shown in Figures 4.4 and 4.5. Figure 4.4 shows the generated validation

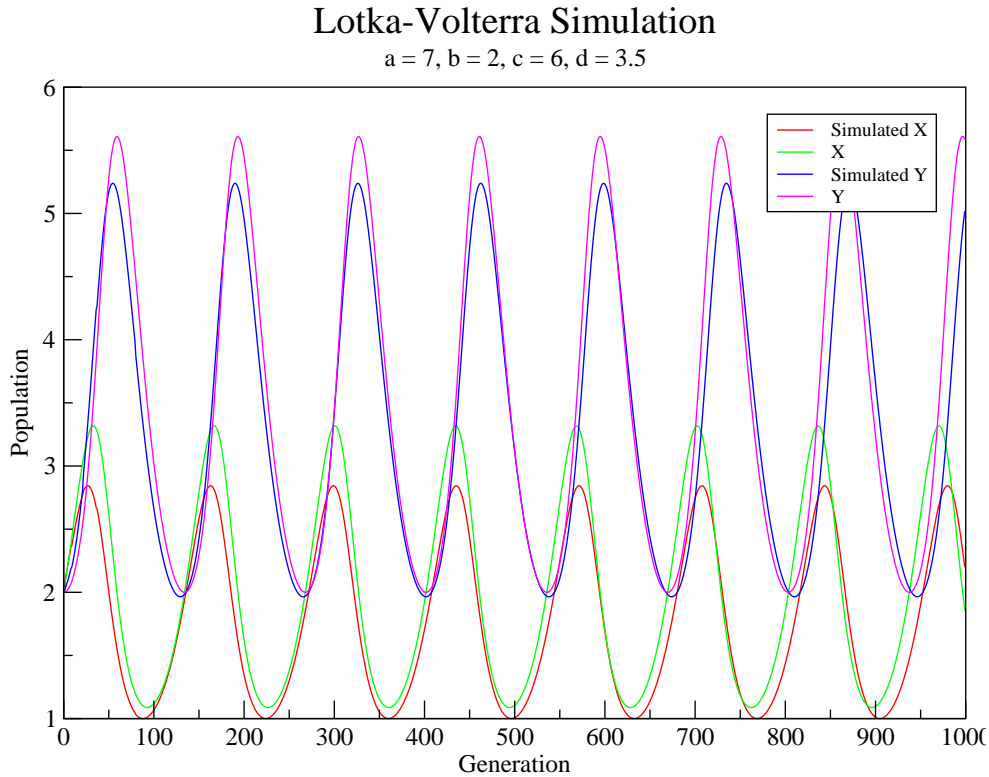


Figure 4.4: Simulation results of the Lotka-Volterra validation run.

data compared to the solved output from the parameters at the end of the Markov Chains. Figure 4.5 shows a plot of the 4 Markov Chains generated by the MHMC algorithm. The initial 3000 generations are the burn-in and represent the region of the Markov Chain where the algorithm is trying to converge on the stationary distribution. The region beyond 3000 generations is likely to be the stationary distribution and this can be used to calculate a posterior probability distribution.

The results of this validation show that the algorithm is capable of parameter estimation and can produce output that is compatible with generating probability distributions. The comparison of the Lotka-Volterra data shows that the algorithm could have been run for more iterations as the solved output doesn't quite match the generated input data. The Markov Chains show that the algorithm has stabilised on values very close to the “true” values of the input data.

Lotka-Volterra parameter search by Metropolis-Hastings

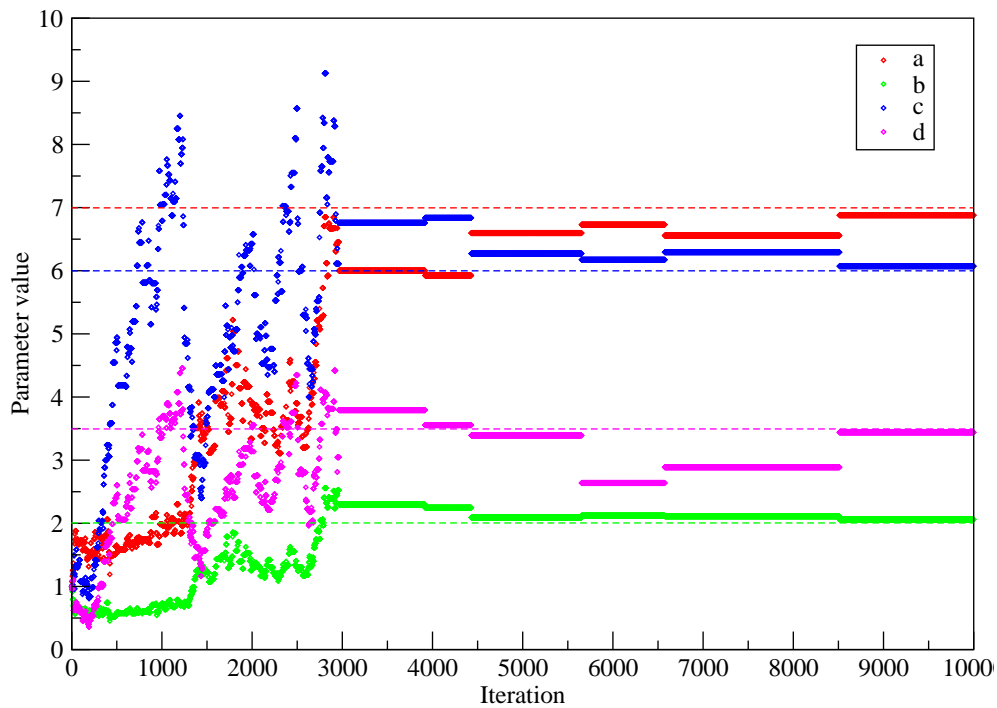


Figure 4.5: MHMC results of the Lotka-Volterra validation run. Note the initial burn-in period followed by the distribution trajectory. True parameter values are indicated by dashed lines in matching colours.

4.4 An Integrated Parameter Estimation Scheme Combining MHMC With Bayesian Inference

In order to correctly parameterise the complex model being investigated it would have been impossible to use a MHMC-based parameter estimation algorithm alone, since it would be difficult to generate dataset which could provide enough information to estimate all the parameters at once. This being the case the parameter estimation algorithm was combined with a Bayesian approach to generating the proposal/prior distributions. Each run of MHMC will generate a Markov-Chain which can be used to calculate a posterior probability distribution for each parameter. These posterior probability distributions could be used to inform a subsequent round of parameter estimation in a Bayesian manner by using these distributions as the proposal/prior distributions for that subsequent round. This approach relies on the overall problem being able to be broken down into smaller

problems which add increasing amounts of information. Thus the initial round of parameter estimation may only be estimating a small percentage of the total number of parameters, *but* the posterior probability distributions generated can be used as informed prior probability distributions for a second round of parameter estimation which includes more parameters. The entire scheme is represented visually in Figure 4.6.

4.5 Implementing the Integrated Scheme

As described previously, one dataset alone is not sufficient to provide enough information to be able to parameterise the model. In order to correctly perform Bayesian informed parameter estimation, the mathematical model needed to be separated into simpler units which could more easily be described by specific sets of experimental data. These simpler units would each provide information on a subset of the total number of parameters in the model.

The model was separated such that the simplest parts could be parameterised first. In this case, the simplest section of the model was those equations which describe oxygen respiration. This only requires one enzyme (although it does still require the electron transport chain). This section of the model also has the simplest experimental dataset.

These simplified datasets are parameterised, with each dataset analysed at least 10 times, generating at least 10 Markov Chains per parameter. These repeats are performed to provide statistical significance by reducing bias that could be introduced by using only 1 Markov Chain.

After this section of the model has been parameterised, posterior probability distributions are calculated, new sections are added and the process (shown in Figure 4.6) repeated, until all of the parameters have been estimated.

At this point the output probability distributions should be representative of the true parameter values for all the components in the model, subject to certain caveats such as the fact that parts of the model are simplified. These probabil-

Integrated Bayesian Parameter Estimation Scheme

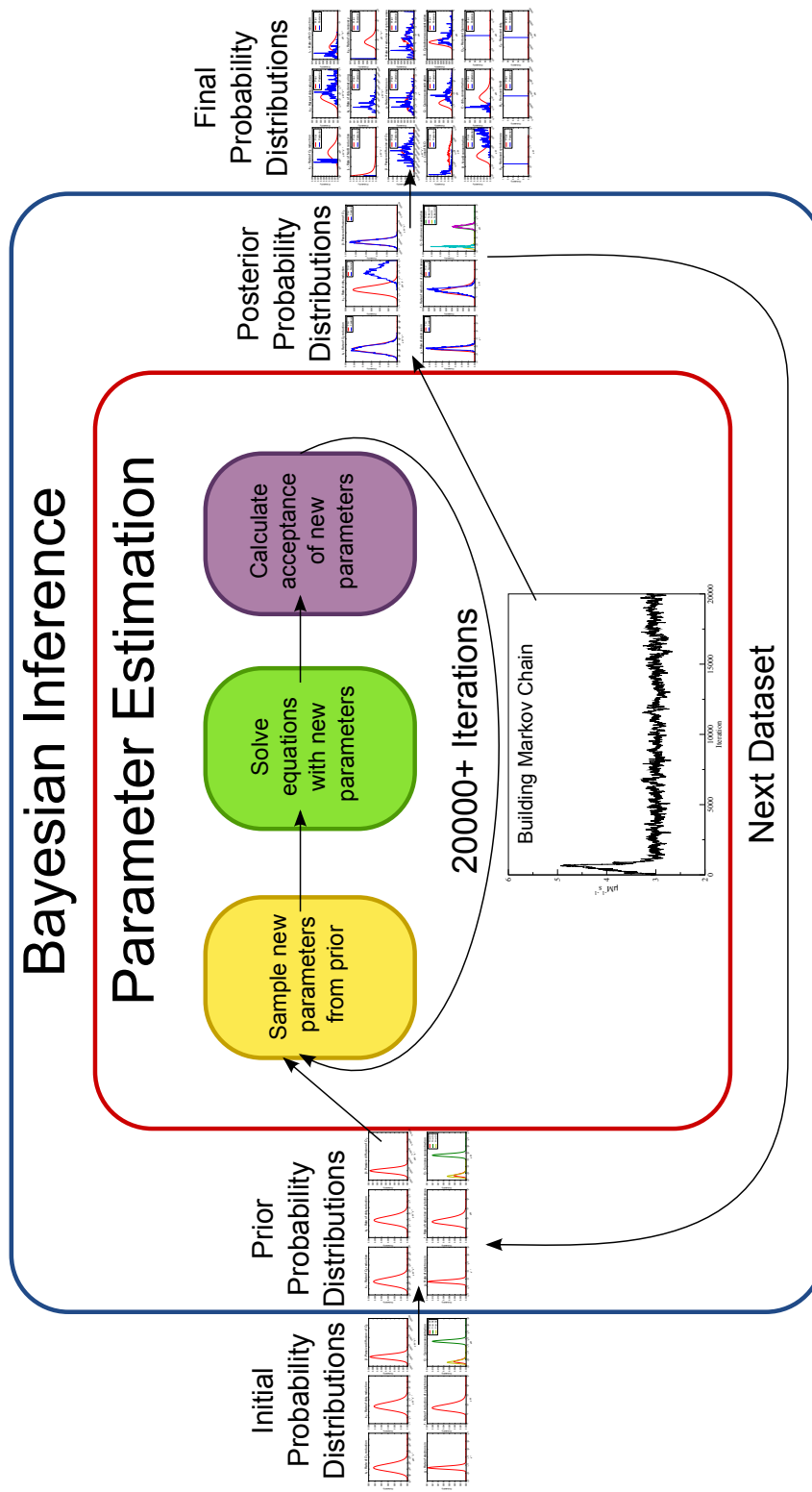


Figure 4.6: The Integrated Bayesian Parameter Estimation Scheme. This figure shows a flow-chart representing the major steps in the scheme. The initial probability distributions may be uniform, depending on how much knowledge is available *a priori*. The experimental data is compared to the simulated data in the purple box. After sufficient iterations of parameter estimation, the Markov Chains are used to produce posterior probability distributions.

ity distributions should be accurate enough that they can be used to predict the behaviour of the biological system *in vivo*.

Chapter 5

Oxygen Reduction in *N. meningitidis*

5.1 Reduction of Oxygen

5.1.1 Introduction

The first dataset used in the iterative approach to parameter estimation was of a simple oxygen reduction experiment carried out in aerobic conditions. This dataset is the simplest biologically as under aerobic conditions and without the presence of any microaerobic substrates (nitrite or nitric oxide) the only respiratory pathway that is active is the oxygen reducing one. Additionally, the other parts of a respiratory chain influence the oxygen reducing pathway either by competing for electrons, or chemically inhibiting it. The relevant portions of the ETC are shown graphically in Figure 5.1.

The equations that describe this portion of the ETC are:

$$\begin{aligned}\frac{d[O_2]}{dt} &= \beta(1 - [O_2]/K_O) - k_1[C_a][O_2] \\ \frac{d[Q_a]}{dt} &= g([Q] - [Q_a]) - l_3[Q_a]([B] - [B_a]) - f[Q_a]([X] - [X_a]) \\ \frac{d[X_a]}{dt} &= -k_3([C] - [C_a] - [C_X])[X_a] - m_3([A] - [A_a])[X_a] + f[Q_a]([X] - [X_a]) \\ \frac{d[C_a]}{dt} &= k_3([C] - [C_a] - [C_X])[X_a] - k_1[C_a][O_2] - k_5[C_a][NO] + k_6[C_X]\end{aligned}$$

These equations describe the change in concentration of oxygen over time, which

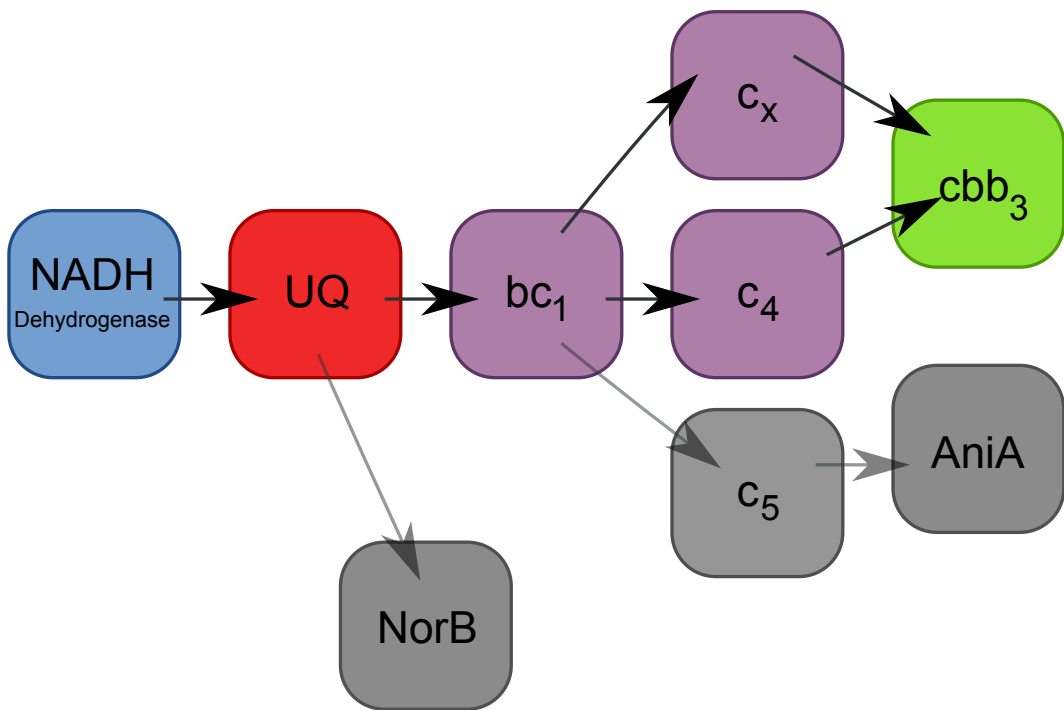


Figure 5.1: **Oxygen reducing electron transport chain of *N. meningitidis*.** This shows the complete electron transport chain of *Neisseria meningitidis* with the components irrelevant to oxygen reduction greyed out. In the mathematical model all of the purple elements (cytochromes) are amalgamated into one entity.

is the experimentally observable value, the reduction state of the quinone pool and the reduction state of the cytochrome “pool”. This portion of the model involved 8 parameters which were to be estimated. This large number of parameters will clearly result in over-fitting, but in the Bayesian scheme this was necessary to generate loose bounds for all of the parameters.

5.1.2 Experimental Results

Generation of oxygen reduction datasets required the growth of MC58 (wild-type *Neisseria meningitidis*) in aerobic conditions until mid log-phase growth had been achieved. This corresponds to an OD₆₀₀ of 0.3-0.9 and usually required an incubation period of roughly 3 hours. Once the required cell density had been obtained, the culture was transferred to the oxygen electrode chamber and the oxygen concentration recorded as the culture respired. At this point the cells are only using whatever amount of oxygen is presently dissolved in the culture medium in addition to that diffusing in through the cap (negligible). Once the

Aerobic Oxygen Reduction in *Neisseria meningitidis*

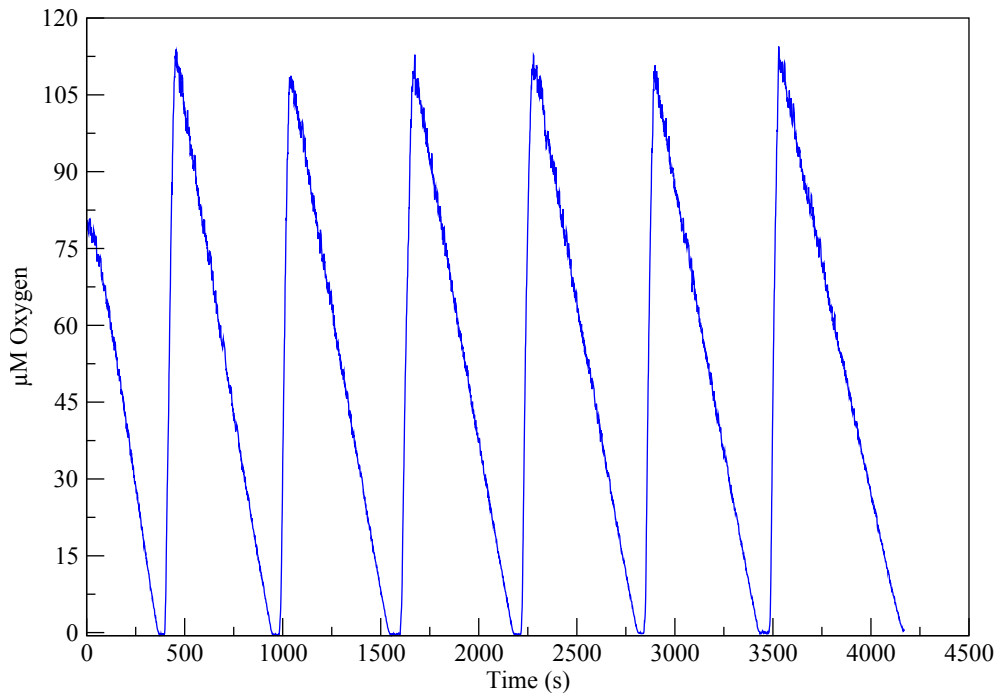


Figure 5.2: Highly repeatable oxygen reduction. This shows an oxygen reducing culture being repeatedly aerated after oxygen depletion with very similar rates of subsequent oxygen reduction

culture had used up all its dissolved oxygen, the electrode chamber cap was removed and the culture medium aerated using a Pasteur pipette. This restores oxygen levels throughout the culture and allows the bacteria to continue respiring in aerobic conditions. A typical oxygen reduction plot is shown in Figure 5.2. This is split into individual reduction sections, which can then be used as input data for parameter estimation. In many cases if the culture is allowed to become completely anaerobic for a prolonged period of time, the bacteria will die, evidenced by a subsequent lack of oxygen reduction, however this is not always the case as shown in Figure 5.3.

The experiments used to generate data for oxygen reduction are highly repeatable and consistently generate the same basic result of a linear reduction of oxygen with time.

The oxygen reduction datasets generated and used for parametrising this portion of the mathematical model are shown in Figure 5.4.

Oxygen Reduction with Delayed Aeration

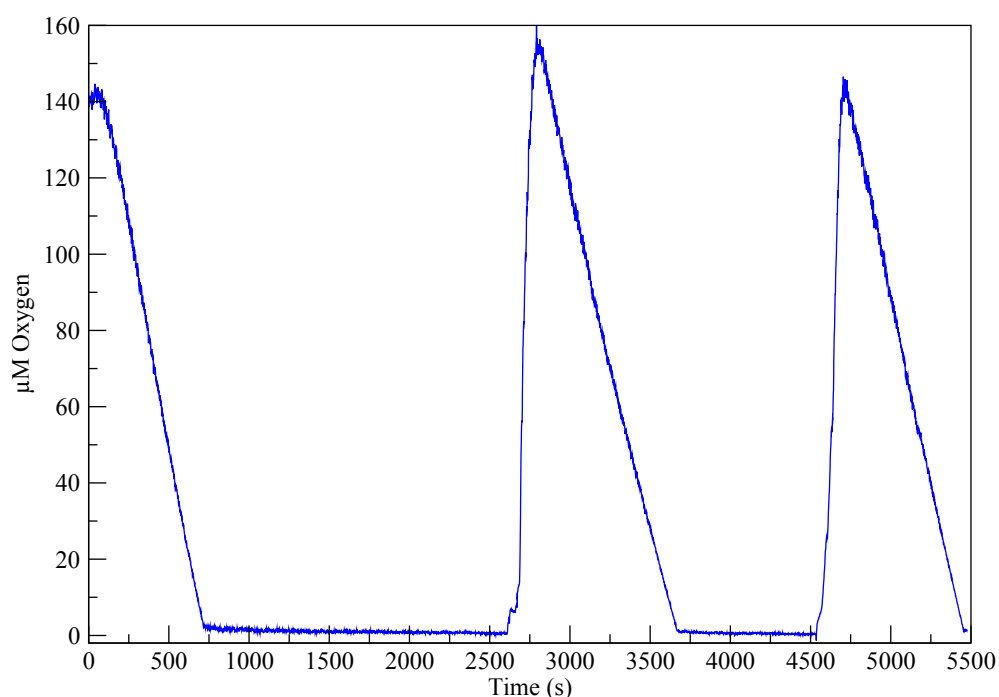


Figure 5.3: **Aerating oxygen reducing cultures with significant delay.** The oxygen reducing ability of *N. meningitidis* can be robust as evidenced by the 1000s delays between aeration with no change in subsequent respiration rate. Also of note is that nitric oxide concentration is not changing, suggesting that reduction of nitrite is not occurring either.

Oxygen Reduction in *Neisseria meningitidis*

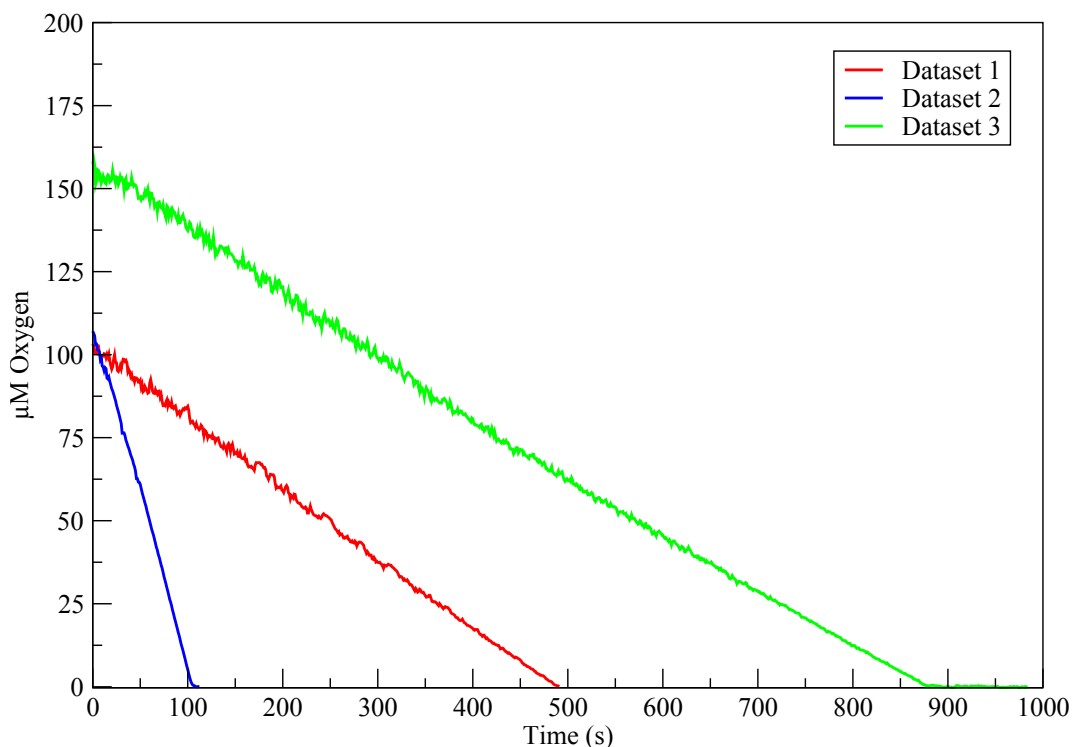


Figure 5.4: **Oxygen Reduction in *Neisseria meningitidis*.** These three experimental datasets were used as input data for the parameter estimation algorithm. They all show the same linear oxygen reduction. The different rates are due to differing starting cell densities. The specific rates are very similar at $1.5 \mu\text{Ms}^{-1}$ per OD unit.

5.1.2.1 Generation of Prior Probability Distributions

In accordance with the integrative scheme that was introduced in Chapter 4, an attempt was made to estimate the distributions of the parameters involved in modelling these data. In order to do this probability distributions were needed to act as priors to feed into the estimation system as this is required for a Bayesian approach. These probability distributions were generated from data obtained in the published literature, which is described in Chapter 3, and preliminary experimental data. It was assumed that all the prior probabilities would be log-normally distributed, therefore the distributions used were created under the following scheme:

- Where the literature value had bounds associated with it (i.e. published with \pm values), the bounds were assumed to cover 3σ of the normal distribution. Thus the variance used for the lognormal distribution is $\left(\frac{\text{bounds}}{3}\right)^2$ with narrow upper and lower limits.
- Where the literature value has no bounds associated with it (i.e. published as a single figure), the bounds were assumed to be $\pm 10\%$ of the literature value, and this was used as σ . Wider upper and lower limits were used in these cases.
- Where there are no literature values available, the value was estimated based on preliminary experimental data and bounds of $\pm 10\%$ were used again. In this case upper and lower limits for the distribution were made very wide to try and accommodate for incorrect assumed prior values.

The distributions were created as histograms with 1000 bins, thus the limits described above actually represent the cut-off values at the lower and upper ends of the histogram. The sampling algorithm that uses these histograms rejects any sample that is outside the range of the histogram (even if in reality it will have an exceptionally small but non-zero probability). This means that the prior probability distributions do in fact have hard limits imposed.

With reference to the above, the values required to create prior probability distributions from Table 3.1 in Chapter 3 are shown in Table 5.1.

Parameter	\bar{x}	σ
k_1	415 $\mu\text{M}^{-1}\text{s}^{-1}$	13.83
k_3	3 $\mu\text{M}^{-1}\text{s}^{-1}$	0.1
β	1.4×10^{-4} $\mu\text{M}^{-1}\text{s}^{-1}$	4.67×10^{-6}
g	0.847 s^{-1}	0.028
f	8.749 $\mu\text{M}^{-1}\text{s}^{-1}$	0.292
Q	0.3 μM	0.01
X	3.97 μM	0.134
C	0.03 μM	0.001
Q_a	0.24 μM	0.008
X_a	3.176 μM	0.105
C_a	0.024 μM	0.0008

Table 5.1: **Prior Probability Table** This table shows the prior means and variances used to create lognormal distributions to be used as the prior probability distributions.

A graphical representation of the data in Table 5.1, the initial probability distributions used to start the Monte-Carlo run are shown in Figure 5.5. Due to the method used to read and generate the probability distributions in software, this and all subsequent figures showing probability distributions are actually histograms with 1000 bins of equal width. The distributions therefore have defined upper and lower limits.

5.1.2.2 Initial Parameter Estimation Results

The parameter estimation process produces a large amount of output data which can be processed. Included in these data are the best simulation results from each run. Best is defined here as the simulation with the best goodness-of-fit, i.e. the one with the closest match to the experimental data. For the oxygen reduction training datasets, of which there are 3, each was run 20 times for 20,000 iterations.

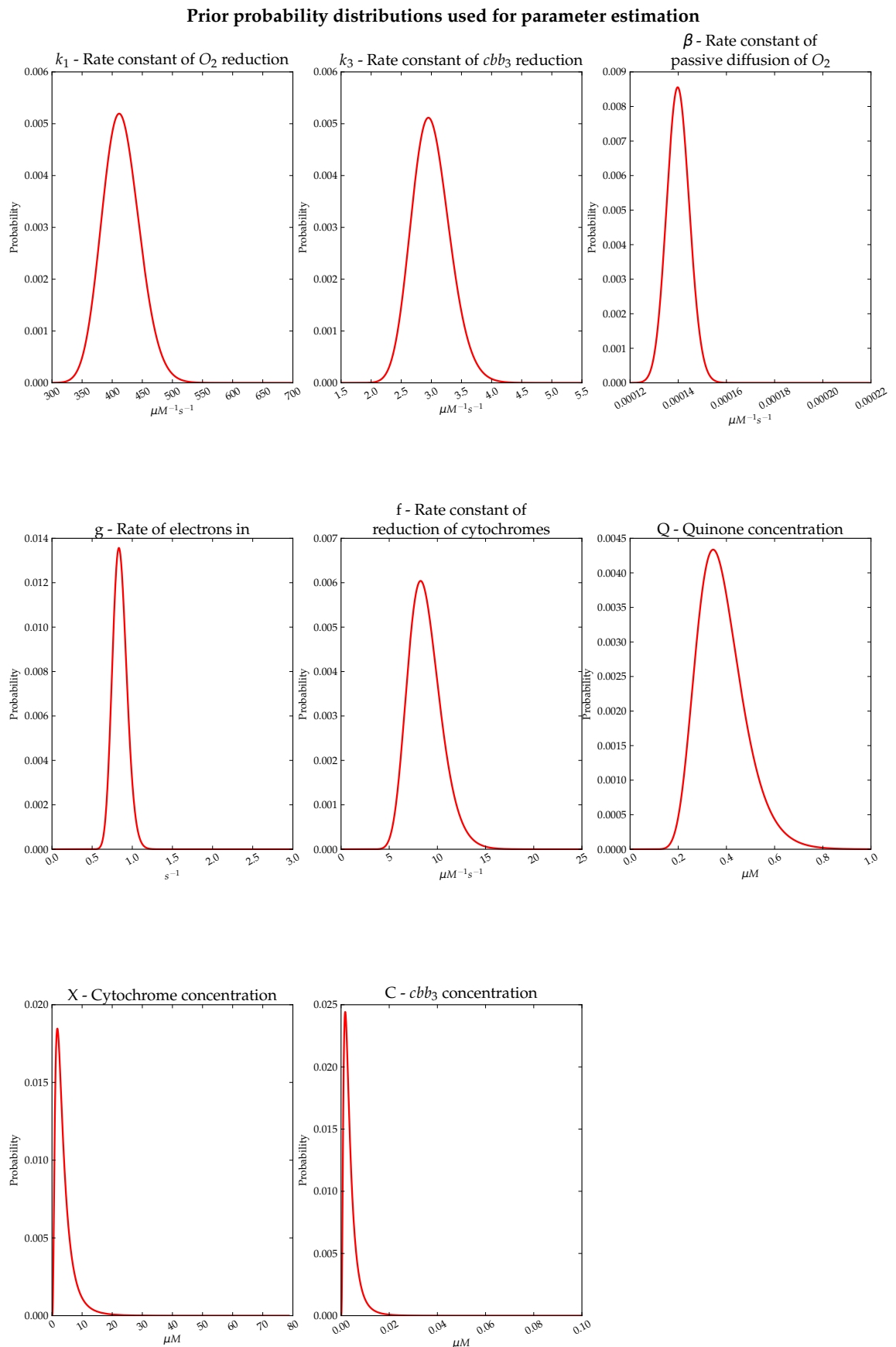


Figure 5.5: **Prior probability distributions for oxygen reduction.** These are the probability distributions used as priors by the parameter estimation algorithm.

This lower iteration count was chosen as a compromise between execution time and statistical accuracy. In fact given that the burn-in time for these runs was relatively short, 20,000 iterations still provides plenty of data. A representative example of the simulated data is shown in Figure 5.6. This figure was generated from the set of parameters that produced the most fit output compared to the input dataset.

Initially the simulation results are not particularly good fits compared to the experimental data and as such have a low goodness-of-fit. The calculation performed actually produces a value that represents the “goodness of fit” related to the distance of the simulated data away from the experimental data and accounting for Gaussian noise. As such the quality of the simulated data will be given in terms of its “goodness-of-fit” or F value. As the parameter estimation progresses the F value reduces as the simulated result gets closer and closer to the experimental data. Quite often this does not take many iterations and a representative plot showing how the simulation’s F value decreases is shown in Figure 5.7. The initial period where the F value is high up until the point it settles at a lower value is classed as “burn-in” and is discarded when generating posterior distributions.

Each of the parameters that are to be estimated produces a trajectory of values for each run of the estimation algorithm. These trajectories are used to generate the posterior probability distributions required for Bayesian inference in subsequent steps. During the “burn in” period the parameter values can be observed to change rapidly from one iteration to the next as they approach their optimum values. Once the “burn in” has completed the values settle and produce largely flat trajectories with minor deviations around the optimum value. This settled region is used as the source for generating the posterior probability distributions.

Figure 5.8 shows the trajectories from each simulation run on a single dataset for the k_3 parameter.

Not all parameters in this stage of the model will produce trajectories like the one shown, as if there is a great deal of freedom as to what value a particular pa-

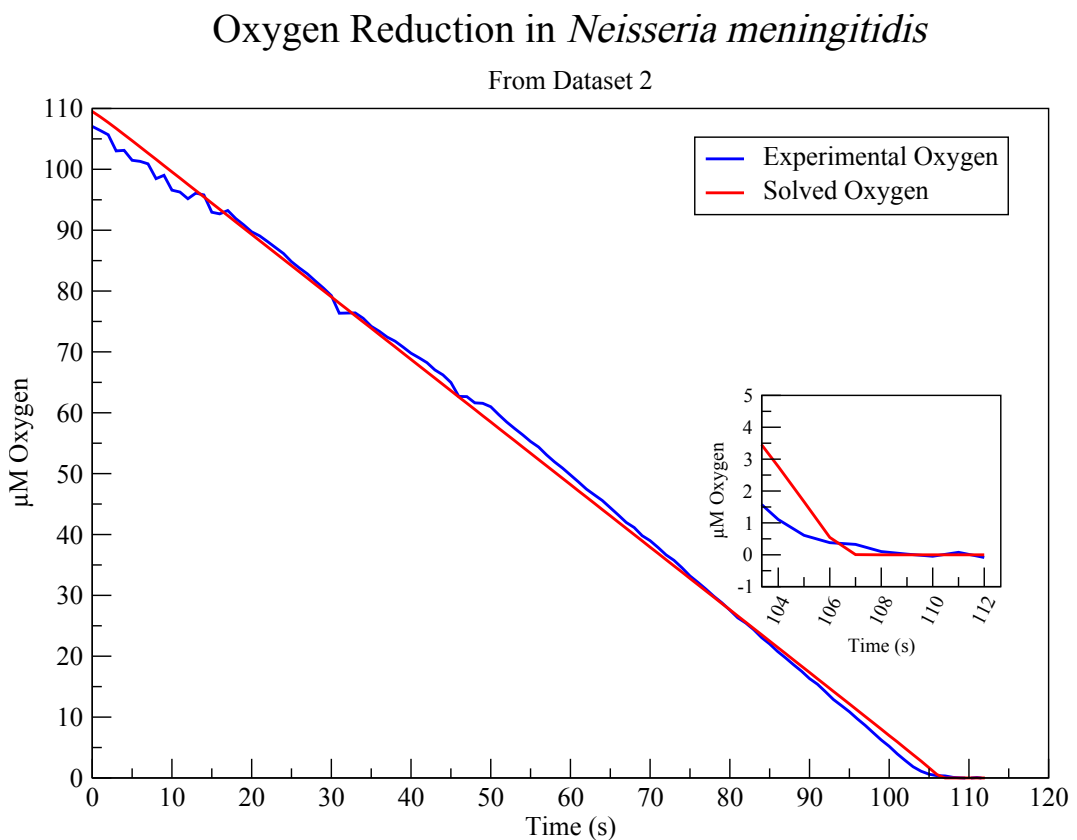


Figure 5.6: **Oxygen Reduction in *Neisseria meningitidis*.** This dataset shows the simple linear reduction of Oxygen in aerobic conditions. The high affinity of cbb_3 for oxygen is evidenced by very little non-linearity at low oxygen concentrations. The solved output is a representative result of the parameter estimation system. The inset shows that the solved output is achieving much higher affinity than the experimental data.

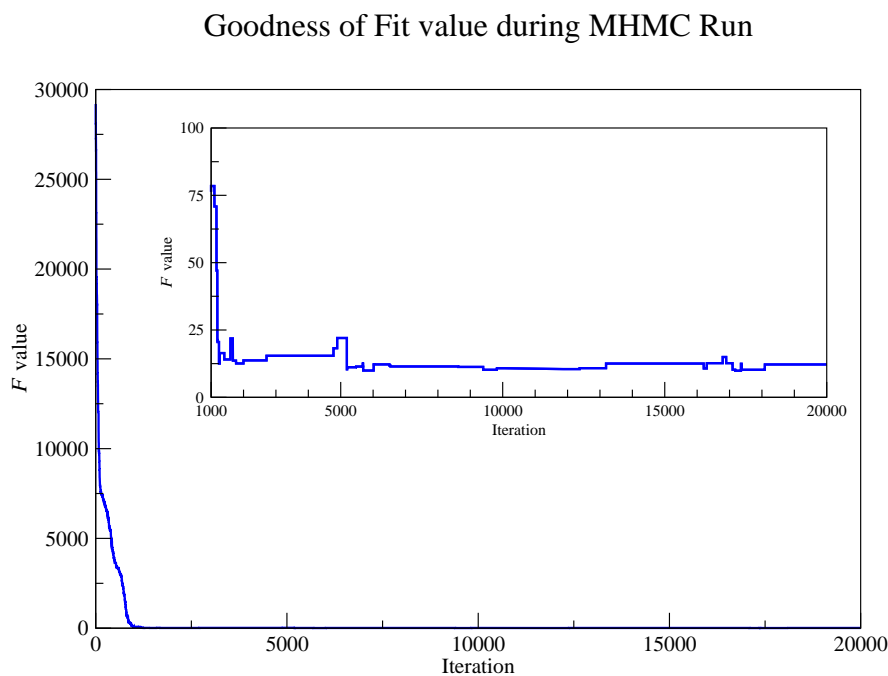


Figure 5.7: **Simulation F value improves as parameter estimation progresses.** This is a representative figure constructed from a single run on one dataset. Initially the F value is high showing that the simulated result does not match the experimental dataset. As the parameter estimation algorithm progresses, the F value decreases as the simulated result approaches the experimental dataset. The inset shows a zoomed in view of the F value after the “burn-in” process has finished.

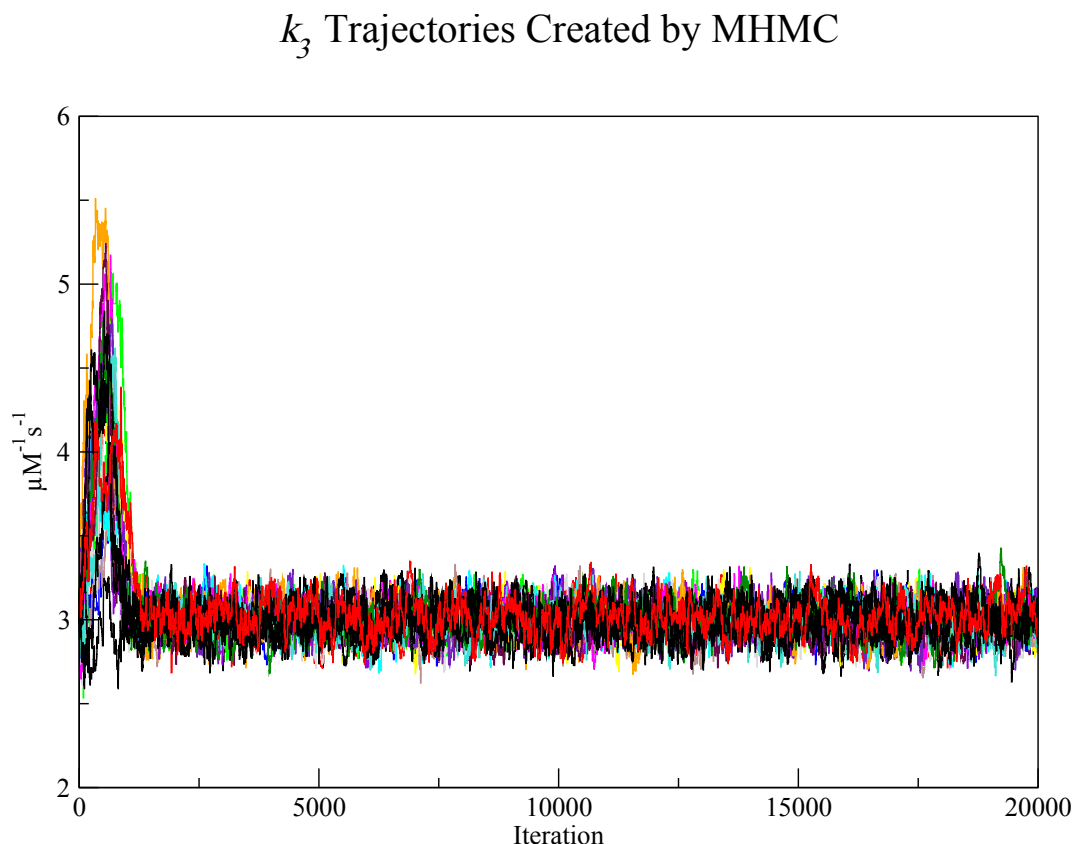


Figure 5.8: **Individual parameter trajectories for multiple runs on the same experimental dataset.** This figure shows the trajectories for the same parameter, in this case k_3 - the rate constant for cbb_3 reduction, from 20 individual runs of parameter estimation upon the same input data. The trajectories show clear convergence after the “burn-in” period.

rameter can take without drastically decreasing the F value it will be accepted by the parameter estimation algorithm. In this case the trajectories will not converge, and will ultimately produce a wide probability distribution. This is not necessarily indicative of a problem however, as this output still contains information that can be used in the next stage of parameter estimation with new datasets.

The trajectories above are processed to produce probability distributions given as histograms. The “burn in” is discarded and the settled data is then binned and counted. For the datasets used, the burn-in period was 1500 iterations (10,000 for dataset 3). These histogram probabilities are then assigned as the posterior distributions and in turn are used directly as prior probability distributions for new datasets. For simplicity’s sake when referring to the distribution of individual parameters for purposes of comparison, these histograms are transformed into log-normal distribution such that they can be represented by two numbers, \bar{x} - the mean, and σ^2 - the variance.

The posterior probability distributions generated from the three experimental datasets, each started with 20 runs are shown in Figure 5.9. In the case of parameters which represent concentrations, such as X and C , the concentrations of cytochromes and cbb_3 respectively, the individual dataset probability distributions are shown, as they cannot be sensibly combined, and it emphasises the fact that the datasets were different.

As can be seen from the posterior distributions, the parameter estimation algorithm has not satisfactorily produced posterior distributions that are contained within the bounds of the prior distributions whilst also still managing to fit to the experimental data. This is especially true of the concentration of Q , where the Markov-chain has tended towards the upper limit of the input prior distribution. This suggests that the prior distribution for Q is incorrect, with a mean that is possibly as much as $10\times$ too low, and with a variance that is too small, as the parameter estimation algorithm has attempted to increase the value of Q right up to the upper limit of the input distribution. This incorrect value for Q is probably

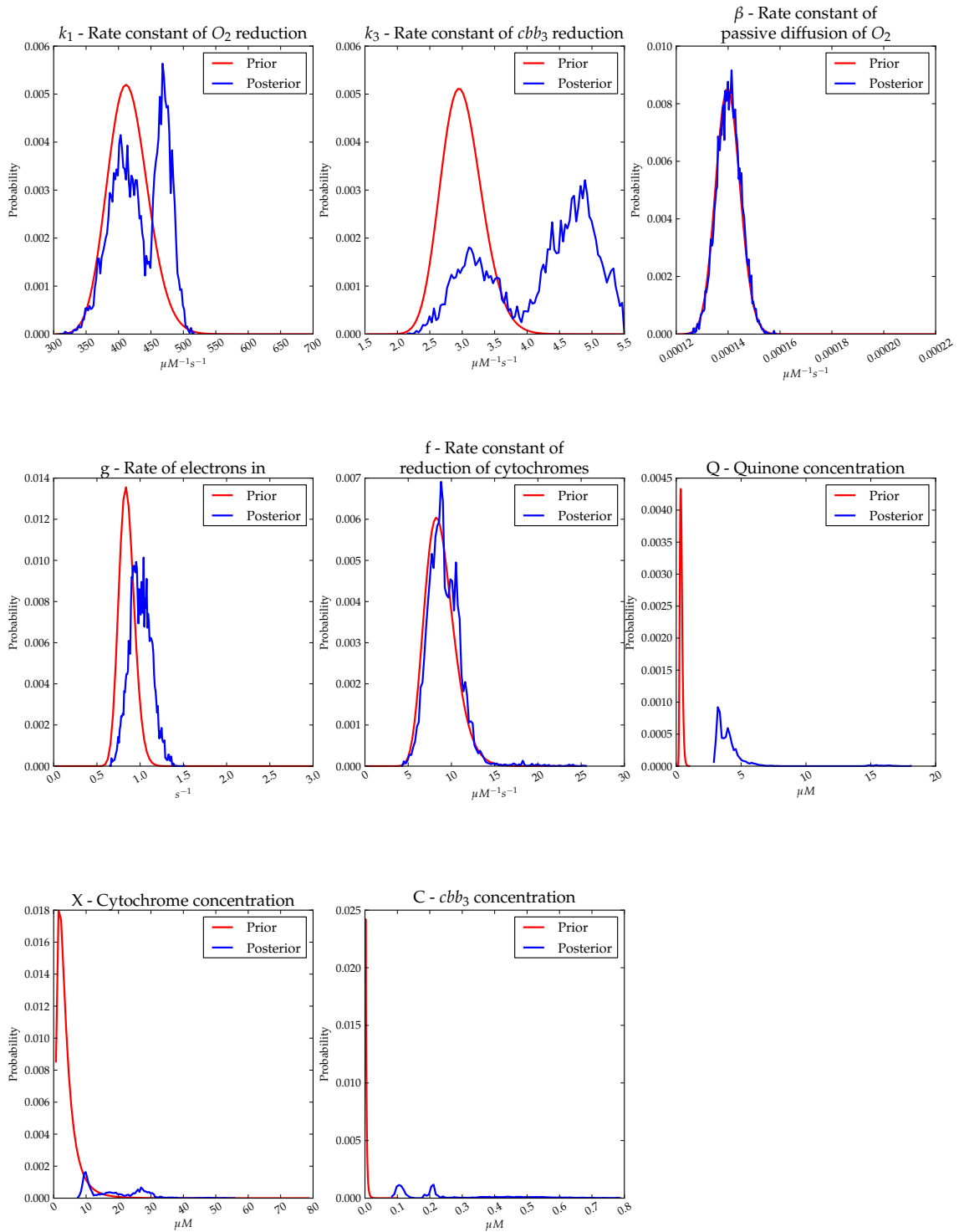
Posterior probability distributions created by parameter estimation


Figure 5.9: **Posterior probability distributions for oxygen reduction.** These are the probability distributions generated by parameter estimation on 3 oxygen reduction datasets. These have been overlaid onto the prior probability distributions used by the parameter estimation algorithm, also shown in Figure 5.5.

the cause of several of the other distributions being flatter and outside of the main body of their prior distributions. Another interesting observation is that the distribution for k_3 shows a distinct bi-modality. It is possible that the true posterior probability distribution is bi-modal, however this is quite likely to be due to the choice of proposal distribution for the parameter estimation algorithm. The left-most region of the bimodal distribution could be caused by the natural bias of the algorithm for values within more likely regions of the prior (proposal) probability distribution. If this is the case, the right-most region is the “true” probability distribution where the increase in likelihood of fitting outweighs the fact that the values selected have a low probability of being selected from the prior distribution. Assuming this is the case, the prior distribution may also be incorrect for k_3 , but the shape of the posterior distribution may also be directly caused by the more obviously incorrect prior distribution of Q .

Since the posterior probability distributions generated at this stage cannot be used as priors for the reasons described above, the prior distributions were altered to try and correct them. These alterations are described in the next section.

5.1.2.3 Secondary Prior Probability Distributions

To improve the prior probability distribution to counteract the behaviour seen in the section above, a number of changes were made to the distribution parameters. All of the rate constant and total concentration parameters were flattened out, that is to say the variance was increased. In addition the mean value for Q was increased tenfold since the previously described results showed this value was far too low. The parameters for reduced enzyme concentration were not altered, as the ODE solver is accurate enough to correct these immediately. The values required to create the updated prior probability distributions are shown in Table 5.2.

A graphical representation of the data in Table 5.2, the initial probability distributions used to start the Monte-Carlo run are shown in Figure 5.10.

Prior probability distributions used for parameter estimation

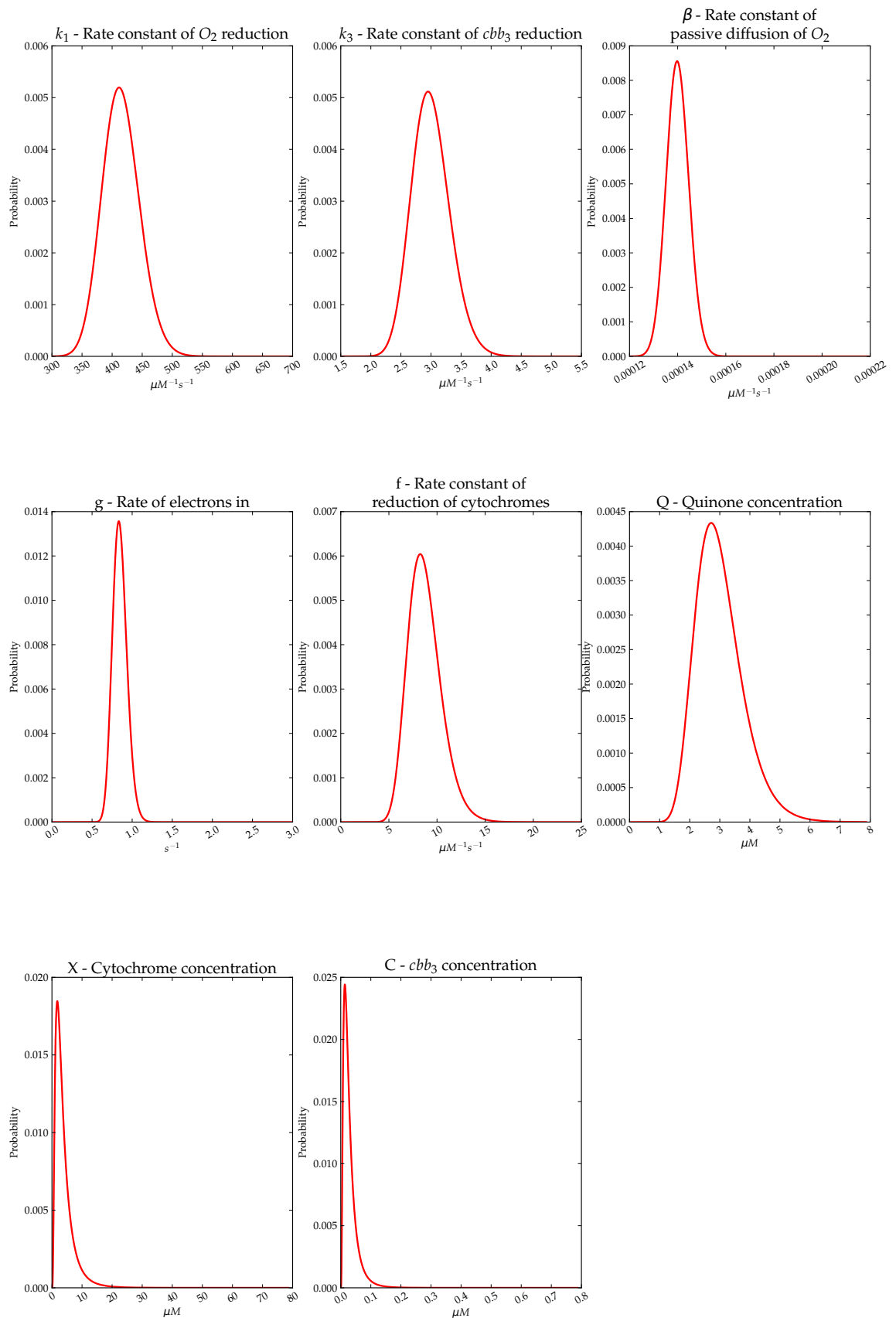


Figure 5.10: Prior probability distributions for oxygen reduction. These are the probability distributions used as priors by the parameter estimation algorithm.

Parameter	\bar{x}	σ
k_1	415 $\mu\text{M}^{-1}\text{s}^{-1}$	30.93
k_3	3 $\mu\text{M}^{-1}\text{s}^{-1}$	0.316
β	0.00014 $\mu\text{M}^{-1}\text{s}^{-1}$	4.67×10^{-6}
g	0.847 s^{-1}	0.089
f	8.749 $\mu\text{M}^{-1}\text{s}^{-1}$	1.732
Q	3 μM	0.1
X	3.97 μM	0.424
C	0.03 μM	0.003
Q_a	0.24 μM	0.008
X_a	3.176 μM	0.105
C_a	0.024 μM	0.0008

Table 5.2: **Prior Probability Table** This table shows the prior means and variances used to create lognormal distributions to be used as the prior probability distributions.

5.1.2.4 Secondary Parameter Estimation Results

The posterior probability distributions for this second attempt were generated in the same way as described previously for the first attempt.

The second attempt at parameter estimation, revealed an issue with the input datasets that were being used. The first dataset contains no information about what happens to the rate of oxygen reduction once oxygen concentration approaches zero, as the experimental data does not extend this far. The second and third datasets do contain this information as they show complete oxygen reduction to zero, in addition to several seconds of data after that point. This can be seen in Figure 5.4.

The result of dataset 1 lacking this additional feature is that the parameter estimation algorithm was able to over-sample from the prior distributions as there was no significant difference in goodness-of-fit between “in prior” and “out of prior” parameter values. If these distributions were to have been included in the overall posterior probability distributions for oxygen reduction they would have skewed the distributions towards the priors rather than their true values. The posterior distributions for dataset 1 are shown in Figure 5.11.

The usable posterior probability distributions were therefore generated from the experimental datasets 2 & 3, each started with 20 runs and are shown in Figure 5.12. In the case of parameters which represent concentrations, such as X and C , the concentrations of cytochromes and cbb_3 respectively, the individual dataset probability distributions are shown, as they cannot be sensibly combined, and it emphasises the fact that the datasets were different.

The distribution of k_3 is perhaps the most interesting as it shows that the estimates used as priors are most likely incorrect as the posterior distribution has shifted significantly to the right, increasing the mean value of the parameter by a factor of $\approx 1.5\times$. The other rates are largely similar to their prior distributions suggesting that the priors were good estimates for the actual values. The prior distribution for Q had already been altered as described previously and the new

Posterior probability distributions created by parameter estimation

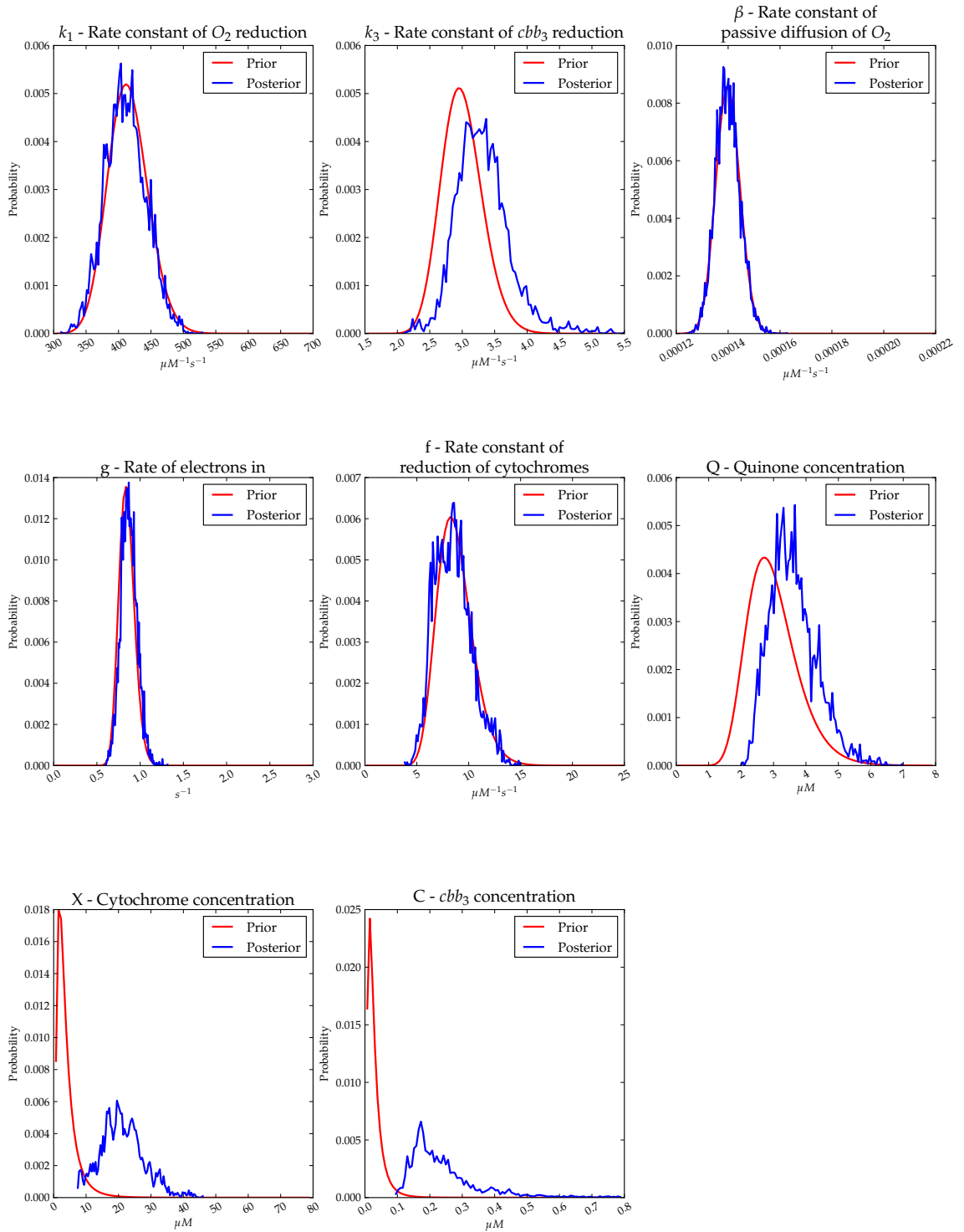


Figure 5.11: **Oversampled Posterior Distributions.** The posterior probability distributions for dataset 1 of oxygen reduction are oversampled from the prior probability distributions. This is not directly obvious by the probability distributions alone, but in conjunction with the input dataset which lacks features present in datasets 2 and 3. In this case both k_1 and k_3 are skewed towards the prior probability distributions, and this causes the distribution of C to be very wide as it can take a very broad range of values without affecting the goodness of fit of the simulated data to the experimental data.

Posterior probability distributions created by parameter estimation

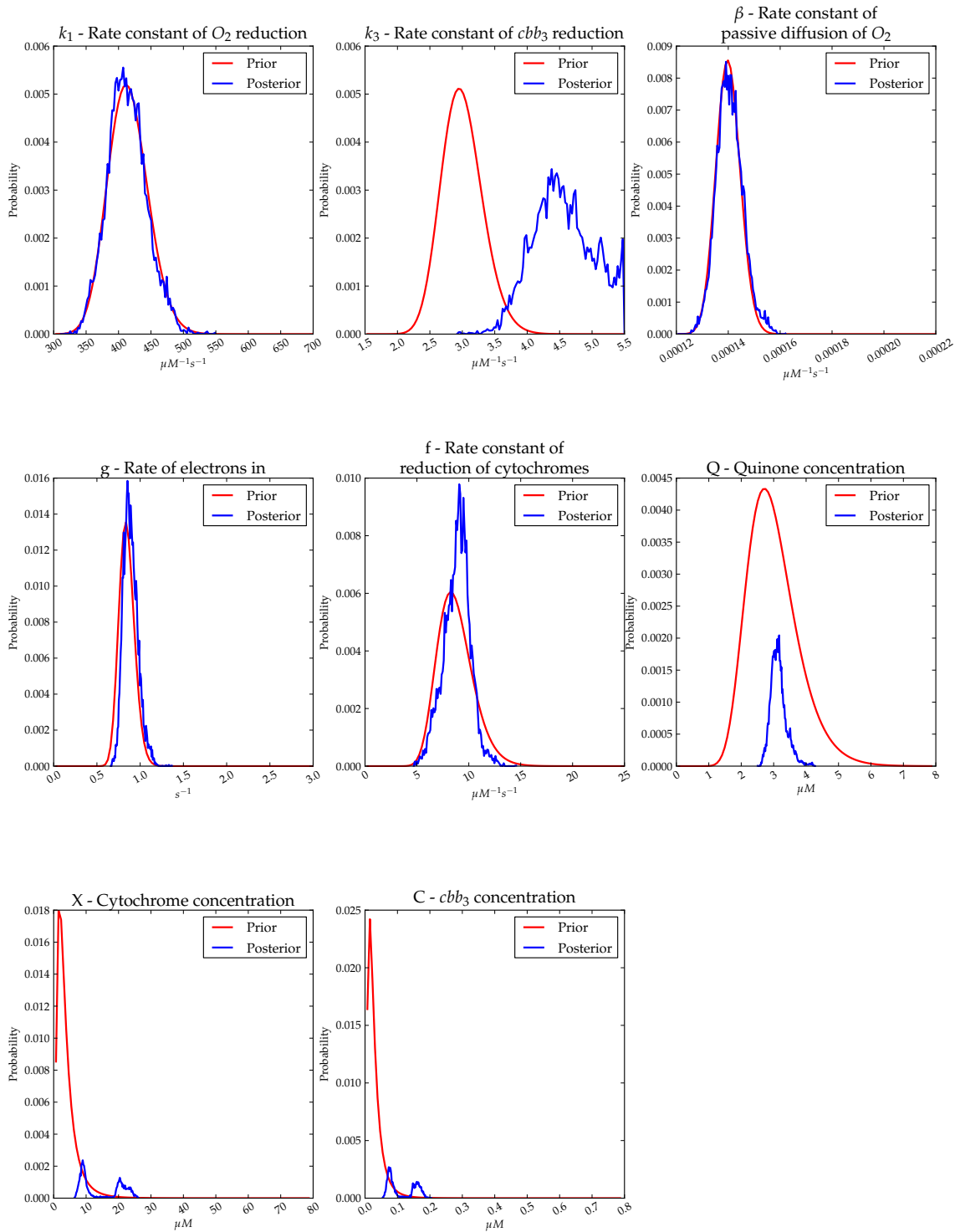


Figure 5.12: **Posterior probability distributions for oxygen reduction.** These are the probability distributions generated by parameter estimation on 2 oxygen reduction datasets. These have been overlaid onto the prior probability distributions used by the parameter estimation algorithm, also shown in Figure 5.10.

Parameter	Priors			Postriors		
	\bar{x}		σ	\bar{x}		σ
k_1	415	$\mu\text{M}^{-1}\text{s}^{-1}$	30.93	413.228	$\mu\text{M}^{-1}\text{s}^{-1}$	30.046
k_3	3	$\mu\text{M}^{-1}\text{s}^{-1}$	0.316	4.496	$\mu\text{M}^{-1}\text{s}^{-1} \uparrow$	0.463 \uparrow
β	0.00014	$\mu\text{M}^{-1}\text{s}^{-1}$	4.67×10^{-6}	0.00012	$\mu\text{M}^{-1}\text{s}^{-1}$	0.00017
g	0.847	s^{-1}	0.089	0.889	s^{-1}	0.089
f	8.749	$\mu\text{M}^{-1}\text{s}^{-1}$	1.732	8.707	$\mu\text{M}^{-1}\text{s}^{-1}$	1.35 \downarrow
Q	3	μM	0.1	3.143	μM	0.240
X	3.97	μM	0.424	4.732	$\mu\text{M} \uparrow$	6.707 \uparrow
C	0.03	μM	0.003	0.043	$\mu\text{M} \uparrow$	0.044 \uparrow

Table 5.3: **Posterior Probability Statistics.** This table shows the parameters required to create lognormal distributions that describe the prior and posterior probability distributions. The values for the priors are as in Table 5.2. The posterior distributions were generated from datasets 2 & 3, and where they relate to concentrations, these have been normalised. The lognormal distributions represent best-fits to the actual posterior distributions. Where there are significant differences between the prior and posterior values for either the mean or standard deviation, these are indicated by \uparrow and \downarrow .

value chosen seems to be a great deal better based on the closeness of the posterior distribution to the altered prior distribution. The concentrations of X and C appear to be underestimated in the prior distributions, as the posteriors show a significant shift to the right as with k_3 . A comparison between the prior probability distributions and the posterior probability distributions can be seen in Table 5.3. In this table the obtained distributions have been fitted to lognormal distribution which can be described by 2 parameters, which makes comparing the distributions much easier.

A graph showing how well the solved output fits the experimental data during the parameter estimation stage is shown in Figure 5.13. This shows the solved output which achieved the best goodness of fit against the experimental data.

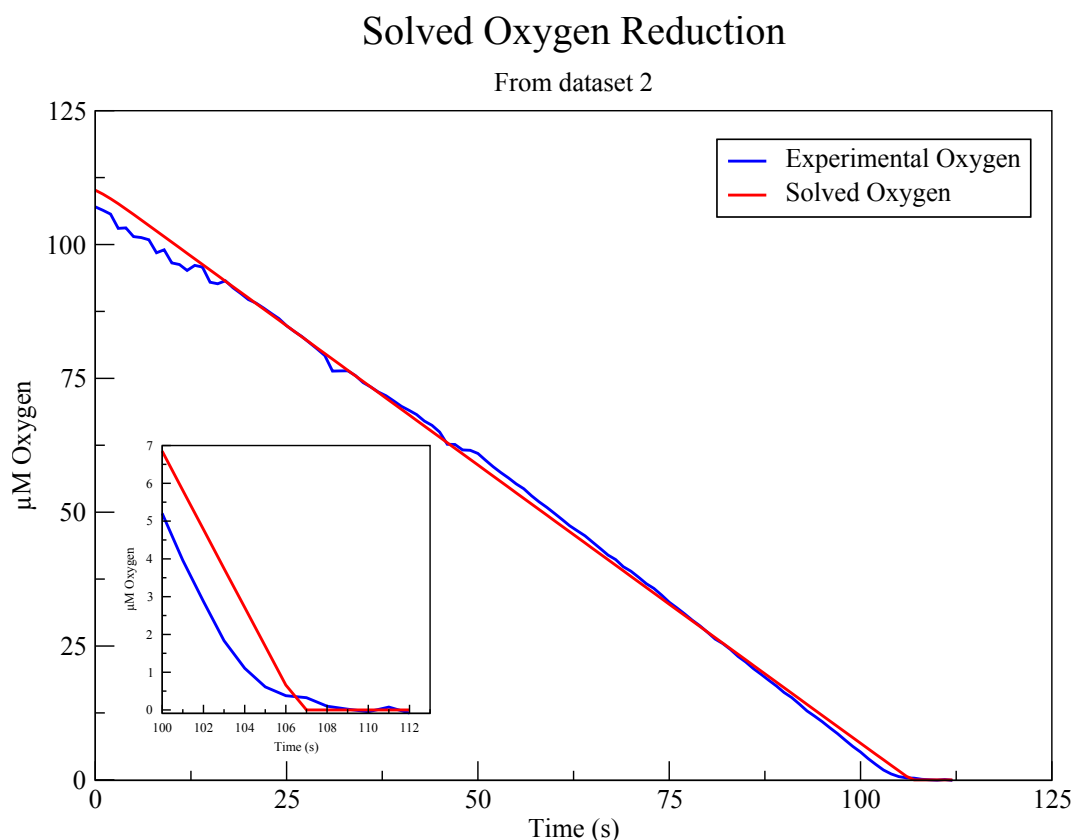


Figure 5.13: **Oxygen Reduction in *Neisseria meningitidis*.** This figure shows how well the best simulated data fits against the experimental data from dataset 2. The inset shows again, that the solved output is achieving much higher affinity than the experimental data.

5.1.2.5 Analysis of Convergence

It is possible to estimate the degree of convergence of the parameters from the Monte Carlo trajectories using the R statistic introduced by Gelman and Rubin¹⁵¹ and Brooks and Gelman¹⁵². This statistic is a single value that represents how close the trajectories for each individual parameter have come to convergence. The R statistic was calculated using the *Bolstad2*¹⁵³ library for R¹⁵⁴ (statistical software package).

Table 5.4 shows the R statistics obtained from the trajectories run for oxygen reduction parameter estimation. The R statistic is a measure of scale-reduction, and fully converged trajectories will have a value of 1.0 whereas trajectories which have not converged will have values greater than 1 with the magnitude depending on how far away from converging they are. Gelman states that if the R statistic is not near 1, and in practice greater than ≈ 1.2 then further simulation runs would be a good idea¹³⁷. The R statistic shows that all of the rate constants appeared to have converged to a reasonably high degree which could also be seen from the distribution plots. The concentration parameters had converged to a much lesser degree however this was not completely unexpected, as there were a larger number of parameters in the model than were required to fit the experimental data and thus the potential range of parameter values was broad at this stage. The apparent lack of convergence of some parameters at this point was not a problem as with subsequent, more complex datasets, the range of potential parameter values should decrease, allowing the trajectories to converge more easily.

5.1.2.6 Analysis of Correlation

Given the large number of parameters, and the simple form of the experimental data it is quite likely that a number of the parameters will be correlated with one another. This effect should also have been exacerbated at this stage due to the limited constraints (by virtue of wide prior probabilities) on the ranges of values

Parameter	R Statistic	Parameter	R Statistic
k_1	1.38	f	1.65
k_3	1.36	Q	2.37
β	1.09	X	11.93
g	1.57	C	9.44

Table 5.4: **Gelman-Rubin Convergence Statistic.** This table shows the Gelman-Rubin Convergence statistic for all the Markov chains from datasets 2 & 3. For parameters which are concentrations, the statistic relates to the values after normalisation (data is normalised based on initial oxygen reduction rate). Concentration parameters exhibit greater inter-dataset differences even after normalisation thus giving high R statistic values. The intra-dataset values are lower.

that parameters can take. In order to investigate this a set of correlation matrices were constructed by calculating the Pearson's Product-Moment Correlation Coefficient (denoted by r , not to be confused with the R statistic) for each of the parameters. This value provides the direction of correlation as indicated by the sign, and the degree of linearity as indicated by the magnitude. A positive correlation indicates that as the value of one parameter increases, the other increases also. A negative correlation indicates that as the value of one parameter increases, the other decreases.

The upper-triangle correlation matrices are shown in Figures 5.5 & 5.6 and were constructed by concatenating all the trajectories created by the parameter estimation system (discarding the burn-in) together and the Pearson's Product-Moment Correlation Coefficient calculated for each combination for each dataset. The datasets were analysed separately to allow examination of intra dataset correlation. The matrices are upper-triangle only as the lower triangle is a duplicate of the same data. The diagonals are shown in grey as they are not useful data since the correlation of X against X is always 1.

The correlation matrices show that most of the model parameters are not correlated with each other, giving low to very low r values. Between the two datasets the only parameters that appear to be correlated are C and X and k_3 and X, and

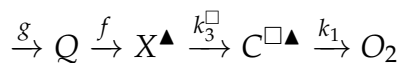
	k_1	k_3	β	g	f	Q	X	C
k_1	1	0.010353	0.007923	0.033363	-0.009149	-0.004965	0.017719	-0.029593
k_3		1	-0.015159	-0.110244	0.050016	-0.020452	-0.318503	-0.479758
β			1	0.002275	-0.009439	-0.003051	0.017707	-0.003679
g				1	-0.042492	-0.123088	0.122328	-0.093617
f					1	-0.052359	-0.060664	-0.029025
Q						1	0.061756	-0.086643
X							1	-0.658657
C								1

Table 5.5: Regression Analysis of Oxygen Reduction Parameters for Dataset 2. This table shows the r values from linear regression analysis on the combined parameter trajectories for Oxygen reduction. Parameters with high correlation have been coloured green ($R > 0.8$) and those with moderation correlation have been coloured orange ($0.8 > R > 0.3$).

	k_1	k_3	β	g	f	Q	X	C
k_1	1	-0.002964	0.149765	0.083521	0.13787	-0.088977	-0.006116	0.011541
k_3	1	0.032078	-0.046175	0.05076	-0.102051	-0.634699	-0.4545	
β		1	0.050182	-0.007235	-0.120098	0.103706	-0.135299	
g			1	0.104896	-0.473135	-0.150992	0.199826	
f				1	-0.127323	-0.090914	-0.022676	
Q					1	0.09321	-0.116721	
X						1	-0.379235	
C								1

Table 5.6: Regression Analysis of Oxygen Reduction Parameters for Dataset 3. This table shows the r values from linear regression analysis on the combined parameter trajectories for Oxygen reduction. Parameters with high correlation have been coloured green ($R > 0.8$) and those with moderation correlation have been coloured orange ($0.8 > R > 0.3$).

these are both negative correlations. The negative correlation between k_3 and X can be explained by the fact that as the concentration of X decreases, an increase in k_3 is required to maintain the same rate of electron flow out of the cytochrome pool. The correlation between C and X can be explained by factoring in the fact that the rate of oxidation of C is very high. This should lead to any reduced cbb_3 being oxidised almost straight away. Therefore if the concentration of X increased, it would lead to an increase in the reduction state of C (as there will be more electrons to move from X to C), so to maintain the same eventual rate of oxygen reduction (by oxidation of C), the concentration of C must decrease. The converse is also true. The fact that there are intra-dataset correlations that don't appear in both datasets suggests that the rates and concentrations in the two datasets haven't been completely decoupled from the optical density (or in this case the reduction rate proxy for OD). The positions in the electron transport chain of these correlations are shown below, marked by superscript \blacktriangle and \square .



5.1.3 Discussion

The experimental datasets showed that oxygen reduction in *N. meningitidis* is a simple almost completely linear system with the reductase having a high affinity for oxygen demonstrated by the almost complete lack of non-linearity as oxygen concentration approaches zero. This simple linearity could be very easily have been modelled to a high degree of accuracy with just 2 parameters in a simple $y = -mx + c$ system. Admittedly this would not include the behaviour when the oxygen concentration reaches zero, where there is some non-linearity. However this essentially meant that there were a much larger number of parameters available to fit than were necessary, which lead to over-fitting of the data. The size of the parameter set meant that there were a very large set of potential combinations that would have lead to a similar result, however this was mitigated somewhat by the prior probability distributions given to the algorithm. Even so, this meant

that the posterior distributions generated were very wide and therefore allowed much greater freedom for the next dataset to explore the parameter space.

With the knowledge of the underlying transport chain and the affinity of *cbb₃* for oxygen, a linear reduction of oxygen with high affinity over nearly two orders of magnitude was expected. This was evidenced in the experimental data. It is however remarkable that this behaviour can be modelled with so few components in the model, as it requires significant changes in the reduction states of the enzymes to achieve this. A brief discussion on the affinity of *cbb₃* for oxygen can be found in the appendix.

Perhaps the most interesting new piece of data to come out of this first round of parameter estimation is the discovery that the literature value used for the concentration of quinones - Q - in the cell was at least an order of magnitude too low. This can be explained however by the fact that the literature value used is not for the same bacteria, and there were a number of assumptions made about *Neisseria meningitidis* cell size and weight.

Chapter 6

Nitric Oxide Reduction in *N. meningitidis*

6.1 Aerobic Nitric Oxide Reduction

6.1.1 Introduction

The next dataset used in the iterative approach to parameter estimation was of aerobic oxygen reduction interrupted by the addition of Nitric Oxide. These datasets are the next most complicated after aerobic oxygen reduction as it introduces the nitric oxide reduction pathway. In this case the oxygen reduction and Nitric Oxide reduction pathways are active. Additionally, inactivation of *cbb₃* by Nitric Oxide was occurring. The portions of the ETC relating to Nitric Oxide reduction are shown graphically in Figure 6.1. However this pathway cannot be isolated *in vivo* as *N. meningitidis* is incapable of completely anaerobic respiration therefore the required parts of the model are actually those from Chapter 5 and those in Figure 6.1.

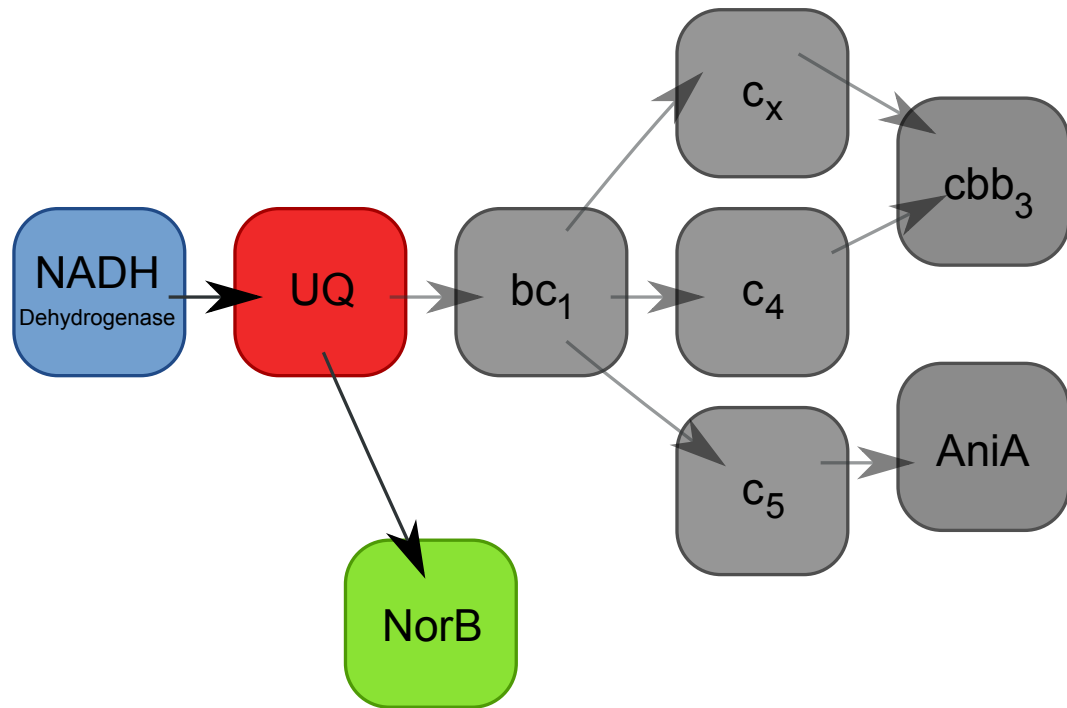


Figure 6.1: **Nitric oxide reducing electron transport chain of *N. meningitidis*.** This shows the complete electron transport chain of *Neisseria meningitidis* with the components irrelevant to nitric oxide reduction greyed out.

The equations that describe this portion of the ETC are:

$$\begin{aligned}
 \frac{d[O_2]}{dt} &= \beta(1 - [O_2]/K_O) - k_1[C_a][O_2] \\
 \frac{d[Q_a]}{dt} &= g([Q] - [Q_a]) - l_3[Q_a]([B] - [B_a]) - f[Q_a]([X] - [X_a]) \\
 \frac{d[X_a]}{dt} &= -k_3([C] - [C_a] - [C_X])[X_a] - m_3([A] - [A_a])[X_a] + f[Q_a]([X] - [X_a]) \\
 \frac{d[C_a]}{dt} &= k_3([C] - [C_a] - [C_X])[X_a] - k_1[C_a][O_2] - k_5[C_a][NO] + k_6[C_X] \\
 \frac{d[NO]}{dt} &= m_1[NO_2^-][A_a] - l_1[NO][B_a] - k_5[C_a][NO] + k_6[C_X] - \gamma[NO] \\
 \frac{d[C_X]}{dt} &= k_5[C_a][NO] - k_6[C_X] \\
 \frac{d[B_a]}{dt} &= l_3[Q_a]([B] - [B_a]) - l_1[NO][B_a]
 \end{aligned}$$

These equations describe the change in concentration of Nitric Oxide over time, which is the experimentally observable value (in addition to the afore modelled oxygen). Also being modelled was the change in concentration of inhibited *cbb3* and the reduction state of NorB. This more complete portion of the model in-

volved 14 parameters which were to be estimated. This number includes the 8 values already estimated in Chapter 5.

6.1.2 Experimental Results

Generation of Nitric Oxide reduction datasets required the growth of MC58 (wild type *Neisseria meningitidis*) in aerobic conditions until mid log-phase growth had been achieved. This corresponds to an OD_{600} of 0.3-0.9 and usually required an incubation period of roughly 3 hours. Once the required cell density had been obtained, the culture was transferred to the oxygen electrode chamber and the oxygen and nitric oxide concentrations recorded as the culture respiration. To model nitric oxide reduction required that nitric oxide solution was added to the culture while it is respiring aerobically. Part-way through aerobic respiration nitric oxide solution was added to various final concentrations all at $\approx 5 \mu\text{M}$ and the culture then left to reduce nitric oxide (in addition to oxygen). The nitric oxide reduction datasets generated and used for parametrisation of this portion of the model are shown in Figures 6.2, 6.3, 6.4 & 6.5. Unfortunately the experimental data upon addition of nitric oxide is very difficult to reliably reproduce, with different cultures having apparently different tolerances to nitric oxide (data not shown).

The dataset in Figure 6.2 appears to show a system that was partially primed for microaerobic respiration. In this case it was speculated that there was a small amount of NorB (nitric oxide reductase) present. Initially the oxygen reduction was carried out in exactly the same manner as in Chapter 5. Upon addition of nitric oxide, oxygen respiration slowed and almost stopped as a result of competition for electrons between cbb_3 and NorB, and the direct chemical inhibition of cbb_3 by NO. Nitric oxide started to be removed as a combination of diffusion (although this rate will be low as shown in the previous two datasets) and reduction via NorB. Once the NO has been removed from the system oxygen reduction resumes at almost the same rate as before and still has the same high affinity feature as the oxygen reduction datasets in Chapter 5.

Nitric Oxide Reduction in *Neisseria meningitidis*

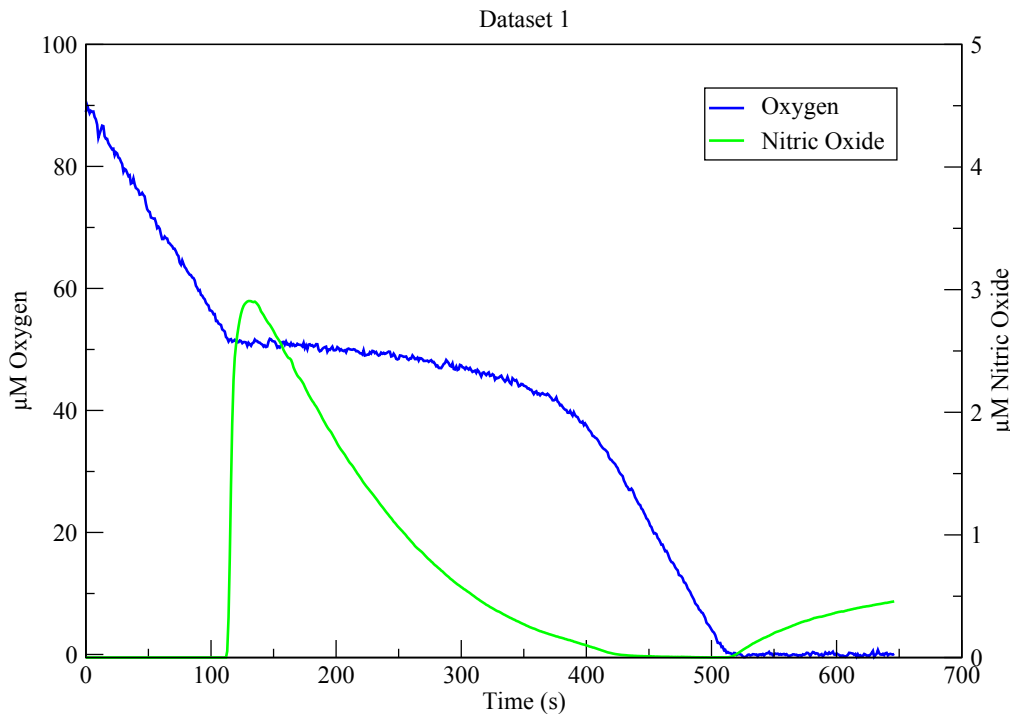


Figure 6.2: Nitric Oxide Reduction in *Neisseria meningitidis*. This dataset shows the effect on rate of oxygen reduction as nitric oxide (to $\approx 3 \mu\text{M}$) is introduced to the respiring system which also appears to have been partially primed for nitric oxide reduction. Note that the increase in nitric oxide concentration seen at the end of the dataset is most likely due to drift in the electrode.

When a larger amount of nitric oxide is introduced to a culture, the rate of oxygen reduction changes more significantly, as can be seen by comparing Figures 6.3 and 6.4. Again the removal of nitric oxide will primarily be due to diffusion, although now at higher concentrations more nitric oxide will interact with *cbb₃* temporarily inhibiting it. This inhibition causes the reduction in oxidase activity, and the sequestering of NO by *cbb₃* also causes some of the visible reduction in nitric oxide concentration. The time-scale over which the nitric oxide disappears strongly suggests that it is not due to nitric oxide reductase activity. This is corroborated by the NO removal time-scale in Figure 6.5 which contains no NorB. It may also be possible that at this concentration of nitric oxide some *cbb₃* may have been permanently inhibited as mentioned in Chapters 1 & 3. Additionally at higher nitric oxide concentrations nitric oxide could react chemically with oxy-

Nitric Oxide Reduction in *Neisseria meningitidis*

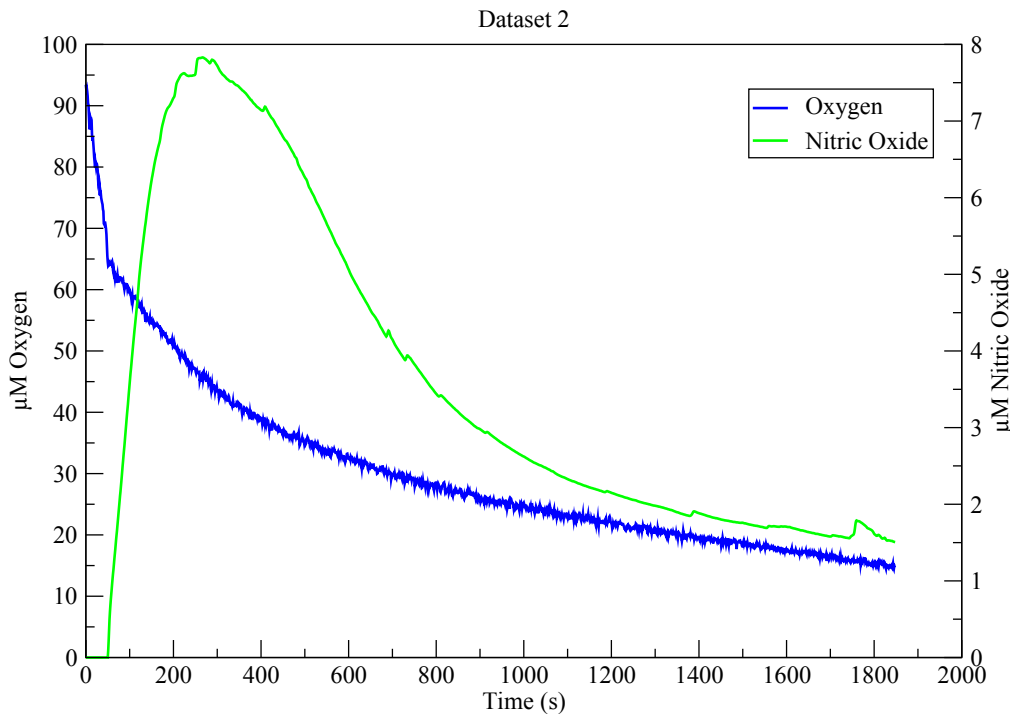
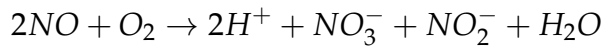


Figure 6.3: **Nitric Oxide Reduction in *Neisseria meningitidis*.** This dataset shows the effect on rate of oxygen reduction as a larger amount of nitric oxide (to $\approx 7.8 \mu\text{M}$) is introduced to the respiring system.

gen under the following scheme:



As the cultures in this dataset were obviously being negatively affected by the addition of such a high concentration of nitric oxide, either by permanent inhibition of cbb_3 or actual cell death, it was unlikely that this particular dataset could be used to accurately predict parameters in the model as it includes factors that were never part of the original model.

The dataset in Figure 6.4 shows very little visible change in the rate of oxygen reduction when a small amount of nitric oxide is added. In actual fact the change in rate was an $\approx 3\%$ reduction after addition of nitric oxide based on linear regression of pre- and post-addition rates. The observed removal of nitric oxide is due primarily to diffusion, although there may also be some preliminary (as the culture has not been primed with nitric oxide) nitric oxide reductase activity.

Nitric Oxide Reduction in *Neisseria meningitidis*

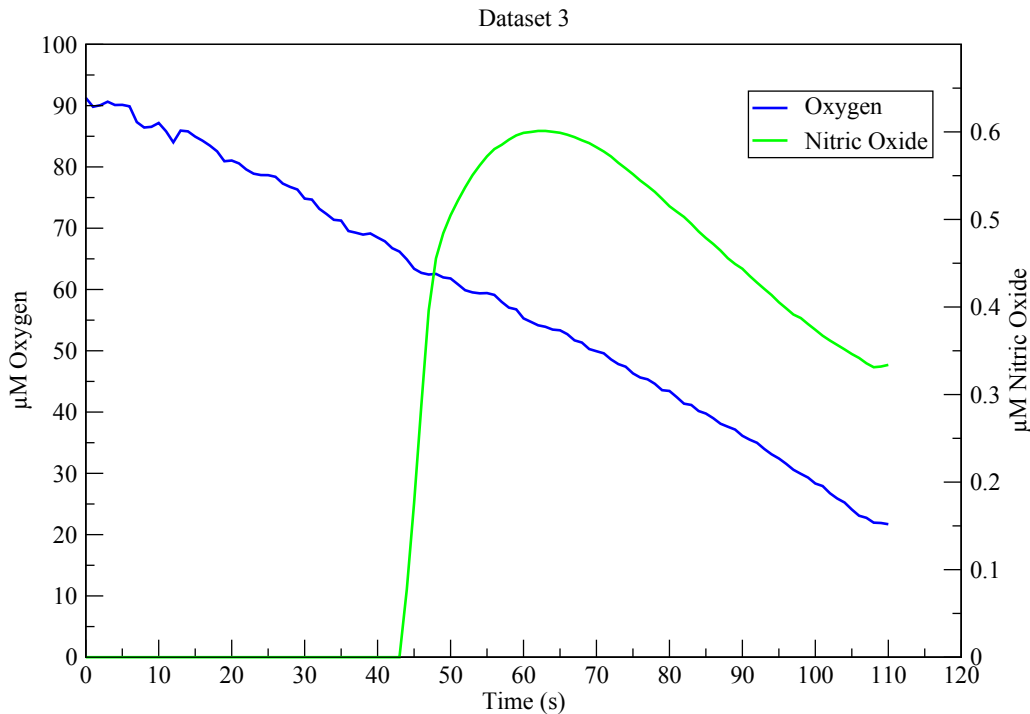


Figure 6.4: **Nitric Oxide Reduction in *Neisseria meningitidis*.** This dataset shows the effect on rate of oxygen reduction as a small amount of nitric oxide (to $\approx 0.6 \mu\text{M}$) is introduced to the respiring system.

However for modelling purposes it was assumed that the nitric oxide reductase activity for this dataset is zero.

The dataset in Figure 6.5 shows a visible change in reduction rate of cbb_3 upon addition of nitric oxide. This is due to inhibition of the cbb_3 directly by nitric oxide. This culture is incapable of reducing nitric oxide, having a $norB^-$ mutation, thus the only route for removal of nitric oxide is by simple diffusion.

6.1.2.1 Prior Probability Distributions

As in Chapter 5 the integrative scheme requires that all the parameters involved have associated prior probability distributions. The posterior probability distributions from Chapter 5 were used as prior probability distributions in this chapter. Where new parameters were introduced (which had not been modelled thus far), the distributions were generated based upon published literature values which are noted in Chapter 3. When using literature values the prior probabil-

Nitric Oxide Reduction in *Neisseria meningitidis*

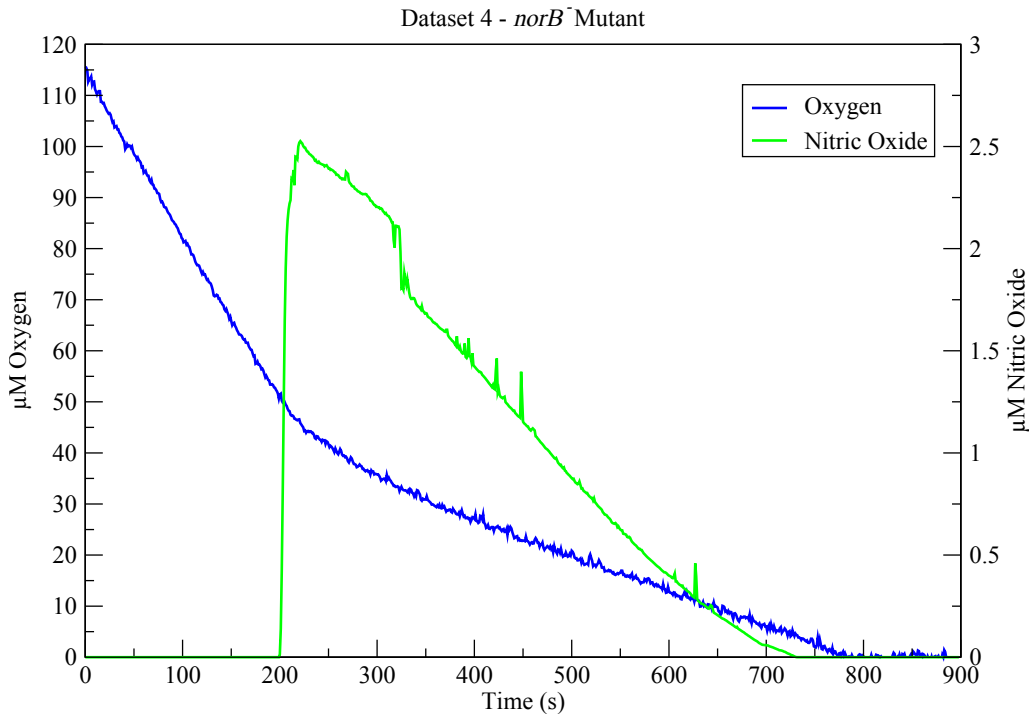


Figure 6.5: **Nitric Oxide Reduction in *Neisseria meningitidis*.** This dataset shows the effect on rate of oxygen reduction as nitric oxide (to $\approx 2.5 \mu\text{M}$) is introduced to a respiration *norB*⁻ mutant culture. Any removal of nitric oxide here is due to diffusion and sequestering by *cbb*₃ alone.

ity distributions were generated according to the same scheme as in Chapter 5. Where the posterior probability distributions from Chapter 5 describe rate constants the raw values from the distributions were used as priors in this chapter. Where the distributions describe component concentrations, idealised lognormal distributions were used based on normalised the values to account for the different culture densities. This ensures that the prior distributions completely encompass the experimental posterior distributions. The distribution of the parameter γ - the rate of loss of NO - was initially assumed (incorrectly) to be similar to β , thus the same probability distribution was used. This was actually a mathematical oversight as the two parameters are not functionally similar, however the resulting data is shown here to demonstrate the effect of this incorrect parameter. For the other new parameters, lognormal distributions were used as priors as described in Chapter 5. The values required to create idealised lognormal probability distributions for each parameter are shown in Table 6.1.

Parameter	\bar{x}	σ
k_1	413.228 $\mu\text{M}^{-1}\text{s}^{-1}$	30.046
k_3	4.496 $\mu\text{M}^{-1}\text{s}^{-1}$	0.463
l_1	6 $\mu\text{M}^{-1}\text{s}^{-1}$	2
l_3	1 $\mu\text{M}^{-1}\text{s}^{-1}$	2
k_5	100 $\mu\text{M}^{-1}\text{s}^{-1}$	10
k_6	38 s^{-1}	8
β	0.00014 $\mu\text{M}^{-1}\text{s}^{-1}$	4.67×10^{-6}
g	0.889 s^{-1}	0.089
f	8.707 $\mu\text{M}^{-1}\text{s}^{-1}$	1.35
γ	0.00014 μMs^{-1}	4.67×10^{-6}
Q	3.143 μM	0.240
X	4.732 μM	6.707
B	0.043 μM	0.044
C	0.043 μM	0.044

Table 6.1: **Prior Probability Table** This table shows the prior means and standard deviations used to create lognormal distributions to be used as the prior probability distributions.

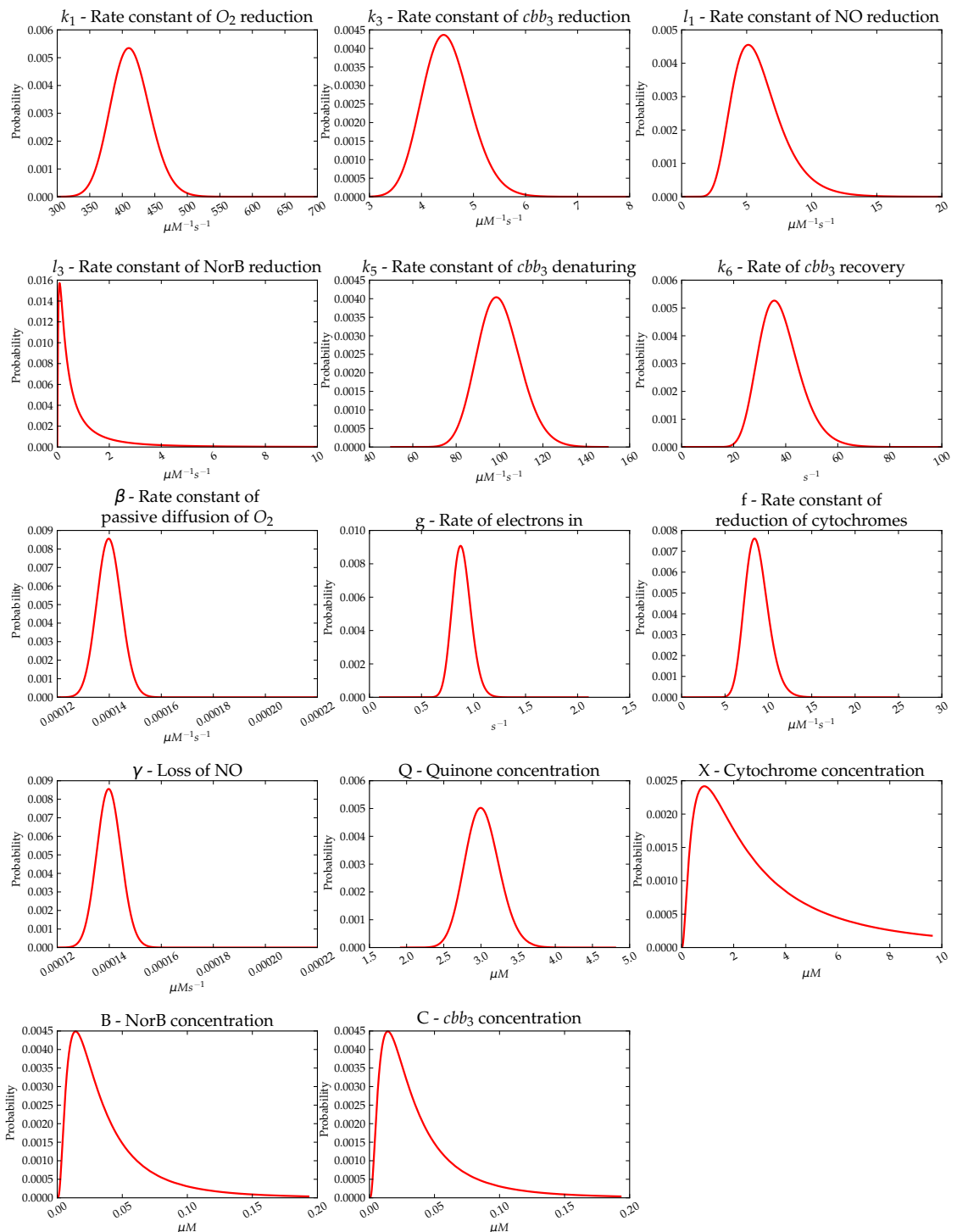
Prior probability distributions used for parameter estimation


Figure 6.6: **Prior probability distributions for aerobic nitric oxide reduction.** These are the probability distributions used as priors by the parameter estimation algorithm.

The initial probability distributions used to start the Monte-Carlo runs are shown in Figure 6.6.

6.1.2.2 Parameter Estimation Results

The parameter estimation process was run in the same fashion as that described in Chapter 5. The 4 experimental datasets were run 20 times (each) for 20,000 iterations using the prior probability distributions shown in Figure 6.6. This generated parameter trajectories from each of the 4 datasets. The second dataset (Figure 6.3) was still analysed even though it is unlikely that the model will successfully be able to be parameterised from it. Unfortunately upon examination of the F values from the MHMC output and the best-fitting solved output it was clear that the prior probability distributions in conjunction with the model are incapable of accurately describing the experimental data. This strongly suggested that the new prior probability distributions (those obtained from the literature for the NO related components) were incorrect. The solved output from datasets 3 & 1 are shown in Figures 6.7 & 6.8 respectively.

In dataset 3, the reduction of oxygen appears to be being modelled quite accurately. This is due to the largely featureless nature of the reduction curve which can easily be accommodated by the wide prior probability distributions given for the parameters involved. The rate change upon addition of a small amount of nitric oxide is only very slight, thus a perfectly straight line will fit it very well. As can be seen however, nitric oxide removal by diffusion is being modelled very poorly indeed. There is no active NorB in this culture, thus there is no modelled nitric oxide reduction. The prior distribution for the diffusion rate of nitric oxide is clearly incorrect, as nitric oxide removal in the solved output is virtually non-existent.

In dataset 1, reduction of oxygen is being modelled very poorly as the parameters produced by the parameter estimation system do not appear to have captured the behaviour that causes oxygen reduction to cease. In this case the F value

has been minimised by generating a linear reduction of oxygen which doesn't accurately represent either of the observed rates. As has been noted about dataset 3, the rate of nitric oxide diffusion is incorrect, thus in order to obtain a sensible rate for removal/reduction of nitric oxide the rate constants for nitric oxide reduction will have been increased artificially in the simulation. This combination of parameters also means that the reduction in rate of oxygen reduction cannot be modelled correctly. This behaviour should be attributed to temporary chemical inhibition of *cbb*₃ by nitric oxide itself (which is now present in high enough concentrations), and by competition for electrons with NorB.

As in Chapter 5, the prior probability distributions were incapable of producing parameter sets which accurately model the experimental data, thus making the posterior probability distributions generated invalid. The prior probability distributions were therefore modified to reflect the increased understanding of the parameters of the model. In addition to altered prior probability distributions a slightly different parameter estimation protocol was employed which is detailed in the next section.

6.1.2.3 Adapted Parameter Estimation Protocol

As dataset 3 was the simplest of the experimental datasets which describe the effects of addition of nitric oxide to aerobically respiring cultures, this dataset could be run as a standalone step in the Bayesian scheme for parameter estimation. This dataset described some of the experimentally observed behaviour in isolation, such as the removal of nitric oxide by diffusion alone, therefore could generate a posterior probability distribution for datasets where that parameter could *not* be examined in isolation. Datasets 1 and 4 ideally required this information as a prior probability distribution as the experimentally observed disappearance of nitric oxide was expected to be due to both diffusion and reduction (by NorB). Therefore dataset 3 could be used to inform the prior probability distribution of datasets 1 and 4. Statistically this did not pose a problem even though the three

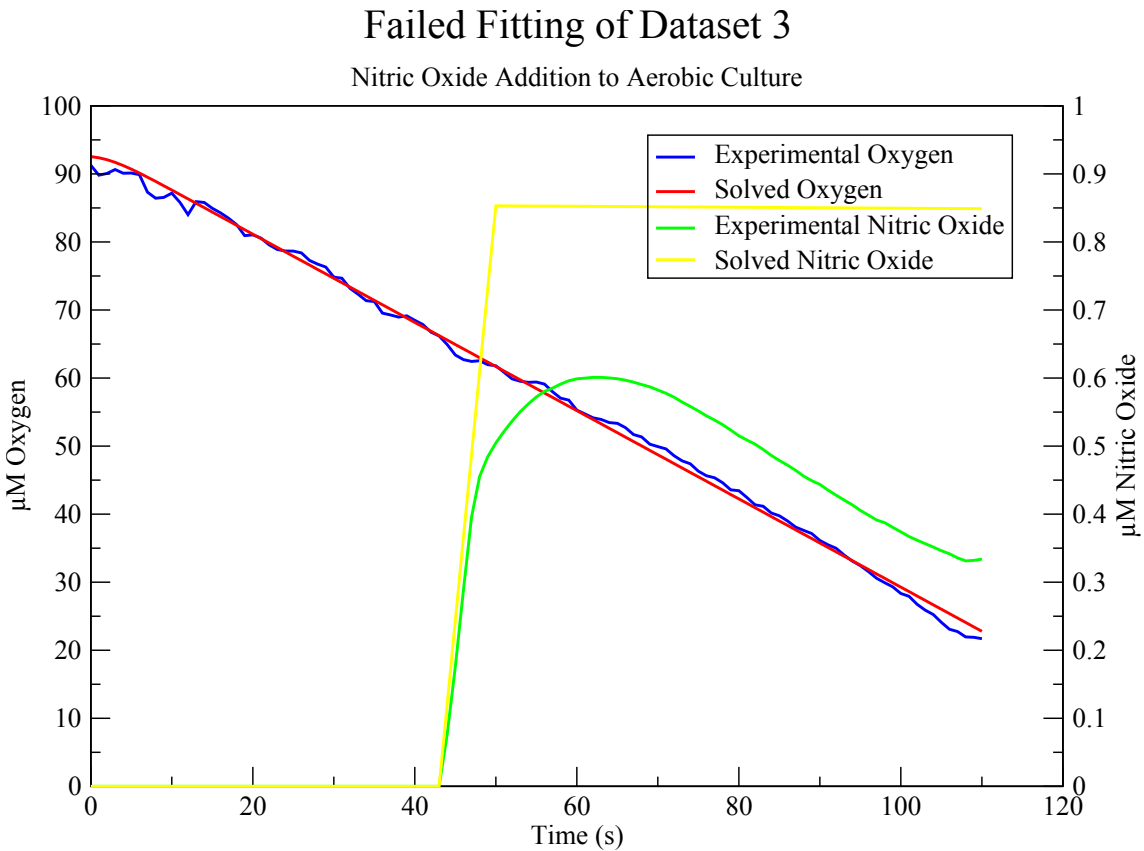


Figure 6.7: **Nitric Oxide Reduction in *Neisseria meningitidis*.** This figure shows the first attempt at fitting the model to experimental data using priors determined from literature values. Nitric oxide disappearance is not being modelled at all.

datasets were run in parallel previously. This was because the numerical output from those previous attempts was not being used as input for the subsequent attempts.

6.1.2.4 Secondary Parameter Estimation Results

Trial and error was employed to produce an initial informed prior value for γ , the rate of diffusion of nitric oxide, which was the problematic parameter for datasets 3 and 4 previously. This value was estimated to be $\approx 0.02 \mu\text{Ms}^{-1}$ based upon visual comparison of the solved output against the experimental data. This value was then used as a prior with no bounds so that the parameter estimation algorithm could home in on the correct distribution. All the other prior probability distributions were left unchanged from the first attempt. It should be noted that γ actually represents a set of physical effects on nitric oxide rather than just

Failed Fitting of Dataset 1

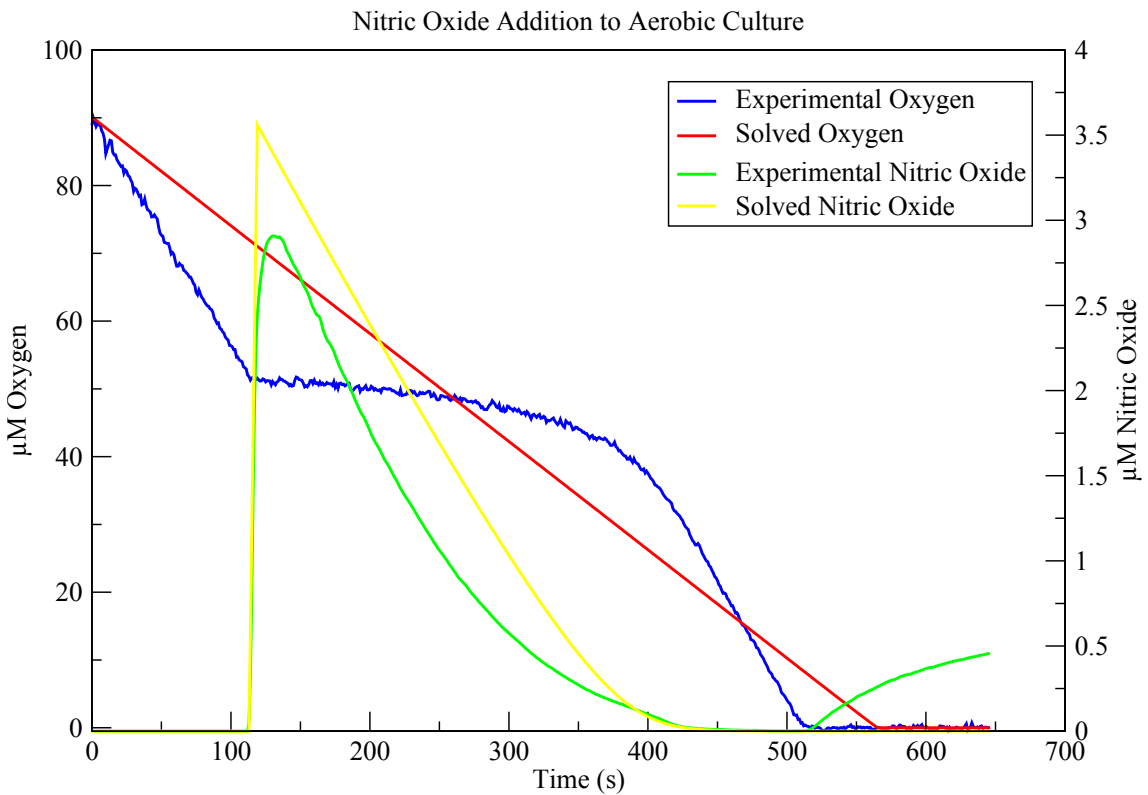


Figure 6.8: Nitric Oxide Reduction in *Neisseria meningitidis*. This figure shows the first attempt at fitting the model to experimental data using priors determined from literature values. Nitric oxide disappearance is now being modelled much more accurately than in Figure 6.7. Oxygen reduction is not being modelled correctly and the best fitting parameters generate a straight line rather than capturing the stopping and restarting of oxygen reduction.

diffusion as with β . γ is actually likely to include binding to metalloproteins, spontaneous degradation and the direct chemical reaction with oxygen in addition to the loss by simple diffusion.

Figure 6.9 shows greatly improved fitting of solved data to experimental values suggesting that the parameters are now correct (or at least reasonably close) for describing the removal of nitric oxide. The model is still not capturing the small effect on oxygen reduction rate visible in the experimental data however. A linear regression of the solved oxygen data suggests that it is in fact a perfectly straight line ($R^2 = 0.9999$, source data not shown) whereas there should be a slight elbow upon addition of nitric oxide. This was not considered to be a significant problem here, as the effect is far more visible in the subsequent dataset(s),

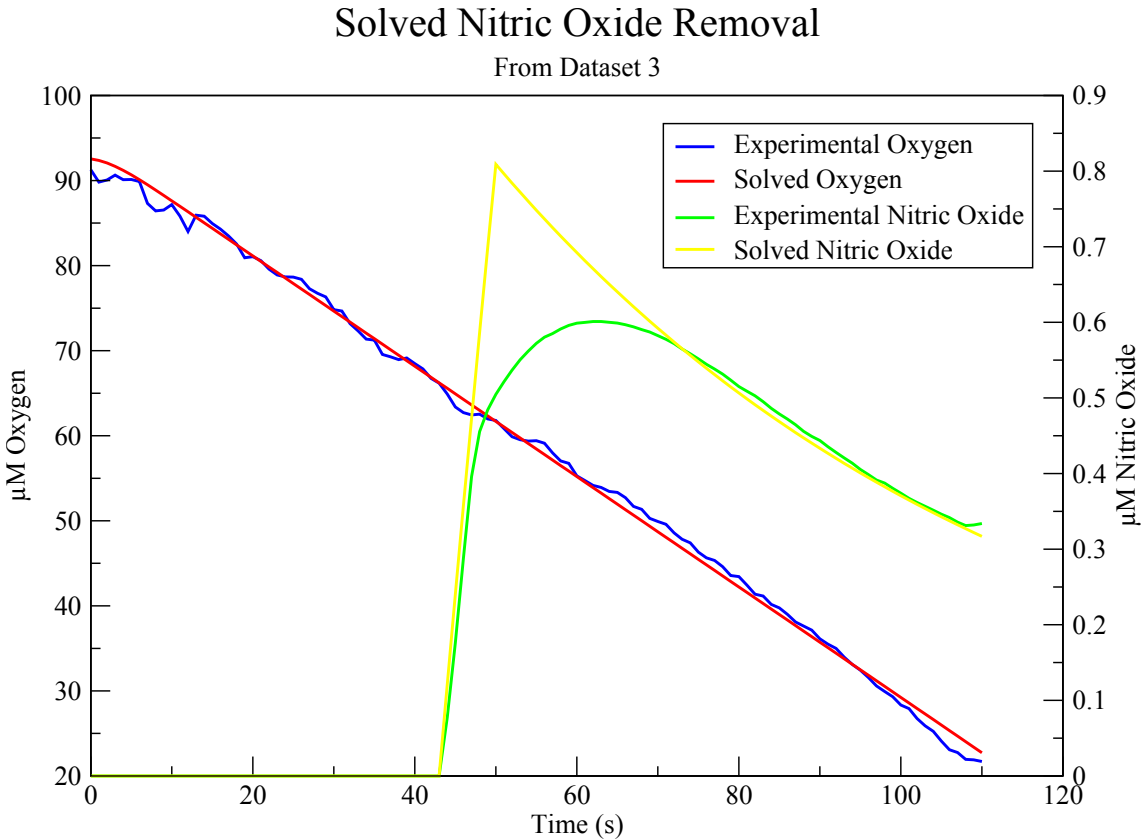


Figure 6.9: **Nitric Oxide Reduction in *Neisseria meningitidis*.** This figure shows the second attempt at fitting the model to experimental data using priors determined from literature values in addition to manually adjusted priors. Oxygen reduction is modelled almost perfectly, and the shape of the nitric oxide reduction curve is captured well also.

therefore would be more easily modelled.

The posterior probability distribution for γ produced by this dataset parameter estimation can be used a prior probability distribution for parameter estimation of datasets 1 and 4, as this now includes the missing information about rate of removal of nitric oxide.

6.1.2.5 Tertiary Parameter Estimation Results

The third round of parameter estimation built upon the results from the previous section. After parametrising the value for γ from dataset 3, it was then possible to attempt parameter estimation on datasets 1 and 4 which also involved l_1 , l_3 , k_5 & k_6 for reduction of nitric oxide and inactivation of cbb_3 by nitric oxide respectively. The prior probability distributions used for this round of parameter estimation were the same as in Figure 6.6 except that the distribution for γ was replaced by

that found in the previous section.

Preliminary test runs (data not shown) using these prior probability distributions suggested that at least one of the two parameters relating to the inactivation of cbb_3 by nitric oxide was incorrect for this model. In order to obtain a oxygen reduction curve that matches the general shape of the experimentally obtained data a ratio of $k_5 : k_6 \approx 2000 : 1$ was required. Since it was unknown which of the two values was more incorrect, both parameters were allowed to be perturbed freely during parameter estimation, i.e. they had no prior probability distribution. Unfortunately this seemed to be the only sensible approach to take given the lack of further data. These preliminary runs suggested that the number of parameter estimation iterations would need to be increased for this dataset also due to the presence of local F value minima caused by the model fitting oxygen as a straight line between the fixed starting point and the point at which oxygen is depleted similar to the result shown in Figure 6.8. Figure 6.10 illustrates local minima phenomenon. Given that this figure shows that a suitably low F value is not achieved until at least 15000 iterations (and in some cases this extended up to 50000 iterations) a value of 100000 iterations was chosen to ensure that a significant number of data-points were available to generate posterior probability distributions.

A representative plot showing the solved data after running the parameter estimation system as described above is shown in Figure 6.11. The model appeared to be able to capture all the features of the oxygen reduction curve including the halting of oxygen reduction upon addition of nitric oxide, and the recovery after nitric oxide has been removed. Similarly to the results seen in Chapter 5 the high affinity of cbb_3 for oxygen is also captured (probably a little too high). Nitric oxide was generally modelled less well than was hoped. The point of nitric oxide depletion appeared to be modelled correctly, but the rate of reduction of nitric oxide starts too fast and slows too quickly resulting in more pronounced curvature than the experimental data shows.

Goodness of Fit value during MHMC Run

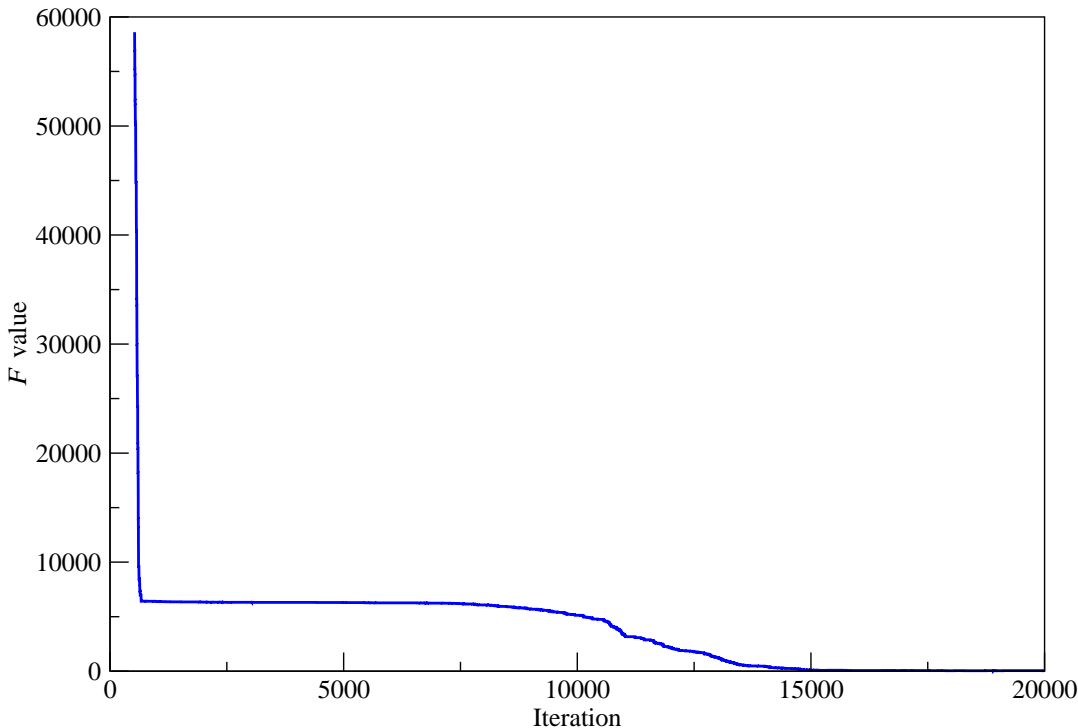


Figure 6.10: Local Fitness Minima During Parameter Estimation. This figure shows the F value as the MHMC progresses on dataset 1. A local fitness minimum is clearly visible at a F value of approximately 7000 where the parameter estimation algorithm has settled on a straight line for oxygen reduction. After a variable number of iterations the MHMC run exits the local fitness minimum and progresses towards a much better fitting set of parameters. This is a typical plot of the F values, however in some runs the fitness minimum is exited much more abruptly rather than the gradual change seen here.

The concentration of nitric oxide present will also affect the rate of cbb_3 reduction (due to the effect of temporary inactivation by nitric oxide), thus implying that the rate constants obtained to describe that effect may not be completely correct. Some of the observed discrepancy between the experimental and solved nitric oxide concentrations may in fact be due to errors introduced into the experimental data by the experimental set up. The nitric oxide electrode was not capable of detecting large changes in concentration quickly and this always resulted in a lag between nitric oxide addition and detection by the electrode. This is obvious in the experimental datasets where the total nitric oxide addition is not captured as the cultures have already started to remove it. This requires backwards extrapolation of the experimental data to determine what the actual added

Solved Nitric Oxide Removal

From Dataset 1

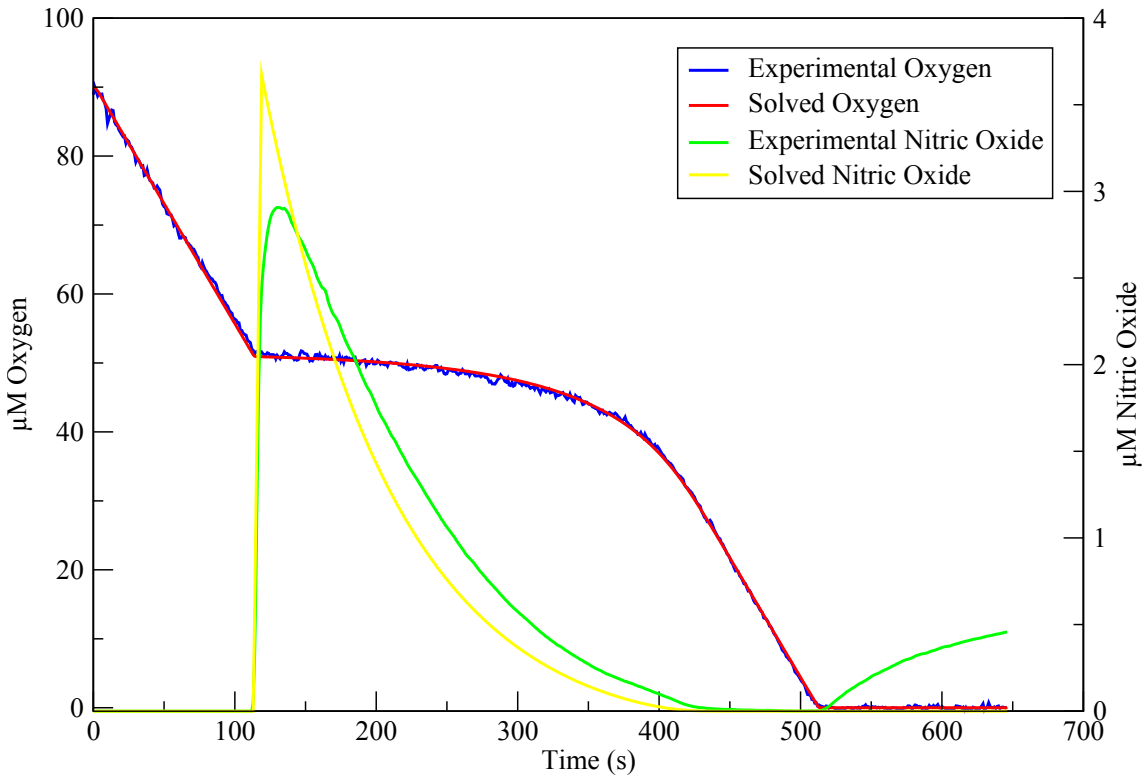


Figure 6.11: **Nitric Oxide Reduction in *Neisseria meningitidis*.** This figure shows the third attempt at fitting the model to experimental data using priors determined from literature values in addition to manually adjusted priors. Oxygen reduction is being modelled remarkably well, whereas the rate of nitric oxide reduction appears to be slightly too high in the solved output.

concentration was (and what should be added *in silico* to the model).

The posterior probability distributions generated from this third round of parameter estimation are shown in Figure 6.12. The distributions generated for the parameters relating solely to oxygen reduction were broadly similar to the prior probability distributions which was to be expected and confirms that these distributions capable of describing the oxygen reduction behaviour. The rate of NO reduction by NorB appeared to be very similar to the prior probability distribution however the rate of NorB reduction seemed to have been vastly overestimated in the prior distribution. The prior distribution for this parameter was unknown however, and was set to a very wide lognormal with mean of 1. The rate of NO diffusion (γ) tended to settle at the lower end of the prior distribution. The most interesting posterior probability distributions were those of k_5 and k_6 which actu-

ally had to be freely perturbed, rather than be constrained by their prior probability distributions. Neither of these two parameters settled anywhere near the prior probability distributions. k_5 never settles on a value less than $\approx 400 \mu\text{M}^{-1}\text{s}^{-1}$. This value turned out to be a critical threshold at which the inactivation of cbb_3 occurs. At lower values of k_5 the inactivation is slower than observed in the experimental dataset and in the solved data the “elbow” is shifted visibly to the right. At or above this threshold the inactivation point closely matches that seen in the experimental dataset. It appeared that that absolute values of k_5 and k_6 are unimportant, only that k_5 is greater than $\approx 400 \mu\text{M}^{-1}\text{s}^{-1}$ and that the ratio of $k_5 : k_6 \approx 2000 : 1$. Unfortunately this meant that it was impossible to determine if the obtained posterior probability distributions were actually representative of the true distributions.

A comparison between the prior and posterior distributions can be seen in tabular form in Table 6.2. This table shows the parameters of the idealised lognormal distributions which describe the obtained probability distributions to more easily represent the data.

6.1.2.6 Analysis of Convergence

The Gelman-Rubin R statistics were calculated for the Monte-Carlo trajectories for each parameter and these are presented in Table 6.3. The newly included parameters all had large R statistic values suggesting that there is still opportunity for scale reduction in the trajectories. This is highly likely to be due to the fact that k_5 and k_6 had to be unconstrained by prior probability distributions, and they are directly affecting the values of l_1 and l_3 in such a way as to prevent them converging fully. This is especially true of l_3 which has an extremely high R statistic. This actually suggests that l_3 is a long way away from being fully converged, or that an anomalous Markov Chain has been included.

Posterior probability distributions created by parameter estimation

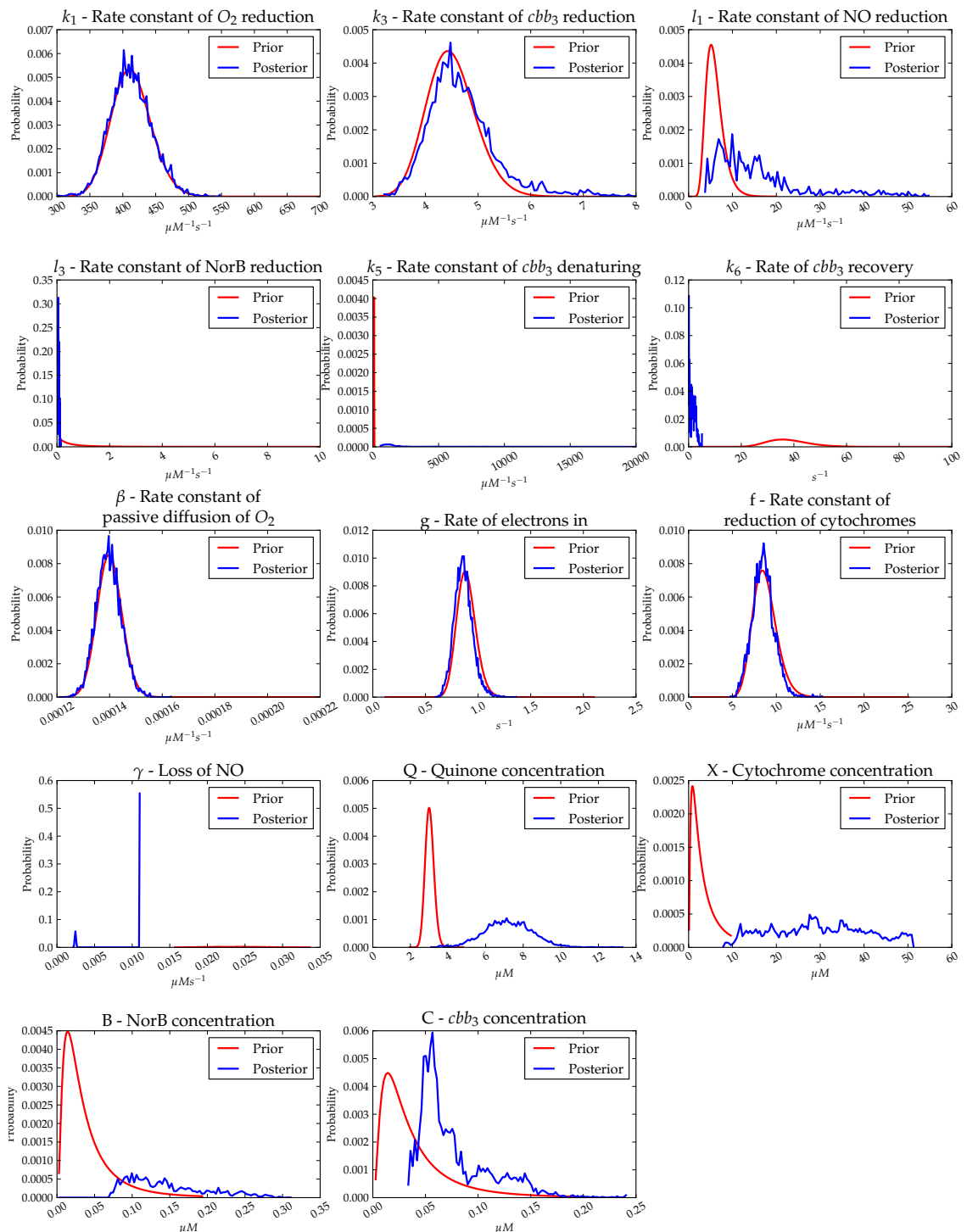


Figure 6.12: Posterior Distributions for Datasets 1 and 4. The posterior probability distributions for datasets 1 and 4 of nitric oxide removal.

Parameter	Priors			Posteriors		
	\bar{x}		σ	\bar{x}		σ
k_1	413.228	$\mu\text{M}^{-1}\text{s}^{-1}$	30.046	417.88	$\mu\text{M}^{-1}\text{s}^{-1}$	31.172
k_3	4.496	$\mu\text{M}^{-1}\text{s}^{-1}$	0.463	4.65	$\mu\text{M}^{-1}\text{s}^{-1}$	0.619
l_1	6	$\mu\text{M}^{-1}\text{s}^{-1}$	2	13.12	$\mu\text{M}^{-1}\text{s}^{-1}$ \uparrow	8.321 \uparrow
l_3	1	$\mu\text{M}^{-1}\text{s}^{-1}$	2	0.058	$\mu\text{M}^{-1}\text{s}^{-1}$ \downarrow	0.021 \downarrow
k_5	100	$\mu\text{M}^{-1}\text{s}^{-1}$	10	1741.8	$\mu\text{M}^{-1}\text{s}^{-1}$ \uparrow	1822.0 \uparrow
k_6	38	s^{-1}	8	1.076	s^{-1} \downarrow	1.473 \downarrow
β	0.00014	$\mu\text{M}^{-1}\text{s}^{-1}$	4.72×10^{-6}	0.00014	$\mu\text{M}^{-1}\text{s}^{-1}$	4.7×10^{-6}
g	0.889	s^{-1}	0.089	0.857	s^{-1}	0.086
f	8.707	$\mu\text{M}^{-1}\text{s}^{-1}$	1.35	8.398	$\mu\text{M}^{-1}\text{s}^{-1}$	1.237
γ	0.017	μMs^{-1}	0.0015			
Q	3.143	μM	0.240	7.06	μM	1.317
X	4.732	μM	6.707	27.45	μM	12.08
B	0.043	μM	0.044	0.137	μM	0.048
C	0.043	μM	0.044	0.071	μM	0.029

Table 6.2: Posterior Probability Statistics. This table shows the parameters required to create lognormal distributions that describe the prior and posterior probability distributions. The values for the priors are as in Table 6.1. The posterior distributions were generated from datasets 1 & 4 (after being run on dataset 3), and where they relate to concentrations, these have been normalised. The lognormal distributions represent best-fits to the actual posterior distributions. Where there are significant differences between the prior and posterior values for either the mean or standard deviation, these are indicated by \uparrow and \downarrow .

Parameter	R Statistic	Parameter	R Statistic
k_1	1.15	g	1.13
k_3	1.31	f	1.20
l_1	4.92	γ	
l_3	131.447	Q	1.54
k_5	6.46	X	3.82
k_6	7.37	B	6.74
β	1.02	C	2.92

Table 6.3: **Gelman-Rubin Convergence Statistic.** This table shows the Gelman-Rubin Convergence statistic for all the Markov chains from datasets 1 & 4. For parameters which are concentrations, the statistic relates to the values after normalisation (data is normalised based on initial oxygen reduction rate).

	k_1	k_3	l_1	l_3	k_5	k_6	g	f	Q	χ	B	C
k_1	1	-0.22	0.07	-0.06	0.07	-0.04	-0.01	-0.06	-0.01	0.04	0.02	0
k_3	1	-0.28	0.12	0.25	0.22	0.05	0.22	0.63	-0.29	-0.01	-0.01	-0.01
l_1		1	0.12	-0.45	-0.52	-0.09	0.06	-0.20	-0.25	-0.11	0.32	
l_3			1	-0.43	-0.40	-0.083	0.16	-0.07	-0.15	-0.81	0.04	
k_5				1	0.76	0.04	-0.15	-0.10	-0.11	0.46	0.08	
k_6					1	0.25	-0.06	-0.02	0.45	0.34	-0.48	
g						1	0.02	0	0.27	0.02	-0.22	
f							1	-0.06	-0.20	-0.10	0.14	
Q								1	0.18	-0.39	-0.19	
χ									1	-0.05	-0.87	
B										1	0.11	
C												1

Table 6.4: **Regression Analysis of Nitric Oxide Reduction Parameters for Dataset 1.** This table shows the r values from linear regression analysis on the parameter trajectories for nitric oxide reduction. Parameters with high correlation have been coloured green ($R \geq 0.8$) and those with moderation correlation have been coloured orange ($0.8 > R \geq 0.3$).

6.1.2.7 Analysis of Correlation

A correlation analysis was performed on each of the parameters using the Monte-Carlo trajectories as in Chapter 5. The upper-triangle correlation matrices are shown in Tables 6.4 and 6.5. There was a very strong positive correlation between k_5 and k_6 , which given the brief discussion earlier in the chapter was to be expected. As it appeared that the ratio and not the absolute values of k_5 and k_6 was important, a strong positive correlation between values would achieve this.

There also appeared to be a strong negative correlation between B , and l_3 , which would make sense if the model were trying to maintain a constant level of NO reduction. More NorB would require less reduction of NorB to maintain the same level of reduction. There are obvious negative correlations between k_5 , k_6 and l_1, l_3 . As more NO is being sequestered by cbb_3 , less needs to be reduced to maintain the same level of inhibition.

6.1.3 Discussion

The parameter distributions obtained from this more convoluted set of datasets are capable of modelling the experimental data impressively well given the lack of prior information available and taking into account the assumptions made about the system. Oxygen reduction can be modelled almost perfectly using posterior distributions from earlier datasets which will still fit new data. Nitric oxide reduction and removal was modelled less well, however it was not clear whether this was due to a limitation of the model itself, or an inherent issue with the experimental set-up. In reality it was probably a combination of both which would be impossible to decouple. The general features of nitric oxide reduction were captured in the model even if a precise fit wasn't achieved. There were a large number of unknowns in these experimental datasets, it was not clear for example how much NorB was present in dataset 1, therefore the concentrations and rates obtained will most likely not reflect *in vivo* values, however they do provide valuable information about how they interact with other parameters. It is

	k_1	k_3	k_5	k_6	g	f	Q	X	B	C
k_1	1	-0.14	-0.02	-0.25	0.02	0.03	0.07	0.13	0.02	0.04
k_3		1	0.05	0.21	-0.08	-0.02	-0.08	-0.29	-0.31	-0.18
k_5			1	0.74	0.06	-0.02	-0.11	-0.07	-0.25	0.25
k_6				1	-0.05	0.01	-0.15	-0.17	0.28	-0.37
g					1	-0.05	-0.01	-0.05	-0.10	0.19
f						1	0.03	0.04	0.04	-0.02
Q							1	0.03	0.07	-0.04
X								1	0.04	0.16
B									1	-0.84
C										1

Table 6.5: **Regression Analysis of Nitric Oxide Reduction Parameters for Dataset 4.** This table shows the r values from linear regression analysis on the parameter trajectories for nitric oxide reduction. Parameters with high correlation have been coloured green ($R \geq 0.8$) and those with moderation correlation have been coloured orange ($0.8 > R \geq 0.3$).

possible that the difference in observed and solved nitric oxide reduction rates is actually due in part to an overestimation of γ introduced by the analysis of the first dataset in Figure 6.4. It was assumed that there was no NorB present in that culture, thus any and all nitric oxide removal would solely be due to diffusion. If this were *not* the case, and in fact there was some small amount of nitric oxide reductase activity, then γ would be overestimated as it would include this NorB activity. The posterior probability distributions for datasets 1 and 4 (Figure 6.12) potentially support this hypothesis as they show the parameter estimation system trying to reduce the value of γ to the lower limit of its range. This inappropriately high value of γ could account for much of the discrepancy between the reduction rates of the experimental and solved data.

There is further evidence of incomplete decoupling of the model parameters from the experimental conditions here, as shown by the concentration posteriors all having shifted from the priors. The major difference can be seen for X - the cytochrome pool. This value doesn't actually represent any *in vivo* component as it is a simplification to represent all the cytochromes, hence the change in this value is not unexpected. Unfortunately, this is probably also the cause of shifting of the other component concentrations.

The simulated results and parameter set generated from parameter estimation are corroborated by experimental data observed by Anjum et al.²⁹ as described below.

Small concentrations of NO added result in no visible change in oxygen reduction rate (Figure 6.13a). Larger concentrations of NO appear to slow the rate of oxygen reduction which is then recovered (Figure 6.13b). A *norB*⁻ mutant treated with a larger concentration of NO shows a much slower recovery of oxygen consumption (Figure 6.13c) which can be shown *in silico* simply by removing NorB as can be seen in Figure 6.14.

As more parameters had been populated in the model it was now possible to examine the reduction states of the various enzymes in the system as respiration

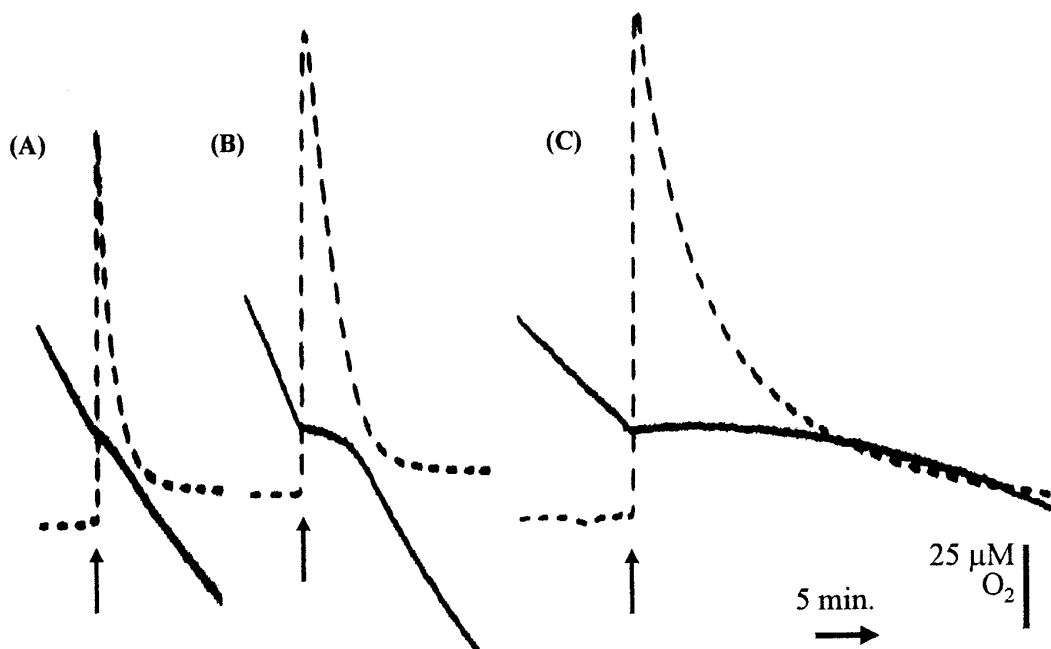


Figure 6.13: **Addition of Nitric Oxide to Aerobic Cultures.** Figure 5 reproduced from Anjum et al.²⁹. Oxygen concentration is represented by solid lines and nitric oxide by dashed lines. a) Addition to wild-type culture, b) Addition to *cycP* mutant, c) Addition to *norB* mutant.

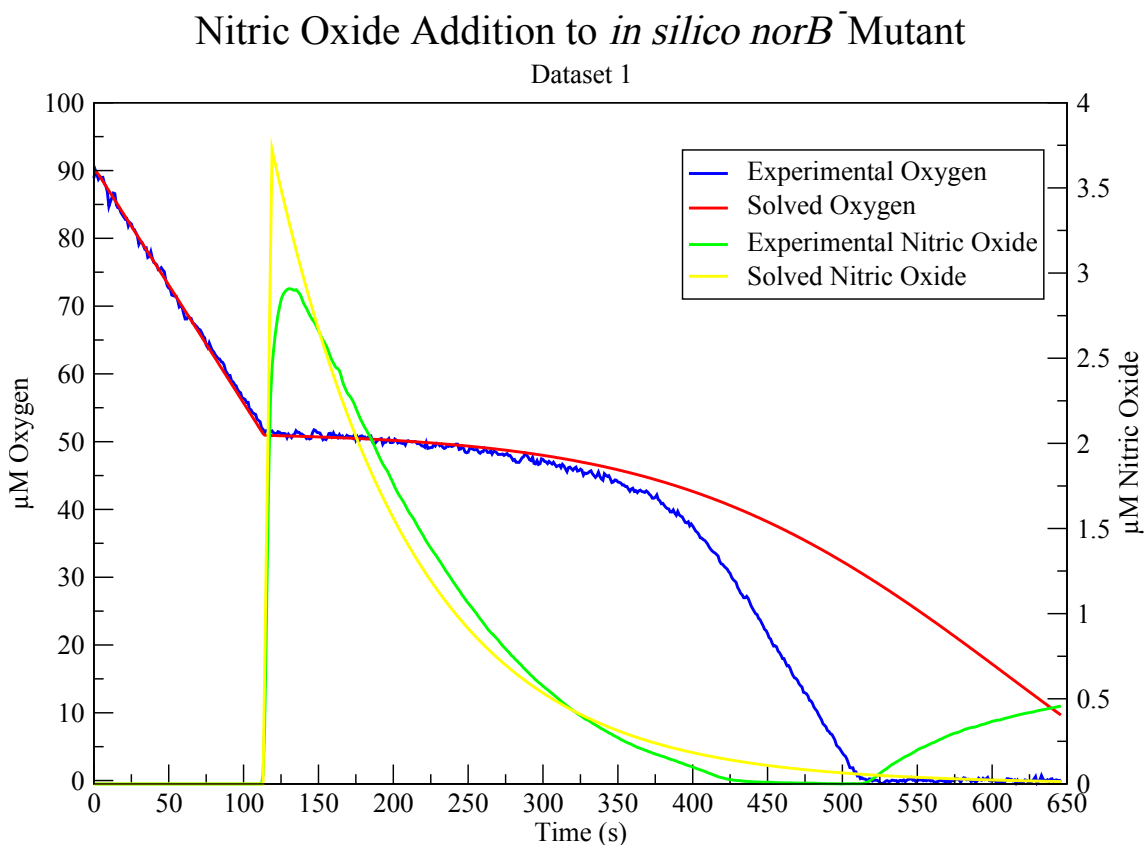


Figure 6.14: **Addition of Nitric Oxide to *in silico norB*⁻ mutant.** Solved output from an *in silico norB*⁻ mutant created by removing NorB from the simulation in Figure 6.11.

progresses. A plot showing these states can be seen in Figure 6.15. This figure shows that the reduction states of the enzymes are quickly adjusted to the correct steady state values (of the order of a few seconds) except for NorB, which seems to have a much slower rate of reduction. This slow rate of reduction means that the initial concentration of reduced NorB in the simulation is much more important, and should in fact be much closer to being in a completely reduced state at t_0 . In the datasets used this doesn't affect the outcome as there is sufficient time for NorB to become reduced before Nitric Oxide starts being reduced. The low rate of NorB reduction and the lack of convergence shown are probably due to a lack of information available in experimental datasets. The virtually instantaneous oxidation of NorB suggests that NorB is very good at reducing nitric oxide. The cytochrome pool appears to stay almost fully reduced throughout the entire simulation, as the rate of cytochrome reduction significantly outweighs the rate of oxidation by downstream components. The high rate of cbb_3 inactivation also means that upon addition of nitric oxide, $\approx 98\%$ of cbb_3 becomes inactivated instantaneously.

6.2 Aerobic Nitric Oxide Reduction in *nsrR⁻* mutant

The *nsrR⁻* mutant, which expresses NorB in an essentially constitutive manner was not effective in generating a usable dataset as it removed any NO almost instantaneously resulting in non-modellable dataset shown in Figure 6.16.

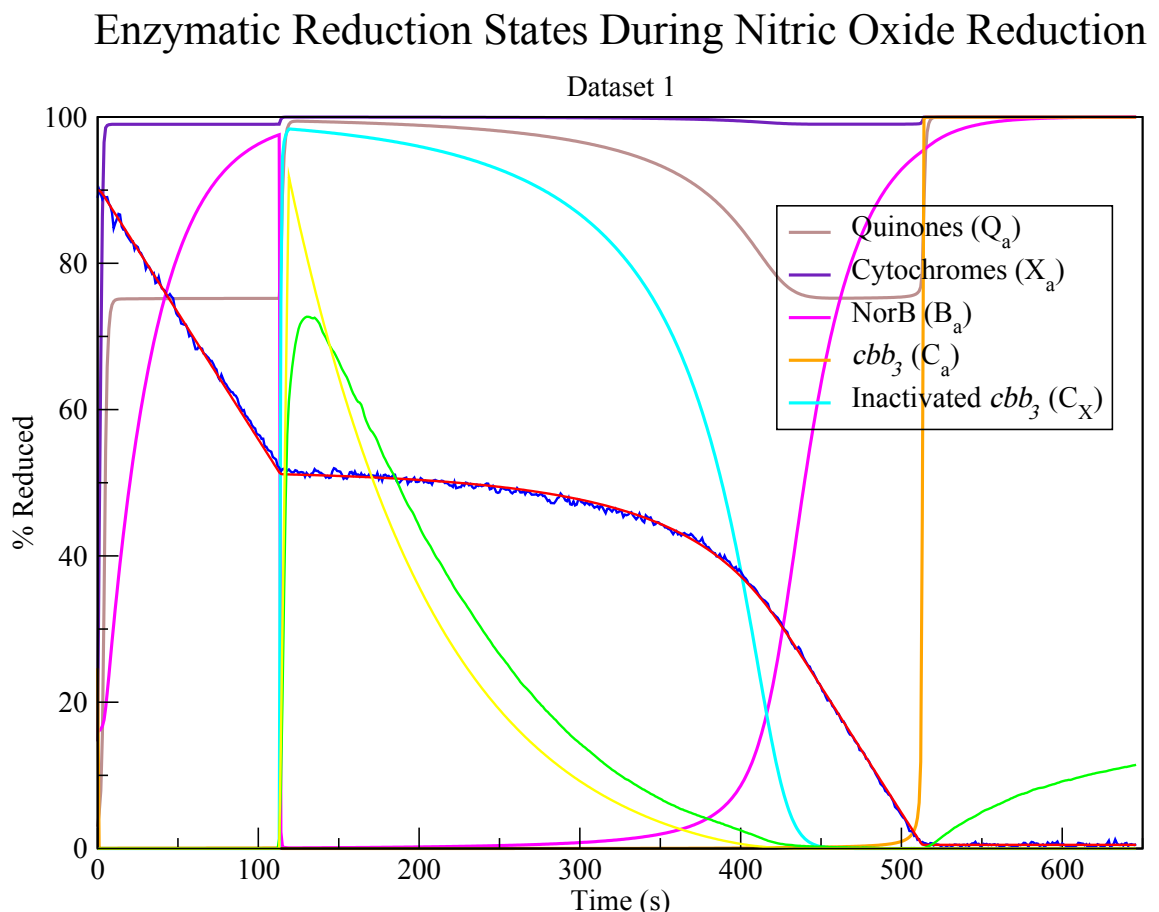


Figure 6.15: **Reduction States During Nitric Oxide Reduction.** This figure shows how the reduction states of the enzymes involved in respiration changes as the culture respires oxygen and then nitric oxide. The experimental and solved observed data are shown as thinner lines for reference.

Nitric Oxide Addition to *aniA*⁻*nsrR*⁻ Mutant

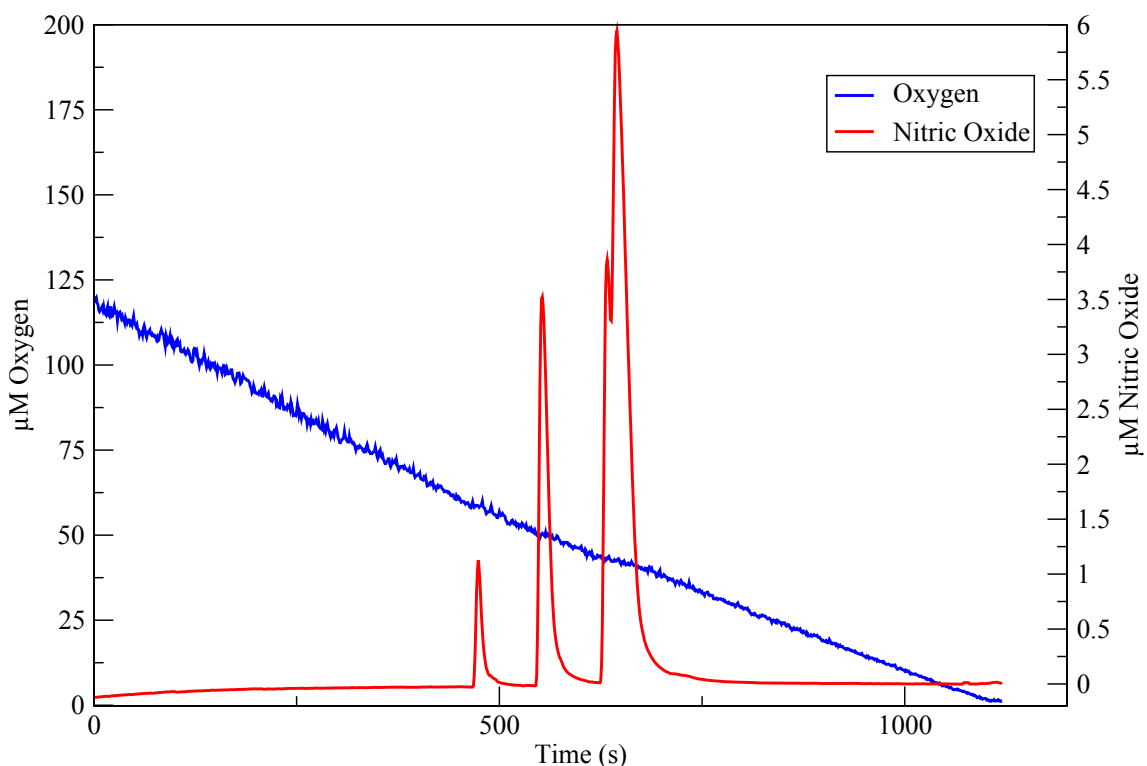


Figure 6.16: Nitric Oxide Reduction in an *nsrR*⁻ Mutant. This figure shows nitric oxide and oxygen reduction in an *aniA*⁻*nsrR*⁻ mutant. In this case the *aniA*⁻ mutation has no effect as no nitrite is being reduced. Addition of nitric oxide has only a very small effect on the rate of oxygen reduction as it is being removed very quickly by the constitutively expressed NorB.

Chapter 7

Nitrite Reduction in *N. meningitidis*

7.1 Microerobic Nitrite Reduction

7.1.1 Introduction

The last datasets to be used in the iterative approach to parameter estimation was of cultures able to respire nitrite in addition to oxygen. In these cultures nitrite was added to a culture already respiring oxygen to observe both the rate of nitrite reduction, and the effect on oxygen respiration caused by the production of nitric oxide. These datasets were the most complex in terms of the information contained within them and the number of model components needed to solve them. In addition to the components being used to model nitric oxide reduction, the nitrite reduction pathway is also active. The portions of the ETC relating to nitrite reduction are shown graphically in Figure 7.1. However since *Neisseria meningitidis* is incapable of growing anaerobically, in actual fact the entire pathway is required, using oxygen, nitric oxide and nitrite reduction.

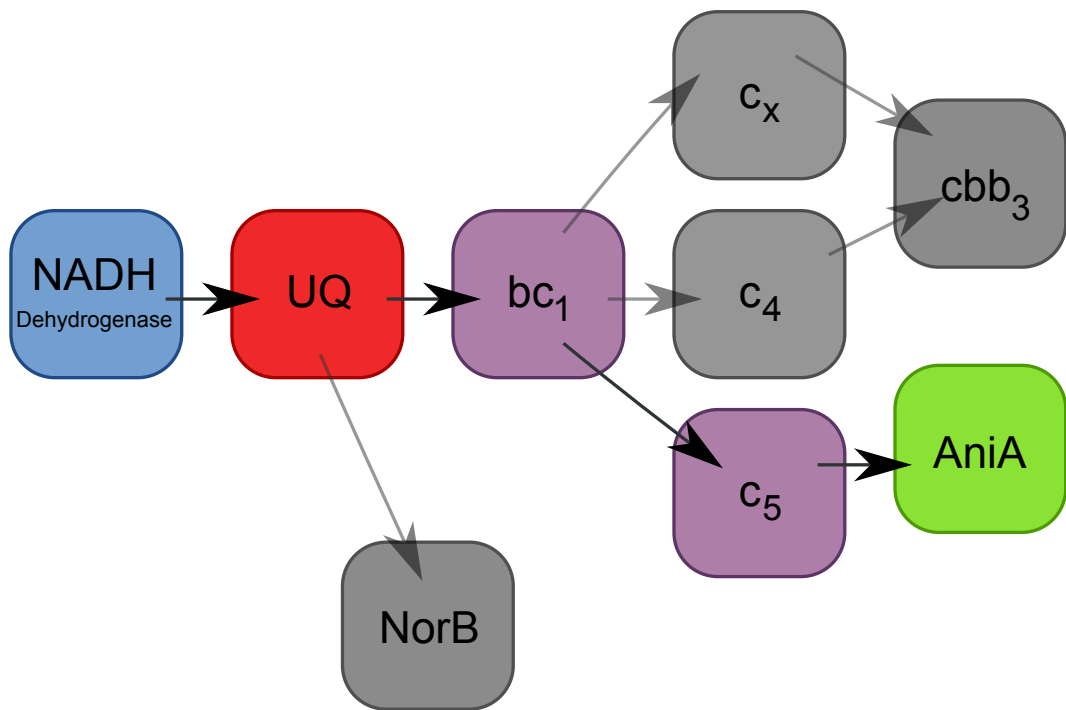


Figure 7.1: **Nitrite reducing electron transport chain of *N. meningitidis*.** This shows the complete electron transport chain of *Neisseria meningitidis* with the components irrelevant to nitrite reduction greyed out. In the mathematical model all of the purple elements (cytochromes) are amalgamated into one entity.

The equations that describe this portion of the ETC are:

$$\begin{aligned}
 \frac{d[O_2]}{dt} &= \beta(1 - [O_2]/K_O) - k_1[C_a][O_2] \\
 \frac{d[Q_a]}{dt} &= g([Q] - [Q_a]) - l_3[Q_a]([B] - [B_a]) - f[Q_a]([X] - [X_a]) \\
 \frac{d[X_a]}{dt} &= -k_3([C] - [C_a] - [C_X])[X_a] - m_3([A] - [A_a])[X_a] + f[Q_a]([X] - [X_a]) \\
 \frac{d[C_a]}{dt} &= k_3([C] - [C_a] - [C_X])[X_a] - k_1[C_a][O_2] - k_5[C_a][NO] + k_6[C_X] \\
 \frac{d[NO]}{dt} &= m_1[NO_2^-][A_a] - l_1[NO][B_a] - k_5[C_a][NO] + k_6[C_X] - \gamma[NO] \\
 \frac{d[NO_2^-]}{dt} &= -m_1[NO_2^-][A_a] \\
 \frac{d[C_X]}{dt} &= k_5[C_a][NO] - k_6[C_X] \\
 \frac{d[A_a]}{dt} &= m_3([A] - [A_a])[X_a] - m_1[NO_2^-][A_a] \\
 \frac{d[B_a]}{dt} &= l_3[Q_a]([B] - [B_a]) - l_1[NO][B_a]
 \end{aligned}$$

These equations describe the change in concentration of nitrite over time,

which is the experimentally observed value (in addition to the afore modelled oxygen and nitric oxide). Also modelled is the reduction state of AniA. This represents the complete mathematical model not including any transcriptional parameters.

7.1.2 Experimental Results

Generating datasets for Nitrite reduction could be performed in with two different cultures; an aerobic *NsrR* deficient mutant, or microaerobic wild-type. Microaerobic cultures appeared to grow very poorly during the course of this work and in most cases did not survive the transition from being in the incubator to being moved to the electrode chamber. Therefore an *nsrR*⁻ mutant was used instead of the wild-type. This mutant expresses AniA and NorB in a constitutive manner, removing the necessity for growing the cultures in microaerobic conditions. The cultures were grown in aerobic conditions until mid-log phase growth had been achieved. This corresponded to an OD_{600} of 0.3 – 0.9 and usually required an incubation period of roughly 3 hours. Once the required cell density had been obtained the culture was transferred to the electrode chamber, Sodium Nitrite was added to a concentration of 1 mM and the nitrite and oxygen concentrations recorded as the culture respiration. Unfortunately nitric oxide concentrations could not be recorded as the NO electrode had failed and could not be replaced.

In addition to the datasets obtained from *nsrR*⁻ mutant cultures, a further dataset was obtained from Rock et al.²⁰ which showed oxygen and nitric oxide concentrations in a microaerobic wild-type culture where nitrite is added part-way through aerobic respiration. The datasets generated and used for parametrisation of this portion of the model are shown in Figures 7.2 & 7.3.

The dataset in Figure 7.2 shows an *nsrR*⁻ mutant which has had 1 mM nitrite added at $t = 0$ s. Nitrite reduction proceeds linearly and at quite a high rate. Oxygen starts linearly but then slows down presumably as nitric oxide is produced

Nitrite and Oxygen Reduction in Microaerobic *Neisseria meningitidis*

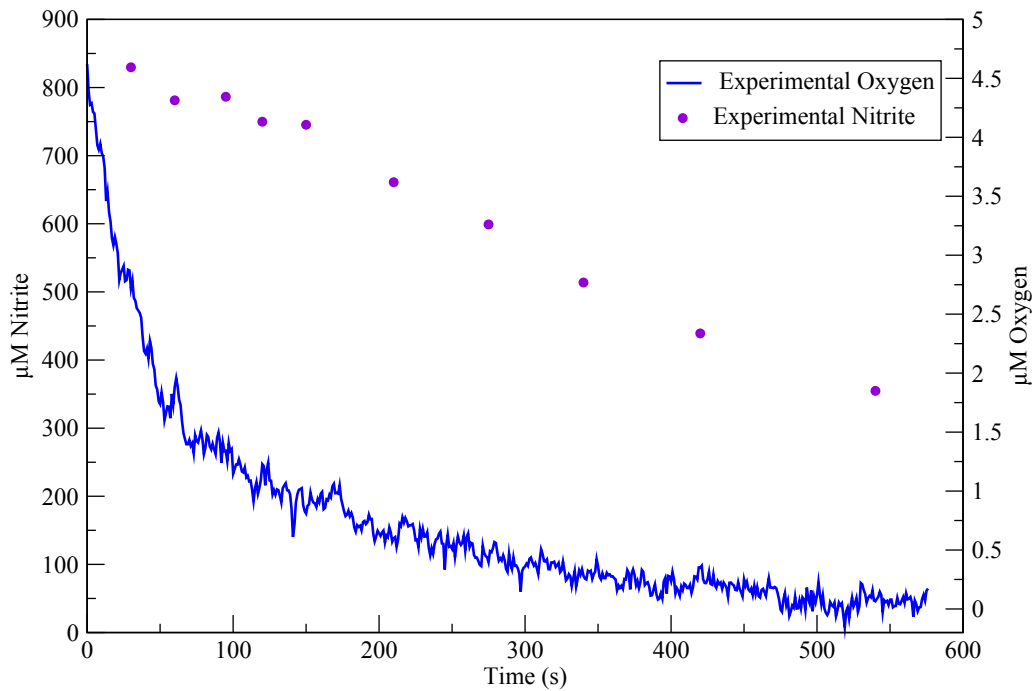


Figure 7.2: **Nitrite Reduction in *Neisseria meningitidis*.** This dataset shows the effect on oxygen respiration of nitrite respiration as nitric oxide is produced. This culture is an *nsrR*⁻ mutant which is expressing AniA and NorB in an essentially constitutive manner.

and inhibits *cbb*₃. It is also possible that given the high rate of nitrite reduction large quantities of nitric oxide are being produced which will react directly with oxygen as described in Chapter 6 affecting the rate of observed oxygen reduction.

The dataset in Figure 7.3 shows a wild-type culture grown in denitrifying conditions, so that it is expressing both AniA and NorB. Nitrite is added at time $t \approx 200$ s to a concentration of ≈ 1 mM (Moir, private communication). Upon nitrite addition a small decrease in oxygen respiration rate is observed, and a large increase in nitric oxide occurs as nitrite is reduced. Nitric oxide is then maintained at a fairly constant level until oxygen is fully reduced at which point a further increase in nitric oxide concentration is observed. It is posited that this final increase in NO concentration is because the electrons that were being pulled through the oxygen respiration pathway are now free to be drawn to AniA allowing more nitrite reduction to take place.

Addition of Nitrite to *Neisseria meningitidis* Respiring Oxygen

Cultures grown in denitrifying conditions

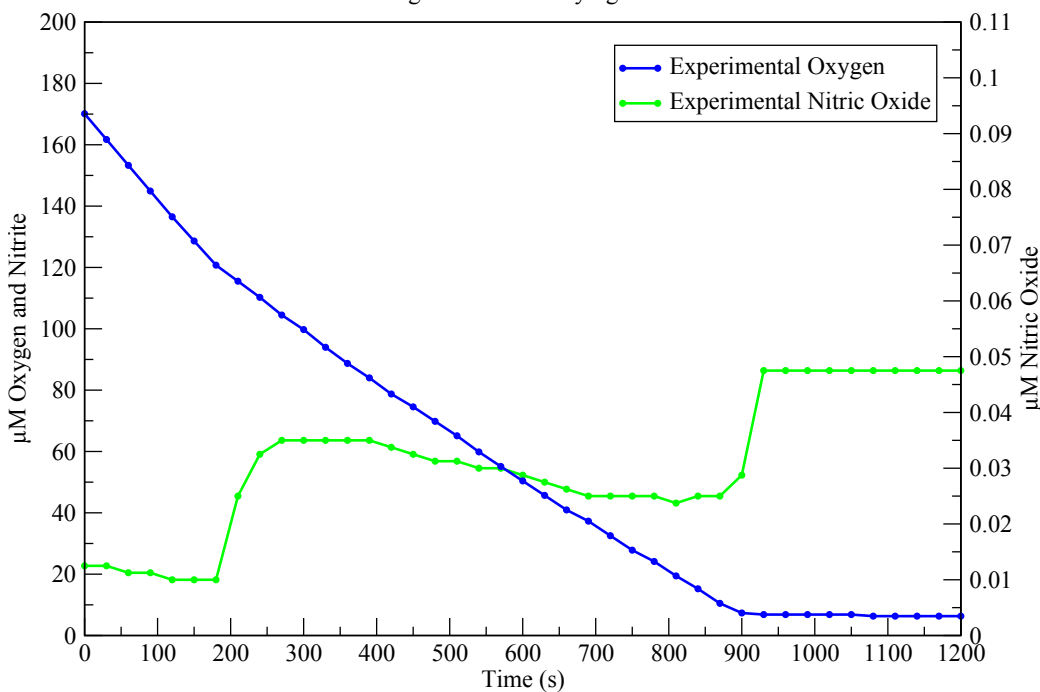


Figure 7.3: **Nitrite Reduction in *Neisseria meningitidis*.** This dataset shows the effect of nitrite addition to an aerobically respiring culture. Nitrite is added at 200 s. Oxygen and Nitric Oxide data-points are recorded with much less frequency than in previous datasets hence the inclusion of dots on the plot.

7.1.3 Prior Probability Distributions

As described previously all parameters must have an associated prior probability distribution. The posterior probability distributions from Chapter 6 were used as prior probability distributions in this chapter. Where new parameters were introduced, the distributions were generated based on published literature values which are noted in Chapter 3. When using literature values the prior probability distributions were generated according to the same scheme as in Chapter 5. The values required to create idealised lognormal probability distributions for each parameters are shown in Table 7.1.

The initial probability distributions used to start the Monte-Carlo runs are shown in Figure 7.4.

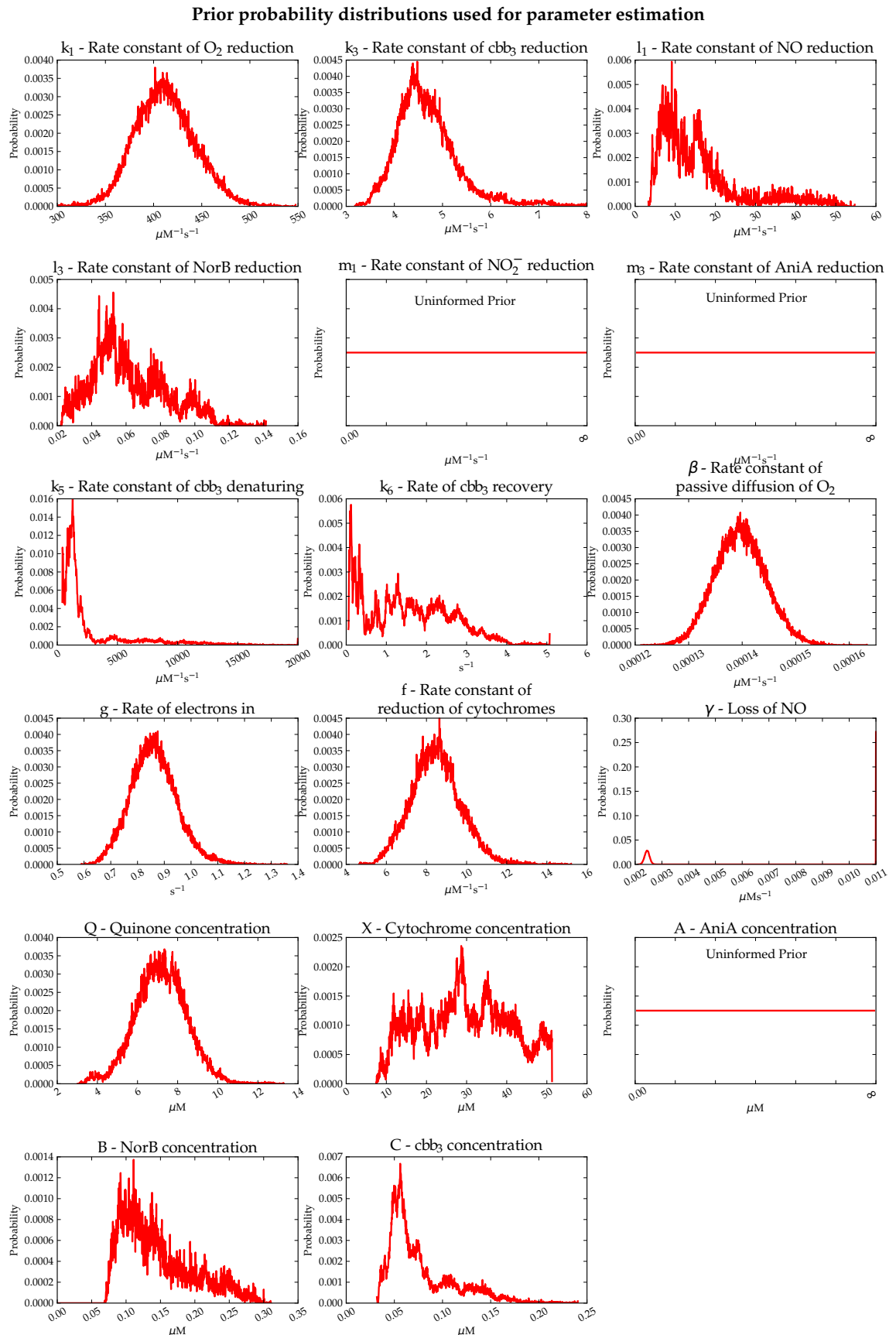


Figure 7.4: Prior probability distributions for microaerobic oxygen and nitrite reduction. These are the probability distributions used as priors by the parameter estimation algorithm.

Parameter	\bar{x}	σ
k_1	417.88 $\mu\text{M}^{-1}\text{s}^{-1}$	31.172
k_3	4.65 $\mu\text{M}^{-1}\text{s}^{-1}$	0.619
l_1	13.12 $\mu\text{M}^{-1}\text{s}^{-1}$	8.321
l_3	0.058 $\mu\text{M}^{-1}\text{s}^{-1}$	0.021
m_1	1 $\mu\text{M}^{-1}\text{s}^{-1}$	1
m_3	4.8 $\mu\text{M}^{-1}\text{s}^{-1}$	0.2
k_5	1741.8 $\mu\text{M}^{-1}\text{s}^{-1}$	1822.0
k_6	1.076 s^{-1}	1.473
β	0.00014 $\mu\text{M}^{-1}\text{s}^{-1}$	4.67×10^{-6}
g	0.857 s^{-1}	0.086
f	8.398 $\mu\text{M}^{-1}\text{s}^{-1}$	1.237
γ	0.00014 μMs^{-1}	4.67×10^{-6}
Q	7.06 μM	1.317
X	27.45 μM	12.08
A	0.137 μM	0.048
B	0.137 μM	0.048
C	0.071 μM	0.029

Table 7.1: **Prior Probability Table** This table shows the prior means and standard deviations used to create lognormal distributions to be used as the prior probability distributions.

Nitrite and Oxygen Reduction in Microaerobic *Neisseria meningitidis*

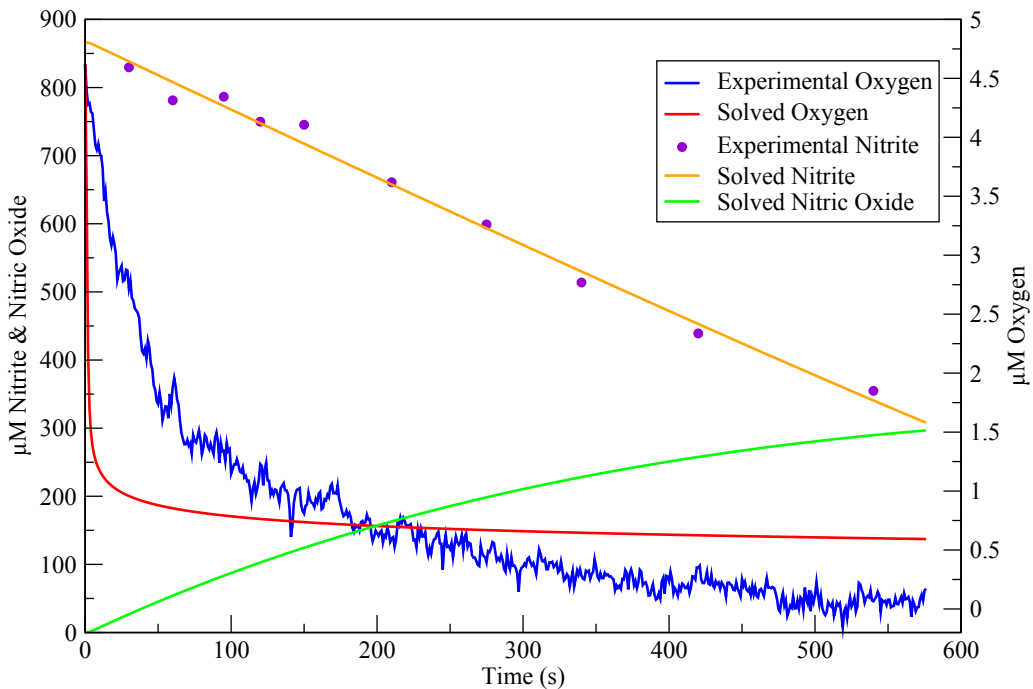


Figure 7.5: **Solved Nitrite Reduction in *Neisseria meningitidis*.** This figure shows the first attempt at fitting the model to experimental data. Nitrite reduction is being modelled well, whereas oxygen reduction is being modelled quite poorly as the solved data shows to high a rate of oxygen reduction. Nitric oxide is solved purely as a product of nitrite reduction and is not compared to any experimental data.

7.1.4 Parameter Estimation Results

The parameter estimation process was run in the same fashion as that described in Chapters 5 & 6. The 2 experimental datasets were run 20 times (each) for 20,000 iterations using the prior probability distributions shown in Figure 7.4. The solved output from datasets 1 and 2 are shown in Figures 7.5 and 7.7 respectively. Given the apparent poor fitting of the solved outputs shown in both of these figures, plots of the redox states for both of these datasets are shown in Figures 7.6 and 7.8.

The solved data shown in Figure 7.5 doesn't fit particularly well to the experimental data. Nitrite reduction appears to be modelled well as it is a simple linear reduction. Oxygen reduction however is modelled very poorly. The initial rate of oxygen consumption is too high, and the slowing of consumption is too abrupt. The halting of oxygen reduction is due to the amount of nitric oxide being pro-

Enzymatic Reduction States During Microaerobic Respiration

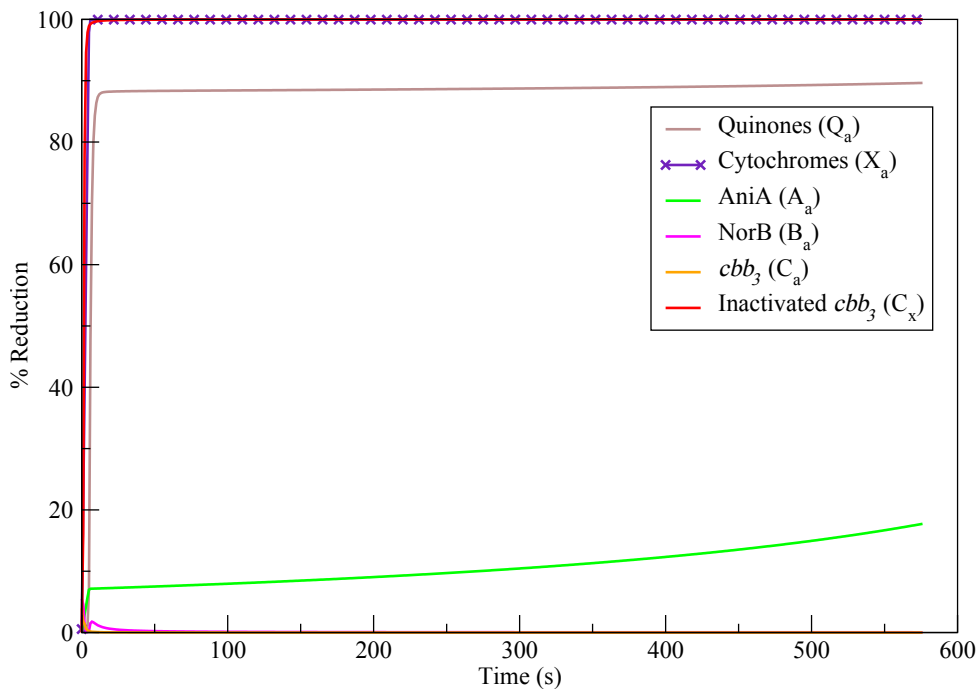


Figure 7.6: **Reduction States During Nitrite Reduction.** This figure shows how the reduction states of the enzymes involved in nitrite reduction change during respiration.

duced by the reduction of nitrite. This level of nitric oxide quickly inhibits the cbb_3 totally as can be seen by the high concentration of NO in Figure 7.5 and in the redox plot in Figure 7.6. The redox plots show that essentially all the electrons in the system are flowing to the nitrite reduction pathway. Nitric oxide is progressing as fast as possible based on the electron flow into NorB. NorB stays in a permanently oxidised state suggesting that the reduction activity of NorB is faster than the rate of reduction of NorB itself. The level of NorB is also not easily modelled correctly using this data as no information is available about the actual levels of nitric oxide being produced during nitrite reduction.

The solved data in Figure 7.7 appears to fit oxygen reduction quite well but fails to fit nitric oxide reduction almost entirely. The most significant feature, that nitric oxide should increase when oxygen reduction ceases is missing. The redox state plot in Figure 7.8 suggests the reason for the lack of this feature. The cytochromes appear to be in a completely reduced state shortly after the start of the

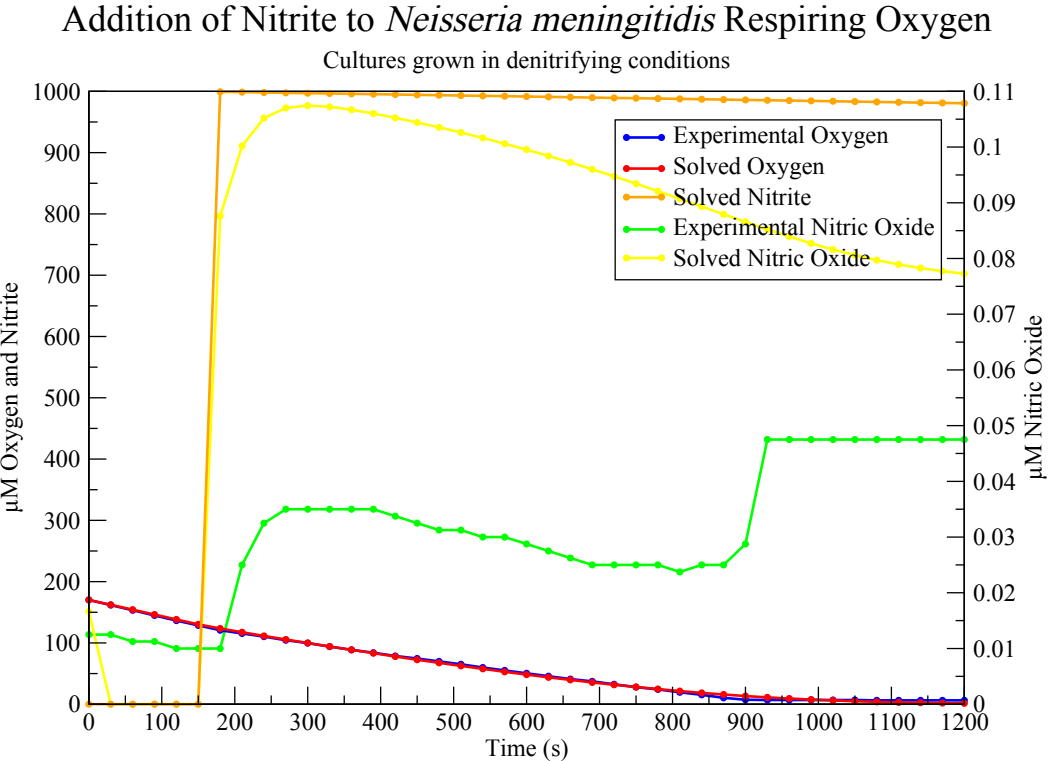


Figure 7.7: **Effect of Nitrite Addition on Aerobically Respiring Cultures.** This figure shows the first attempt at fitting the model to experimental data. Oxygen respiration appears to be modelled quite well, but nitric oxide is being modelled particularly badly. The most significant feature of the nitric oxide dataset is absent in the solved data.

simulation. This permanently reduced state means that when oxygen reduction ceases there is essentially no difference to the flow of electrons to either NorB or AniA. This suggests that parameters g and f , the reduction of cytochromes and the reduction of the quinone pool are too high, leading to the permanent reduction of both those components. The nitrite levels are equally difficult to model as nitric oxide in the previous dataset as the levels are unknown.

The posterior probability distributions for the above results are not shown here as they do not provide any useful information at this point.

7.1.5 Second Parameter Estimation Results

A second attempt was made to try and better fit the solved data to the experimental data by adapting the priors for dataset 2 using knowledge from the previous parameter estimation attempt. The prior probability distributions for dataset 2

Enzymatic Reduction States During Microaerobic Respiration

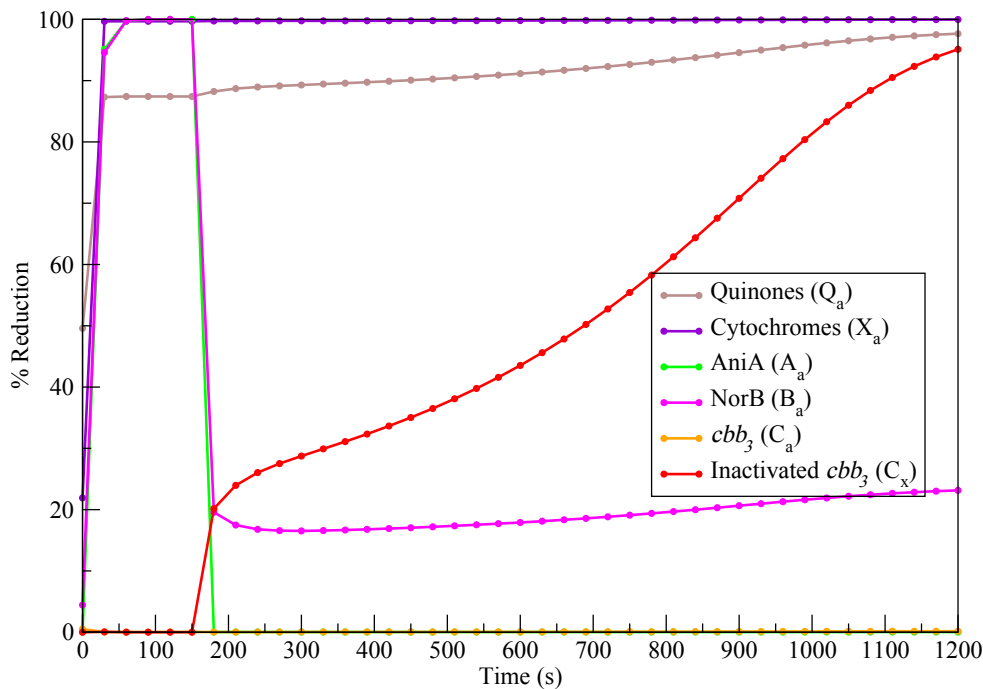


Figure 7.8: **Reduction States During Nitrite Reduction.** This figure shows how the reduction states of the enzymes involved in nitrite reduction change during respiration.

were altered such that the means of f and g were reduced 10 fold, and the distributions were broadened significantly. Additionally the m_3 rate constant prior distribution was set correctly as in the previous round it was erroneously set to have a uniform prior. The other distributions were left unchanged. The new prior probability distributions are shown in Figure 7.9.

The new prior probability distributions proved to be difficult for the parameter estimation system to use, as out of 10 runs only 2 produced reasonable fitted data. One of these fits is shown in Figure 7.10. This shows a vastly improved fit over Figure 7.7. Oxygen is being modelled almost perfectly, and the major features of the nitric oxide data are also qualitatively present. In addition, the similarity between the oxygen reduction rates and nitrite reduction rates is corroborated by Rock et al.²⁰ who showed that under denitrifying conditions nitrite reduction rate should roughly equal oxygen reduction rate.

The redox state plot shown in Figure 7.11 shows how the change in substrate

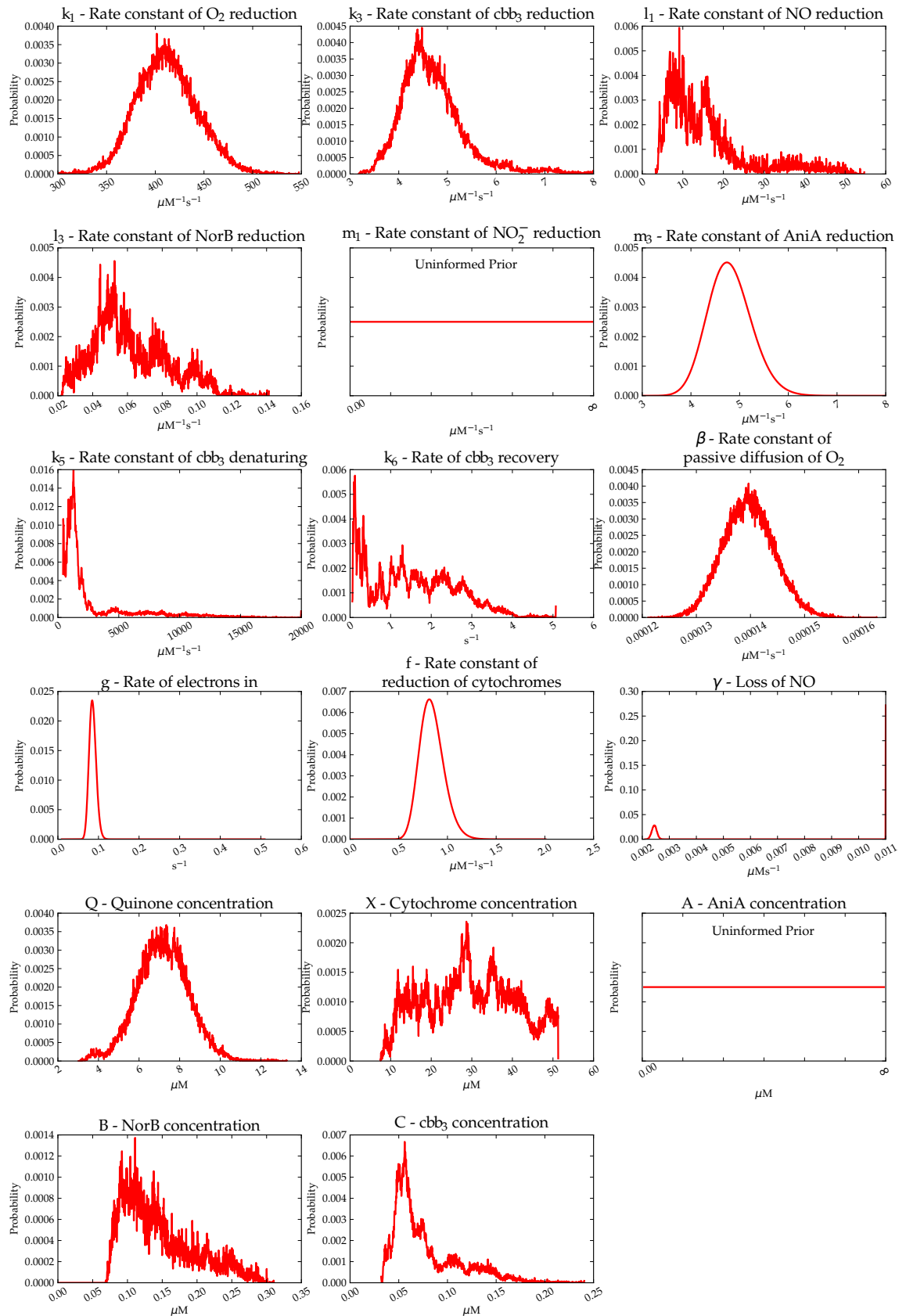
Prior probability distributions used for parameter estimation


Figure 7.9: Prior probability distributions for microaerobic oxygen and nitrite reduction. These are the modified probability distributions used as priors by the parameter estimation algorithm.

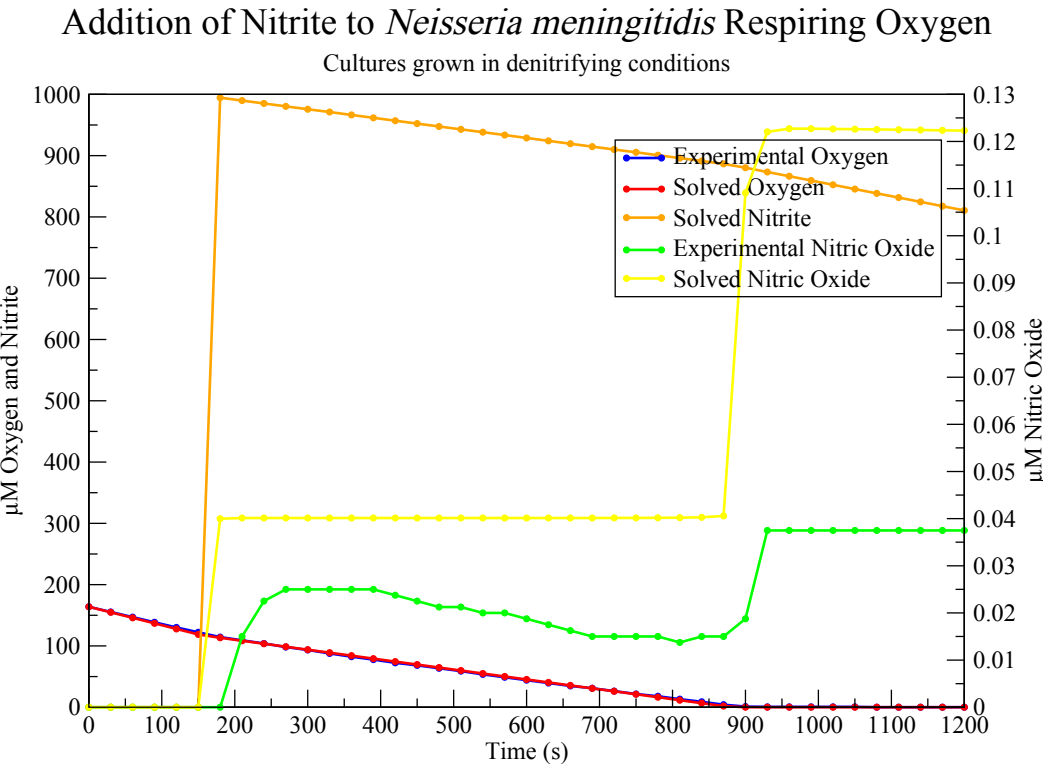


Figure 7.10: **Effect of Nitrite Addition on Aerobically Respiring Cultures.** This figure shows the second attempt at fitting the model to experimental data. Oxygen respiration appears to be modelled well. Nitric oxide production is being modelled well qualitatively, as the major features of the experimental data are present. Clearly though further rounds of parameter estimation are in order to improve the quantitative fit.

reduction has come about. The cytochrome and quinones are no longer in a permanently reduced state, and once oxygen is depleted NorB is able to access some of the electrons that were previously directed towards *cbb₃*, causing the increase in nitric oxide concentration. Additionally the cytochrome pool increases its overall reduction state once oxygen is depleted, as one of the sinks for electrons is no longer active, this also has a small effect on the reduction state of AniA which increases due to the larger supply of upstream electrons available to it. The increase in electrons available to AniA also causes an increase in the rate of nitrite reduction. The more marked reduction state change of the quinone pool once the culture starts respiration nitrite is partially corroborated by data obtained by Otten et al.¹⁵⁵. They found that the reduction state of the quinone pool in *Paracoccus* should differ between aerobic respiration and denitrification, however in their experiments “denitrification” was simulated by knocking out the *bc₁* complex,

Enzymatic Reduction States During Microaerobic Respiration

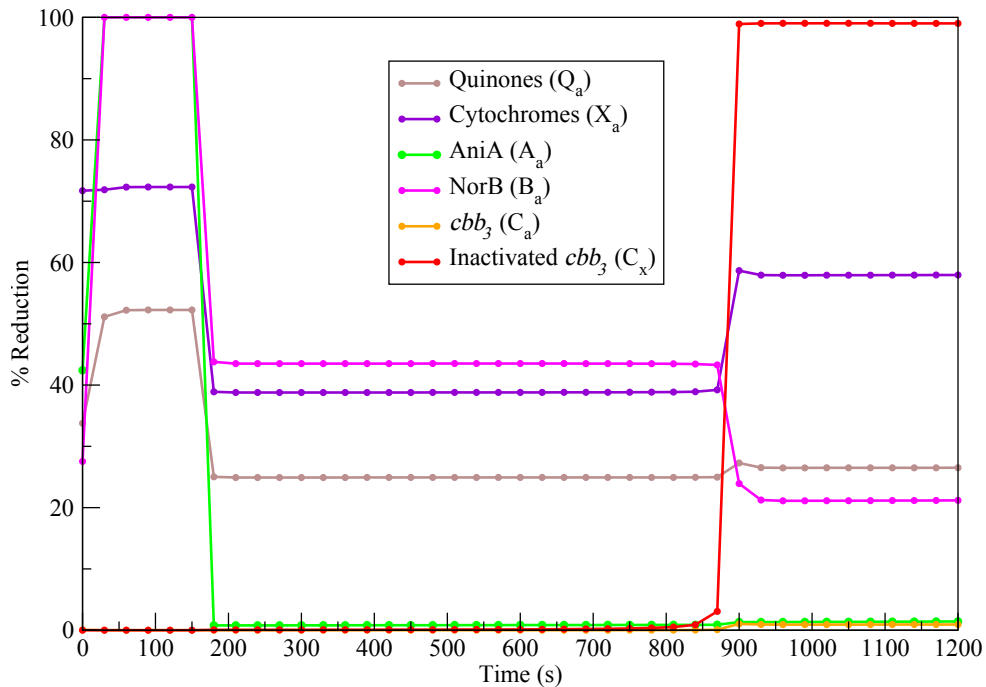


Figure 7.11: **Reduction States During Nitrite Reduction.** This figure shows how the reduction states of the enzymes involved in nitrite reduction change during respiration.

the equivalent of stopping oxygen and nitrite reduction in *Neisseria meningitidis* while leaving the quinol reductase (NorB in *N. meningitidis*) intact. Their results showed that the quinone pool should become *more* reduced under “denitrifying” conditions not less. This discrepancy may be related to the difference in organisms and could indicate more complex interactions between the components in *Neisseria meningitidis*.

The posterior probability distributions generated from this second attempt at parameter estimation are shown in Figure 7.12. These were generated only from the two Markov Chains that produced simulation output that qualitatively matched the input data. The other Markov Chains settled on solved output which did not have the correct dataset features.

The idealised lognormal distribution parameters that fit the posterior probability distributions are shown in Table 7.2 and compared to the prior probability distributions.

As can be seen from Table 7.2 and Figure 7.12 most of the rate constant proba-

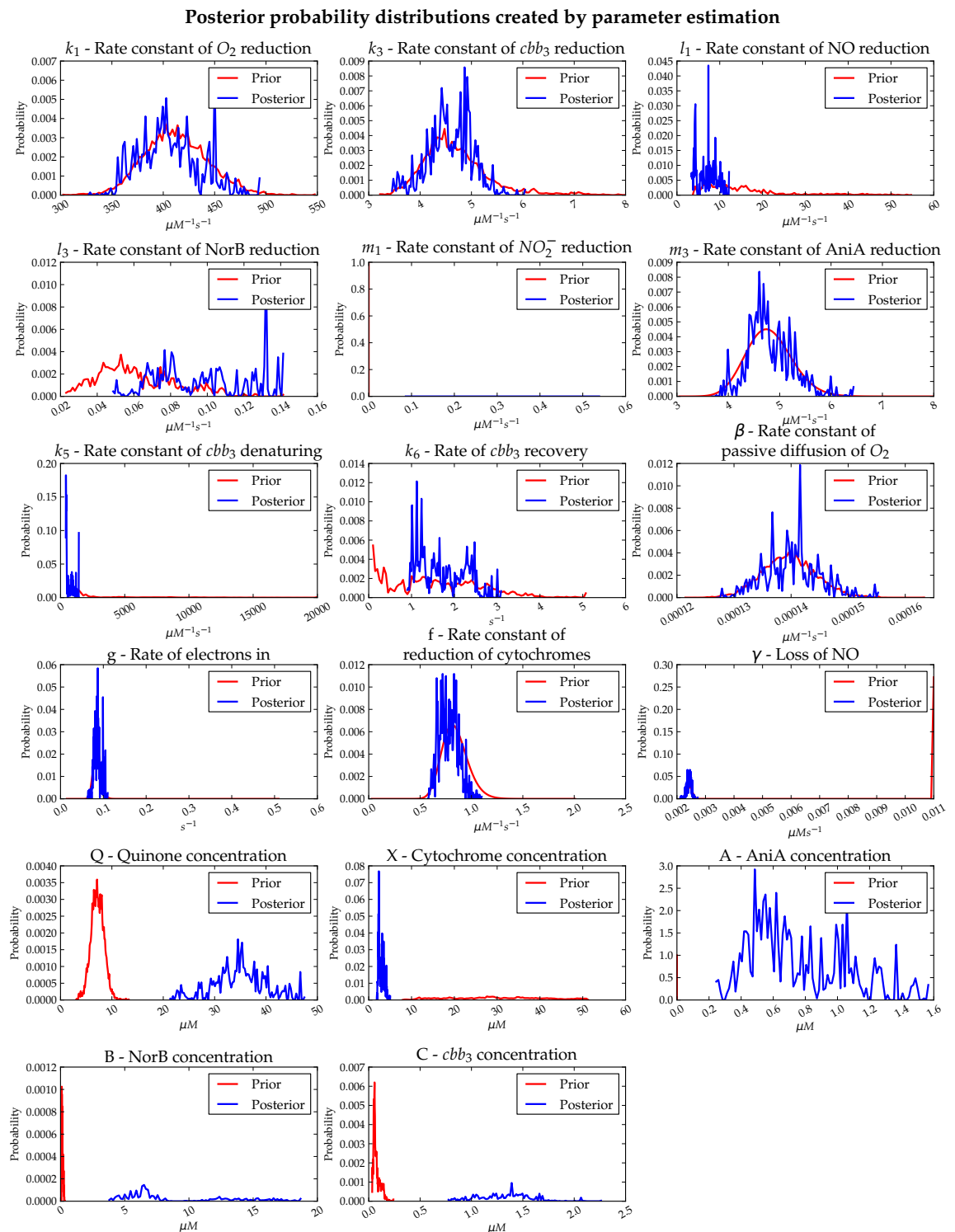


Figure 7.12: Posterior probability distributions for microaerobic oxygen and nitrite reduction. These are the final posterior probability distributions generated by the parameter estimation system for microaerobic oxygen and nitrite reduction, all concentrations have been normalised to assume an OD₆₀₀ of 1.

Parameter	Priors		Posteriors	
	\bar{x}	σ	\bar{x}	σ
$k_1 (\mu\text{M}^{-1}\text{s}^{-1})$	417.88	31.172	403.51	27.59
$k_3 (\mu\text{M}^{-1}\text{s}^{-1})$	4.65	0.619	4.58	0.436
$l_1 (\mu\text{M}^{-1}\text{s}^{-1})$	13.12	8.321	6.42	2.33↓
$l_3 (\mu\text{M}^{-1}\text{s}^{-1})$	0.058	0.021	0.096	0.025
$m_1 (\mu\text{M}^{-1}\text{s}^{-1})$	1	1	0.175 ↓	0.087
$m_3 (\mu\text{M}^{-1}\text{s}^{-1})$	4.8	0.2	4.79	0.042
$k_5 (\mu\text{M}^{-1}\text{s}^{-1})$	1741.8	1822.0	138.66 ($\gamma = 399.86$)	338.18↓
$k_6 (\text{s}^{-1})$	1.076	1.473	1.59	0.527
$\beta (\mu\text{M}^{-1}\text{s}^{-1})$	0.00014	4.7×10^{-6}	0.00014	4.7×10^{-6}
$g (\text{s}^{-1})$	0.857	0.086	0.085	0.0078↓
$f (\mu\text{M}^{-1}\text{s}^{-1})$	8.398	1.237	0.771 ↓	0.096↓
$\gamma (\mu\text{Ms}^{-1})$	0.0024	9×10^{-5}	0.0024	8.8×10^{-5}
$Q (\mu\text{M})$	7.06	1.317	34.31 ↑	5.49↑
$X (\mu\text{M})$	27.45	12.08	2.81 ↓	0.595↓
$A (\mu\text{M})$	0.137	0.048	0.704 ↑	0.3↑
$B (\mu\text{M})$	0.137	0.048	7.80 ↑	3.63↑
$C (\mu\text{M})$	0.071	0.029	1.3 ↑	0.259↑

Table 7.2: Posterior Probability Statistics. This table shows the parameters required to create lognormal distributions that describe the prior and posterior probability distributions. The values for the priors are as in Table 7.1. The posterior distributions were generated from dataset 2, and where they relate to concentrations, these have been normalised. The lognormal distributions represent best-fits to the actual posterior distributions. Where there are significant differences between the prior and posterior values for either the mean or standard deviation, these are indicated by ↑ and ↓. Where a γ value is shown in brackets it means that a 3 parameter lognormal had to be used, and γ is the location parameter for the distribution.

Parameter	R Statistic	Parameter	R Statistic
k_1	1.07	g	1.03
k_3	1.06	f	2.27
l_1	1.30	γ	1.02
l_3	2.89	Q	2.31
m_1	3.47	X	2.39
m_3	1.14	A	2.39
k_5	2.11	B	5.64
k_6	1.76	C	1.59
β	1.01		

Table 7.3: **Gelman-Rubin Convergence Statistic.** This table shows the Gelman-Rubin Convergence statistic for the two Markov chains from dataset 2. For parameters which are concentrations, the statistic relates to the values after normalisation (data is normalised based on initial oxygen reduction rate).

bility distributions have remained fairly stationary throughout the multiple rounds of parameter estimation (from Chapters 5 & 6). The distribution of l_1 has narrowed towards the lower end of the prior bounds. The distributions of f and g are almost identical to their modified prior distributions with very little deviation. The concentration distributions however have all been modified significantly from their prior distributions.

7.1.6 Analysis of Convergence

The Gelman-Rubin R statistics were calculated for the Monte-Carlo trajectories for each parameter and these are presented in Table 7.3. These values show very high levels of convergence for all parameters, however it should be noted that these values may not be truly representative as in fact only 2 trajectories are being analysed here since these were the only ones that produced usable output.

7.1.7 Analysis of Correlation

Correlation analysis was performed on each of the parameters using the Monte-Carlo trajectories as in Chapters 5 and 6. The upper-triangle matrix is shown in Figure 7.4. There are quite a few cross correlations between parameters in this dataset, although they are all classed as “moderate” rather than “high”. There are some obvious correlations such as the concentration of AniA and the reduction rate constant of Nitrite being negatively correlated, and that AniA and cbb_3 are negatively correlated to the concentration of cytochromes. This is explained by the fact that the more cytochromes, the faster AniA and cbb_3 can be reduced which means fewer are required to maintain the same level of substrate reduction. Interestingly cbb_3 and rate of reduction of oxygen do not appear to be correlated at all. This is most likely due to the fact that the reduction rate constant of oxygen by cbb_3 is so high that any oxygen is reduced almost instantaneously meaning that changes in that rate constant make very little difference if the concentration of cbb_3 is changed.

7.1.8 Discussion

The parameter estimates generated from this new set of data are capable of modelling experimental data particularly well, even if only in a qualitative manner. It also shows that the initial prior estimates for the values of f and g were (at least) an order of magnitude too high. These estimates were generated very early on in the modelling process during a trial-and-error period trying to find values that made sense biologically yet also allowed the model to fit the data. Impressively these initial values worked very well for most of the datasets where the nitrite pathway way was not being employed, and it only became obvious in the later sets that these values were too high. The nitrite datasets shows that the rate of flow of electrons into the system was too high causing the cytochromes and quinone pool to stay in a permanently reduced state leading to very little change in enzyme activity when substrates were added or were depleted. The

	k_1	k_3	l_1	l_3	m_1	m_3	k_5	k_6	β	g	f	γ	Q	X	A	B	C
k_1	1	0.02	0.19	0.01	-0.11	0.05	0.24	-0.03	0.05	-0.10	-0.07	0.03	0.21	-0.07	0.12	0.01	-0.02
k_3		1	-0.03	0.31	-0.30	-0.05	0.17	-0.04	0.05	0.03	-0.19	-0.01	0.21	-0.48	0.44	-0.14	0.25
l_1			1	-0.21	0.15	0.22	0.36	-0.13	-0.01	-0.20	-0.02	0.01	0.05	0.43	-0.07	0.60	-0.34
l_3				1	-0.52	-0.25	0.33	-0.14	0.04	0.17	-0.34	-0.09	0.36	-0.49	0.61	-0.67	0.46
m_1					1	-0.10	-0.53	-0.12	-0.02	-0.04	0.46	0.06	-0.72	0.64	-0.75	0.26	-0.52
m_3						1	0.06	0.15	0.06	0.18	0.00	0.06	0.02	-0.03	-0.13	0.34	0.02
k_5							1	-0.46	0.03	-0.13	-0.41	0.02	0.53	-0.35	0.60	0.01	0.43
k_6								1	-0.09	0.17	0.22	-0.03	-0.11	0.00	-0.07	0.06	-0.06
β									1	0.13	-0.01	-0.03	0.05	-0.07	0.06	-0.06	-0.03
g										1	0.06	0.0	-0.19	-0.25	0.17	-0.25	0.12
f											1	0.01	-0.51	0.23	-0.42	0.28	-0.23
γ												1	-0.05	0.01	-0.02	0.14	0.02
Q													1	-0.52	0.78	-0.16	0.24
X														1	-0.74	0.48	-0.77
A															1	-0.33	0.61
B																1	-0.36
C																	1

Table 7.4: **Regression Analysis of Nitrite Reduction Parameters for Dataset 2.** This table shows the r values from linear regression analysis on the combined parameter trajectories for nitrite reduction. Parameters with high correlation have been coloured green ($R > 0.8$) and those with moderation correlation have been coloured orange ($0.8 > R > 0.3$).

enzymes essentially had an unlimited supply of readily available electrons from both sources. Reducing the rate of both flow of electrons into the system, and the flow from the quinone pool to the cytochromes caused a massive change in the behaviour of the system as neither could be maintained in a fully reduced state. This completely altered the dynamics of the system as there was now true competition for electrons from the quinone pool and the cytochromes. The model became capable of modelling, in a qualitatively correct manner, the behaviour of the system when substrates were added and became depleted. Perhaps more impressively, none of the other rate constants needed to change, although the concentrations of the various enzymes were altered. Additionally the simple change of reducing the flux of electrons through the system actually brought the reduction states of the quinones and cytochromes into line with what was already published in the literature ($\approx 50\%$ reduced)¹⁵⁵.

7.1.8.1 Using Nitrite Posterior Parameters on Previous Datasets

To further investigate the posteriors generated from parameter estimation, the best parameters that produced the output shown in Figure 7.10 were used to create solved datasets for aerobic oxygen respiration, and for the addition of nitric oxide and compared against their equivalent experimental datasets. The enzyme concentrations were all scaled to match their respective datasets, and the solver was run using those parameters (no parameter estimation was performed). The results from these simulations are shown in Figures 7.13, 7.14 and 7.15.

Figure 7.13 shows the results of a simulation using the parameters obtained from nitrite parameter estimation compared to a simple aerobic oxygen reduction dataset. The concentration parameters have been appropriately scaled to match the experimental dataset (normalised based on observed oxygen reduction rate). The overall rate is too slow, however the simulation shows the same high affinity feature as the experimental dataset even with the reduced electron flux through the system. The difference in reduction rate is highly likely to be caused by the

Aerobic Oxygen Fitting Using Nitrite Posteriors

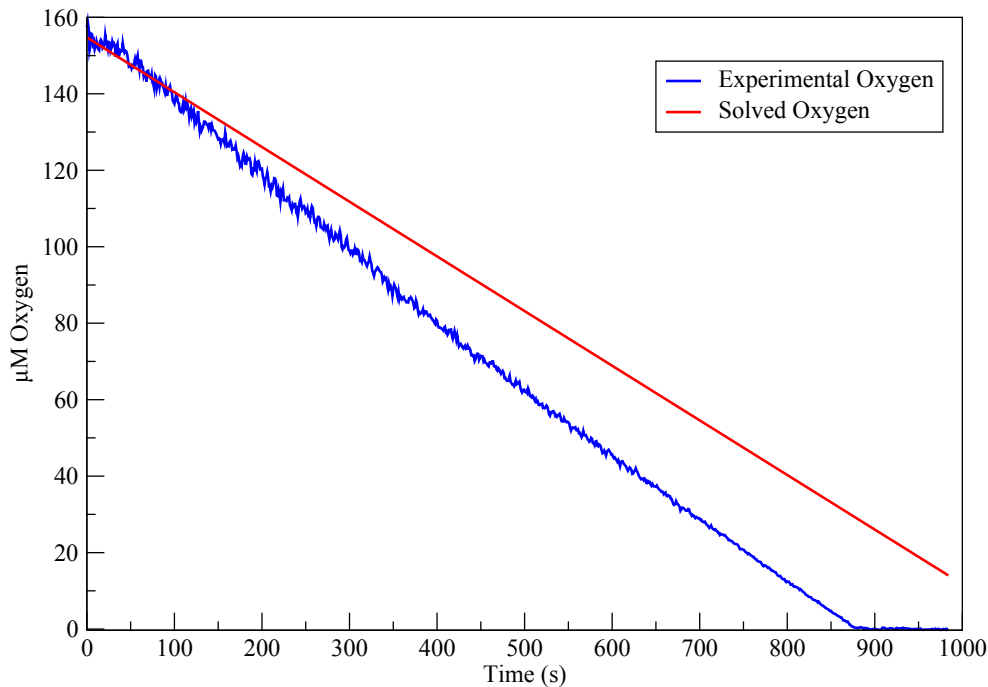


Figure 7.13: Aerobic Oxygen Respiration with Nitrite Posteriors. This figure shows the simulation results using the posteriors from nitrite parameter estimation with appropriately scaled concentrations.

incomplete decoupling of cell culture density from other parameters.

Figure 7.14 shows the results of a simulation using the parameters obtained from nitrite parameter estimation compared to an aerobic oxygen reducing dataset where nitric oxide is added. The concentration parameters have been scaled appropriately to match the experimental dataset (as above). The concentration of NorB was altered further because this experimental dataset was not grown in microaerobic conditions and will not be expressing a high level of NorB. Thus NorB concentration was reduced to a value of $0.01 \mu\text{M}$. This was required to achieve a reasonable fit for the removal of nitric oxide. If the parameter obtained from nitrite fitting was used the nitric oxide was removed almost instantaneously. Additionally in order to produce a similarly shaped oxygen reduction curve, the value of k_5 , the rate constant of cbb_3 inhibition by nitric oxide, had to be increased by $\approx 660\times$. This was required to reduce the rate of oxygen reduction to a suitable rate while there was nitric oxide present. The result is another qualitatively

Aerobic Nitric Oxide Addition Using Nitrite Posteriors

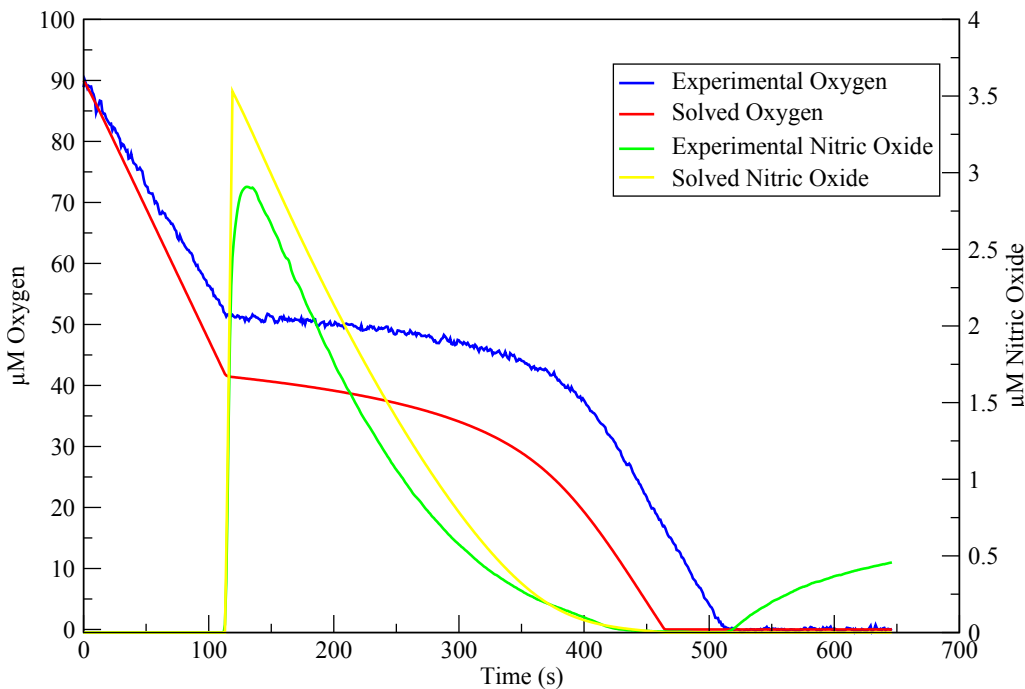


Figure 7.14: Aerobic Oxygen Respiration with Nitric Oxide Addition with Nitrite Posteriors. This figure shows the simulation results using the posteriors from nitrite parameter estimation with appropriately scaled concentrations. The concentration of NorB (B) had to be reduced significantly to obtain a similar nitric oxide reduction rate, and the value of k_5 had to be increased 66x to create a similarly shaped oxygen reduction curve.

correct fit to the experimental data. The discrepancies again may be related to incorrect density decoupling.

Figure 7.15 shows the results of a simulation using the nitrite posteriors with the same modification to k_5 as described for Figure 7.14, to assess the difference it makes to the original result shown in Figure 7.10. The oxygen and nitrite results are almost identical, only the nitric oxide shows any significant change. The qualitative result is still very good as there is still an increase in nitric oxide concentration after oxygen runs out, however the change is much more sigmoidal than in the original simulation. This may not necessarily be a problem however as the original experimental data is of low resolution and would be incapable of capturing a more curved increase in nitric oxide concentration. It is highly likely in fact that both increases in nitric oxide concentration, after nitrite addition and after oxygen depletion are much more curved than the experimental data would

Nitrite Reduction Using Nitrite Priors

With modified k_5 value from nitric oxide dataset

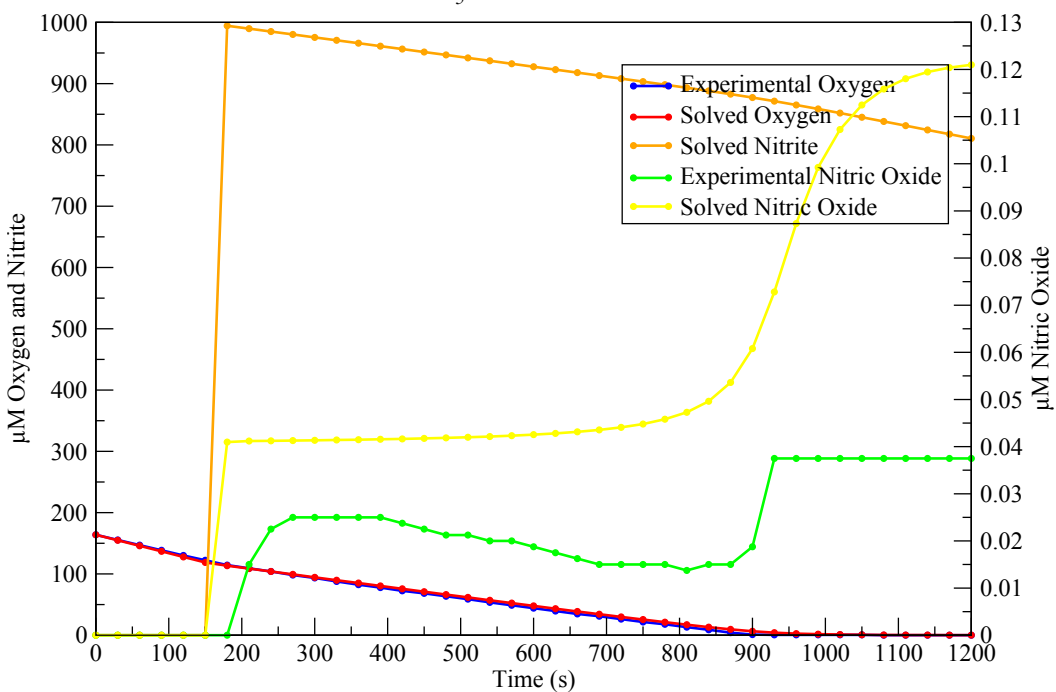


Figure 7.15: Nitrite Reduction using Modified Nitrite Postiors. This figure shows the simulation results of the nitrite reduction dataset using the modified value of k_5 as described for Figure 7.14. The change has not hugely affected the result except for making the increase in nitric oxide concentration when oxygen runs out a lot less sharp. This however may be closer to the *in vivo* result. The experimental data is of a low enough resolution that it is very difficult to tell.

suggest.

The fact that the value of k_5 can increase by such a large amount and only have such a limited effect on the outcome is due to the fact that the original parameter estimation results tended towards lower values where the probability was higher (as dictated by the priors). However increasing the value for k_5 would have had very little difference because the nitric oxide would be acting on vanishingly small concentrations of reduced cbb_3 since it spends most of its time in a fully oxidised state. In this case the posterior distribution is a little misleading as the value of this parameter actually has very little effect on the outcome of the simulation.

Chapter 8

Discussion and Completed Model

From Chapter 1, the stated aims of this thesis were:

1. **Construct a mathematical model of the *N. meningitidis* respiratory chain.**
This will involve the conversion of the kinetic reactions involved in respiration into mathematical equations that can be linked together, and if justified simplifying the chain.
2. **Obtain experimental data on respiratory rates and enzyme kinetics.** This will involve performing experiments on respiring *N. meningitidis* and recording the concentrations of respiratory substrates under different conditions.
3. **Parametrise the model using experimental data.** To do this a system will need to be developed which can iteratively fit experimental data to specific parts of the mathematical model.

With reference to the above, a mathematical model was constructed as described in Chapter 3, the equations shown below:

$$\begin{aligned}
 \frac{d[O_2]}{dt} &= \beta(1 - [O_2]/K_O) - k_1[C_a][O_2] \\
 \frac{d[NO]}{dt} &= m_1[NO_2^-][A_a] - l_1[NO][B_a] - k_5[C_a][NO] + k_6[C_X] - \gamma[NO] \\
 \frac{d[NO_2^-]}{dt} &= -m_1[NO_2^-][A_a] \\
 \frac{d[Q_a]}{dt} &= g([Q] - [Q_a]) - l_3[Q_a]([B] - [B_a]) - f[Q_a]([X] - [X_a]) \\
 \frac{d[X_a]}{dt} &= -k_3([C] - [C_a] - [C_X])[X_a] - m_3([A] - [A_a])[X_a] + f[Q_a]([X] - [X_a]) \\
 \frac{d[C_a]}{dt} &= k_3([C] - [C_a] - [C_X])[X_a] - k_1[C_a][O_2] - k_5[C_a][NO] + k_6[C_X] \\
 \frac{d[C_X]}{dt} &= k_5[C_a][NO] - k_6[C_X] \\
 \frac{d[A_a]}{dt} &= m_3([A] - [A_a])[X_a] - m_1[NO_2^-][A_a] \\
 \frac{d[B_a]}{dt} &= l_3[Q_a]([B] - [B_a]) - l_1[NO][B_a]
 \end{aligned}$$

Additionally if the preliminary suggested expression equations are to be included this list is extended to include:

$$\begin{aligned}
 \frac{d[A]}{dt} &= \left(R \left(1 - \frac{[O_2] + k_{10}[NO]}{[O_2] + k_{10}[NO] + k_{11}} \right) - S \left(1 - \frac{[NO]}{[NO] + k_{13}} \right) \right) - k_8[A] \\
 \frac{d[B]}{dt} &= T \left(\frac{[NO]}{[NO] + k_{15}} \right) - k_{16}[B]
 \end{aligned}$$

The data required to populate the parameters has been obtained by experimental means as described in Chapters 5-7. These data provided information on both respiratory rates and enzyme kinetics. Additional information was gathered from the literature as shown in Chapter 3.

To use the information obtained from the literature and from experimental data, an integrated parameter estimation scheme was devised, which combined Bayesian inference with a Monte-Carlo type parameter estimation system into an iterative method for extracting parameter values from progressively more complex datasets as described in Chapter 4. This iterative method produces posterior

probability distributions for each of the parameters in the model calculated from the various rounds of parameter estimation for each successive dataset. The final parameter probability distributions are shown in tabular form in Table 8.1. This table shows the values required to produce idealised lognormal distributions of each of the parameters. Plots of the actual obtained distributions are shown in Figure 8.1.

The value of k_5 has no associated bounds in the table as it was concluded that the value reported is actually much lower than the true value as evidenced in Chapter 7 whereby the posterior parameters from nitrite reduction were unable to model the true effect of NO inhibition of oxygen shown in Chapter 6. Increasing the value of k_5 could restore the correct behaviour in the NO reduction dataset without a significant detrimental effect on the nitrite dataset. Unfortunately this makes the bounds on this value indeterminate without further Monte-Carlo simulation being run with the adapted value. The distribution shown in Figure 8.1 shows the un-adapted values for comparison.

8.1 Amalgamation of Cytochromes

The choice to replace the multiple cytochromes bc_1 , c_x , c_4 and c_5 with one single entity was a modelling one, to both simplify the modelling process by reducing the total component count and number of rate constants, and to allow the model to focus on simple electron transport chain branching and competition for electrons. The rate constants for each of the cytochromes could be subsumed by the respective “out rates” from the amalgamated cytochrome to its downstream electron acceptor. The downside of this approach is that it means that any rates obtained for X are probably not going to be biologically relevant as it is essentially masking the behaviour of multiple different hidden components. This simplification does not appear to have affected the model in a detrimental way when using the datasets in this work.

Symbol	Description	Mean Value	σ
k_1	Rate constant for O_2 reduction by reduced cbb_3	$403.51 \mu M^{-1}s^{-1}$	27.59
k_3	Rate constant for cbb_3 reduction by cytochrome pool	$4.58 \mu M^{-1}s^{-1}$	0.436
l_1	Rate constant for NO reduction by reduced NorB	$6.42 \mu M^{-1}s^{-1}$	2.33
l_3	Rate constant for NorB reduction by quinone pool	$0.096 \mu M^{-1}s^{-1}$	0.025
m_1	Rate constant for NO_2^- reduction by reduced AniA	$0.175 \mu M^{-1}s^{-1}$	0.087
m_3	Rate constant for AniA reduction by cytochrome pool	$4.79 \mu M^{-1}s^{-1}$	0.042
k_5	Rate constant for cbb_3 inhibition by NO	$\approx 66000 \mu M^{-1}s^{-1}$	Indeterminate
k_6	Rate constant for recovery of NO inhibited cbb_3	$1.59 s^{-1}$	0.527
β	Rate constant for passive diffusion in of O_2	$0.00014 \mu M^{-1}s^{-1}$	4.7×10^6
K_O	Saturation O_2 level	$48 \mu M$	0
g	Rate of electrons in from NADH	$0.085 s^{-1}$	0.0078
f	Rate constant for reduction of cytochromes by quinones	$0.771 \mu M^{-1}s^{-1}$	0.096
γ	Spontaneous loss of NO	$0.0024 \mu Ms^{-1}$	8.8×10^5
Q	Concentration of quinones	$34.31 \mu M$	5.49
X	Concentration of cytochromes	$2.81 \mu M$	0.595
A	Concentration of AniA	$0.704 \mu M$	0.3
B	Concentration of NorB	$7.8 \mu M$	3.63
C	Concentration of cbb_3	$1.3 \mu M$	0.259

Table 8.1: **Model parameters.** This table shows all the parameter values that have been generated by iterative parameter estimation throughout this work. For values that show concentrations of components, they represent the value for a culture with $OD_{600} = 1.00$.

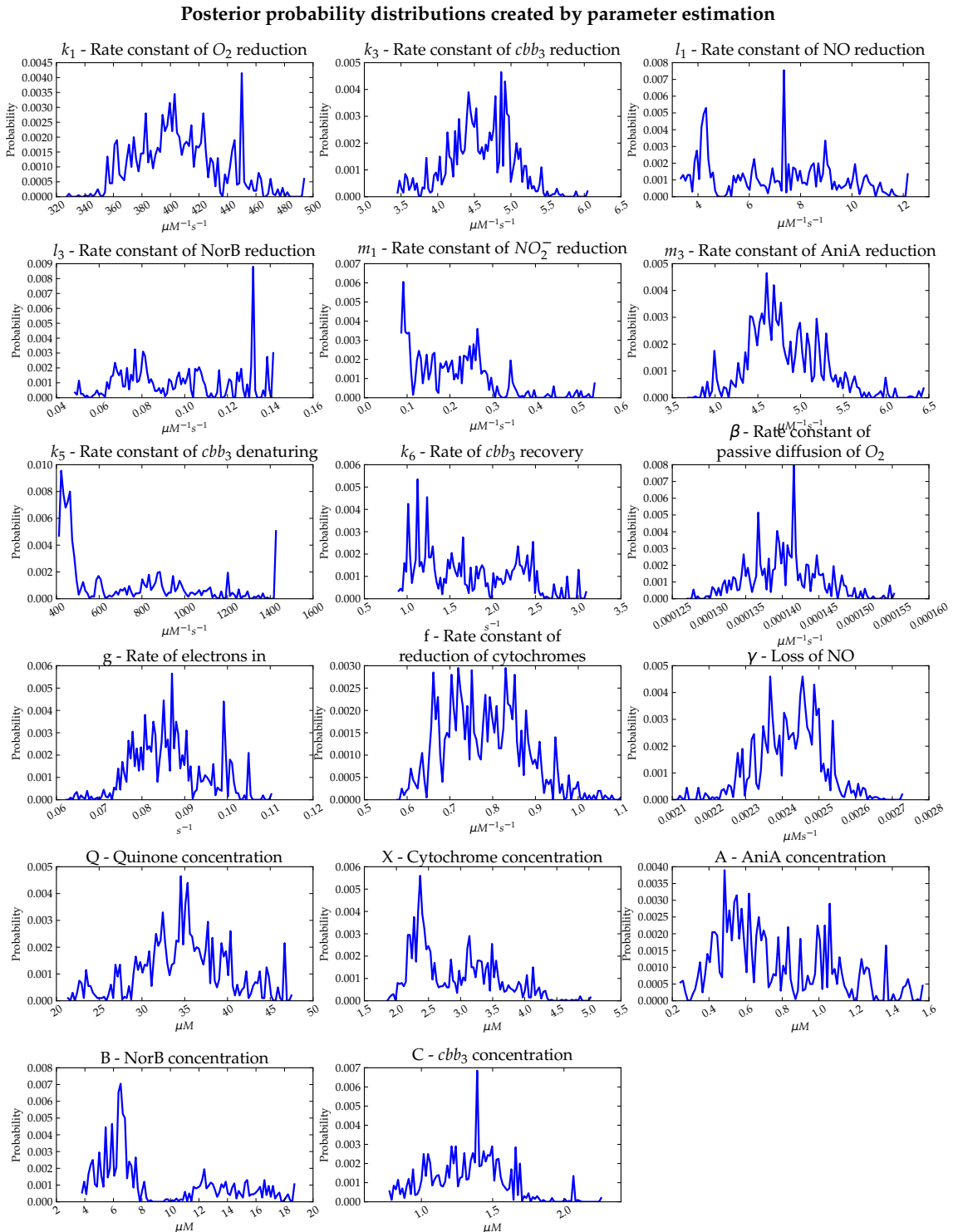


Figure 8.1: Final Posterior probability distributions. These are the final posterior probability distributions generated by the parameter estimation system, all concentrations have been normalised to assume an OD_{600} of 1. Note the value of k_5 will be significantly different from that shown.

Parameter	Prior	Oxygen Posterior	NO Posterior	Nitrite Posterior
k_1	415	413.228	417.88	403.51
k_3	3	4.496	4.65	4.5
l_1	6	→	13.12	6.42
l_3	1	→	0.058	0.096
m_1	1	→	→	0.175
m_3	4.8	→	→	4.79
k_5	100	→	1741.8	66000
k_6	38	→	1.076	1.59
β	0.00014	0.00012	0.00014	0.00014
g	0.847	0.889	0.857	0.085
f	8.749	8.707	8.398	0.771
γ	0.017	→	0.0024	0.0024
Q	0.3	3.143	7.06	34.31
X	3.97	4.732	27.45	2.81
A	0.137	→	→	0.704
B	0.043	→	0.137	7.8
C	0.03	0.043	0.071	1.3

Table 8.2: **Change in Parameter Values.** This table shows the mean of each parameter value at each stage of the model. Where parameters are not used and therefore generate no posterior distribution, a → is used instead.

8.2 Parameter Changes Throughout this Work

The way the parameters change throughout the various rounds of parameter estimation described in this work is presented in Table 8.2 and discussed below.

- k_1 - Changes very little and the final distribution resembles the prior distribution very closely.
- k_3 - Increases slightly to achieve the required oxygen reduction rate and affinity.
- l_1 - Increases by a factor of two initially however this is a very broad distribution suggesting that the magnitude is less important at this point. It

settles back to a value closer to the prior when a more appropriate dataset is used.

- l_3 - Reduces significantly to achieve desired NO reduction rate.
- m_1 - Reduces significantly to achieve desired nitrite reduction rate.
- m_3 - Changes very little from prior distribution.
- k_5 - Increases significantly in order to inhibit cbb_3 by the amount seen in experimental data.
- k_6 - Decreases significantly for the same reason as above.
- β - No change.
- g - No change initially, but final posterior shows a $10\times$ decrease to prevent permanent reduction of cytochromes.
- f - No change initially, but final posterior shows a $10\times$ decrease to prevent permanent reduction of quinone pool.
- γ - Initial decrease to prevent NO being lost too quickly from the *in silico* results.
- Q - Initial increase to allow enough electron flux through the system. Final large increase as a result of reducing electron flux *into* the system.
- X - Significant change seen for NO reduction, but this change is negated in the final posteriors after reducing electron flux.
- A - Significant increase required to attain observed Nitrite reduction rate after reducing electron flux.
- B - Increases required to attain Nitric Oxide reduction rate, and after reducing electron flux.
- C - Significant increase required to attain Oxygen reduction rate, exacerbated by the reduction of electron flux.

Nitric Oxide Addition to *aniA⁻-nsrR⁻* Mutant

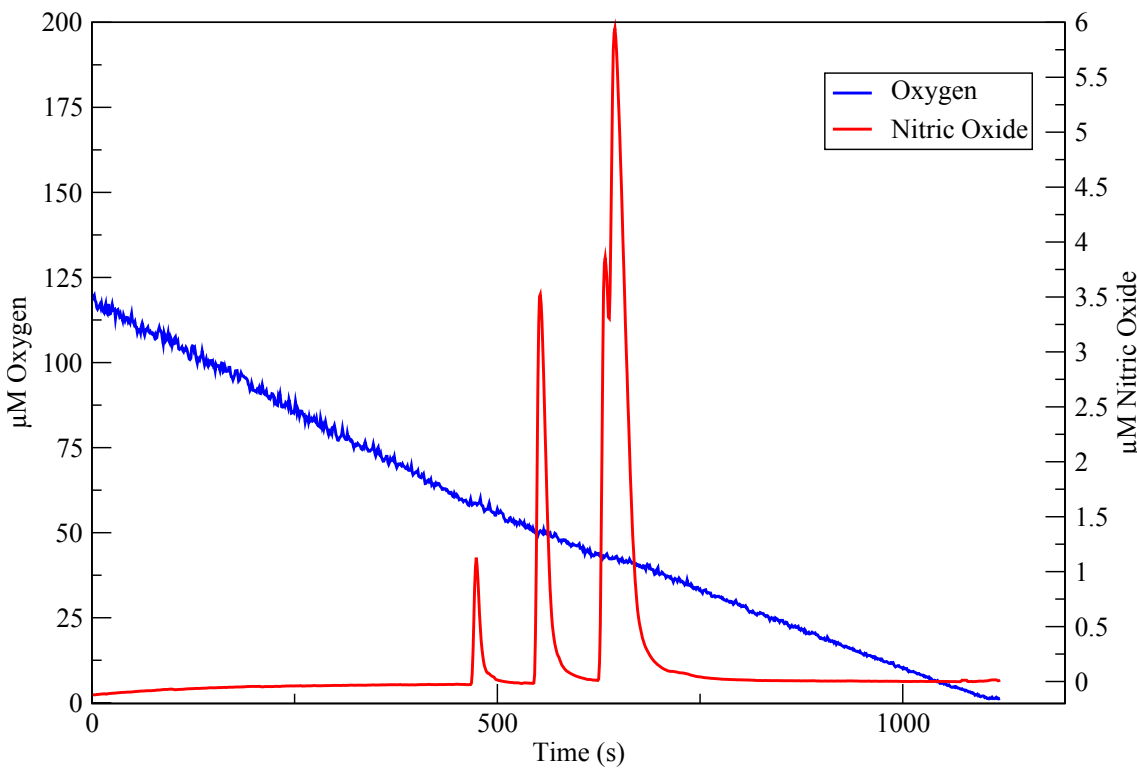


Figure 8.2: Nitric Oxide Reduction in an *nsrR⁻* Mutant. This figure shows nitric oxide and oxygen reduction in an *aniA⁻-nsrR⁻*. In this case the *aniA⁻* mutation has no effect as no nitrite is being reduced. Addition of nitric oxide has only a very small effect on the rate of oxygen reduction as it is being removed very quickly by the constitutively expressed NorB.

8.3 Testing the Model

8.3.1 Addition of Nitric Oxide to an *nsrR⁻* mutant

The *nsrR⁻* mutant should express NorB at significantly higher levels than in wild-type cultures, by as much as 100× according to Rock et al.³². This is a simple *in silico* test to do as it simply requires the concentration of NorB to be increased by 100×. Additionally a representative experimental dataset which has not been used during parameter estimation can be used to compare the *in silico* result with the *in vivo* data. This experimental dataset is shown in Figure 6.16 and repeated here in Figure 8.2. The *in silico* test was performed using the same parameter values used to generate Figure 7.14 with the value for NorB increased by 100×. The result of this simulation is shown in Figure 8.3. This figure shows significant simi-

Nitric Oxide Addition to *In Silico nsrR⁻* Mutant

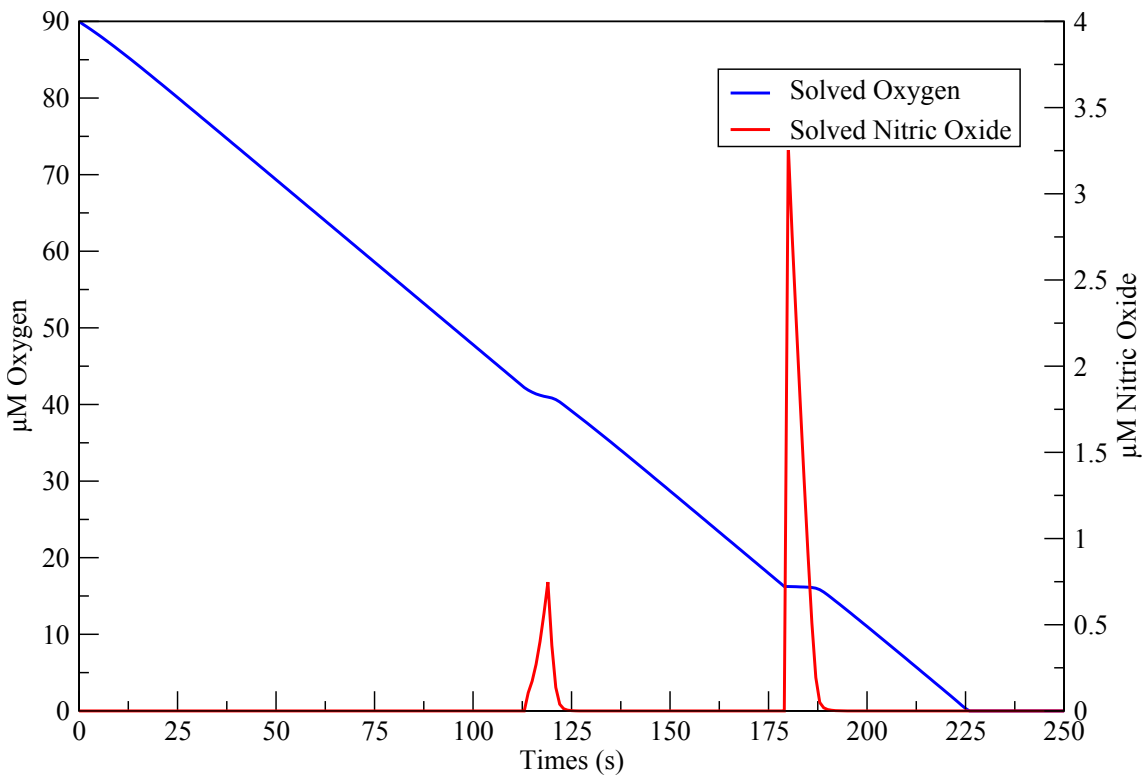


Figure 8.3: **Nitric Oxide Addition to *In silico nsrR⁻* Mutant.** This figure shows the effect of adding two aliquots of increasing concentration of nitric oxide to a simulated *nsrR⁻* mutant.

larity with the experimentally observed result capturing the fast removal of nitric oxide due to the large quantities of NorB, and also models the slight reduction in oxygen reduction rate whilst the NO is being removed.

8.3.2 *In silico* cyt Knockouts

It is possible to predict the effect on both the electron transport chain and the rates of respiration of knocking out some of the cytochromes that are encompassed within parameter X. This can be done by simply reducing the concentration of X and leaving all other parameters unchanged. In this case the concentration was reduced by 25% (this value is somewhat arbitrary but might be similar in effect knocking out 1 of the c-type cytochromes). This is a simplification of actually knocking out a specific cytochrome as this will actually affect all components downstream of X.

Comparison of Simulated Wild-Type and Cytochrome Knockout

Switching from aerobic to microaerobic respiration

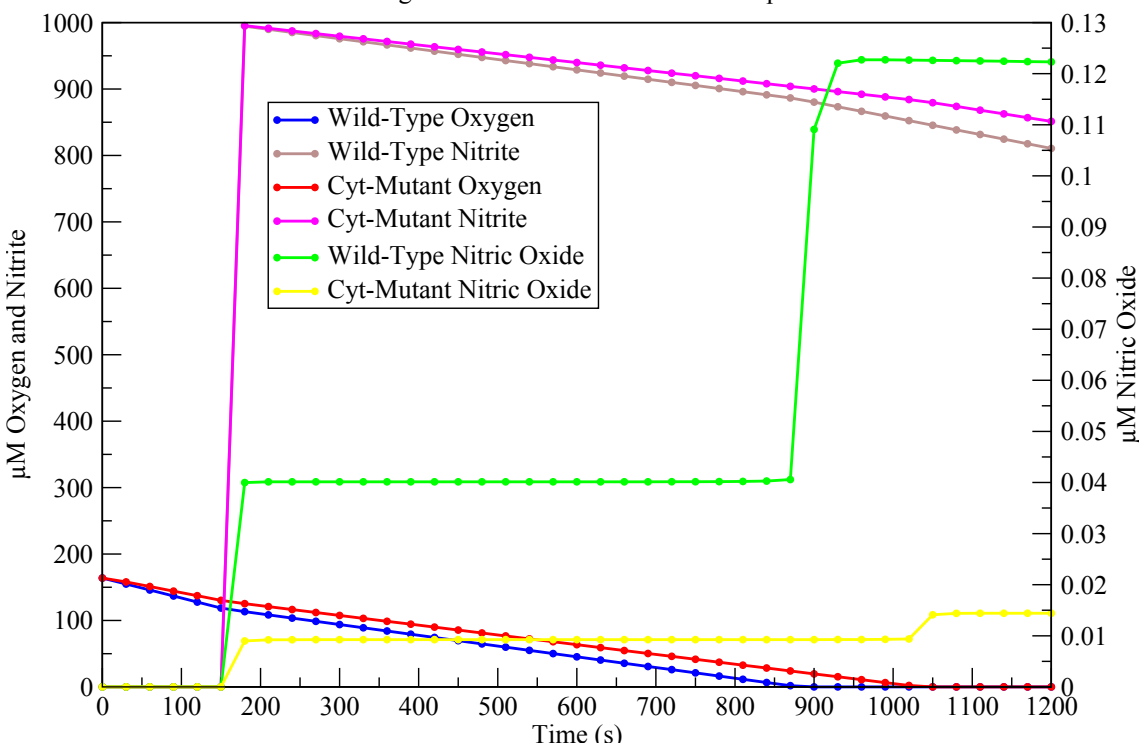


Figure 8.4: *In silico* Cytochrome Mutant. This figure shows the effect of reducing the total amount of cytochromes while leaving all other components unchanged. All the reaction rates have slowed as a result of this change.

The experimental dataset used for comparison is that in Figure 7.10. The result of the simulated dataset is shown in Figure 8.4 compared to the solved result from the wild-type.

The simulated cytochrome mutant shows that all reaction rates have slowed, although not by large amounts. The most obvious difference in the figure is the change in production and removal of nitric oxide, which is reduced to approximately 10% of its production compared to the wild-type. This predicted result could easily be tested with an experiment using a c-type cytochrome knockout mutant grown in microaerobic conditions.

The reduction state plot can be seen in Figure 8.5. It also compares the simulated cytochrome mutant to the wild-type. As can be seen, the redox states of cbb_3 and AniA do not change significantly as they are very efficient electron donors, remaining in an oxidised state. NorB remains in a more reduced state

Comparison of Redox States Between Wild-Type and Cyt Knockout

Switching from aerobic to anaerobic respiration

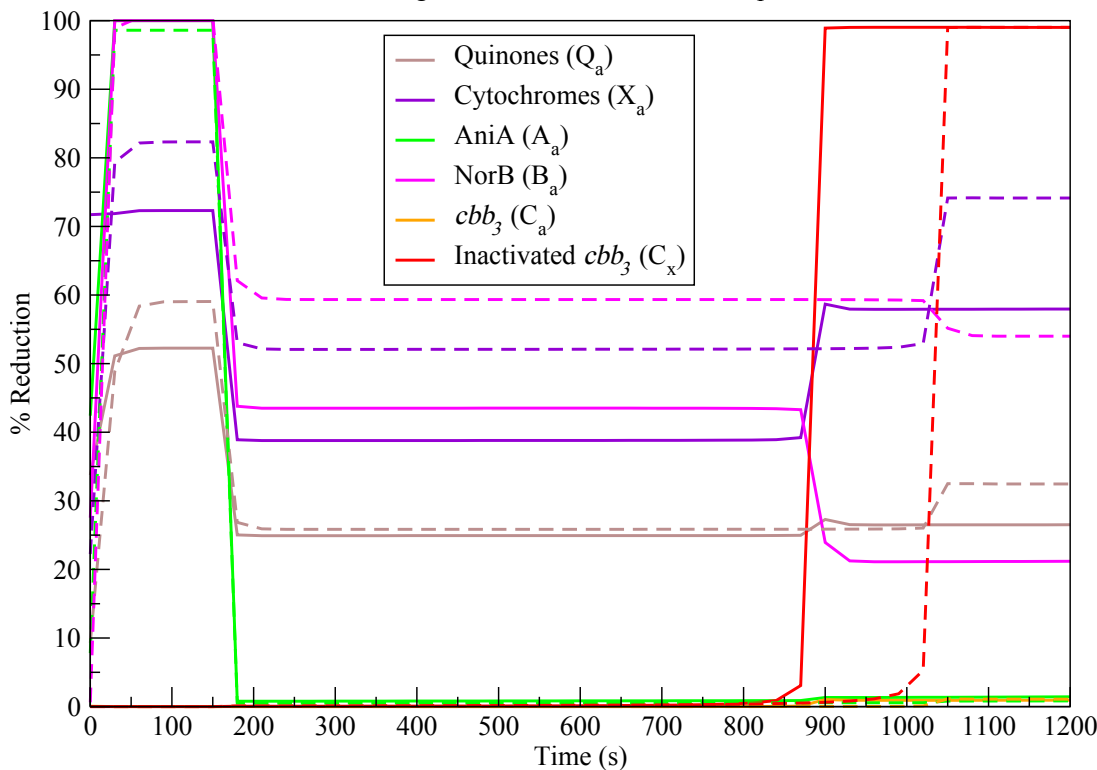


Figure 8.5: *In silico* Cytochrome Mutant Redox States. This figure shows the effect on the enzymatic reduction states of reducing the total number of cytochromes to simulate a cytochrome knockout mutant. The wild-type is represented by solid lines, and the synthetic mutant by dashed lines.

in the cytochrome mutant as there is less NO to ultimately reduce resulting in fewer electrons donated. The reduction state of the quinones is quite similar between the two simulations throughout. The reduction state of the cytochromes is significantly different, being higher than the wild-type at all times. This can be explained by looking at the quinone pool reduction state. As it remains fairly similar to the wild-type, the same flux of electrons must be passing through it, thus the same amount of electrons are being passed to fewer cytochromes. Since the rate of donation of electrons by the cytochromes has not been altered, the electrons build up in the cytochromes until a new steady-state is reached where the overall reduction state of the cytochromes is higher.

Improved Fit Using Scaling Factor

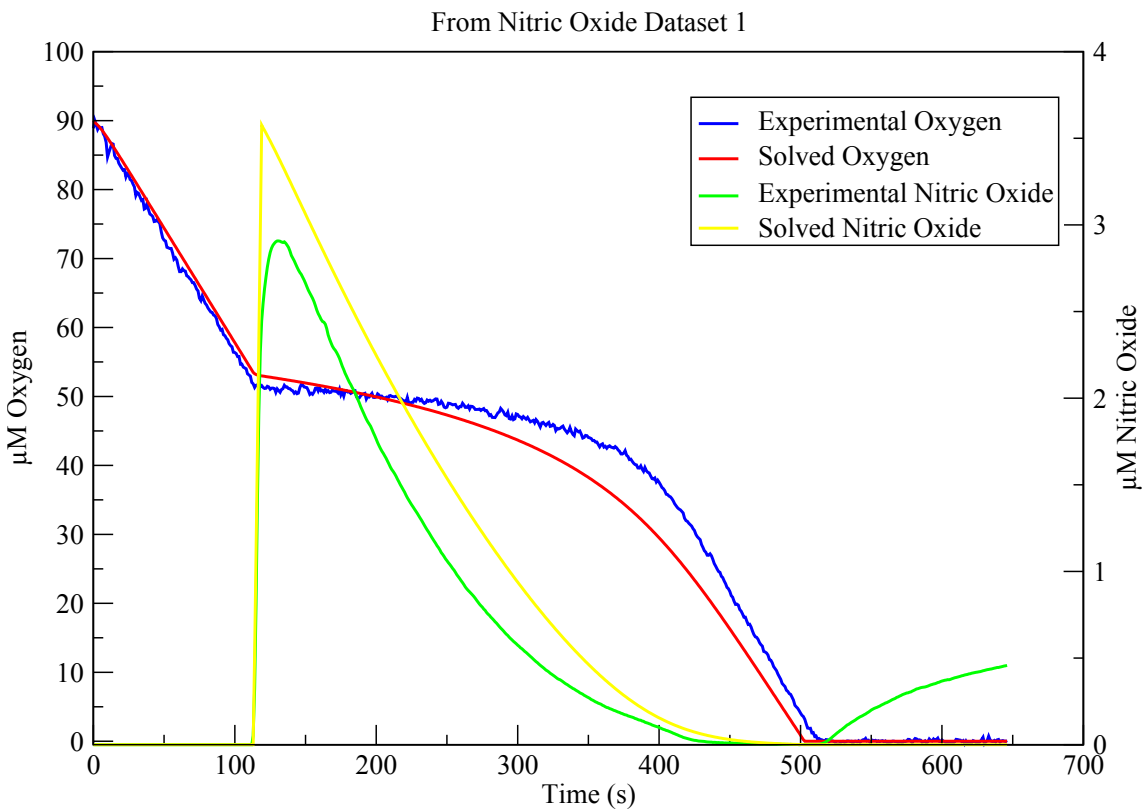


Figure 8.6: **Improved Fit with Scaling Factor.** This figure shows the best fit achieved using a scaling factor rather than an approximate OD to calculate component concentrations. Compare with 7.14.

8.4 Single Parameter Scaling Fits

As has been discussed previously the proxy being used to try and estimate cell density appears to be inadequate as it does not scale correctly with the normalised data. It is however possible to obtain very good fits to all the experimental datasets with the exception of nitrite dataset 1 - which is an *nsrR*⁻ mutant - by simply introducing a “scale factor” which is applied to all concentrations in the system. An example of the better fit after using the scale factor is shown in Figure 8.6 in comparison to Figure 7.14.

The magnitude of the scale factor required for each dataset is shown in Table 8.3 along with the Oxygen Reduction Activity which formed part of the initial scaling.

The fact that NorB needed to be scaled by a smaller amount in Nitrite dataset

Dataset	Scale Factor	O_2 Reduction Activity ($\mu M s^{-1}$)
Oxygen Dataset 1	$\frac{1}{7}$	0.211027
Oxygen Dataset 2	$\frac{1}{2.4}$	1.016159
Oxygen Dataset 3	$\frac{1}{8}$	0.181488
Nitric Oxide Dataset 1	$\frac{1}{5.5}$	0.336669
Nitric Oxide Dataset 3	$\frac{1}{3}$	0.597478
Nitric Oxide Dataset 4	$\frac{1}{5.8}$	0.324286
Nitrite Dataset 2	$\frac{1}{5.8}$ (NorB $\frac{1}{5}$)	0.275

Table 8.3: Dataset Scale Factors

2 suggests that the value for NorB is actually underestimated in the priors. This does not affect the other datasets as they either have no NorB or only very low levels.

A plot of the scaling factors compared to the dataset oxygen reduction rates is shown in Figure 8.7. A simple linear regression through the datapoints suggests that the relationship between the two is approximately linear with a gradient of 0.36366.

8.5 Concluding Remarks

The parameterised model created in this work appears to be capable of at least qualitatively modelling the behaviour of all the datasets presented, using the final set of parameter distributions. The model is not 100% quantitative, although this was not an explicit requirement for the model. It should still be capable of offering insight into how the system behaves even if it cannot predict changes precisely. The non-quantitative nature of the model was to be expected given the high level of complexity in the model and some of the assumptions made regarding cytochromes, backward reaction rates etc. The most obvious “fault” in the model is that there is an incomplete decoupling of cell density from other components. Unfortunately this is most probably because the proxy used was not completely accurate as a replacement for cell density.

Dataset Scaling Factors against Oxygen Reduction Activity

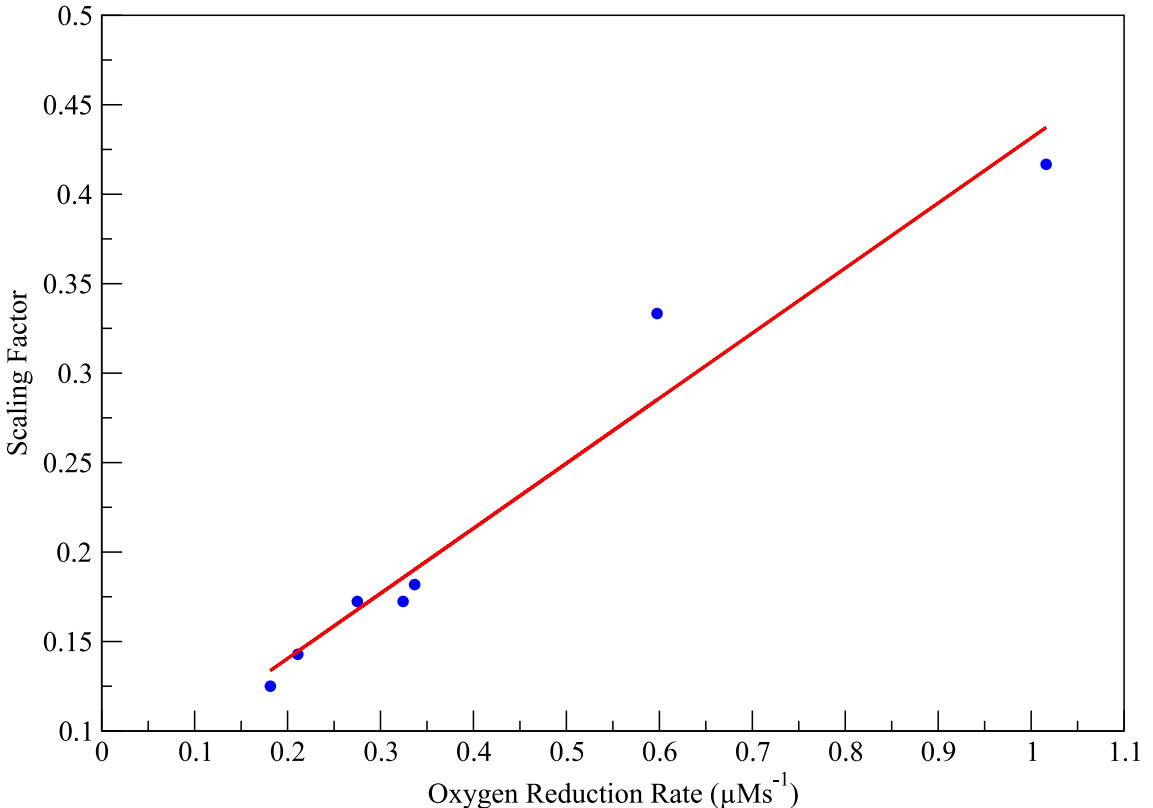


Figure 8.7: **Dataset Scaling Factors.** This figure shows the magnitude of the scaling factor relative to the experimental oxygen reduction rates. The red lines indicates a linear regression through the datapoints.

The integrated parameter estimation system created for this work operates as intended and could be extended to parameterise other systems if the same Bayesian approach were taken to data gathering. It is not however a system that could be used without human curation though, as it can still produce mathematically correct results with parameters that are actually very unlikely *in vivo*. This was shown in Chapter 7 where the values for 2 parameters were an order of magnitude too high in the prior probability distributions causing the simulation to fail. These same values worked “perfectly” for the datasets in Chapters 5 and 6. Such human interaction with the system is important however as it forms part of the Bayesian approach whereby we provide the “prior” knowledge to the system.

In conclusion, a novel system for parametrising a respiration system model has been created and utilised which has been able to successfully populate the

model and produce probability distributions for all parameters. These parameters are able to be used in a qualitative manner to match existing experimental data, and to provide insight into the hidden behaviour of the system.

Chapter 9

Further Work - AniA and NorB Expression in *N. meningitidis*

The expression of AniA and NorB has not been mentioned in this work thus far as it adds a further level of complication to an already complex model. The data shown in the previous chapters shows that it seems to be possible to model, with reasonable accuracy, many of the facets of respiration without the need for modifying the levels of expression of the respiratory enzymes. However regulation of expression systems *do* exist in the respiratory system and it would be an oversight to omit them from discussion here.

Unfortunately due to time constraints it was not possible to fully investigate expression in this respiratory system, however the following was theorised as a potential method for including expression of AniA and NorB in the model.

It is posited that expression of AniA and NorB could be modelled by treating them as being expressed using Michaelis-Menten kinetics. This being the case, the rate of change of the two enzymes in the system can be expressed as differential equations in the following manner:

$$\frac{d[A]}{dt} = \left(R \left(1 - \frac{[O_2] + k_{10}[NO]}{[O_2] + k_{10}[NO] + k_{11}} \right) - S \left(1 - \frac{[NO]}{[NO] + k_{13}} \right) \right) - k_8[A]$$

$$\frac{d[B]}{dt} = T \left(\frac{[NO]}{[NO] + k_{15}} \right) - k_{16}[B]$$

The parameters required for NorB expression can be explained simply: T is equivalent to the V_{max} of enzyme expression and k_{15} is equivalent to the K_M . k_{16} is included to model the degradation rate of the enzyme. The expression rate of NorB is dependent solely on the concentration of NO present.

AniA expression is more complicated to model as it is not only repressed by oxygen, but activated *and* repressed by NO. The NO activation is modelled by S and k_{13} which correspond to the V_{max} and K_M of the activation respectively. This ensures that AniA isn't expressed when NO is too low. The repression of activation by oxygen and NO is modelled by R, k_{10} and k_{11} which represent the V_{max} , "NO inhibition scale factor", and K_M of the repression respectively. The "NO inhibition scale factor" effectively sets the cut-off concentration of NO at which it starts repressing AniA expression. As with NorB expression, k_8 here represents the degradation rate of AniA.

The first part of the AniA equation models the regulation by FNR, and the second part in addition to the NorB equation models the regulation by NsrR. As detailed in Chapter 1, NsrR is a repressor of both AniA and NsrR, and FNR (Fumarate and nitrite reductase regulator) is an activator of AniA. Nitric Oxide inhibits the NsrR protein leading to an increase in expression of both NorB and AniA since the repression by NsrR is no longer present. Higher concentrations of Nitric Oxide cause FNR to be inhibited which effectively represses AniA. High concentrations of Oxygen also cause inhibition of FNR meaning that AniA isn't expressed until low concentrations of Oxygen are present.

These two new differential equations could easily be incorporated into the

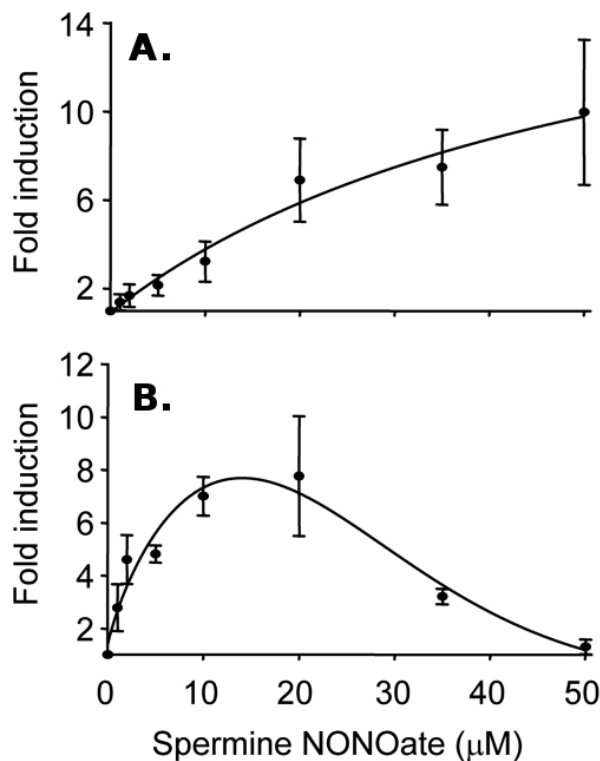


Figure 9.1: **Effect of Nitric Oxide on NsrR and FNR Dependent Gene Expression.** Expression of (A) NorB and (B) AniA in wild-type *Neisseria meningitidis*. Figure adapted from Heurlier et al.³⁰.

model to complement the original 9 equations. There are two datasets which could potentially be used to populate these new parameters. The first is from Heurlier et al.³⁰ which details levels of expression in response to regulation by Nitric Oxide (produced by Spearmine NONOate). This is shown in Figure 9.1. The second is from Rock et al.²⁰ which details the effect on Oxygen reduction and Nitric Oxide creation and reduction during microaerobic respiration, and this is shown in Figure 9.2.

Effect of AniA and NorB expression on Respiration

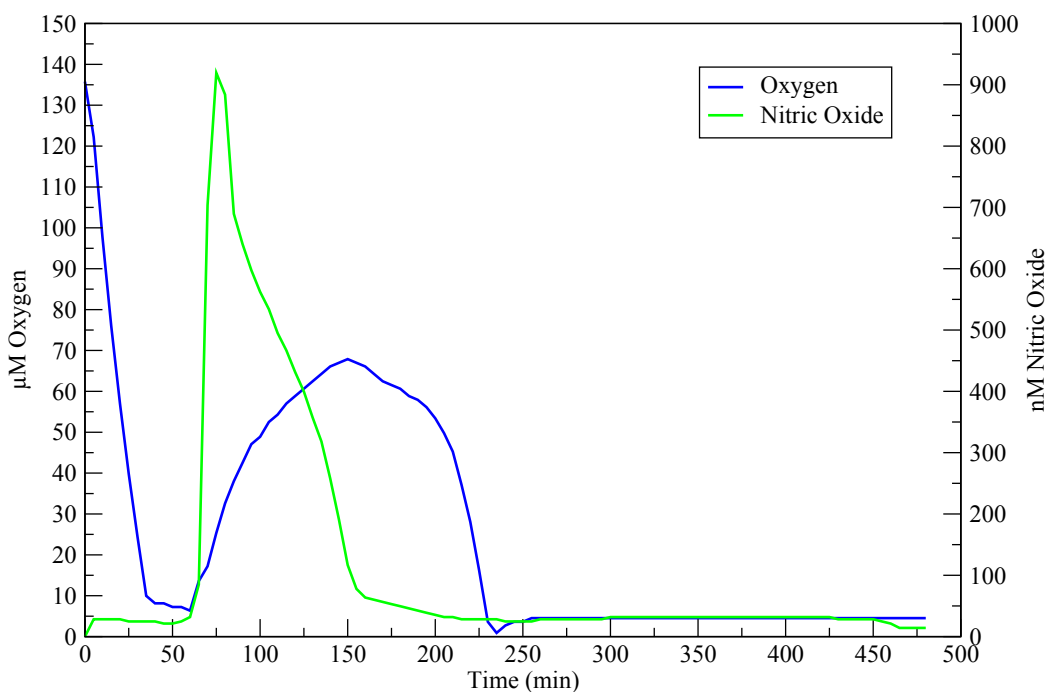


Figure 9.2: **Effect of Expression of AniA and NorB.** This figure shows an aerobically respiring culture in media with nitrite present. When oxygen is depleted, AniA and NorB begin to be expressed causing an increase and then decrease of NO. While NO is being reduced, Oxygen concentration slowly rises due to diffusion, and begins to be reduced once more when NO is depleted. Data from Rock et al.²⁰.

Appendix A

Appendix

A.1 Monte Carlo Estimation of π

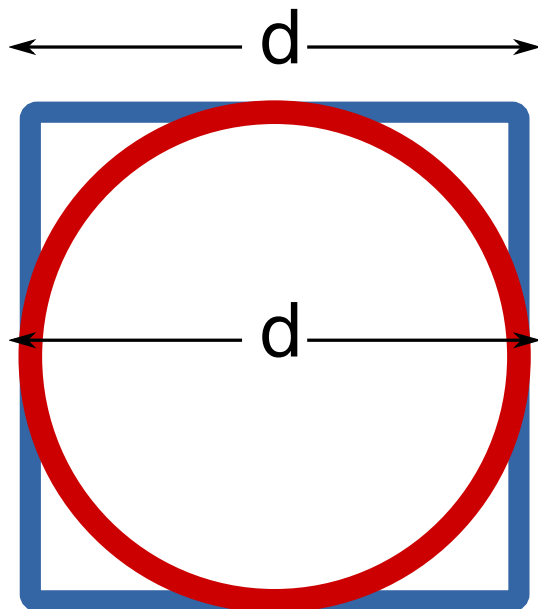


Figure A.1: **Circle circumscribed by a square.** A Circle of diameter d inside a square of side d .

Using the example shown in Figure A.1:

- The area of the square is d^2 .
- The area of the circumscribed circle is $\pi \times \left(\frac{d}{2}\right)^2 = \frac{\pi}{4} \times d^2$.
- The ratio of the two is therefore $\frac{\frac{\pi}{4} \times d^2}{d^2} = \frac{\pi}{4}$.

Pi can be estimated by calculating the ratio of randomly distributed points that fall within the circle to those that fall within the square.

A.2 Adaptive step sizes and numerical instability

An adaptive step size routine was required for the ordinary differential equation algorithm to prevent numerical instability issues from arising and producing bogus results. At points during the simulation, a number of parameters can take on very small values, or are changing rapidly and a fixed step size algorithm can cause problems here by assuming that the value stays small, or stays constant during the length of the fixed step. The result of these assumptions is numerical instability whereby the erroneous values of these parameters affects other parameters in the simulation. The most obvious and disastrous effect is of concentrations in the simulation going negative.

To prevent this issue an adaptive step size was implemented whereby if the parameters are changing slowly the step size can be large, but this is adaptively decreased (and conversely increased) when parameters are changing more quickly. In the absence of an adaptive step size routine, the fixed step size would have to be set small enough to solve the rapidly changing regions correctly, but would then be unnecessarily small in the slowly changing regions.

A.3 Affinity of cbb_3 for Oxygen

A large amount of data was gathered during the course of this work of oxygen reduction which could be used for analysis of the affinity of cbb_3 for oxygen. Simple observation of these datasets which can be seen in Chapter 5 shows that cbb_3 must have a high affinity for oxygen by virtue of the fact that oxygen reduction continues linearly all the way down to almost zero oxygen. A lower oxygen affinity would show a marked slowing of the reduction rate as the concentration of oxygen decreased. A simple way of visualising the change in rate during oxygen reduction is to plot the instantaneous rate against the concentration of oxygen.

A more appropriate way to visualise the rates is to use a Lineweaver-Burk (double reciprocal) plot. This allows the V_{max} and K_M to be calculated from a

regression line through the data. The x-axis intercept is equal to $-\frac{1}{K_M}$, and the y-axis intercept is equal to $\frac{1}{V_{max}}$. A Lineweaver-Burk plot for a representative oxygen reduction dataset is shown in Figure A.2.

Lineweaver-Burk Plot for Oxygen Reduction by cbb_3

v calculated from average rate over 5s

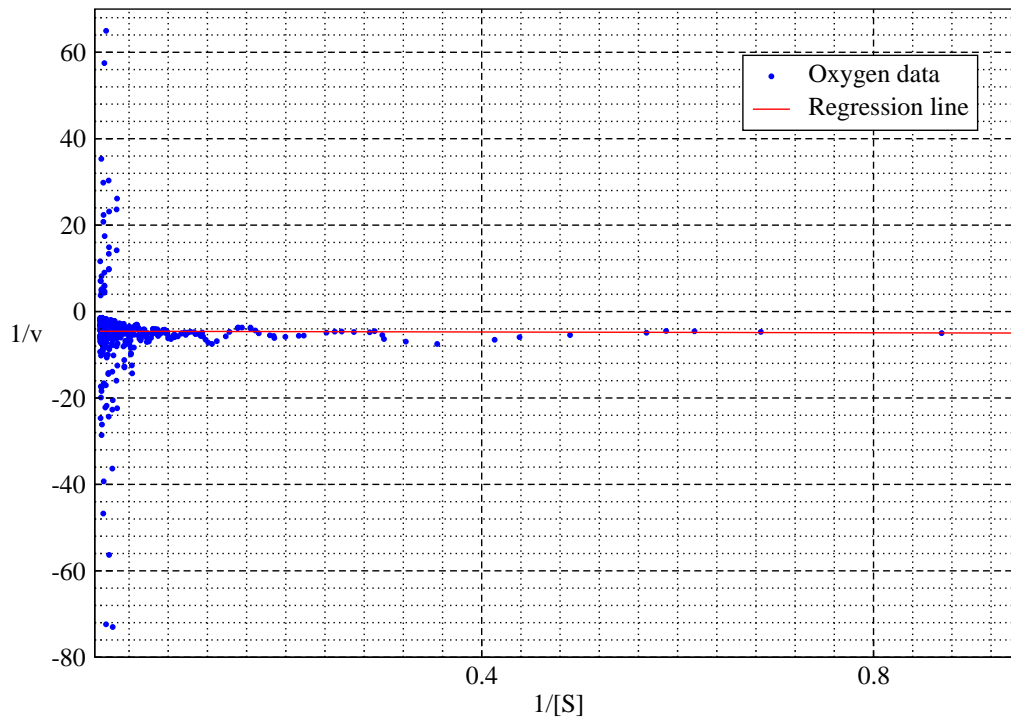


Figure A.2: **Lineweaver-Burk Plot for Oxygen Reduction in *Neisseria meningitidis*.** V was calculated as a 5 second rolling average rate to try and smooth out some of the data. The rates are largely negative as oxygen was being removed from the system. The regression line shown is a simple linear regression through all datapoints.

Unfortunately the combination of particularly noisy data generated by the oxygen electrode, and the limited sampling rate (of 1s^{-1}) mean that the degree of affinity could not be explored further. The essentially flat regression line through the Lineweaver-Burk plot here would imply a completely linear reduction rate and extremely high affinity of cbb_3 for oxygen.

A.4 Software Used During this Work

The main code of the integrated parameter estimation system was written in JavaTM with various helper scripts written in Python. Initial visualisation of re-

sults was carried out using GNUPlot. Calculation of the Gelman-Rubin R statistic was performed using the statistical software package 'R', and the correlation analysis used the `scipy` library for Python. This thesis was typeset using L^AT_EX, figures if drawn were created using Inkscape, data plots were created with Grace, probability plots with Matplotlib¹⁵⁶ for Python. Figure 1.5 was created with UCSF Chimera¹⁵⁷.

References

1. van Deuren M, Brandtzaeg P, van der Meer JWM (2000) Update on Meningococcal Disease with Emphasis on Pathogenesis and Clinical Management. *Clinical Microbiology Reviews* 13: 144–166.
2. Stephens DS (2009) Biology and Pathogenesis of the Evolutionarily Successful, Obligate Human Bacterium *Neisseria meningitidis*. *Vaccine* 27: B71–B77.
3. Rosenstein NE, Perkins BA, Stephens DS, Popovic T, Hughes JM (2001) Meningococcal Disease. *New England Journal of Medicine* 344: 1378–1388.
4. DeVoe IW (1982) The Meningococcus and Mechanisms of Pathogenicity. *Microbiology and Molecular Biology Reviews* 46: 162–190.
5. Aas JA, Paster BJ, Stokes LN, Olsen I, Dewhirst FE (2005) Defining the Normal Bacterial Flora of the Oral Cavity. *Journal of Clinical Microbiology* 43: 5721–5732.
6. Madigan M, Martinko J, editors (2005) *Brock Biology of Microorganisms*. 11th ed., Prentice Hall.
7. Carbonnelle E, Hill DJ, Morand P, Griffiths NJ, Bourdoulous S, et al. (2009) Meningococcal Interactions with the Host. *Vaccine* 27: B78–B89.
8. Stephens DS, Greenwood B, Brandtzaeg P (2007) Epidemic Meningitis, Meningococcaemia, and *Neisseria meningitidis*. *Lancet* 369: 2196–2210.

9. Holst J (2007) Strategies for Development of Universal Vaccines Against Meningococcal Serogroup B Disease: the Most Promising Options and the Challenges Evaluating Them. *Human Vaccines* 3: 290–294.
10. Moe GR, Tan S, Granoff DM (1999) Molecular Mimetics of Polysaccharide Epitopes as Vaccine Candidates for Prevention of *Neisseria meningitidis* Serogroup B Disease. *FEMS Immunology and Medical Microbiology* 26: 209–226.
11. Larson JA, Higashi DL, Stojiljkovic I, So M (2002) Replication of *Neisseria meningitidis* Within Epithelial Cells Requires TonB-Dependent Acquisition of Host Cell Iron. *Infection and Immunity* 70: 1461–1467.
12. Archibald FS, DeVoe IW (1978) Iron in *Neisseria meningitidis*: Minimum Requirements, Effects of Limitation, and Characteristics of Uptake. *Journal of Bacteriology* 136: 35–48.
13. Perkins-Balding D, Ratliff-Griffin M, Stojiljkovic I (2004) Iron Transport Systems in *Neisseria meningitidis*. *Microbiology and Molecular Biology Reviews* 68: 154–171.
14. Yazdankhah SP, Caugant DA (2004) *Neisseria meningitidis*: An Overview of the Carriage State. *Journal of Medical Microbiology* 53: 821–832.
15. Beddek AJ, Li MS, Kroll JS, Jordan TW, Martin DR (2009) Evidence for Capsule Switching between Carried and Disease-Causing *Neisseria meningitidis* Strains. *Infection and Immunity* 77: 2989–2994.
16. Moxon ER, Rainey PB, Nowak MA, Lenski RE (1994) Adaptive Evolution of Highly Mutable Loci in Pathogenic Bacteria. *Current Biology* 4: 24–33.
17. Pathan N, Faust SN, Levin M (2003) Pathophysiology of Meningococcal Meningitis and Septicaemia. *Archives of Disease in Childhood* 88: 601–607.

18. Exley RM, Shaw J, Mowe E, Sun YH, West NP, et al. (2005) Available Carbon Source Influences the Resistance of *Neisseria meningitidis* Against Complement. *Journal of Experimental Medicine* 201: 1637–1645.
19. Beno DW, Devine LF, Larson GL (1968) Identification of *Neisseria meningitidis* Carbohydrate Fermentation Patterns in Mueller-Hinton Broth. *Journal of Bacteriology* 96: 563.
20. Rock JD, Mahnane MR, Anjum MF, Shaw JG, Read RC, et al. (2005) The Pathogen *Neisseria meningitidis* Requires Oxygen, but Supplements Growth by Denitrification. Nitrite, Nitric Oxide and Oxygen Control Respiratory Flux at Genetic and Metabolic Levels. *Molecular Microbiology* 58: 800–9.
21. Rock JD, Moir JWB (2005) Microaerobic Denitrification in *Neisseria meningitidis*. *Biochemical Society Transactions* 33: 134–6.
22. Tuttle DM, Scherp HW (1952) Studies On The Carbon Dioxide Requirement Of *Neisseria meningitidis*. *Journal of Bacteriology* 64: 171–182.
23. Lundberg JO, Weitzberg E, Cole JA, Benjamin N (2004) Nitrate, Bacteria and Human Health. *Nature Reviews Microbiology* 2: 593–602.
24. Deeudom M, Rock J, Moir J (2006) Organization of the Respiratory Chain of *Neisseria meningitidis*. *Biochemical Society Transactions* 34: 139–42.
25. Deeudom M (2007) The Electron Transport Chains of *Neisseria meningitidis*. Ph.D. thesis, University of York.
26. Preisig O, Zufferey R, Thöny-Meyer L, Appleby C, Hennecke H (1996) A High-affinity cbb3-Type Cytochrome Oxidase Terminates the Symbiosis-Specific Respiratory Chain of *Bradyrhizobium japonicum*. *Journal of Bacteriology* 178: 1532–1538.

27. Brown GC, Cooper C (1994) Nanomolar Concentrations of Nitric Oxide Reversibly Inhibit Synaptosomal Respiration by Competing with Oxygen at Cytochrome Oxidase. *FEBS Letters* 356: 295–298.
28. Sharpe MA, Cooper CE (1998) Interaction of Peroxynitrite with Mitochondrial Cytochrome Oxidase. *Journal of Biological Chemistry* 273: 30961–30972.
29. Anjum MF, Stevanin TM, Read RC, Moir JWB (2002) Nitric Oxide Metabolism in *Neisseria meningitidis*. *Journal of Bacteriology* 184: 2987–2993.
30. Heurlier K, Thomson MJ, Aziz N, Moir JWB (2008) The Nitric Oxide (NO)-Sensing Repressor NsrR of *Neisseria meningitidis* has a Compact Regulon of Genes Involved in NO Synthesis and Detoxification. *Journal of Bacteriology* 190: 2488–95.
31. Deedom M, Koomey M, Moir JWB (2008) Roles of C-type Cytochromes in Respiration in *Neisseria meningitidis*. *Microbiology* 154: 2857–64.
32. Rock JD, Thomson MJ, Read RC, Moir JWB (2007) Regulation of Denitrification Genes in *Neisseria meningitidis* by Nitric Oxide and the Repressor NsrR. *Journal of Bacteriology* 189: 1138–44.
33. Isabella V, Wright LF, Barth K, Spence JM, Grogan S, et al. (2008) Cis- and Trans-Acting Elements Involved in Regulation if NorB (NorZ), The Gene Encoding Nitric Oxide Reductase in *Neisseria gonorrhoeae*. *Microbiology* 154: 226–239.
34. Blaise GA, Gauvin D, Gangal M, Authier S (2005) Nitric Oxide, Cell Signaling and Cell Death. *Toxicology* 208: 177–192.
35. Govers R, Oess S (2004) To NO or not to NO: 'Where?' is the Question. *Histol Histopathol* 19: 585–605.

36. Wink DA, Kasprzak KS, Maragos CM, Elespuru RK, Misra M, et al. (1991) DNA Deaminating Ability and Genotoxicity of Nitric Oxide and its Progenitors. *Science* 254: 1001–1003.
37. Hibbs J Jr, Taintor RR, Vavrin Z, Rachlin EM (1988) Nitric Oxide: A Cytotoxic Activated Macrophage Effector Molecule. *Biochemical and Biophysical Research Communications* 157: 87–94.
38. Jones-Carson J, Laughlin JR, Stewart AL, Voskuil MI, Vázquez-Torres A (2012) Nitric Oxide-Dependent Killing of Aerobic, Anaerobic and Persistent *Burkholderia pseudomallei*. *Nitric Oxide* 27: 25–31.
39. Moir JW (2011) A Snapshot of a Pathogenic Bacterium Mid-evolution: *Neisseria meningitidis* is Becoming a Nitric Oxide-Tolerant Aerobe. *Biochemical Society Transactions* 39: 1890–1894.
40. Privett BJ, Broadnax AD, Bauman SJ, Riccio DA, Schoenfisch MH (2012) Examination of Bacterial Resistance to Exogenous Nitric Oxide. *Nitric Oxide* 26: 169–173.
41. Thomson MJ, Stevanin TM, Moir JWB (2008) Measuring Nitric Oxide Metabolism in the Pathogen *Neisseria meningitidis*. *Methods in Enzymology* 437: 539–560.
42. Laver JR, Stevanin TM, Messenger SL, Lunn AD, Lee ME, et al. (2010) Bacterial Nitric Oxide Detoxification Prevents Host Cell S-Nitrosothiol Formation: A Novel Mechanism of Bacterial Pathogenesis. *FASEB Journal* 24: 286–295.
43. Pitcher RS, Watmough NJ (2004) The Bacterial Cytochrome cbb3 Oxidases. *Biochimica et Biophysica Acta (BBA) - Bioenergetics* 1655: 388 – 399.
44. Puustinen A, Verkhovsky MI, Morgan JE, Belevich NP, Wikstrom M (1996) Reaction of the *Escherichia coli* Quinol Oxidase Cytochrome bo3 with

- Dioxygen: The Role of a Bound Ubiquinone Molecule. Proceedings of the National Academy of Sciences of the United States of America 93: 1545–1548.
45. van der Oost J, de Boer AP, de Gier JW, Zumft WG, Stouthamer AH, et al. (1994) The Heme-Copper Oxidase Family Consists of Three Distinct Types of Terminal Oxidases and is Related to Nitric Oxide Reductase. FEMS Microbiology Letters 121: 1–9.
 46. García-Horsman JA, Barquera B, Rumbley J, Ma J, Gennis RB (1994) The Superfamily of Heme-Copper Respiratory Oxidases. Journal of Bacteriology 176: 5587–5600.
 47. Keilin D, Hartree EF (1939) Cytochrome and Cytochrome Oxidase. Proceedings of the Royal Society of London Series B, Biological Sciences 127: pp. 167–191.
 48. Huang Y, Reimann J, Singh LMR, Adelroth P (2010) Substrate Binding and the Catalytic Reactions in Cbb3-type Oxidases: The Lipid Membrane Modulates Ligand Binding. Biochimica et Biophysica Acta 1797: 724–731.
 49. Buschmann S, Warkentin E, Xie H, Langer JD, Ermler U, et al. (2010) The Structure of cbb3 Cytochrome Oxidase Provides Insights into Proton Pumping. Science 329: 327–330.
 50. Zufferey R, Preisig O, Hennecke H, Thöny-Meyer L (1996) Assembly and Function of the Cytochrome cbb3 Oxidase Subunits in *Bradyrhizobium japonicum*. Journal of Biological Chemistry 271: 9114–9119.
 51. Preisig O, Zufferey R, Hennecke H (1996) The *Bradyrhizobium japonicum* fixGHIS Genes are Required for the Formation of the High-Affinity cbb3-type Cytochrome Oxidase. Archives of Microbiology 165: 297–305.
 52. Householder TC, Fozo EM, Cardinale JA, Clark VL (2000) Gonococcal Nitric Oxide Reductase is Encoded by a Single Gene, NorB, Which is Re-

- quired for Anaerobic Growth and is Induced by Nitric Oxide. *Infection and Immunity* 68: 5241–5246.
53. Wasser IM, de Vries S, Moënne-Locoz P, Schröder I, Karlin KD (2002) Nitric Oxide in Biological Denitrification: Fe/Cu Metalloenzyme and Metal Complex NO(x) Redox Chemistry. *Chemical Reviews* 102: 1201–1234.
 54. Barth KR, Isabella VM, Clark VL (2009) Biochemical and Genomic Analysis of the Denitrification Pathway within the Genus *Neisseria*. *Microbiology* 155: 4093–4103.
 55. Clark VL, Campbell LA, Palermo DA, Evans TM, Klimpel KW (1987) Induction and Repression of Outer Membrane Proteins by Anaerobic Growth of *Neisseria gonorrhoeae*. *Infection and Immunity* 55: 1359–1364.
 56. Weiss H, Friedrich T, Hofhaus G, Preis D (1991) The Respiratory-Chain NADH Dehydrogenase (Complex I) of Mitochondria. *European Journal of Biochemistry* 197: 563–576.
 57. Carroll J, Fearnley IM, Shannon RJ, Hirst J, Walker JE (2003) Analysis of the Subunit Composition of Complex I from Bovine Heart Mitochondria. *Molecular and Cellular Proteomics* 2: 117–126.
 58. Friedrich T, Böttcher B (2004) The Gross Structure of the Respiratory Complex I: a Lego System. *Biochimica et Biophysica Acta* 1608: 1–9.
 59. Yagi T (1991) Bacterial NADH-Quinone Oxidoreductases. *Journal of Bioenergetics and Biomembranes* 23: 211–225.
 60. Gemperli AC, Dimroth P, Steuber J (2002) The Respiratory Complex I (NDH I) from *Klebsiella pneumoniae*, a Sodium Pump. *Journal of Biological Chemistry* 277: 33811–33817.
 61. Thöny-Meyer L (1997) Biogenesis of Respiratory Cytochromes in Bacteria. *Microbiology and Molecular Biology Reviews* 61: 337–76.

62. Darrouzet E, Valkova-Valchanova M, Ohnishi T, Daldal F (1999) Structure and Function of the Bacterial bc1 Complex: Domain Movement, Subunit Interactions, and Emerging Rationale Engineering Attempts. *Journal of Bioenergetics and Biomembranes* 31: 275–288.
63. Snyder CH, Gutierrez-Cirlos EB, Trumpower BL (2000) Evidence for a Concerted Mechanism of Ubiquinol Oxidation by the Cytochrome bc 1 Complex. *Journal of Biological Chemistry* 275: 13535–13541.
64. Berry EA, Huang LS (2011) Conformationally Linked Interaction in the Cytochrome bc(1) Complex Between Inhibitors of the Q(o) Site and the Rieske Iron-Sulfur Protein. *Biochimica et Biophysica Acta* 1807: 1349–1363.
65. Crofts AR, Shinkarev VP, Kolling DRJ, Hong S (2003) The Modified Q-Cycle Explains the Apparent Mismatch Between the Kinetics of Reduction of Cytochromes c1 and bh in the bc1 Complex. *Journal of Biological Chemistry* 278: 36191–36201.
66. Wood PM (1983) Why do c-type Cytochromes Exist? *FEBS Letters* 164: 223–226.
67. Ambler RP (1991) Sequence Variability in Bacterial Cytochromes c. *Biochimica et Biophysica Acta* 1058: 42–47.
68. Chang HY, Ahn Y, Pace LA, Lin MT, Lin YH, et al. (2010) The Diheme Cytochrome C(4) from *Vibrio cholerae* is a Natural Electron Donor to the Respiratory cbb(3) Oxygen Reductase. *Biochemistry* 49: 7494–7503.
69. Clark VI, Isabella VM, Barth K, Overton TW (2010) Regulation and Function of the Neisserial Denitrification Pathway: Life with Limited Oxygen. In: Genco CA, Wetzler L, editors, *Neisseria: Molecular Mechanisms of Pathogenesis*, chap. 2, pp. 19–39, Caister Academic Press.

70. Edwards J, Cole LJ, Green JB, Thomson MJ, Wood AJ, et al. (2010) Binding to DNA Protects *Neisseria meningitidis* Fumarate and Nitrate Reductase Regulator (FNR) from Oxygen. *Journal of Biological Chemistry* 285: 1105–1112.
71. Overton TW, Whitehead R, Li Y, Snyder LAS, Saunders NJ, et al. (2006) Coordinated Regulation of the *Neisseria gonorrhoeae*-Truncated Denitrification Pathway by the Nitric Oxide-Sensitive Repressor, NsrR, and Nitrite-Insensitive NarQ-NarP. *Journal of Biological Chemistry* 281: 33115–33126.
72. Baart GJE, Zomer B, de Haan A, van der Pol LA, Beuvery EC, et al. (2007) Modeling *Neisseria meningitidis* Metabolism: From Genome to Metabolic Fluxes. *Genome Biol* 8: R136.
73. Baker SC, Ferguson SJ, Ludwig B, Page MD, Richter OM, et al. (1998) Molecular Genetics of the Genus Paracoccus: Metabolically Versatile Bacteria with Bioenergetic Flexibility. *Microbiology and Molecular Biology Reviews* 62: 1046–1078.
74. Nicholls DG, Ferguson SJ (1992) *Bioenergetics* 3. 2nd ed., Academic Press.
75. Bekker M, de Vries S, Ter Beek A, Hellingwerf KJ, de Mattos MJT (2009) Respiration of *Escherichia coli* can be fully uncoupled via the nonelectrogenic terminal cytochrome bd-II oxidase. *J Bacteriol* 191: 5510–5517.
76. Borisov VB, Murali R, Verkhovskaya ML, Bloch DA, Han H, et al. (2011) Aerobic Respiratory Chain of *Escherichia coli* is not Allowed to Work in Fully Uncoupled Mode. *Proc Natl Acad Sci U S A* 108: 17320–17324.
77. Ferguson SJ, Jackson JB, McEwan AG (1987) Anaerobic Respiration in the *Rhodospirillaceae*: Characterisation of Pathways and Evaluation of Roles in Redox Balancing During Photosynthesis. *FEMS Microbiology Reviews* 46: 117–143.

78. Daldal F, Mandaci S, Winterstein C, Myllykallio H, Duyck K, et al. (2001) Mobile Cytochrome c2 and Membrane-Anchored Cytochrome cy are Both Efficient Electron Donors to the cbb3- and aa3-Type Cytochrome c Oxidases During Respiratory Growth of *Rhodobacter sphaeroides*. *Journal of Bacteriology* 183: 2013–2024.
79. Pappas CT, Sram J, Moskvin OV, Ivanov PS, Mackenzie RC, et al. (2004) Construction and Validation of the *Rhodobacter sphaeroides* 2.4.1 DNA Microarray: Transcriptome Flexibility at Diverse Growth Modes. *Journal of Bacteriology* 186: 4748–4758.
80. Kahlem P, Birney E (2006) Dry Work in a Wet World: Computation in Systems Biology. *Molecular Systems Biology* 2: 40.
81. Doyle FJr, Stelling J (2006) Systems Interface Biology. *Journal of the Royal Society, Interface* 3: 603–16.
82. Kitano H (2002) Computational Systems Biology. *Nature* 420: 206–10.
83. Kitano H (2002) Systems Biology: A Brief Overview. *Science* 295: 1662–4.
84. Valencia A, Pazos F (2002) Computational Methods for the Prediction of Protein Interactions. *Current Opinion in Structural Biology* 12: 368–73.
85. Mündermann L, Erasmus Y, Lane B, Coen E, Prusinkiewicz P (2005) Quantitative Modeling of Arabidopsis Development. *Plant Physiology* 139: 960–8.
86. Prusinkiewicz P (2004) Modeling Plant Growth And Development. *Current Opinion in Plant Biology* 7: 79–83.
87. Prusinkiewicz P, Rolland-Lagan AG (2006) Modeling Plant Morphogenesis. *Current Opinion in Plant Biology* 9: 83–8.

88. Crampin EJ, Halstead M, Hunter P, Nielsen P, Noble D, et al. (2004) Computational Physiology and the Physiome Project. *Experimental Physiology* 89: 1–26.
89. Barabási AL, Oltvai ZN (2004) Network Biology: Understanding the Cell's Functional Organization. *Nature Reviews Genetics* 5: 101–13.
90. Peercy BE, Cox SJ, Shalel-Levanon S, San KY, Bennett G (2006) A Kinetic Model of Oxygen Regulation of Cytochrome Production in *Escherichia coli*. *Journal of Theoretical Biology* 242: 547–563.
91. Almeida JS, Reis MAM, Carrondo MJT (1997) A Unifying Kinetic Model of Denitrification. *Journal of Theoretical Biology* 186: 241–249.
92. Jin Q, Bethke CM (2003) A New Rate Law Describing Microbial Respiration. *Applied and Environmental Microbiology* 69: 2340–2348.
93. Cavaliere M, Ardelean II (2006) Applications of Membrane Computing, chap. Modeling Respiration in Bacteria and Respiration/Photosynthesis Interaction in Cyanobacteria Using a P System Simulator, pp. 129–158. Springer.
94. Klamt S, Grammel H, Straube R, Ghosh R, Gilles ED (2008) Modeling the Electron Transport Chain of Purple Non-Sulfur Bacteria. *Molecular Systems Biology* 4: 156.
95. Aguiar-González B, Packard TT, Berdalet E, Roy S, Gómez M (2012) Respiration Predicted From an Enzyme Kinetic Model and the Metabolic Theory of Ecology in Two Species of Marine Bacteria. *Journal of Experimental Marine Biology and Ecology* 412: 1 – 12.
96. Korzeniewski B (1996) Simulation of Oxidative Phosphorylation in Hepatocytes. *Biophys Chem* 58: 215–224.

97. Korzeniewski B (1996) Simulation of State 4 → State 3 Transition in Isolated Mitochondria. *Biophysical Chemistry* 57: 143–153.
98. Korzeniewski B (2001) Theoretical Studies on the Regulation of Oxidative Phosphorylation in Intact Tissues. *Biochimica et Biophysica Acta* 1504: 31–45.
99. Klipp E, Herwig R, Kowald A, Wierling C, Lehrach H (2005) Systems Biology in Practice. Concepts, Implementation and Application. WILEY-VCH Verlag GmbH & Co. KGaA, Weinheim.
100. Gillespie DT (1977) Exact Stochastic Simulation of Coupled Chemical Reactions. *The Journal of Physical Chemistry* 81: 2340–2361.
101. Sauro HM, Hucka M, Finney A, Wellock C, Bolouri H, et al. (2003) Next Generation Simulation Tools: The Systems Biology Workbench and BioSPICE Integration. *OMICS: A Journal of Integrative Biology* 7: 355–372.
102. Hoops S, Sahle S, Gauges R, Lee C, Pahle J, et al. (2006) COPASI—a COMplex PAthway SImulator. *Bioinformatics* 22: 3067–3074.
103. Radhakrishnan K, Hindmarsh AC (1993) Description and Use of LSODE, the Livermore Solver for Ordinary Differential Equations. Tech. rep., NASA.
104. Gibson MA, Bruck J (2000) Efficient Exact Stochastic Simulation of Chemical Systems with Many Species and Many Channels. *The Journal of Physical Chemistry A* 104: 1876–1889.
105. Mathematica (2008) version 7. Champaign, Illinois: Wolfram Research, Inc.
106. MATLAB (2010) version 7.10.0 (R2010a). Natick, Massachusetts: The MathWorks Inc.

107. Mendes P (1993) GEPASI: a Software Package for Modelling the Dynamics, Steady States and Control of Biochemical and Other Systems. Computer Applications in the Biosciences 9: 563–571.
108. Mendes P (1997) Biochemistry by Numbers: Simulation of Biochemical Pathways with Gepasi 3. Trends in Biochemical Sciences 22: 361–363.
109. Tomita M, Hashimoto K, Takahashi K, Shimizu TS, Matsuzaki Y, et al. (1999) E-CELL: Software Environment for Whole-Cell Simulation. Bioinformatics 15: 72–84.
110. Wierling C, Herwig R, Lehrach H (2007) Resources, Standards and Tools for Systems Biology. Briefings in Functional Genomics and Proteomics 6: 240–251.
111. Funahashi A, Morohashi M, Kitano H, Tanimura N (2003) CellDesigner: A Process Diagram Editor for Gene-Regulatory and Biochemical Networks. BIOSILICO 1: 159 – 162.
112. Funahashi A, Matsuoka Y, Jouraku A, Kitano H, Kikuchi N (2006) CellDesigner: A Modeling Tool for Biochemical Networks. In: Proceedings of the Winter Simulation Conference. WSC 06, pp. 1707–1712.
113. Funahashi A, Matsuoka Y, Jouraku A, Morohashi M, Kikuchi N, et al. (2008) CellDesigner 3.5: A Versatile Modeling Tool for Biochemical Networks. Proceedings of the IEEE 96: 1254–1265.
114. Puchałka J, Kierzek AM (2004) Bridging the Gap Between Stochastic and Deterministic Regimes in the Kinetic Simulations of the Biochemical Reaction Networks. Biophysical Journal 86: 1357–1372.
115. McGuinness B, Barlow AK, Clarke IN, Farley JE, Anilionis A, et al. (1990) Deduced Amino Acid Sequences of Class 1 Protein (Pora) from Three Strains of *Neisseria meningitidis*. Synthetic Peptides Define the Epitopes

- Responsible for Serosubtype Specificity. *Journal of Experimental Medicine* 171: 1871–1882.
116. Clark LC, Wolf R, Granger D, Taylor Z (1953) Continuous Recording of Blood Oxygen Tensions by Polarography. *Journal of Applied Physiology* 6: 189–193.
117. Rank Brothers Ltd (2012) Oxygen Electrode Exploded Views. <http://www.rankbrothers.co.uk/prod1exp.htm>.
118. YSI Incorporated (2012) Oxygen Solubility Table. <http://www.ysi.com/media/pdfs/DO-Oxygen-Solubility-Table.pdf>.
119. Liu X, Liu Q, Gupta E, Zorko N, Brownlee E, et al. (2005) Quantitative Measurements of NO Reaction Kinetics with a Clark-Type Electrode. *Nitric Oxide* 13: 68 – 77.
120. Bedioui F, Villeneuve N (2003) Electrochemical Nitric Oxide Sensors for Biological Samples: Principle, Selected Examples and Applications. *Electroanalysis* 15: 5–18.
121. Serpe MJ, Zhang X (2007) The Principles, Development and Application of Microelectrodes for the In Vivo Determination of Nitric Oxide. In: Michael AC, Borland LM, editors, *Electrochemical Methods for Neuroscience*, chap. 21, CRC Press.
122. Nicholas DJ, Nason A (1957) Determination of Nitrate and Nitrite. In: *Methods in Enzymology*, vol. 3, pp. 981–984, Academic Press.
123. Aga RG, Hughes MN (2008) The Preparation and Purification of NO Gas and the Use of NO Releasers: The Application of NO Donors and Other Agents of Nitrosative Stress in Biological Systems. In: Poole RK, editor, *Globins and Other Nitric Oxide-Reactive Proteins, Part A*, vol. 436 of *Methods in Enzymology*, pp. 35 – 48, Academic Press.

124. Cole LJ, Huston WM, Moir JWB (2008) Delivery of Nitric Oxide for Analysis of the Function of Cytochrome C'. In: Poole RK, editor, Globins and Other Nitric Oxide-Reactive Proteins, Part A, vol. 436 of Methods in Enzymology, pp. 21 – 33, Academic Press.
125. Blomberg LM, Blomberg MR, Siegbahn PE (2005) A Theoretical Study on the Binding of O₂, NO and CO to Heme Proteins. *Journal of Inorganic Biochemistry* 99: 949 – 958.
126. Giuffre A, Barone MC, Mastronicola D, D'Itri E, Sarti P, et al. (2000) Reaction of Nitric Oxide with the Turnover Intermediates of Cytochrome c Oxidase: Reaction Pathway and Functional Effects. *Biochemistry* 39: 15446–15453.
127. Forte E, Urbani A, Saraste M, Sarti P, Brunori M, et al. (2001) The Cytochrome cbb3 from *Pseudomonas stutzeri* Displays Nitric Oxide Reductase Activity. *European Journal of Biochemistry* 268: 6486–6491.
128. Hunter H (2007) Characterisation of the Oxidase Activity in *Neisseria lactamica*, University of York BSc Honours Project Report.
129. Nojiri M, Koteishi H, Nakagami T, Kobayashi K, Inoue T, et al. (2009) Structural Basis of Inter-Protein Electron Transfer for Nitrite Reduction in Denitrification. *Nature* 462: 117–120.
130. Blackmore RS, Greenwood C, Gibson QH (1991) Studies of the Primary Oxygen Intermediate in the Reaction of Fully Reduced Cytochrome Oxidase. *Journal of Biological Chemistry* 266: 19245–9.
131. Hedrick DB, White DC (1986) Microbial Respiratory Quinones in the Environment: I. A Sensitive Liquid Chromatographic Method. *Journal of Microbiological Methods* 5: 243 – 254.

132. Holländer R, Wolf G, Mannheim W (1977) Lipoquinones of Some Bacteria and Mycoplasmas, with Considerations on their Functional Significance. *Antonie van Leeuwenhoek* 43: 177–185.
133. Butcher JC (2003) Numerical Methods for Ordinary Differential Equations. John Wiley and Sons.
134. Cash JR, Karp AH (1990) A Variable Order Runge-Kutta Method for Initial Value Problems with Rapidly Varying Right-hand Sides. *ACM Transactions on Mathematical Software* 16: 201–222.
135. Press WH, Teukolsky SA, Vetterling WT, Flannery BP (1992) Numerical Recipes in C. 2nd ed., Cambridge University Press.
136. Nakamura (Particle Data Group) K (2010) Review of Particle Physics. *Journal of Physics G: Nuclear and Particle Physics* 37: 075021 and 2011 partial update for the 2012 edition.
137. Gilks W, Richardson S, Spiegelhalter D (1996) Markov Chain Monte Carlo in Practice. Chapman & Hall/CRC.
138. Kirkpatrick S, Gelatt CD, Vecchi MP (1983) Optimization by Simulated Annealing. *Science* 220: pp. 671–680.
139. Černý V (1985) Thermodynamical Approach to the Traveling Salesman Problem: An Efficient Simulation Algorithm. *Journal of Optimization Theory and Applications* 45: 41–51.
140. Bertsimas D, Tsitsiklis J (1993) Simulated Annealing. *Statistical Science* 8: pp. 10–15.
141. Marjoram P, Molitor J, Plagnol V, Tavaré S (2003) Markov Chain Monte Carlo without Likelihoods. *Proceedings of the National Academy of Sciences of the United States of America* 100: 15324–15328.

142. Toni T, Welch D, Strelkowa N, Ipsen A, Stumpf MPH (2009) Approximate Bayesian Computation Scheme for Parameter Inference and Model Selection in Dynamical Systems. *Journal of The Royal Society Interface* 6: 187.
143. Ronquist F, Teslenko M, van der Mark P, Ayres D, Darling A, et al. (2011) MrBayes 3.2: Efficient Bayesian Phylogenetic Inference and Model Choice Across a Large Model Space. *Systematic Biology* in press: 0–0.
144. Beaumont MA, Zhang W, Balding DJ (2002) Approximate Bayesian Computation in Population Genetics. *Genetics* 162: 2025–2035.
145. Sisson SA, Fan Y, Tanaka MM (2007) Sequential Monte Carlo Without Likelihoods. *Proceedings of the National Academy of Sciences of the United States of America* 104: 1760–1765.
146. Beaumont MA (2010) Approximate Bayesian Computation in Evolution and Ecology. *Annual Review of Ecology, Evolution, and Systematics* 41: pp. 379–406.
147. Metropolis N, Rosenbluth AW, Rosenbluth MN, Teller AH, Teller E (1953) Equation of State Calculations by Fast Computing Machines. *The Journal of Chemical Physics* 21: 1087–1092.
148. Hastings WK (1970) Monte Carlo Sampling Methods Using Markov Chains and Their Applications. *Biometrika* 57: 97–109.
149. Lotka A (1925) Elements of Physical Biology. Williams and Wilkins, Baltimore.
150. Volterra V (1931) Animal Ecology, pp. 409–448. McGraw-Hill, New York.
151. Gelman A, Rubin DB (1992) Inference from Iterative Simulation Using Multiple Sequences. *Statistical Science* 7: pp. 457–472.

152. Brooks SP, Gelman A (1998) General Methods for Monitoring Convergence of Iterative Simulations. *Journal of Computational and Graphical Statistics* 7: 434–455.
153. Curran J (2011) Bolstad2: Bolstad functions.
154. R Development Core Team (2010) R: A Language and Environment for Statistical Computing. R Foundation for Statistical Computing, Vienna, Austria.
155. Otten MF, Reijnders WN, Bedaux JJ, Westerhoff HV, Krab K, et al. (1999) The Reduction State of the Q-pool Regulates the Electron Flux Through the Branched Respiratory Network of *Paracoccus denitrificans*. *European Journal of Biochemistry* 261: 767–774.
156. Hunter JD (2007) Matplotlib: A 2D Graphics Environment. *Computing in Science & Engineering* 9: 90–95.
157. Pettersen EF, Goddard TD, Huang CC, Couch GS, Greenblatt DM, et al. (2004) UCSF Chimera—A Visualization System for Exploratory Research and Analysis. *J Comput Chem* 25: 1605–1612.